High-Speed Compensation of the Meniscus Effect in Phase Contrast Microscopy

High-Speed-Kompensation des Meniskuseffekts bei der Phasenkontrastmikroskopie

Von der Fakultät für Maschinenwesen
der Rheinisch-Westfälischen Technischen Hochschule Aachen
zur Erlangung des akademischen Grades eines Doktors
der Ingenieurwissenschaften genehmigte Dissertation

vorgelegt von

Florian Nienhaus, geb. Narrog

Berichter: Univ.-Prof. Dr.-Ing. Robert Schmitt
Univ.-Prof. Dr. rer. nat. Dipl.-Ing. Carlo Holly

Tag der mündlichen Prüfung: 28.01.2026

Diese Dissertation ist auf den Internetseiten der Universitätsbibliothek online verfügbar.

Vorwort

Diese Arbeit entstand während meiner Tätigkeit als wissenschaftlicher Mitarbeiter in der Abteilung Produktionsmesstechnik am Fraunhofer-Institut für Produktionstechnologie IPT. Ich kann mich glücklich schätzen, dort frühzeitig ein spannendes Forschungsprojekt zur eigenverantwortlichen Bearbeitung gefunden zu haben, auf dessen Ergebnissen ich diese Dissertation aufbauen konnte. Dies war nur möglich durch die Unterstützung durch meinen Doktorvater Prof. Dr. Robert Schmitt, der mir ausgezeichnete Rahmenbedingungen am Institut ermöglichte. Außerdem hatte ich viel Unterstützung durch meinen Abteilungsleiter Niels König, welcher mir von der Ideenfindung bis zur finalen Abgabe immer zur Seite stand und mir gleichzeitig die Freiheit zur eigenständigen Bearbeitung des Projekts gegeben hat.

Vielen weiteren Dank gilt meinen Gruppenleitern während dieser Zeit, erst Dr. Bastian Nießing und anschließend Caroline Girmen, welche mich in großem Maße unterstützt haben. Dies gilt allgemein für meine Kollegen aus dem Bereich 300 und des gesamten IPT. Mich freut insbesondere die Mentalität, sich gegenseitig zu unterstützen, ohne eine Gegenleistung zu verlangen – das ist nicht überall selbstverständlich. Hierdurch habe ich fachlich sehr profitiert. Fast noch wichtiger aber waren gemeinsame Freizeitaktivitäten als wichtige Ablenkung von der stressigen Doktorarbeit.
Unter meinen Kollegen möchte ich mich insbesondere bei Dr. Andreas Mathwieser, Caroline Girmen, Dr. Kai Janning, Alexander Mattern und David Hellmann für das Korrekturlesen dieser Arbeit und die hilfreichen Hinweise darüber hinaus bedanken.

Neben meinen Kollegen aus der Abteilung haben Abschlussarbeiter und studentische Hilfskräfte einen bedeutenden Beitrag zu dieser Arbeit geleistet. Insbesondere Konstantin Zlobin, Benedikt Grzeschik, Jonas Krämer, Finn Burkhardt und Johannes Audy möchte ich für ihren Einsatz und qualitativ hochwertige Arbeit danken.

Mein größter Dank gilt meiner Familie, insbesondere meiner Frau Hannah, die mich unentwegt unterstützt hat. Ich bin mir bewusst, dass wir uns schönere Abende hätten machen können als die vielen, die ich nur am Schreibtisch verbracht habe. Dies habe ich nicht zuletzt für unseren Sohn Karl gemacht, dessen nahende Geburt mich umso stärker motiviert hat, diese Arbeit zeitig zu Ende zu bringen. Ich freue mich nun darauf, Zeit mit meiner Familie zu verbringen und dabei zu wissen, diesen anstrengenden, aber erfüllenden Schritt hinter mir zu haben.

Aachen, 1. Februar 2026

Abstract

The trend towards laboratory automation has resulted in an increasing demand for efficient quality control of cell cultures, driving the development of high-throughput solutions. A widely used method in quality control in cell cultivation is phase contrast microscopy, as it allows for the visualization of high-contrast images without requiring cell staining. However, its effectiveness is limited by the meniscus effect, which confines the visible region in cell culture vessels, such as microtiter plates (MTPs), to the small flat center of each well. Moreover, state-of-the-art phase contrast microscopy is time-consuming for large samples. This thesis addresses both limitations by exploring a rapid method to counteract the meniscus effect in well plates, enabling the acquisition of high-contrast composite images across entire wells.

A meniscus effect compensation technique termed *adaptive phase contrast microscopy* is developed, which inserts adaptive elements into the microscope's illumination path. Experiments revealed that replacing the fixed condenser annulus with a Liquid Crystal Display (LCD) yields the best results among adaptive elements, outperforming an adjustable liquid-filled prism. High-speed imaging is achieved through a continuous scanning technique that captures numerous microscopy images during sample movement, which are subsequently stitched into a large composite image. The LCD adaptively modifies the illumination for each image to compensate for the meniscus effect.

To evaluate the phase contrast area within MTPs, the relative background intensity in images proved to be a reliable indicator of phase contrast conditions. Experimental results demonstrate that adaptive phase contrast microscopy significantly enhances the phase contrast area. The phase contrast area increased up to ninefold, depending on the MTP type and magnification used. Key factors influencing the phase contrast area include the magnification and numerical aperture of the objective lens, shading from the well walls, image field curvature, and total internal reflection at steep surface angles. Notably, the rapid acquisition speed, matching the LCD's refresh rate of 60 Hz, did not compromise image quality.

Furthermore, experiments demonstrated that imaging durations could be effectively reduced to be only slightly slower than those achieved by high-speed microscopy for conventional phase contrast microscopy, and up to 25 times faster than traditional stop-and-go methods. Crucial factors affecting acquisition speed include the LCD's refresh rate and latency, the necessity to limit acceleration to prevent liquid sloshing, and the range of the microscope stage.

In conclusion, it was demonstrated that the phase contrast area in MTPs can be significantly enhanced through meniscus effect compensation, and high-speed imaging is feasible without degrading image quality.

Zusammenfassung

Der Trend zu vollständig automatisierten Laboren steigert die Nachfrage nach Qualitätskontrolle von Zellkulturen und treibt die Entwicklung von Hochdurchsatzmethoden voran. Eine weitverbreitete Methode zur Qualitätskontrolle bei der Zellkultivierung ist die Phasenkontrastmikroskopie. Ihre Wirksamkeit wird jedoch durch den Meniskuseffekt eingeschränkt, der den sichtbaren Bereich in Zellkulturgefäßen wie Mikrotiterplatten (MTPs) auf die kleine flache Mitte jedes Wells beschränkt. Darüber hinaus benötigt Phasenkontrastmikroskopie sehr lange, um große Proben zu scannen. Diese Arbeit adressiert beide Herausforderung durch die Entwicklung eines Verfahrens, das den Meniskuseffekt in MTPs kompensiert, um kontrastreiche Bilder vollständiger Wells aufzunehmen.

Dazu wird die Technik der *adaptiven Phasenkontrastmikroskopie* entwickelt, bei der adaptive Komponenten in den Beleuchtungspfad des Mikroskops integriert werden. Experimente zeigen, dass der Austausch der festen Ringblende durch einen Flüssigkristallbildschirm (LCD) die besten Ergebnisse aller adaptiven Komponenten hinsichtlich Bildqualität und Geschwindigkeit liefert. Hochgeschwindigkeits-Bildaufnahmen werden durch eine Scan-Methode mit kontiuierlicher Probenbewegung erzeugt, bei der Bilder fortlaufend aufgenommen werden. Gleichzeitig passt das LCD die Beleuchtung zur Meniskuskompensation in Echtzeit an, was eine signifikante Vergrößerung der Phasenkontrastfläche ermöglicht.

Zur Evaluierung dieser Fläche hat sich ein Verfahren auf Basis der relativen Hintergrundintensität als zuverlässig erwiesen. Die Phasenkontrastfläche konnte je nach MTP-Typ und Vergrößerung um das bis zu Neunfache gesteigert werden. Die Vergrößerung und numerische Apertur des Objektivs, Abschattung durch Well-Wände, Bildfeldwölbung und Totalreflexion stellen wesentliche Einflussfaktoren auf diesen Wert dar. Die hohe Aufnahmegeschwindigkeit, die der Bildwiederholrate des LCDs von 60 Hz entspricht, beeinträchtigt die Phasenkontrastfläche dagegen nicht.

Darüber hinaus belegen Experimente, dass die Dauer der Bildaufnahme so weit reduziert werden kann, dass dieser Prozess nur geringfügig langsamer ist als die High-Speed-Mikroskopie bei Standard-Phasenkontrastmikroskopie und bis zu 25-mal schneller als herkömmliche Stop-and-Go-Methoden. Hierbei bilden die Bildwiederholrate und die Latenzzeit des LCD-Bildschirms, die Begrenzung der Beschleunigung zur Vermeidung von Flüssigkeitsschwappen und der Verfahrbereich des Mikroskoptisches limitierende Faktoren.

Zusammenfassend zeigt sich, dass durch die Kompensation des Meniskuseffekts die Phasenkontrastfläche in MTPs erheblich vergrößert werden kann, und dass Hochgeschwindigkeitsaufnahmen ohne Beeinträchtigung der Bildqualität möglich sind, was die Anwendbarkeit der Phasenkontrastmikroskopie in der Zellkulturüberwachung erheblich verbessert.

Contents

1 Introduction

Biotechnology has emerged as a rapidly expanding industry that has garnered significant attention in the 21st century [Mar21]. It is a driving force behind advancements and innovations in medicine, facilitating the development of personalized medicine, novel therapies, and targeted treatments [Gui22; Hop20]. These advancements necessitate a substantial increase in the production of biotechnological products, rendering manual laboratory processes insufficient for both their development and manufacture [Bie21]. To enhance throughput and manage increasingly complex processes, laboratory tasks currently performed manually must be automated [Jai11; Lip19].

A crucial aspect of laboratory automation is cell cultivation, such as for the development of advanced therapy medicinal products (ATMPs) [Och22]. Automated cell culture systems provide precise control over environmental parameters, resulting in enhanced experimental reproducibility, reduced variability, and increased throughput. To achieve these benefits, advanced screening methods are essential for monitoring cell cultures throughout all growth phases [Bou15]. For efficient automated cell cultivation, a screening method must support high-throughput capabilities.

Microscopy is one of the most prevalent methods for cell screening today. Phase contrast microscopy, invented by Frits Zernike in the 1930s, is widely utilized for observing transparent objects [Pip12; Zer42]. This technique allows for the visualization of living cells by increasing the contrast without the need for staining or labeling, thereby avoiding harm to the cells and serving as a common alternative to fluorescence microscopy [Dav07; Yin12].

However, phase contrast microscopy faces a challenge known as the meniscus effect [Hor06; Mur12]. This effect arises because cells are typically cultivated in transparent plastic vessels, known as microtiter plates (MTPs), which allow for the simultaneous growth of individual cell cultures in separate cylindrical wells filled with cell culture medium. Due to capillary forces, the surface of the medium is not flat but forms a liquid lens, referred to as the meniscus [Fuc23]. The refraction caused by the meniscus curvature reduces image contrast near the edges of a well. Consequently, only a limited area within a cell culture vessel is observable using phase contrast microscopy – this area is referred to as *phase contrast area* within this thesis. The observable area varies from approximately 30% to less than 2%, contingent upon the well diameter. The severity of the meniscus effect is more pronounced in vessels with smaller diameters.

This limitation to phase contrast microscopy poses a significant challenge for applications aiming for 100% quality control, such as drug discovery [Bla20; Lin20]. Additionally, because cell cultures experience varying growth conditions due to differential access to resources,

growth within MTPs can be inhomogeneous, making it misleading to observe only the center of a well [Man21]. Nevertheless, the increasing demand for higher throughput drives the use of MTPs with more wells and smaller diameters, thus exacerbating the impact of the meniscus effect [Fuc23].

Phase contrast microscopy is also a time-consuming process. Given that laboratory automation aims to boost throughput, there is a significant demand to speed up microscopy methods [Sch15]. One strategy to enhance throughput is high-speed microscopy (HSM), initially proposed by Friedrich Schenk [Sch16a]. This approach captures high-resolution images of large samples by continuously acquiring images as the sample moves. As a result, MTPs can be imaged within minutes, as opposed to taking three hours or more. However, this method has only been employed with conventional phase contrast microscopy so far, meaning the meniscus effect remains unaddressed.

This thesis aims to address these challenges by introducing a high-throughput phase contrast microscopy technique designed to compensate for the meniscus effect. It will assess the factors that influence phase contrast conditions and imaging time. The proposed method, termed *adaptive high-speed phase contrast microscopy*, aims to automatically capture high-resolution images of entire MTPs, achieving phase contrast conditions extending closer to the edge of a well. To accomplish this, a mechanism counteracting the refraction induced by the meniscus effect will be investigated to restore optimal phase contrast conditions. Initially, the thesis focuses on phase contrast compensation without incorporating the high-throughput component; in this context, the method is termed *adaptive phase contrast microscopy*.

The primary objective of this thesis is to explore a method that effectively enlarges the observable area in cell culture vessels via phase contrast microscopy, utilizing a high-speed scanning approach to minimize acquisition time. Thus, the main research question is:

Can the optical compensation of the meniscus effect in phase contrast microscopy be performed during sample movement in combination with continuous image acquisition?

This main research question is further supplemented by sub-research questions (SRQs), which will be formulated through an analysis of the state of the art in Chapter 3.

1.1 Research Procedure

The research procedure of this thesis is based on the empirical sciences research methodology as outlined by Ulrich [Ulr81], contrasting with the more theoretical approaches typical of formal sciences. This approach is selected because the problem originates from observations of real-world issues in practical applications. A solution is thus developed and evaluated in close connection with these applications. The goal is to create a solution that

can be implemented in practice without the need for completely redeveloping phase contrast microscopes.

The initial step of this thesis involves analyzing scientific and technical literature to investigate existing solutions. Useful existing methodologies are adapted for specific sub-problems and integrated with newly developed problem-specific theories to construct a framework capable of addressing the thesis's specific problem. Solution strategies are iteratively evaluated through experimental testing. Implementing and assessing these strategies forms a critical component of the research process.
Ultimately, a comprehensive solution approach is developed, integrating strategies for partial problems. Validation is performed using a practice-relevant use case, namely the observation of mesenchymal stem cells (MSCs). Results are compared with existing approaches and analyzed within their application context to underscore practical relevance.

1.2 Structure of the Thesis

This thesis is organized into eight chapters, which are introduced in this section. Figure 1.1 illustrates how the seven steps of Ulrich's research methodology correspond to the chapters of this thesis. Each SRQ is explored in an individual chapter. These chapters detail the methodology specific to the SRQ, along with experiments and validation processes.

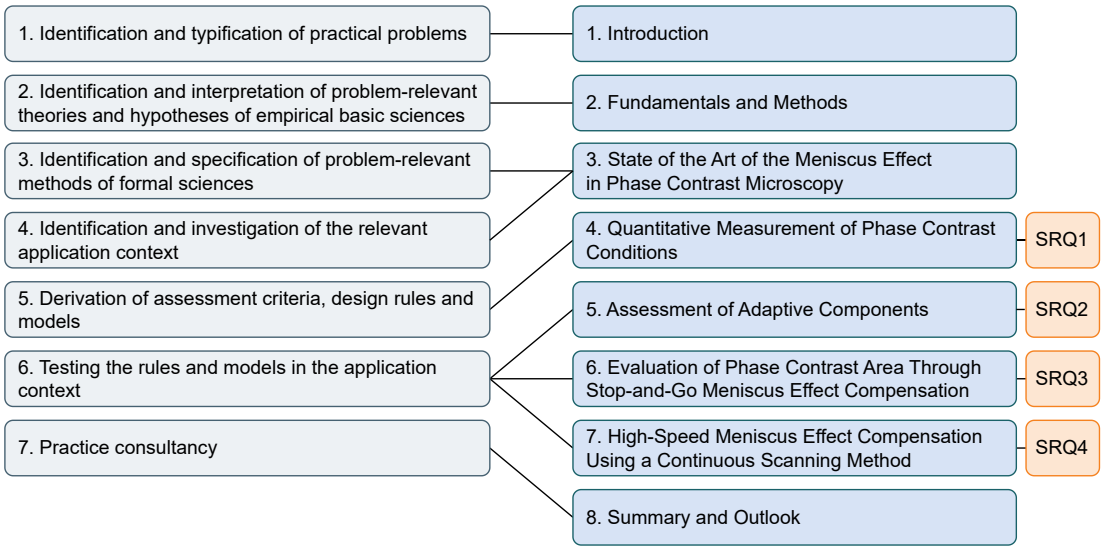

Figure 1.1: Thesis structure in correspondence to Ulrich [Ulr81].

Chapter 1 – Introduction This chapter sets the research context and articulates the main research question. The methodology underlying the research is outlined, and the thesis structure is contextualized within this framework.

Chapter 2 – Fundamentals and Methods Chapter 2 presents essential concepts that are crucial for understanding this thesis. It provides an overview of the methods commonly applied throughout the thesis, encompassing optical principles, light microscopy, optoelectronic devices and equipment utilized in phase contrast microscopy, as well as digital image processing techniques.

Chapter 3 – State of the Art of the Meniscus Effect in Phase Contrast Microscopy Chapter 3 focuses on the meniscus effect observed in cell cultures within MTPs and explores mitigation strategies. The application of high-speed microscopy for biological samples is initially examined. Subsequently, the causes and impacts of the meniscus effect are analyzed. The chapter then examines methods to quantify the area within an MTP that is unaffected by the meniscus effect, where optimal phase contrast conditions can be established. A systematic literature review assesses existing approaches to counteract the meniscus effect and identifies their limitations. This review leads to the identification of research gaps and the formulation of four SRQs.

Chapter 4 – Quantitative Measurement of Phase Contrast Conditions Chapter 4 is devoted to developing a metric for quantifying phase contrast conditions within an MTP. Such a metric is crucial for validating the solution against existing methods, prompting a study to identify suitable criteria. One criterion is identified that effectively indicates phase contrast conditions within a cell culture vessel. Based on this criterion, an algorithm is devised to quantify the phase contrast area within a well in an MTP.

Chapter 5 - Assessment of Adaptive Components The analysis of the state of the art concludes that adaptive optical components are necessary to compensate for refraction at the meniscus surface across the MTP. Chapter 5 conceptualizes various adaptive components to regulate the light beam path within the microscope. These components are evaluated based on specific criteria through general considerations, experiments, and optical simulations.

Chapter 6 - Evaluation of Phase Contrast Area through Stop-and-Go Meniscus Effect Compensation Chapter 6 details a measurement procedure designed to maximize the phase contrast area. A demonstrator setup is developed, incorporating an adaptive component. The chapter includes the development of the procedure and its validation through experiments. To mitigate issues associated with high-speed imaging using continuous scanning and to provide a reference for subsequent experiments, this procedure utilizes a stop-and-go scanning process, pausing for each image acquisition. An empirical method is also devised to calculate optimal parameters for the adaptive components. Experimental validation determines the phase contrast area for various MTP types and magnifications.

Chapter 7 - High-Speed Meniscus Effect Compensation using a Continuous Scanning Method Chapter 7 expands upon the methodology from Chapter 6 to enhance acquisition time by employing high-speed image acquisition during continuous sample movement. This chapter presents an advanced concept, its experimental validation, and a discussion of the results. Initially, the chapter discusses the factors that limit acquisition time. Subsequently, the procedure and its software implementation are developed. Comprehensive validation through experiments is conducted to evaluate acquisition time and assess the impact of high-speed scanning on the phase contrast area. Finally, the results are discussed and compared to competing approaches.

Chapter 8 - Summary and Outlook Chapter 8 summarizes the thesis and evaluates its results. The outlook presents ideas for further scientific utilization of the project results.

2 Fundamentals and Methods

This chapter presents key concepts essential for understanding the methodologies and frameworks discussed in this thesis, along with the methods employed. Section 2.1 outlines optical principles pertinent to phase contrast microscopy and the adaptive elements utilized to mitigate the meniscus effect. The fundamentals of light microscopy for cell observation in general and phase contrast microscopy in particular are outlined in Section 2.2. Optoelectronic devices, which are designed to convert light into electrical signals or vice versa, are detailed in Section 2.3, including scientific cameras. Images captured by scientific cameras in microscopy are typically subjected to digital image processing for analysis. Given the reliance of several methods in this thesis on image processing, foundational techniques in digital image processing are delineated in Section 2.4.

2.1 Optical Principles Relevant for Adaptive Phase Contrast Microscopy

Phase contrast microscopy employs visible light, consisting of electromagnetic waves with wavelengths ranging from 380 nm to 740 nm, to capture magnified images of specimens [Mur12; Nec22]. The formation of images involves various optical effects, which can be categorized into *ray optics* and *wave optics* [Bor86]. Wave optics are applicable when the interacting objects are similar in size to the wavelength, whereas ray optics are suitable for scenarios where the wavelength is significantly smaller than the object [Sal20]. This section explores the pertinent optical phenomena for phase contrast microscopy, starting with wave optics before addressing ray optics. A detailed introduction to the operational principle of phase contrast microscopes is afterwards provided in Section 2.2.

2.1.1 Interference

When multiple electromagnetic waves coexist in space and time, they collectively form a combined wave function. This resultant wave function arises from the superposition of all individual wave functions [Sal20]. However, the optical intensity of this resultant wave is not simply the sum of the individual intensities due to the phenomenon known as *interference*. For two monochromatic waves with complex amplitudes, their superposition can be

mathematically expressed by Equation 2.1 [Sal20]:

$$U\left(\vec{r},t\right)=U_1\left(\vec{r},t\right)+U_2\left(\vec{r},t\right), \tag{2.1}$$

where U, U_1, and U_2 represent the complex amplitudes, and $\vec{r}$ denotes the spatial position and t the time. The relationship between a wave's amplitude U_1 and its intensity I_1 is given by Equation 2.2 [Sal20]:

$$U_1=\sqrt{I_1}\exp\left(i\phi_i\right), \tag{2.2}$$

where ϕ signifies the phase of the light and i is the imaginary number. Transforming Equation 2.2 leads to Equation 2.3:

$$I_1=\left\|U_1\right\|^2, \tag{2.3}$$

where the $\|$ operator denotes the absolute value in terms of the time t. Substituting Equations 2.1, 2.2, and 2.3 into each other results in Equation 2.4, which is called the *interference equation* [Sal20]:

$$I=I_1+I_2+2\sqrt{I_1I_2}\cos\phi \tag{2.4}$$

with $\phi=\phi_2-\phi_1$. This equation underscores that, due to its non-linearity, during the superposition of two light waves, the individual intensities cannot be simply added. Instead, the resultant intensity is dependent on the phase difference between the two waves. When both waves possess identical amplitudes, such as when originating from the same source, and the phase difference is $\phi=0$, the interference equation simplifies to Equation 2.5 [Sal20]:

$$I=I_1+I_1+2\sqrt{I_1I_1}\cos 0=4I_1, \tag{2.5}$$

resulting in an amplitude described by Equation 2.6 [Sal20]:

$$U=2U_i. \tag{2.6}$$

This phenomenon is known as *constructive interference*. Conversely, if the phase difference is $\phi=\pi$, the intensity becomes $I=0$, and consequently the amplitude $U=0$. This is referred to as *destructive interference*. In cases where two waves with different wavelengths interfere, the superposition must be calculated by integrating the wave functions over all wavelengths, which can be accomplished using a Fourier transform.

2.1.2 Diffraction

Diffraction is a phenomenon that occurs when light waves encounter an obstacle or aperture, causing them to bend or spread, as explained by Huygens' principle [Sal20]. This bending enables light to illuminate regions that would otherwise be in the shadow of the obstacle. When a light beam traverses multiple small apertures, the secondary wavelets produced by each aperture interfere with each other, resulting in characteristic interference patterns. This effect is most pronounced when the aperture size is on the order of the wavelength of the light. Diffraction through one or more apertures can be mathematically described by

Equation 2.7 [Bor86]:

$$w \sin \theta_n = n\lambda \tag{2.7}$$

where w represents the aperture width, n is a positive integer, λ denotes the light's wavelength, and θ_n is the angle corresponding to the n$^{\text{th}}$ minimum of light intensity.

2.1.3 Polarization

In an electromagnetic wave, the magnetic field B and the electric field H are orthogonal to each other and the direction of light propagation, as illustrated in Figure 2.1 [Nec22].

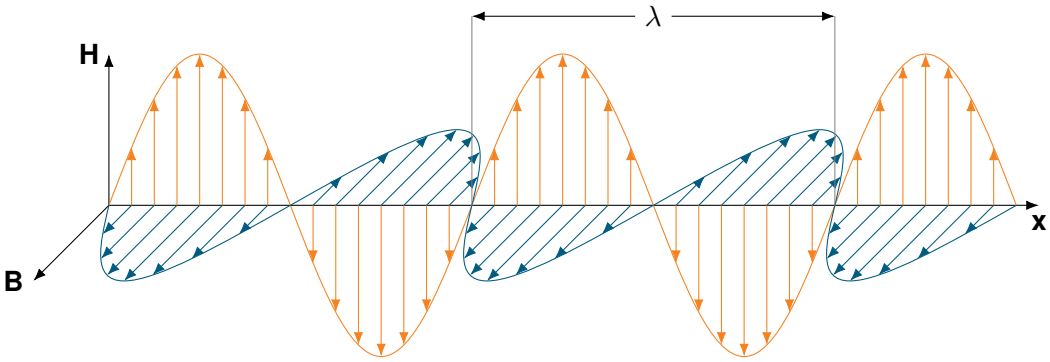

Figure 2.1: Electromagnetic wave with wavelength λ (adapted from [Com23]).

A light ray typically consists of multiple waves that travel in the same direction [Haz22]. When all these waves oscillate in a single plane, they are termed linearly polarized. The polarization direction is defined by the orientation of the electric field. Light can oscillate entirely within the plane of the electric field, referred to as *transverse electric* or *s-polarized*, or entirely within the plane of the magnetic field, known as *transverse magnetic* or *p-polarized*. Besides linear polarization, circular and elliptical polarizations are also possible.
In natural light and most artificial light sources, the orientation of wave oscillations is random, resulting in unpolarized light. Polarized light can be generated from unpolarized light by passing it through a polarization filter (also called a *polarizer*), which permits only the component of light waves aligned with a specific polarization direction to pass through. When already polarized light traverses a polarizer, the intensity of the transmitted light is reduced according to *Malus's law*, expressed in Equation 2.8 [Mur12]:

$$I = I_0 \cos^2 \xi, \tag{2.8}$$

where I is the intensity after the polarizer, I_0 is the initial intensity, and ξ is the angle between the polarization axis of the incoming light and the polarizer. Consequently, light aligned with the polarizer's orientation remains unaffected, whereas light perpendicular to it is completely blocked.

2.1.4 Reflection and Refraction

When light encounters the boundary between two phases, it undergoes *reflection* and *refraction*. This principle is most effectively described using ray optics. Reflection occurs when part or all of the incident ray is redirected back into the original medium, maintaining the same angle of reflection $\theta_{\text{reflection}}$ as the angle of incidence θ_i, relative to the normal vector perpendicular to the surface, as expressed by Equation 2.9 [Gre04]:

$$\theta_{\text{reflection}} = \theta_i. \tag{2.9}$$

The remaining portion of the light is refracted, meaning it enters the second medium and changes its direction. Figure 2.2 demonstrates a light ray transitioning from a less dense to a denser medium, with components both reflected and refracted. The angle of refraction, θ_r, can be calculated from the angle of incidence using Equation 2.10, which is called *Snell's law* [Gre04]:

$$n_1 \sin(\theta_i) = n_2 \sin(\theta_r), \tag{2.10}$$

where n_1 and n_2 denote the refractive indices of the initial and subsequent media, respectively. In a denser optical medium, the angle θ is smaller due to the medium's higher refractive index.

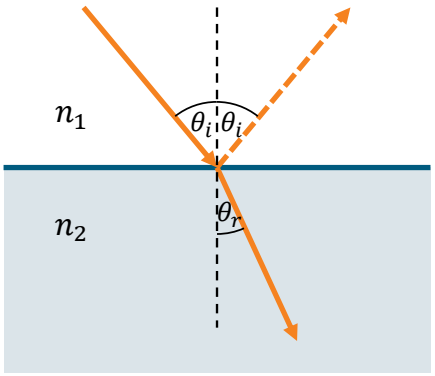

Figure 2.2: Principle of refraction and reflection (adapted from [Gre04]). The relationship between the refractive indices is $n_2 > n_1$, therefore, $\theta_r < \theta_i$.

When a ray moves from a medium with a higher refractive index to one with a lower refractive index, there is a critical angle of incidence θ_t that results in an angle of refraction of 90°, which is expressed by Equation 2.11 [Gre04]:

$$n_1 \sin(\theta_t) = n_2 \sin(90°) \tag{2.11}$$

$$\theta_t = \arcsin\left(\frac{n_2}{n_1}\right). \tag{2.12}$$

Exceeding this critical angle causes all light to be reflected, a phenomenon known as *total internal reflection* [Axe01; Haz22].

To determine the proportion of light that is reflected and refracted, the *reflective coefficient* R is described by the *Fresnel equations*, which indicate the fraction of reflected light intensity relative to the incident light intensity [Bor86]. The reflective coefficient consists of two components: R_s for s-polarized light and R_p for p-polarized light, which are calculated by Equation 2.13 and Equation 2.14 [Bor86]:

$$R_s = \left(\frac{n_1 \cos(\theta_i) - n_2 \cos(\theta_r)}{n_1 \cos(\theta_i) + n_2 \cos(\theta_r)} \right)^2, \tag{2.13}$$

$$R_p = \left(\frac{n_1 \cos(\theta_r) - n_2 \cos(\theta_i)}{n_1 \cos(\theta_r) + n_2 \cos(\theta_i)} \right)^2. \tag{2.14}$$

The effective reflection R_{eff} is given by Equation 2.15 [Bor86]:

$$R_{\text{eff}} = \frac{1}{2} (R_s + R_p). \tag{2.15}$$

The part of light that is not refracted is transmitted, with the share of transmitted light denoted by the transmission coefficient T, which is calculated by Equation 2.16 [Bor86]:

$$T = 1 - R. \tag{2.16}$$

In optically anisotropic materials, the refractive index varies with the polarization and propagation direction of light [Mur12]. This characteristic, known as *birefringence*, results in double refraction, where a light ray traversing the material is divided by polarization into two distinct rays, each following slightly different paths.

2.1.5 Lenses

Lenses are transparent objects, typically made of glass or plastic, that magnify objects by manipulating light rays through refraction [Sal20]. An ideal lens focuses parallel light rays at a singular *focal point* F. Lenses are often approximated as thin when their thickness is significantly smaller than their focal length f, which simplifies optical calculations. The optical properties of lenses are governed by the lens equation (Equation 2.17) [Gre04]:

$$\frac{1}{f} = \frac{1}{d_o} + \frac{1}{d_i}, \tag{2.17}$$

where d_o represents the object distance and d_i the image distance from the lens. Convex lenses are distinguished by a positive focal length, whereas concave lenses possess a negative focal length. The faces of a lens can be shaped differently, allowing for combinations of convex and concave configurations. Figure 2.3 illustrates the magnifying characteristics of a bi-convex lens.

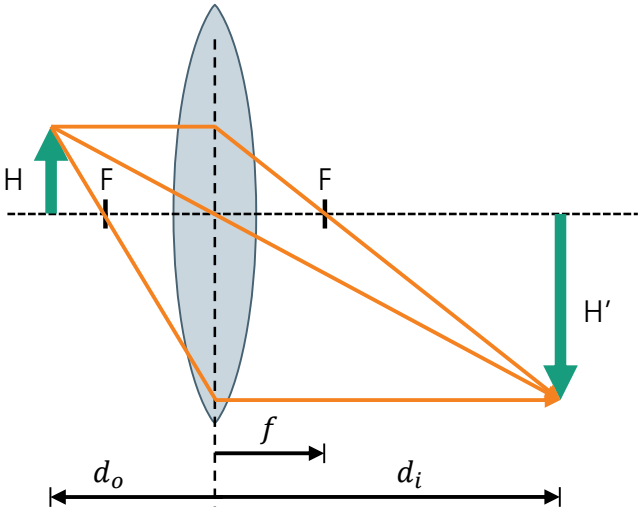

Figure 2.3: Illustration of the magnifying characteristics of a bi-convex lens with focal length f. The object H is magnified, appearing as the image H' (adapted from [Gre04]).

2.1.6 Prisms

Prisms are optical components typically characterized by the extrusion of a plane polygon, which disperse light and modify its path through refraction [Gre04]. To operate as a prism, light must traverse two surfaces angled towards each other. When light passes through such angled surfaces, its trajectory is altered. If the surfaces are parallel, however, the refractions cancel each other out, resulting in only a lateral shift of the light beam. The most common type is the triangular prism, often referred to as a wedge, which is depicted in Figure 2.4 [Kau23]. The degree of beam deflection increases with the wedge's opening angle. Due to the wavelength dependence of the refractive index, light of varying wavelengths exits the prism at distinct angles.

2.1.7 Beam Splitters

Beam splitters are optical devices that divide an incident light beam into multiple separate beams through reflection and transmission [Nec22]. They are widely utilized in various optical systems, including microscopes and interferometers. The ratio of transmitted to reflected light is defined by the transmission and reflection coefficients, where $R + T = 1$ according to Equation 2.16. Beam splitters are often configured to achieve $R = T = 0.5$. Certain beam splitters can transmit light within a specific wavelength band while reflecting light of other wavelengths, and these are termed *dichroic*.

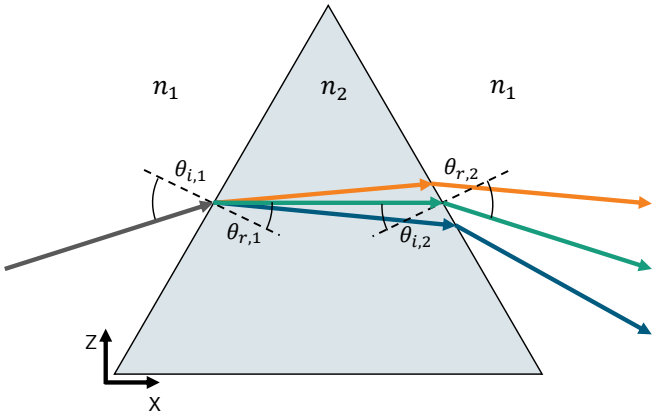

Figure 2.4: White light passing through a triangular prism, where $n_2 > n_1$. The light is dispersed into its components. The angles of incidence $\theta_{i,1}$ and $\theta_{i,2}$ and angles of refraction $\theta_{r,1}$ and $\theta_{r,2}$ are shown for the green component of the light.

2.1.8 Petzval Field Curvature

Petzval field curvature is an optical aberration that projects a fronto-parallel planar surface onto a curved image surface [Nec22; Wan14]. This results in a region where the original object is sharply represented on the image plane while areas farther from it become progressively defocused and blurred. This phenomenon is schematically illustrated in Figure 2.5.

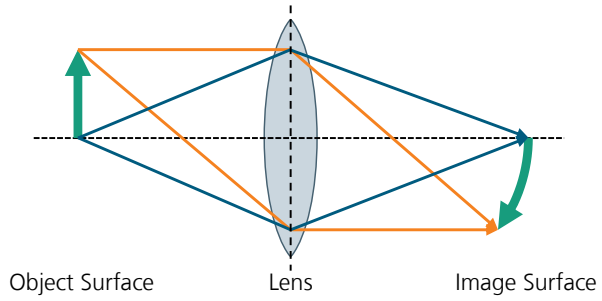

Figure 2.5: Effect of Petzval field curvature, transforming a planar surface into a curved surface (illustration based on [Mat15]).

The field curvature can be mathematically described by the Petzval sum P, given by Equation 2.18 [Mat15]:

$$P = \frac{1}{r_P} = \sum_{i=1}^{k} \frac{1}{n_i f_i}, \tag{2.18}$$

where r_P is the radius of the Petzval field curvature, k is the number of optical elements (e.g., lenses), n_i denotes the refractive index of each element, and f_i is the focal length of each element. A higher Petzval sum indicates greater optical aberration due to different optical

path lengths caused by the field curvature. Other optical aberrations, such as *spherical aberration*, also degrade image quality by causing light rays from the periphery of a spherical lens to focus at a slightly different point than rays passing through its center. Correcting Petzval field curvature often necessitates additional lens elements to flatten the image plane, employing lenses with both positive and negative focal lengths. Therefore, objective lenses in microscopes typically comprise multiple lenses. Field curvature is not limited to glass lenses but occurs in any object functioning as a lens, such as a liquid meniscus.

2.1.9 Scattering

Scattering describes the deviation of light from its initial trajectory due to interactions with particles or irregularities within a medium [Nec22]. The extent and nature of scattering are determined by the size of these particles or irregularities in relation to the wavelength of the incident light. If the particles or irregularities are significantly larger than the wavelength, the principles of ray optics apply. In such cases, scattering results from multiple refractions at different particles, leading to diffuse light. Conversely, if the particles or irregularities are similar in size or smaller than the wavelength, wave optics principles dominate. In this case, scattering arises from interference and diffraction phenomena.

2.2 Light Microscopy for Cell Observation

Light microscopes are used in cell cultivation to magnify small objects like cells in cell cultures [Nec22]. Cell cultures are grown inside MTPs as specimens on the microscope stage. Magnification is achieved by directing light through a series of lenses and mirrors, which work in tandem to enlarge the specimen's apparent size. The overall magnification is the product of the magnification factors of the objective lens with the ocular lens or tube lens.
Observers may use their eyes with manual microscopes or employ cameras in digital systems to view the magnified image. Given the transparent or semi-transparent nature of biological specimens and their cultivation in transparent vessels, transmitted light microscopy is favored over other modes for these applications [Mur12].

2.2.1 Transmitted Light Microscopy

Transmitted light microscopy involves illuminating the specimen from one side while the objective lens is placed on the opposite side, allowing light to pass through the specimen [Mur12]. This configuration enables differentiation of the specimen from the background based on variations in light intensity. Different light intensities result from spatial variations in specimen thickness, density, and material.
Techniques within transmitted light microscopy include brightfield, darkfield, and phase contrast microscopy [Mur12]. Brightfield microscopy represents the most straightforward form

of transmitted light microscopy, suitable for examining specimens that partially or fully absorb transmitted light. Conversely, phase contrast microscopy is specifically designed for viewing transparent specimens [Mua18]. Figure 2.6 illustrates a simplified optical path of a transmitted light microscope applicable to both brightfield and phase contrast microscopy.

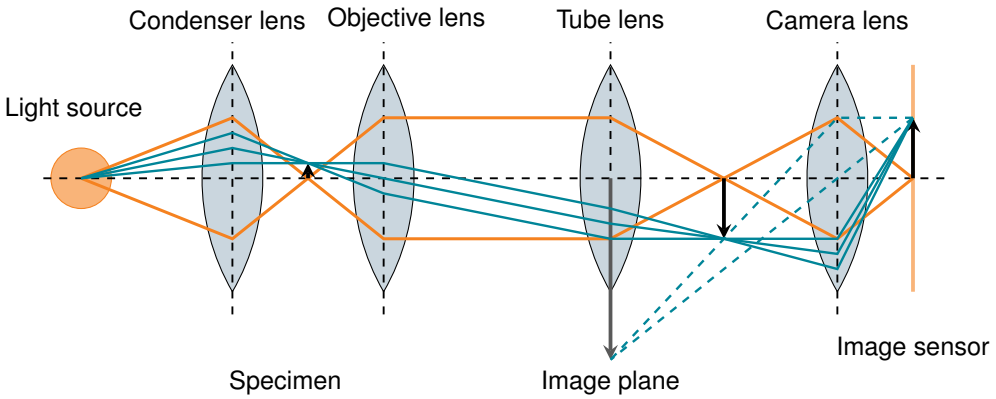

Figure 2.6: Working principle of an infinity-corrected transmitted light microscope (inspired by [Mur12; Nec22; Pel20]). The tube lens and camera lens can also be integrated into a single lens.

A light source is essential for directing illumination toward the specimen [Mur12]. Typically, a condenser lens focuses the light from the source onto the specimen. The specimen is positioned on a microscope stage, enabling precise adjustments in the x and y directions. Focus is maintained by adjusting the z-position of the stage, or alternatively, by altering the distance of the objective lens relative to the specimen. The objective lens gathers light that interacts with the specimen, forming a magnified real image at the intermediate image plane near the ocular [Nec22]. For optimal imaging, the specimen must be aligned within the focal plane of the objective lens.

Modern microscopes generally employ infinity-corrected optics, wherein light rays exiting the objective lens remain parallel if they emanate from the same source [Mur12; Nec22]. This configuration allows for variable distances between the objective lens and tube lens and facilitates the integration of additional optical components such as mirrors, filters, and beam splitters beyond the objective. The tube lens subsequently focuses these parallel rays at an intermediate image plane. The light is then directed either to a camera (in digital microscopes) or to the observer's eyes (in manual microscopes). In manual systems, an eyepiece, also called an ocular lens, provides additional magnification for the observer. In real-world microscopes, the objective lens, condenser lens, and ocular are composed of multiple lenses to correct artifacts such as image distortion due to chromatic aberration, spherical aberration or field curvature.

2.2.2 Resolution Limit in Light Microscopes

The optical resolution of a microscope is fundamentally limited by diffraction. This limitation is characterized by the *point spread function*, which defines the minimum distance between two points that can be resolved as distinct objects. The minimum resolvable distance d, as formulated by Ernst Abbe, differs among various microscopy techniques. For transmitted light microscopes, this distance is expressed by Equation 2.19 [Mur12]:

$$d = \frac{\lambda}{NA_{\text{Objective}} + NA_{\text{Condenser}}}. \tag{2.19}$$

Here, λ denotes the wavelength and *NA* represents the numerical aperture (NA), which quantifies the light-gathering capacity of an optical system and its ability to resolve fine details. It is defined by the maximum angle of light rays entering the optical system relative to the object, as expressed by Equation 2.20 [Mur12]:

$$NA = n \sin \alpha, \tag{2.20}$$

where n describes the refractive index of the surrounding medium and α is the aperture angle to the vertical. Figure 2.7 illustrates the geometric construction of the numerical aperture.

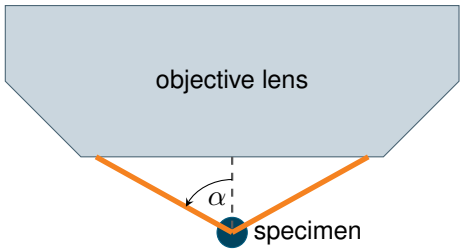

Figure 2.7: Numerical aperture as opening angle α of the optical component (adapted from [Wik25]).

The resolution defined by Equation 2.19 is attainable only when the focal points of the condenser and objective lenses coincide, with their optical axes aligned [Mur12]. Additionally, it is essential to uniformly illuminate the entire region of interest (ROI) in the specimen plane. This condition is called *Köhler illumination*. It ensures that each point of the specimen is precisely projected onto a corresponding point in the image plane, resulting in a sharp image. Minor deviations in alignment are permissible and can still yield sharp images if the deviation in the focal point remains smaller than the camera's pixel size in digital microscopy.

The maximum permissible deviation in focal distance is termed the *depth of field* or *focal depth*. In diffraction-limited optics, the depth of field Z is described by Equation 2.21 [Mur12]:

$$Z = \frac{n\lambda}{NA^2}, \tag{2.21}$$

where n is the refractive index of the surrounding medium and λ is the wavelength of light. This equation indicates that while high NAs enhance resolution, they simultaneously reduce the depth of field significantly.

2.2.3 Phase Contrast Microscopy

Specimens that appear darker than their surroundings by blocking transmitted light in microscopy are referred to as *amplitude objects*, which attenuate the light's amplitude [Mua18]. Conversely, transparent objects do not affect the light's amplitude, making them invisible under brightfield microscopy. Phase contrast microscopy is specifically developed to render these transparent objects visible. Due to their optical density being higher than the surrounding medium, transparent objects induce a phase shift in the light, categorizing them as *phase objects*. This phenomenon is illustrated in Figure 2.8.

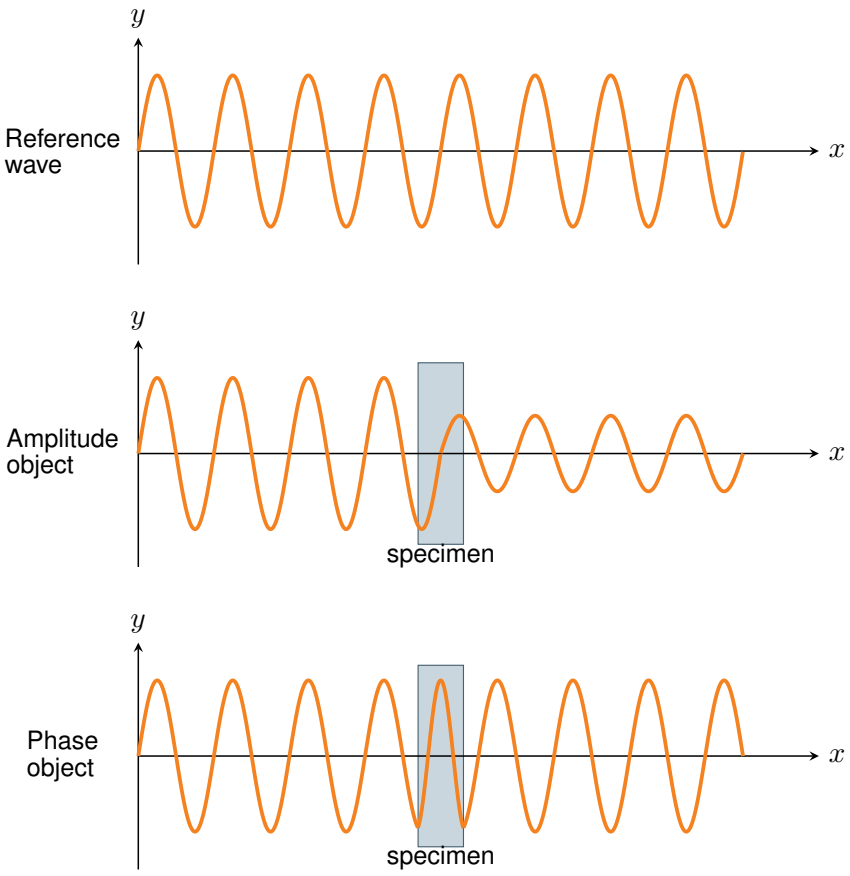

Figure 2.8: Difference between amplitude objects and phase objects (adapted from [Mur12]). The x-axis denotes the spatial extension of the wave, whereas the y-axis represents its amplitude.

Phase contrast microscopy, developed by Dutch physicist Frits Zernike in the 1930s, employs interference (see Section 2.1.1) between light that has traversed the objects and light that has not [Zer55]. Zernike's innovation earned him the Nobel Prize in Physics in 1953 [Mur12]. It enhances the visibility of transparent specimens without the need for staining, enabling detailed examination of structures such as cells, organelles, and microorganisms, thus proving invaluable in laboratory automation processes [Och21]. A schematic diagram demonstrating the operational principle of phase contrast microscopy is shown in Figure 2.9.

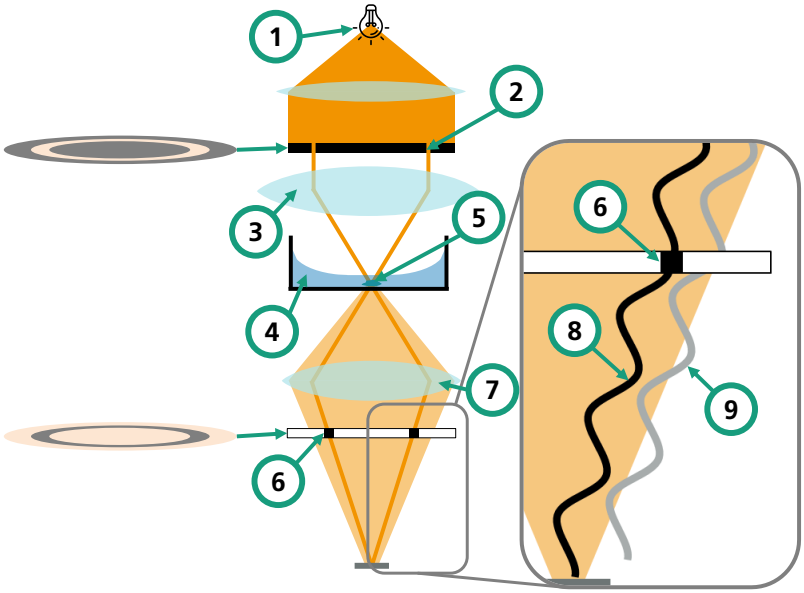

Figure 2.9: Cross-sectional schematic diagram illustrating the beam path in a phase contrast microscope. The alignment of the condenser annulus and phase ring establishes the necessary conditions for phase contrast. The sectional view depicts interference between phase-shifted and undisturbed light. 1) Light source. 2) Condenser annulus. 3) Condenser lens. 4) Liquid medium. 5) Specimen. 6) Phase ring. 7) Objective lens. 8) Phase-shifted direct light wave. 9) Undisturbed scattered light wave.

The process begins with partially coherent light emitted by a light source. This light passes through a *condenser annulus*, also known as a *ring aperture*, *annular diaphragm*, *phase annulus*, or *phase stop*, converting it into a hollow cone of illumination [Mur12]. While cone-shaped illumination is not strictly necessary, it achieves a higher NA compared to other configurations, such as simple central circular illumination [Zer55]. Alternative methods have also been developed, including configurations featuring multiple circular apertures [Mau08]. The illumination is focused onto the specimen by the condenser lens, similar to a conventional transmitted light microscope [Mur12]. Upon reaching the specimen plane, some light interacts with the specimen, which possesses a higher refractive index than its surroundings. This interaction retards the phase of the light due to its reduced speed in the denser medium. Additionally, the specimen scatters the light, while light that does not interact with

the specimen continues directly. Subsequently, the objective lens collects the light. Unlike conventional objective lenses, a phase contrast objective lens integrates a *phase ring*. The phase ring, situated directly in the path of the direct light and composed of an optically denser material, induces a phase shift in the transmitted light. This phase shift differentiates two techniques: *positive* and *negative* phase contrast. In negative phase contrast, the phase ring induces a phase shift of $-\pi/2$, whereas in positive phase contrast, the shift is $+\pi/2$. The subsequent section elaborates on the principles of negative phase contrast microscopy. Significant deviation in the specimen's thickness from the design thickness prevents the achievement of phase contrast conditions, as the induced phase shift will be either greater or less than expected.

After passing through the phase ring, the light is focused on the detector by the tube lens [Mur12]. In addition to the direct phase-shifted light, some scattered light is also refocused on the detector. The direct and scattered light interfere, creating interference patterns (see Section 2.1.1). These interferences translate the phase shift into amplitude differences. Direct and scattered light that passed through a region where the specimen is located interfere constructively, increasing light intensity. Conversely, light that has passed through the background interferes destructively, reducing the light intensity. This principle enhances the contrast in places with high specimen thickness, such as cell walls. Additionally, the phase ring is coated with a partially absorbing metal film, reducing background light intensity by 70-75%, which is crucial for increasing specimen contrast relative to the background light.

To achieve phase contrast conditions, the condenser annulus and phase ring must be consistently aligned [Mur12]. Misalignment causes the background light intensity to exceed that of the interference patterns, thereby significantly reducing the contrast of transparent objects, making images resemble brightfield images [Hor06]. To verify the alignment of the condenser annulus and phase ring, a *Bertrand lens*, also known as an *eyepiece telescope*, can be used. This lens focuses on the back aperture of the objective lens where the phase ring is located, allowing observation of the overlap between the phase ring and the condenser annulus. A beam splitter may be utilized to redirect a portion of the light through the Bertrand lens while the remainder proceeds to the tube lens, enabling concurrent observation of condenser annulus and phase ring alignment and the specimen.

Typical phase contrast images of biological cells are shown in Figure 2.10. It can be observed that phase contrast images display a dark background and bright specimen contours [Mur12]. In contrast, images lacking phase contrast due to misalignment of the condenser annulus and phase ring appear much brighter and lack contrast.

Phase contrast microscopy creates characteristic artifacts where the observed intensity does not correspond to the optical path difference of the specimen. These phenomena are known as the *halo effect* and the *shade-off effect* [Mau08]. In negative phase contrast microscopy, halos appear as bright areas encircling the boundaries of dark objects. In contrast, the shade-off effect manifests as a gradual intensity transition at the periphery of a structure. While this can enhance contrast and improve boundary visibility, it results in uneven intensities in regions that are otherwise uniform. Both the halo and shade-off effects

arise because not only does the 0^{th}-order light traverse the phase ring, but some scattered light also inadvertently passes through, becoming phase-shifted unintentionally.

(a) Phase ring (black) and condenser annulus (white) aligned.

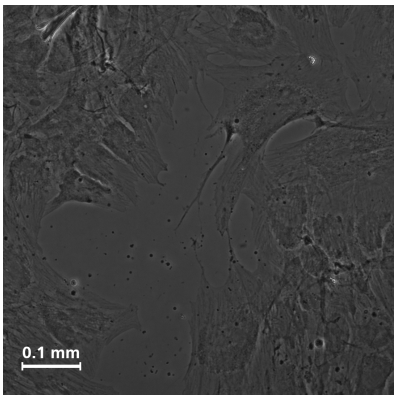

(b) Phase contrast image.

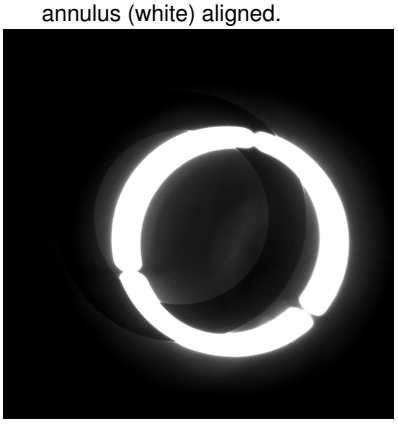

(c) Phase ring (black) and condenser annulus (white) misaligned.

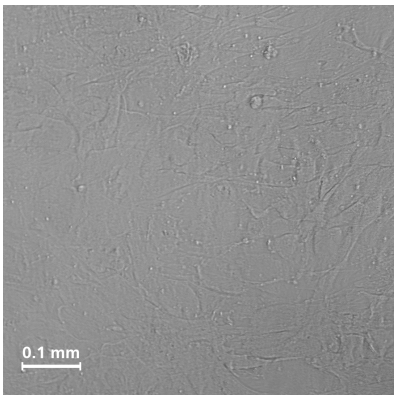

(d) Brightfield image.

Figure 2.10: Images of MSCs captured using phase contrast microscopy with 10x magnification. The alignment of the phase ring and condenser annulus is demonstrated in (a) and (c), with the respective specimen images shown in (b) and (d). The overlap of the condenser annulus and phase rings depicted in (a) establishes the phase contrast conditions in (b). Non-aligning phase ring and condenser annulus in (c) causes the brightfield images in (d). The images were taken of specimens within the same well but not at the same position.

2.3 Optoelectronic Devices

Digital microscopy utilizes various optoelectronic devices that exploit the interaction between light and electronics to achieve effects such as light emission, modulation, or image capture. This section provides an overview of common components found in light microscopes and the devices employed in the implementation of adaptive phase contrast microscopy.

Typically, digital microscopes use light-emitting diodes (LEDs) for illumination and scientific cameras for image capture. In this thesis, digital mirror devices (DMDs) and liquid crystal displays (LCDs) are discussed for integration into phase contrast microscopes for experimental purposes and are therefore also introduced in this section.

2.3.1 Light-Emitting Diodes (LEDs)

LEDs are semiconductor devices that emit light through electroluminescence when electricity passes through them [Che16]. Their high efficiency has established them as the primary choice for modern illumination technologies. LEDs can rapidly toggle between on and off states, making them particularly advantageous for pulsed light applications [Wil10]. Unlike lasers, which also offer high-speed switching, LEDs emit a broader wavelength spectrum, with spectral widths typically ranging from 10 nm to 30 nm, thereby minimizing speckle patterns.
For optimal high-power performance, LEDs are best regulated by voltage rather than current due to their non-linear response, where small voltage changes lead to significant brightness variations. Furthermore, LEDs can be overdriven, allowing them to operate above 100% of their rated brightness for brief periods. These characteristics make them particularly well-suited for applications requiring short-pulsed and intense light sources. Specialized LED controllers and pulse sources are engineered to deliver light pulses lasting only a few microseconds, which can be synchronized with other components using electrical trigger signals.

2.3.2 Scientific Cameras

Scientific cameras are specialized digital cameras that represent the state-of-the-art technology for capturing images in digital microscopes [Kui15]. Unlike conventional digital cameras, they are distinguished by their uniform light response, exceptional sensitivity, low noise levels, and wide dynamic range. The key component of a camera is the sensor, also referred to as the chip, which captures light and converts it into electrical signals. CMOS and CCD are the main technologies employed for this purpose [Hol11]. These signals are represented as voltage levels that correspond to brightness, with higher voltages indicating brighter areas. In color cameras, a color filter, such as a Bayer filter, is positioned in front of the sensor [Sho05]. The sensor is divided into uniformly spaced *pixels*, with one million pixels referred to as Megapixels (MPs). An analog-digital converter converts the voltages from each pixel into integer values for further processing with a computer. The resolution of this conversion, known as *bit depth*, typically ranges from 8 to 16 bits, allowing for $2^8 = 256$ to $2^{16} = 65,536$ possible shades. This thesis only employs monochrome cameras, which represent images in grayscale.
While the spatial resolution of digital cameras is often used interchangeably with the pixel count, a meaningful comparison necessitates consideration of the sensor size [Gon18]. A

sensor with a greater pixel count than another of identical size will exhibit higher resolution.

Frame Rate

The frame rate, measured in frames per second (fps), describes the number of images a camera can capture per unit of time [Mey09]. This rate is typically constrained by the camera's data transfer capabilities. For example, cameras adhering to the CoaXPress 2.0 standard can transmit up to 12.5 GBit/s per cable, resulting in a maximum frame rate of 156 fps for a 10 MP signal with an 8-bit depth per pixel (actual rates are slightly lower due to transmission overhead) [The19]. While most sensors support higher frame rates, they are often limited by bandwidth.
If only a portion of the image is relevant, a smaller area of the image can be cropped out. The specific imaging area selected on the sensor is referred to as the ROI. Reducing the ROI can increase the frame rate, which allows a better use of the available bandwidth. In the previous example, cropping the ROI to 1 MP would elevate the frame rate to 1560 fps. This adjustment is advantageous when a smaller field of view (FOV) suffices, yet higher temporal resolution is desired. Furthermore, *binning* allows multiple pixels to operate as one, enhancing sensitivity at the expense of spatial resolution [Yoo15]. Binning can be implemented on the sensor by aggregating the charge of groups of pixels (e.g., 2×2 or 3×3). Alternatively, it can be performed digitally through post-processing.

Influences on Image Quality

Various factors can degrade image quality. *Motion blur* arises from relative motion between the camera and the observed specimen, reducing sharpness [Nav11]. The effect is exacerbated by faster relative motion and longer exposure times. Improper focus settings can also lead to blurry images if the subject is not at the focal point [Gon18]. Maintaining a constant distance between the camera and the subject can prevent this issue. Another issue is *sensor noise*, which manifests as graininess in images. This noise is intensified by increased sensor temperatures, often resulting from prolonged camera usage [Iri09]. Furthermore, noise becomes more noticeable when the specimen is underexposed, as it becomes significant relative to the actual image details, a condition measured by the signal-to-noise ratio (SNR).

2.3.3 Digital Mirror Devices (DMDs)

DMDs are microelectromechanical system devices that function as spatial light modulators (SLMs) [Ren15]. These devices consist of an array of microscopic mirrors that can tilt to control light [Ma15]. A mirror, when tilted to a specific angle, directs incoming light onto a projection surface. Each mirror functions as an individual pixel, with independent control

over its orientation. A typical DMD contains millions of mirrors, featuring pixel pitches as small as approximately 10 µm. Upon application of an electric current, a mirror typically tilts around 12°, toggling between *on* and *off* states. In the *on* position, mirrors reflect light onto a lens, forming a white pixel, whereas in the *off* position, they redirect light away to render the pixel black. Gray levels are produced using pulse-width modulation, enabled by the mirrors' rapid switching capabilities. Image transitions occur within microseconds. Due to their high-speed performance, DMDs are used in digital projectors and display systems.

2.3.4 Liquid Crystal Displays (LCDs)

LCDs are widely used flat-panel displays, with applications ranging from smartphone screens and calculators to televisions [Che18]. LCDs utilize polarization and light-modulating liquid crystals to produce virtual images [Yan14]. Brightness is regulated by altering the polarization orientation of light as it traverses the liquid crystals. LCDs do not emit light themselves; hence, they require a backlight or must reflect light from the front. The LCD panel is divided into numerous pixels, with each pixel's liquid crystals being individually controllable. A digital controller manages this process by transforming digital images into electrical signals that control the behavior of the liquid crystals.

Liquid Crystals

Liquid crystals are a state of matter exhibiting properties of both liquids and crystalline solids [Yan14]. Unlike conventional liquids, they maintain a degree of order in molecular orientation, which can be influenced by external factors such as temperature and electric fields. In LCDs, the nematic phase is the predominant liquid crystal type, distinguished by its rod-shaped molecules aligning parallel to one another in the absence of an electric field [Gha20; Niu21; Sal20]. This molecular alignment influences the polarization angle of transmitted light. The angle of polarization relates to multiple factors, such as the liquid crystal twist angle, the thickness of the liquid crystal layer, the wavelength of the passing light, and the birefringence. Changing the crystal's orientation does not occur instantaneously, resulting in a transition period called *response time*, which is longer for significant contrast changes, such as transitioning from all black to all white [Elz12].

Layers of LCDs

At the heart of an LCD's architecture is a layered, sandwich-like configuration consisting of multiple components, as depicted in Figure 2.11. The specific number and functions of these layers can differ across various models.

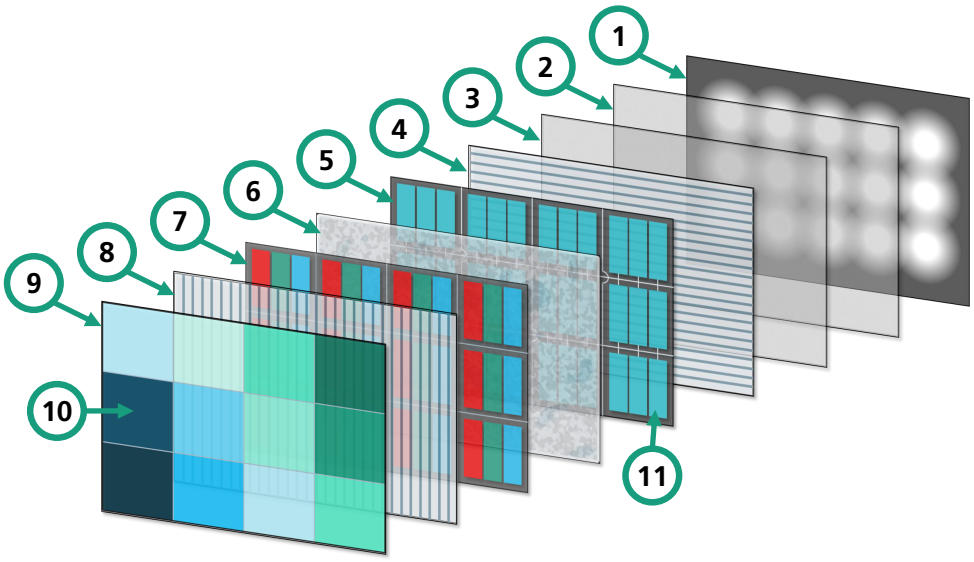

Figure 2.11: Layers of a liquid crystal display with integrated backlight (illustration adapted from [Pre25]). (1) Backlight. (2) Light guide. (3) Light diffuser. (4) Horizontal polarizer. (5) Thin-film transistor. (6) Liquid crystals. (7) Color filters. (8) Vertical polarizer. (9) Front layer. (10) Individual pixel. (11) Sub-pixel.

Since the LCD inherently does not emit light, a backlight is frequently integrated into its layered structure (layer 1 in the illustration). However, the backlight is not essential for the LCD's light-modulating capabilities and can be omitted without affecting this function. Certain LCDs, such as those used in calculators, lack a backlight entirely and depend solely on reflected light.
When present, the backlight serves as the first layer from the rear, tasked with providing uniform illumination. To reduce costs and size, LEDs are not uniformly distributed across the area; instead, one or more light guides and diffuser layers (layers 2 and 3) are employed to spread the light evenly [Yan14].

Light originating from the rear encounters a polarizing film (layer 4), only allowing vertically or horizontally polarized light through [Yan14].
The 5^{th} layer depicted in the illustration is a thin-film transistor (TFT) layer. This layer is crucial for controlling the light modulation of the subsequent liquid crystal layer by applying a variable voltage to each pixel, facilitated by independently controllable transistors for each pixel [Gha20]. In color LCDs, each pixel is further subdivided into sub-pixels to facilitate the display of different colors [Yan14].
The layer following the TFT is the liquid crystal layer (layer 6). Depending on the voltage applied by the transistor logic, the liquid crystals adjust their orientation, rotating the polarization of the transmitted light by up to 90°[Goo75].

Each sub-pixel within a color LCD is equipped with a distinct color filter, accommodating red, green, and blue hues (layer 7) [Yan14]. The prevalent configuration positions these

three colors side by side in a single row, with each sub-pixel being three times taller than it is wide, collectively forming a square pixel. A disadvantage of color filters is the reduced brightness, as they permit only a specific wavelength band to pass through. In a standard red, green, blue (RGB) filter arrangement, this design results in a brightness reduction by at least a factor of three.

The subsequent layer (layer 8) consists of another polarizing filter, oriented perpendicularly to the initial polarizer [Yan14]. This arrangement ensures that polarized light, which has not been rotated by the liquid crystals, is obstructed from traversing the display, in accordance with Malus's law (Equation 2.8). Consequently, pixels where the light remains unrotated appear black. If the liquid crystals alter the polarization direction, the light can penetrate the polarizer with varying intensity, contingent upon the degree of rotation effected by the liquid crystal layer.
The 9^{th} and final layer is the front glass, featuring a contrast-enhancing coating, which functions to safeguard the LCD and augment contrast.

Controller

The LCD controller is tasked with controlling the liquid crystals to generate and refresh images on the LCD [Elz12]. It receives digital signals through interfaces like HDMI and converts them into electrical signals for each pixel and sub-pixel of the LCD. LCDs are typically configured to update at fixed intervals, with a frequency known as the *refresh rate*, commonly at 60 Hz or 120 Hz [Jia12]. Without regular updates, the LCD's colors fade [Pat05]. Information about upcoming frames is stored in a frame buffer, which the LCD controller accesses during refresh cycles [Jia12; Pat05].
Due to the varying computational demand for rendering images, the intervals between rendering consecutive images may fluctuate. The frame buffer ensures the screen is updated consistently at fixed intervals, regardless of fluctuations in rendering times [Pat05]. If a new image is not rendered in time for the subsequent refresh, the previous frame is re-displayed on the LCD. To avoid repeating the same frame and the resulting perceived instability and *flickering*, many displays implement double or triple buffering [Yan14]. This approach involves storing multiple images in the frame buffer and always displaying the first image that has been fully rendered.

2.4 Digital Image Processing

Images obtained through digital microscopes frequently require processing, as they may not be immediately interpretable or may lack contextual information. Consequently, image processing is crucial in digital microscopy. Apart from enhancing image quality, digital processing aids in extracting and interpreting information. This section outlines image processing techniques commonly applied to microscope images. Figure 2.12 provides examples of these techniques applied to a photograph of an MTP.

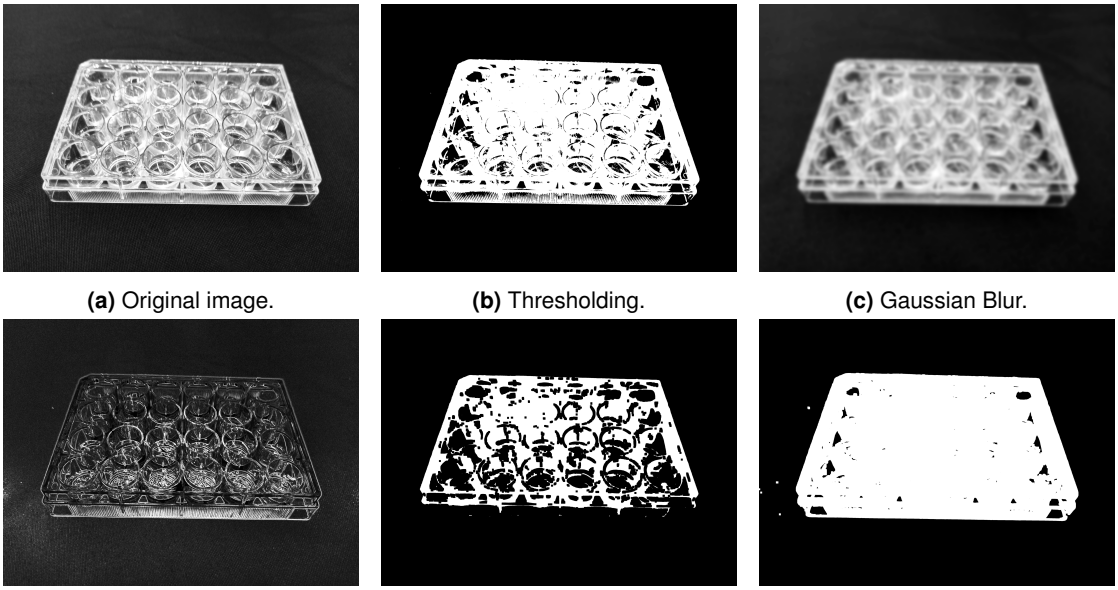

(a) Original image. **(b)** Thresholding. **(c)** Gaussian Blur.

(d) Sobel Edges. **(e)** Erosion. **(f)** Dilation.

Figure 2.12: Various image processing techniques applied to an image of an MTP.

2.4.1 Thresholding

Thresholding is a widely utilized segmentation technique aimed at emphasizing features with specific brightness levels [Gon18]. Segmentation algorithms partition an image into distinct segments or regions. Typically, thresholding transforms a grayscale image into a binary image composed solely of 0 and 1 values, though certain algorithms can generate more than two distinct pixel values. An example of basic thresholding is shown in Figure 2.12b.
The most straightforward and frequently employed method is *global thresholding*, which applies a uniform threshold across the entire image. The algorithm evaluates each pixel value in the original matrix $f(x, y)$, converting values above the threshold T to 1 and all others to 0, resulting in a matrix $h(x, y)$, described by Equation 2.22 [Gon18]:

$$h(x,y) = \begin{cases} 1 & \text{if } f(x,y) > T \\ 0 & \text{if } f(x,y) \leq T. \end{cases} \tag{2.22}$$

There are also *variable thresholding* techniques, where T is not fixed or multiple thresholds are employed. In *adaptive thresholding* algorithms, T is a function of the position, denoted as $T(x, y)$. Adaptive thresholding typically adjusts to the mean or median brightness within a section of the image to accommodate variations in overall brightness, such as shading. Thresholding is prone to noise interference. As a result, preprocessing steps like low-pass filtering are often performed first to eliminate outlier pixels.

2.4.2 Gaussian Blur

Gaussian blur is a widely used blurring technique in image processing aimed at reducing noise and eliminating outlier pixels [Gon18]. This operation is mathematically characterized by a filtering process, which involves convolution. In convolution, a filter kernel $w(x, y)$ is applied over an image $f(x, y)$, with the overlapping values between the kernel and the image being multiplied and summed to generate the filtered image $h(x, y)$ according to Equation 2.23 [Gon18]:

$$h(x,y) = (f * w)(x,y) = \sum_{m=-M}^{M} \sum_{n=-N}^{N} f(x-m, y-n) \cdot w(m,n), \tag{2.23}$$

where $*$ denotes the convolution operator and the filter kernel dimensions are $(2M+1) \times (2N+1)$, ensuring an odd-numbered shape for symmetry.

Equation 2.23 describes spatial domain filtering, but convolution can be more efficiently executed in the frequency domain, where spatial convolution corresponds to simple multiplication, as expressed by Equation 2.24 [Gon18]:

$$H(u,v) = F(u,v) \cdot W(u,v), \tag{2.24}$$

with $H(u, v)$, $F(u, v)$, and $W(u, v)$ representing the Fourier transforms of $h(x, y)$, $f(x, y)$, and $w(x, y)$, respectively.

In a Gaussian filtering operation, the filter kernel $W(u, v)$ is represented by the Gaussian filter kernel $G(u, v)$, which resembles a Gaussian function, expressed in Equation 2.25 [Gon18]:

$$G(u,v) = \frac{1}{2\pi\sigma^2} \exp\left(-\frac{u^2+v^2}{2\sigma^2}\right), \tag{2.25}$$

where σ represents the standard deviation of the Gaussian bell curve.
A key property of the Gaussian function is that its Fourier transform is also a Gaussian function. Consequently, it can be described by the same equation in the spatial domain, with the variables u and v replaced by x and y.

The primary concept of Gaussian filtering is that pixels near the center of the kernel contribute more significantly to the filtered image. Smoothing is achieved by incorporating the values of neighboring pixels, with weights that decrease as the distance from the kernel's center increases. Since high-frequency noise corresponds to components farther from the kernel's center, the Gaussian filter effectively suppresses such noise. Figure 2.12c illustrates Gaussian blurring applied to an image of an MTP.

2.4.3 Edge Detection

Filtering can also be applied to enhance gradients, a technique frequently employed for edge detection [Gon18]. Numerous filter operations are designed to amplify gradients, many of which rely on the two-dimensional gradient ∇f of an image $f(x, y)$. It is expressed by Equation 2.26 [Gon18]:

$$\nabla f = \begin{bmatrix} \frac{\partial f}{\partial x} \\ \frac{\partial f}{\partial y}. \end{bmatrix} \tag{2.26}$$

The gradient is often discretized using the *Sobel* operator, a common method for computing image gradients, which employs two filters for the horizontal gradient s_x (described in Equation 2.27) and the vertical gradient s_y (described in Equation 2.28) [Gon18]:

$$s_x = \begin{bmatrix} -1 & 0 & 1 \\ -2 & 0 & 2 \\ -1 & 0 & 1 \end{bmatrix} \tag{2.27}$$

$$s_y = \begin{bmatrix} -1 & -2 & -1 \\ 0 & 0 & 0 \\ 1 & 2 & 1 \end{bmatrix} \tag{2.28}$$

The gradient magnitude using the Sobel operator $S(x, y)$, representing the vector length ∇f, is given by Equation 2.29 [Gon18]:

$$S(x, y) = |\nabla f| = \sqrt{(s_x * f)^2 + (s_y * f)^2}. \tag{2.29}$$

Results of edge detection using the Sobel operator are shown in Figure 2.12d.

2.4.4 Erosion and Dilation

Erosion and *dilation* are fundamental morphological operations performed on binary images [Gon18]. These processes modify the shapes of regions, which consist of contiguous foreground pixels (set to 1), by altering their structure. To apply these operations, the image must first be segmented, often using thresholding methods.

Erosion entails the removal of pixels on object boundaries [Gon18]. It reduces the size of foreground regions within an image, effectively removing small-scale noise and separating closely positioned objects. This process is executed by positioning a kernel over the image; the central pixel of this kernel is removed if it fully overlaps with the object. Figure 2.12e illustrates an example of erosion.

Conversely, dilation extends the perimeters of objects by adding pixels [Gon18]. It enlarges the regions of foreground pixels, filling in small holes and connecting disjointed objects. In dilation, the kernel is placed over the image, and the central pixel is added if the structuring

element overlaps with any segment of the object. The outcome of dilation is depicted in Figure 2.12f. Both operations, erosion and dilation, are often applied sequentially to enhance the definition of object shapes within an image, which is demonstrated in Figure 2.13.

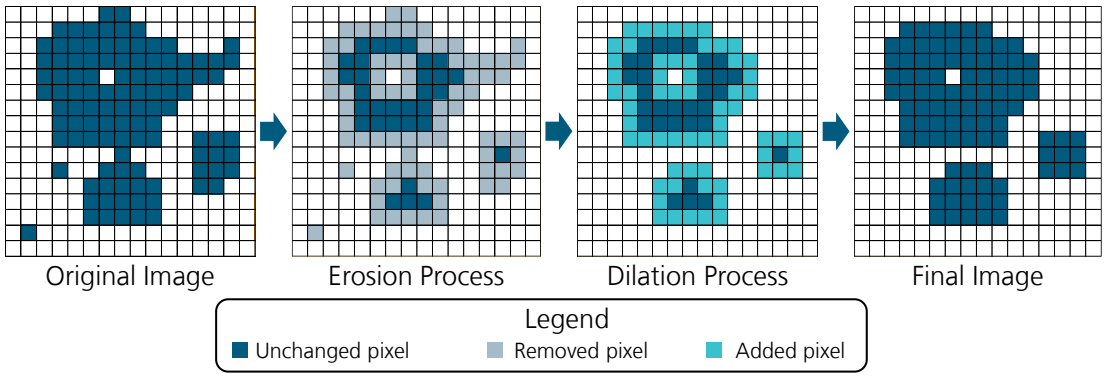

Figure 2.13: Process that includes erosion followed by dilation with a kernel size of 3×3. Each cell in the grid represents one pixel.

2.4.5 Histogram Adjustment

Another technique to improve image quality is called *histogram adjustment* or *histogram equalization* [Gon18]. This digital image processing method enhances contrast by redistributing pixel intensity values to achieve a more uniform distribution across the intensity range, thereby maximizing the image's dynamic range. The process involves mapping pixel intensities to a new range. Additionally, this technique can reduce the bit depth of an image, such as converting a 16-bit raw image to 8-bit, with minimal impact on contrast. The principle is illustrated in Figure 2.14.

Several methods for histogram adjustment exist, encompassing both linear and non-linear approaches. This thesis employs a linear transformation defined by Equation 2.30 [Gon18]:

$$h(x,y) = \left(2^b - 1\right) \frac{f(x,y) - l_{\text{min}}}{l_{\text{max}} - l_{\text{min}}}, \tag{2.30}$$

where $h(x,y)$ represents the adjusted grayscale image, $f(x,y)$ is the raw image, b is the bit depth, and l_{max} and l_{min} denote the upper and lower gray value limits, respectively.
By stretching the histogram to a new range, histogram adjustment enhances contrast for human perception without adding new information to the image. As a result, while this technique is valuable for improving the visual appearance of images, it does not influence subsequent algorithmic evaluations. The impact of histogram adjustment on a specimen image is presented in Figure 2.15.

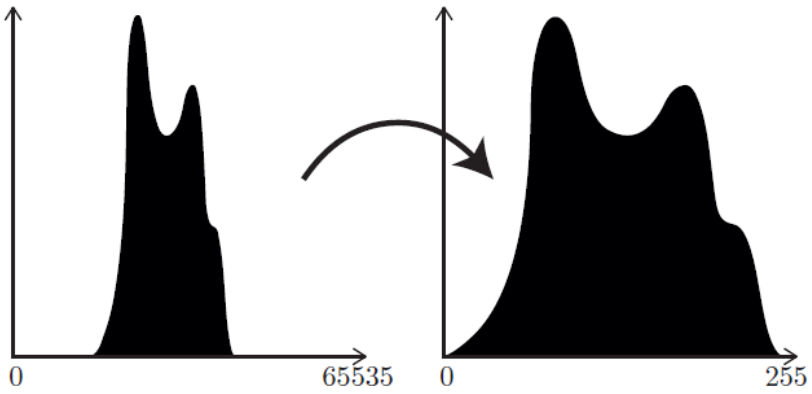

Figure 2.14: Principle of histogram adjustment. The pixel intensities of a 16-bit image are mapped to 8-bit, stretching the range to achieve maximum contrast [Sch16a].

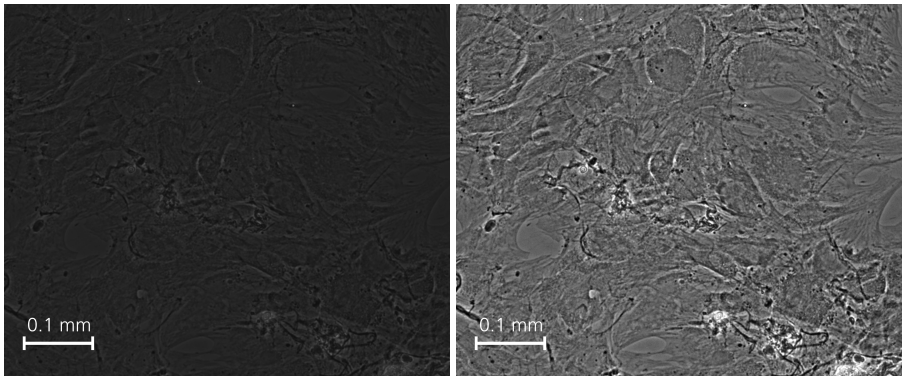

(a) Before histogram adjustment. **(b)** After histogram adjustment.

Figure 2.15: Histogram adjustment applied on an MSC image (10x magnification).

2.4.6 Stitching

Stitching is a computational technique used when the subject is too large to be captured within the camera's FOV [Wan20]. This process combines multiple overlapping images into a seamless composite, as sketched in Figure 2.16.

Several methods are available for stitching [Wan20]. The most straightforward approach is position-based, which depends on precisely knowing the location of each shot in the composite image [Sun06]. However, accurately determining the position of each shot can be difficult due to various constraints in the image acquisition process, such as inaccurate positioning of the subject or camera. In this thesis, feature-based algorithms are utilized to ascertain the positions of individual shots within the composite image. Therefore, images

are captured with an overlap to ensure precise alignment. Features in the overlapping regions, such as corners, are used to compute the translational and rotational offsets between images. For microscope images, translation usually suffices for aligning the images relative to each other because camera rotations can be avoided.

The alignment process commences by detecting and matching feature points between adjacent images, establishing correspondences to guarantee accurate alignment [Sze06]. Subsequently, a transformation model, such as an affine or homography, is applied to geometrically align the images based on these correspondences. Algorithms like *Scale-Invariant Feature Transform* (SIFT), *Speeded Up Robust Feature* (SURF), and *Orientated FAST and Robust BRIEF* (ORB) are employed for feature detection and matching [Sze06]. Once alignment is achieved, images can either be overlaid in the overlapping regions or blended to create smooth transitions, ensuring visual continuity.

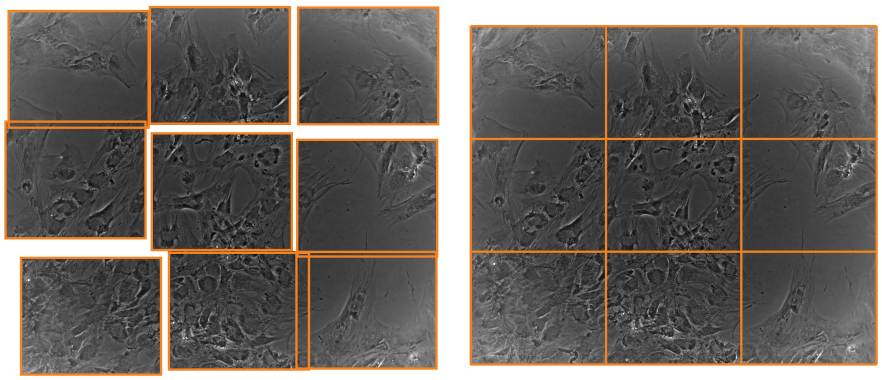

(a) Individual images with overlap before stitching.

(b) Stitched image comprised of multiple individual images.

Figure 2.16: Stitching performed on multiple microscopy images of MSCs.

In addition to feature-based methods, non-feature-based image stitching techniques exist [Wan20]. These include direct methods that optimize a global cost function to align images based on pixel intensities without relying on predefined features [Sze06]. Transformation-based methods employ geometric transformations like affine or projective transformations, optimizing parameters to minimize misalignment. Frequency domain techniques convert images into the frequency domain using methods such as the Fourier or wavelet transforms, facilitating more efficient identification of matching features.

2.4.7 Shading Correction

A critical aspect of creating composite images through stitching is maintaining consistent lighting conditions [Gon18]. Variations in illumination, interference from ambient light, or camera pixel imperfections can result in lighting inconsistencies in the individual images that form a stitched image [Mur12]. These inconsistencies lead to artifacts in the composite

images, as illustrated in Figure 2.17. Artifacts arising from disparities in the microscope's beam path, unequal brightness of the light source, or the camera sensor appear uniformly across all images. Thus, *shading correction* can be employed to standardize the lighting across each image using reference images.

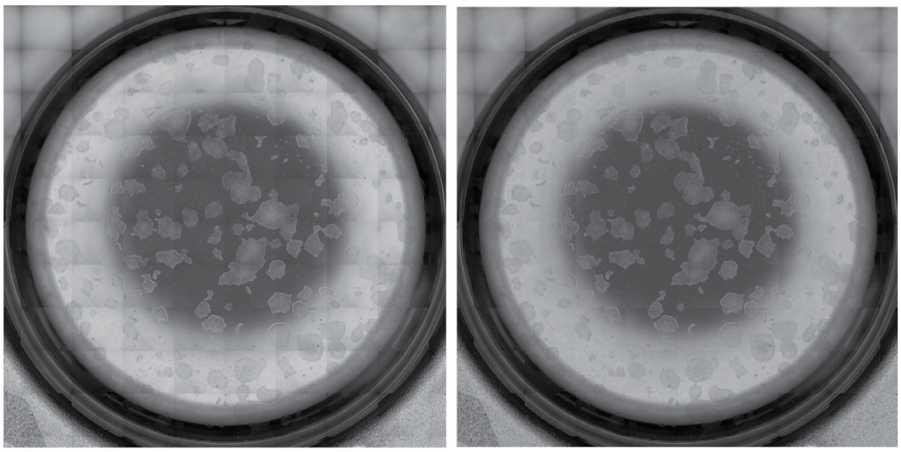

(a) Before shading correction. **(b)** After Shading correction.

Figure 2.17: Shading correction applied on composite microscope image of a whole well in an MTP [Sch16b].

Shading correction requires capturing both white and black reference images prior to acquiring the actual specimen images. These reference images inherently share the same defects as the specimen images and are utilized to mathematically eliminate these imperfections. The white reference image is obtained without a specimen and with the illumination turned on, thereby recording only noise, non-uniform illumination, and sensor artifacts. In contrast, the black reference image is captured without a specimen and without any illumination, capturing solely the camera noise.
For a camera sensor with linear response characteristics, the corrected image $h\left(x,y\right)$ is calculated using Equation 2.31 [Gon18]:

$$h\left(x,y\right)=K\frac{f\left(x,y\right)-f_{\text{black}}\left(x,y\right)}{f_{\text{white}}\left(x,y\right)-f_{\text{black}}\left(x,y\right)}, \tag{2.31}$$

where $f\left(x,y\right)$ denotes the matrix of the raw image captured by the camera, $f_{\text{black}}\left(x,y\right)$ represents the black reference image, $f_{\text{white}}\left(x,y\right)$ is the white reference image, and K is a constant scaling factor. The same scaling factor and reference images must be applied across all images within a composite image to ensure smooth transitions between the images. It is crucial to maintain consistent illumination and ambient lighting conditions when capturing actual images, in comparison to the reference images.

2.4.8 Sharpness Calculation

Evaluating image sharpness is predominantly used for focus assessment according to scientific literature [Yan20]. In this thesis, however, sharpness calculation serves a dual purpose: it is applied not only for focus detection but also for assessing contrast levels in phase contrast images. In this context, contrast and sharpness are considered equivalent terms. Several methods are available for calculating image sharpness, including the grayscale difference method [Zhu23], mean normal variance, edge-detection techniques such as the Canny-edge and Sobel-edge operators, the Laplacian Operator, and gradient-based methods like the Sobel-Tenengrad operator [Hua24; Yan20; Zhu13]. Recently, artificial intelligence (AI)-based algorithms have also been developed to evaluate image sharpness [Jin24]. While the first four methods offer greater computational efficiency, the Sobel-Tenengrad operator (henceforth referred to as *Tenengrad*) provides superior accuracy, robustness, and sensitivity [Yan20; Zhu13]. The Tenengrad sharpness $s_{\text{Tenengrad}}$ is computed as outlined in Equation 2.32 [Hua24]:

$$s_{\text{Tenengrad}} = \frac{1}{MN} \sum_{x=1}^{M} \sum_{y=1}^{N} \sqrt{S_x^2 \left(f(x,y)\right) + S_y^2 \left(f(x,y)\right)}, \tag{2.32}$$

where M and N denote the number of columns and rows of the image $f(x, y)$, respectively, and S_i represents the Sobel operator in the i-direction.

Due to its efficiency and simplicity, the Laplace operator $\nabla^2 f(x, y)$ is widely employed for sharpness calculation, as it effectively highlights regions of rapid intensity changes [Her19]. It is defined as a second-order partial derivative, as expressed in Equation 2.33 [Her19]:

$$\nabla^2 f(x,y) = \frac{\partial^2 f}{\partial x^2} + \frac{\partial^2 f}{\partial y^2}. \tag{2.33}$$

When applied to a discrete image $f(x, y)$, it is approximated by a convolution operation with the kernel L, as described in Equation 2.34 [Her19]:

$$L = \begin{bmatrix} 0 & 1 & 0 \\ 1 & -4 & 1 \\ 0 & 1 & 0 \end{bmatrix}. \tag{2.34}$$

Convoluting the image with this kernel approximates the second-order derivative at each point within the image. Sharpness is subsequently determined by summing all the values in this derivative matrix, where a higher sum indicates greater sharpness.

3 State of the Art of the Meniscus Effect in Phase Contrast Microscopy

This chapter provides an overview of the challenges posed by the meniscus effect on phase contrast microscopy for cell observation. Its objective is to identify research gaps and formulate SRQs that must be addressed to answer the main research question.
Initially, Section 3.1 discusses cell cultivation within the context of laboratory automation. It highlights the trend towards high-throughput solutions, which also extends to quality control. Given the demand for high-throughput, Section 3.2 presents the recently developed HSM technique. Section 3.3 deals with the meniscus effect, describing its formation and detrimental impact on cell observation via phase contrast microscopes. To quantify this effect, Section 3.4 systematically reviews literature on metrics for assessing the phase contrast area. Subsequently, Section 3.5 conducts a systematic literature review to identify strategies for compensating for the meniscus effect. Finally, Section 3.6 summarizes the state of the art and formulates SRQs, which are addressed in the subsequent chapters.

3.1 Cell Cultivation

Cell cultivation is the process of growing live cells in a nutrient medium outside their natural environment, typically carried out in a laboratory setting [Tri03]. These cells may be derived from tissues or entire organisms and require an appropriate nutrient-rich medium for successful culture. Maintaining cells in a controlled environment is crucial for experimental reproducibility. The nutrient medium mostly consists of water and supplies essential components for cell growth and proliferation, such as amino acids and salts, while also ensuring a stable pH and osmotic balance [Bal12]. Cells are typically maintained in an incubator at a temperature of 37 °C with 5% CO_2. Extended periods outside the incubator can lead to cell death.

As the population density, known as *confluence*, increases, growth conditions deteriorate due to competition for nutrients and limited space. Additionally, resource availability varies at different positions within the vessel where they are cultivated, resulting in variable growth conditions for the colony [Man21]. Therefore, regular monitoring of confluence under reproducible conditions is necessary to assess cell health. Microscopy is an important technique for examining adherent cell cultures, which grow on the bottom of their vessels [Nie21].

Induced pluripotent stem cells (iPSCs) are a type of stem cell reprogrammed from adult cells, enabling them to differentiate into any body cell type [Cer24]. Due to their versatility, they play a pivotal role in developing new medical treatments, such as for osteoarthritis. MSCs are stromal stem cells that are already differentiated from pluripotent stem cells but can still differentiate into various cell types [Hyn16]. Since the manual cultivation of iPSCs and MSCs is labor-intensive, developing automated high-throughput processes remains an active research area [Och21]. IPSCs and MSCs are commonly cultured in MTPs, serving as the test specimens for all validation experiments presented in this thesis [Her23].

3.1.1 Microtiter Plates (MTPs)

MTPs are widely used cell culture vessels, primarily due to their ability to facilitate the simultaneous handling of multiple cell cultures and experiments [Due07]. These plates feature multiple circular compartments, known as *wells*, typically arranged in a grid pattern. Illustrations of common MTP types are shown in Figure 3.1.

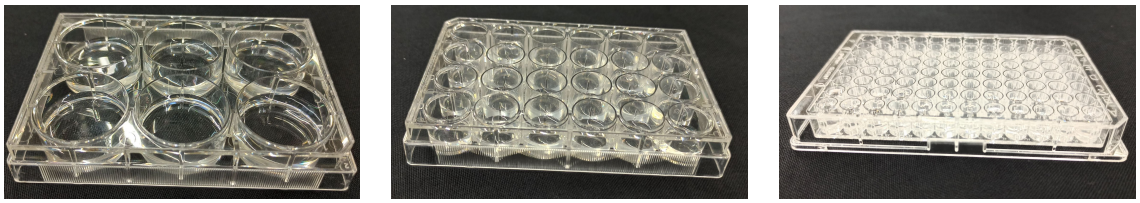

(a) MTP6. **(b)** MTP24. **(c)** MTP96.

Figure 3.1: Different types of MTPs. The numbers indicate the numbers of wells.

MTPs enable the parallel processing of multiple specimens within a compact format, as each well can be independently used for different experiments. Constructed from plastic or glass, MTPs measure approximately 128 mm $\times$ 86 mm and are prevalent in fields such as drug discovery, genomics, and proteomics, where managing and analyzing extensive specimen sets is crucial [Due07]. MTPs are commonly identified by their well count, so MTPs with six wells are termed 6-well MTPs. Throughout this thesis, such designations will often be abbreviated, for example, as MTP6. Despite variations in well count, MTPs maintain the same outer dimensions, resulting in smaller wells for plates with a higher number of wells. The well count of common MTP types ranges from 6 to 3456 wells. Especially higher-order MTPs are increasingly used to increase the throughput of laboratory processes [Zha22].

3.1.2 High-Throughput Cell Cultivation

Developments in personalized medicine and advanced therapy medicinal products (ATMPs) have led to an increasing demand for automating laboratory processes that offer flexible cell cultivation in MTPs [Her23]. This demand is particularly critical with advancements in human induced pluripotent stem cells (hiPSC) technology, which have enhanced disease

modeling, personalized medicine, and novel therapeutic interventions [Ela20]. In addition to hiPSC, various types of iPSCs and MSCs are frequently employed in these applications. Despite this, stem cells such as iPSCs and MSCs continue to be predominantly cultivated manually, though numerous approaches for automating these processes are under exploration [Nie21].
Achieving full laboratory automation requires transforming the entire manual workflow into an automated sequence [Her23]. This transformation includes automating tasks such as specimen preparation, liquid handling, liquid transfer, plate handling, quality control, and data analysis. Automation is implemented through control software that integrates various devices, such as incubators, liquid handling units, plate readers, and microscopes [Nie21]. Specimens in automated plants are typically cultured in MTPs and transported using robotic arms.
Quality control of specimens is crucial to modify their ambient conditions and determine the timing of process steps, such as harvesting [Och21]. Microscopy is among the most important methods for quality control due to its versatility and ease of use. Microscopic images provide insights into parameters like cell morphology, viability, contamination, and confluence [Kas17]. Phase contrast microscopy is particularly effective for measuring these parameters.

3.1.3 Requirements for Quality Control Through Microscopy

Various microscopy modes are utilized for observing cell cultures, including fluorescence microscopy and phase contrast microscopy [Ste03]. Compared to many research procedures, automated cell cultivation imposes stricter requirements on microscopy because cells need to remain viable over extended periods. Thus, cells must not be harmed during observation, nor should their behavior be altered. For example, adding substances to specimens is often undesired, which excludes fluorescence microscopy for numerous applications, given that it necessitates staining of the cell cultures [Hic21].

Conditions within an MTP well vary, as resource access differs between the center and edge [Man21]. As a result, cell growth varies based on location, necessitating observation of a large share of the well to obtain reliable specimen information. However, conventional microscopes typically have a limited FOV, requiring numerous images to cover a large well area, making the process time-consuming.
It is crucial to consider that exposure to ambient conditions outside an incubator can threaten cell cultures, so that time spent outside these environments should be limited [Tal24]. This poses a risk, as temperatures within a well can drop significantly within just three minutes outside an incubator [Kor20]. Thus, limiting exposure to less than ten minutes outside an incubator is recommended [Kor20]. However, this duration depends on cell types, experimental design, and ambient conditions, complicating the establishment of a fixed limit. Nonetheless, minimizing the time a sample spends outside an incubator for imaging is beneficial, which underscores the need for a high-throughput imaging solution.

Conventional microscopes face challenges in high-throughput laboratory automation settings, as capturing large samples requires numerous images due to their restricted FOV [Ker19]. Consequently, high-speed microscopes have been employed in certain applications such as adherent stem cell observation [Och21], quality control of stem cell spheroids [Kri21], and cell separation [Nar23] to accelerate the generation of 2D image data, which will be detailed in the following section.

3.2 High-Speed Microscopy

Conventional microscopy is extensively used for its high resolution, yet it is limited by a restricted FOV [Ker19]. For instance, utilizing a 5 MP image sensor with a 1 inch size and a standard pixel pitch of 5 µm at 10x magnification results in a field of view of only about 1 mm^2. Nevertheless, many applications require a larger area, spanning several millimeters or centimeters in each direction [Sch16a]. This extensive ROI is achieved by stitching up to multiple thousand images into a composite that covers the entire area (see Section 2.4.6). Acquiring such a large number of images is a time-consuming process. Traditionally, the procedure involves repositioning the specimen with the microscope's stage between image acquisitions, halting completely to acquire each image, and then resuming movement. This *stop-and-go* process, also referred to as *stop-and-stare*, results in a time duration that scales linearly with the number of images, rendering it inefficient for large specimens.
An alternative to stop-and-go is a continuous scanning method where the microscope stage does not pause for image capture. The specimen area is divided into parallel rows that are scanned in sequence. This technique, termed *high-speed microscopy (HSM)* and first described by Schenk et al. [Sch16a], permits high acquisition rates, achieving several hundred frames per second while scanning along a row. The HSM approach has been successfully applied to enhance phase contrast microscopy for induced pluripotent stem cell screening, among other applications [Sch16b].
Key challenges of this method include component synchronization, automatic focusing, and image processing. Synchronization of the microscope stage, camera, light source, and focus positioning is achieved using a path-synchronous trigger signal from the microscope stage, ensuring precise timing among the components. The key features of high acquisition speed and autofocus are detailed in the following subsections.

3.2.1 Acquisition Speed

Capturing images during motion presents a significant challenge due to the occurrence of motion blur, as discussed in Section 2.3.2. HSM addresses this challenge by utilizing short-pulse flash illumination to reduce blur effects [Nav11]. This technique requires that the object displacement during exposure remains less than a fraction of a pixel. The permissible

maximum exposure time, denoted as t_{flash}, can be calculated using Equation 3.1 [Flu96]:

$$t_{\text{flash}} = \frac{\Pi}{Mvk}, \tag{3.1}$$

where M is the magnification, Π is the camera's pixel pitch, v is the stage velocity, and k is a safety factor, typically set to two. The pixel pitch is often significantly larger than the optical system's physical resolution limit. However, in cases were the system's physical resolution is larger, oversampling occurs between pixel count and actual resolution, which permits longer maximum exposure times without inducing motion blur. Substituting the resolution limit d for the pixel pitch divided by magnification in Equation 3.1 yields Equation 3.2:

$$t_{\text{flash}} = \frac{d}{vk}. \tag{3.2}$$

High-intensity LEDs are utilized to provide bright illumination within the constrained exposure time [Sch16a]. The maximum acquisition rate of HSM is determined by stage velocity, camera frame rate, and flash intensity. Stage velocity must be adjusted so the FOV of each image aligns precisely with the adjacent FOVs, apart from a small overlap necessary for stitching. The FOV is calculated by the camera's chip size divided by the microscope's total magnification. For a given frame rate, the maximum possible stage velocity v is calculated by Equation 3.3:

$$v = \frac{(1-o)n_{\text{pixel}}\Pi}{M} f, \tag{3.3}$$

where n_{pixel} is the camera's pixel count in the direction of motion, o is the overlap between images, and f is the camera frame rate. If the theoretically possible stage velocity surpasses the hardware's maximum physical velocity, the camera's frame rate must be reduced. In some scenarios, although the stage velocity and camera frame rate may suffice, the exposure time may be too brief for the LED driver, or images may be underexposed due to insufficient LED brightness. In such situations, the stage velocity and camera frame rate must be decreased until sufficient illumination is achieved.

3.2.2 Autofocus Scan

Focal blur, alongside motion blur, can significantly degrade image quality [Sch16a]. Given the limited depth of field in microscopy, it is crucial to maintain a constant focal distance between the objective lens and the specimen (see Section 2.2.1). Without proper adjustments, the focal distance may fluctuate due to factors such as uneven MTP surfaces and misalignments in the optical axes. As a result, the objective's height position must be repeatedly adjusted to observe different regions of the specimen.
While manual microscopes allow for focus adjustment by turning a knob, achieving focus during continuous specimen movement presents challenges. To address this, a fast and precise z-movement actuator, typically a piezo actuator due to its accuracy and speed, is mounted either to the objective lens or the stage to dynamically adjust the distance between

the specimen and the lens. Before the main image scanning process, an *autofocus scan* is conducted to acquire height data, which is subsequently used to generate a height map of the specimen. This height map is utilized to determine the focal height for the piezo actuator at each image position.

There are several methods to perform an autofocus scan [Gro85]. Image stacking is the most prevalent and straightforward option [Vol80]. It requires no additional hardware, as it involves stacking images at fixed x and y positions. Multiple images are captured at varying z-positions while maintaining constant x and y coordinates, and a subsequent sharpness calculation (see Section 2.4.8) determines the sharpest z-plane, which is recorded as the z-coordinate for that position. The principle is illustrated in Figure 3.2.

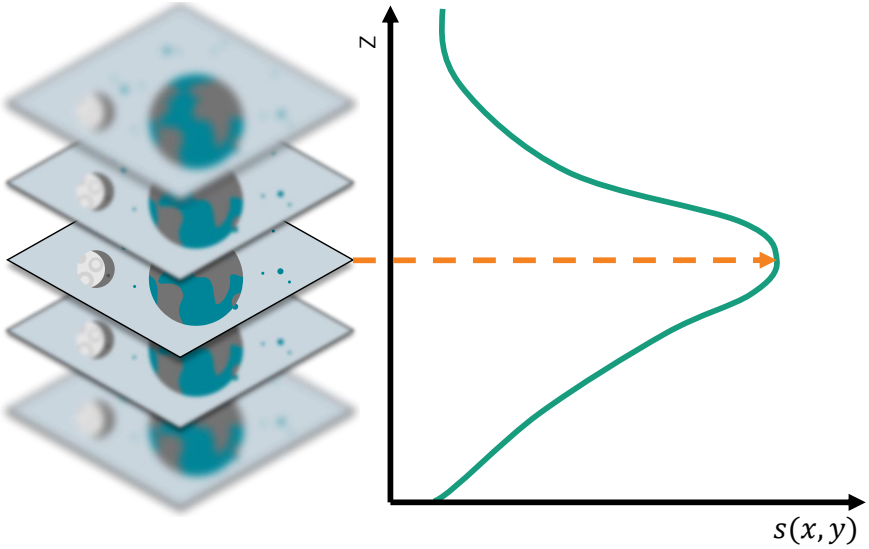

Figure 3.2: Software autofocus principle to determine the optimal focal position using image stacking along the z-axis. The optimal focal position is achieved at the z-position with the highest sharpness $s(x, y)$ (inspired by [Con25]).

Image stacking is conducted at multiple positions across the specimen [Sch16a]. These values serve as base points for interpolating focal positions throughout the rest of the specimen. To expedite focus scanning, the z-axis can be moved continuously during acquisition, similar to high-speed image scanning. This is facilitated by the fast and precise piezo actuator.

External distance sensors present an alternative to image stacking [Sch16a]. These sensors deliver significantly faster measurements than image stacking due to their higher sampling rates compared to cameras' frame rates, enabling the assessment of a larger number of focal points. They can be utilized to create a high-resolution focus map of the specimen, facilitating more precise autofocus correction. Potential sensors include confocal chromatic sensors and interferometer-based technologies such as optical coherence tomography and white-light interferometry [Fer03]. The primary disadvantage of these technologies is the

requirement for an additional costly sensor, which must be fitted into the limited space of the microscope.

3.3 Meniscus Effect

The meniscus effect poses a challenge for the comprehensive observation of specimens in liquid-filled vessels when using phase contrast microscopy [Hor06]. A meniscus refers to the curved shape of a liquid surface within a well, resulting from capillary forces. This curvature affects light as it passes through, due to refraction.
The meniscus shape is described by the contact angle between the liquid's surface and the well walls. A contact angle smaller than 90° indicates a concave meniscus, commonly observed in most liquids exposed to air, such as water. Menisci in wells with small diameters are fully curved, whereas those in wells with larger diameters display a flat center. A typical meniscus is illustrated in Figure 3.3.

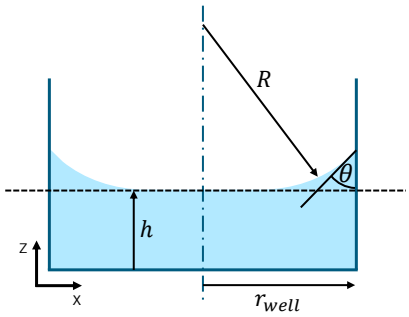

Figure 3.3: A liquid meniscus with a flat section in the center and a height h, contact angle θ, and a local radius of R in a well with radius r_{well}.

The formation of the meniscus can be explained by hydrostatic effects, which are detailed in Section 3.3.1. The refraction of light at the meniscus surface is examined in Section 3.3.2, along with its impact on imaging specimens in cell culture vessels.

3.3.1 Hydrostatic Description of the Meniscus

The liquid meniscus constitutes a multiphase system, comprising the liquid within the well, which can be modeled as a cylindrical tube, and the surrounding air. Multiphase systems strive to minimize the system's overall energy. Two types of energy are pertinent in describing a meniscus at rest: potential energy and surface energy. Forces emerge to minimize these energies. The shape of the meniscus results from an equilibrium between these forces and the boundary conditions determined by the contact angle between the liquid, air, and well wall.

Potential Energy

The forces within the meniscus are governed by fluid dynamics and are thus describable by the *Navier-Stokes equation* [Boy13]. For a meniscus at rest, fluid dynamics laws simplify to hydrostatics. The liquid forming the meniscus is incompressible. Consequently, describing the meniscus shape involves considering incompressible Newtonian fluids at rest, with gravity as the sole relevant body force, leading to the simplified Navier-Stokes equation shown in Equation 3.4 [Fox04]:

$$\nabla p = -\rho \vec{g}, \tag{3.4}$$

where ∇ denotes the gradient operator, p represents the pressure, ρ is the fluid density, and $\vec{g}$ signifies the gravitational acceleration.

Therefore, Equation 3.4 describes the pressure difference due to differences in potential energy [Boy13; Fox04]. This indicates that pressure changes occur along the gravitational direction, i.e., the liquid's height [Fin86]. Consequently, the hydrostatic pressure within the meniscus is derived by integrating Equation 3.4 with respect to the liquid's height, resulting in Equation 3.5 [Fox04]:

$$p = p_0 + \rho g h, \tag{3.5}$$

where p_0 refers to the atmospheric pressure at the fluid surface and h is the average height of the fluid column.

Surface Energy

Surface tension γ refers to the force per unit length that strives to minimize surface energy by reducing the surface area [Hen04]. It acts parallel to the interface between the liquid and the surrounding air. The pressure difference induced by surface tension on a curved liquid surface is described by the *Young-Laplace equation*, presented in Equation 3.6 [Hen04]:

$$\Delta p = \gamma \left(\frac{1}{R_1} + \frac{1}{R_2} \right), \tag{3.6}$$

where Δp denotes the pressure difference $p - p_0$, and R_1 and R_2 are the principal radii of curvature of the surface. R_1 and R_2 define the shape of a curved surface and are equal only if the surface is spherical.

Relationship Between Potential and Surface Energy

The relationship between gravitational forces and surface forces is quantified by the *Bond number* B [Esl19]. The Bond number is defined by Equation 3.7 [Esl19]:

$$B = \frac{\Delta \rho g L^2}{\gamma}, \tag{3.7}$$

where L represents the characteristic length of the system, specifically the well radius r_{well} for a liquid-filled well. The Bond number incorporates the *capillary length* l_c of a system, defined by Equation 3.8 [Esl19]:

$$l_c = \sqrt{\frac{\gamma}{\Delta\rho g}}. \tag{3.8}$$

This length indicates the distance over which surface tension can support a liquid against gravity. Consequently, the Bond number can also be expressed by Equation 3.9 [Esl19]:

$$B = \left(\frac{L}{l_c}\right)^2. \tag{3.9}$$

Besides the equilibrium between potential and surface energy, the meniscus shape is defined by boundary conditions, such as the contact angle.

Contact Angle

When a liquid is contained within a vessel, a three-phase contact line forms where the interface between the liquid and the ambient air intersects the vessel walls [Esl19]. In a cross-sectional view, this line reduces to a tri-point, as illustrated in Figure 3.3. The angle at this point, between the liquid and the well wall, is the contact angle θ. The contact angle between three known phases is calculated using *Young's equation*, which considers the balance of intermolecular forces at the interface, as described by Equation 3.10 [Esl19]:

$$\cos\theta = \frac{\gamma_{\mathrm{SV}} - \gamma_{\mathrm{SL}}}{\gamma_{\mathrm{LV}}}, \tag{3.10}$$

where γ_{SV} is the solid-vapor surface energy (energy per unit area of the solid in contact with air), γ_{SL} is the solid-liquid surface energy, and γ_{LV} is the liquid-vapor surface energy. These surface energies are influenced by the well geometry and the materials involved [Hen04].

Meniscus Shape in Narrow Wells

For systems with small Bond numbers, the meniscus shape can be approximated as spherical [Esl19]. The capillary length of water is approximately 2.7 mm [Lew22], meaning this spherical approximation is applicable to wells with radii significantly smaller than this length. This approximation simplifies the Young-Laplace equation, as shown in Equation 3.11 [Hen04]:

$$\Delta p = \frac{2\gamma}{R}, \tag{3.11}$$

with $R = R_1 = R_2$.

Due to the spherical shape of the meniscus, the relationship between the contact angle and principal radius of curvature is given by Equation 3.12 [Hen04]:

$$\cos\theta = \frac{r_{\text{well}}}{R}, \tag{3.12}$$

where r_{well} denotes the radius of the well.
In narrow wells, surface forces prevail over gravitational forces, causing the liquid column to rise to a height h. This height can be determined by equating the pressure differences in Equations 3.5 and 3.11, and inserting the contact angle from Equation 3.12, leading to Equation 3.13 [Hen04]:

$$h = \frac{2\gamma\cos\theta}{\rho g r_{\text{well}}}. \tag{3.13}$$

Thus, the complete meniscus shape can be determined if either the principal radius or contact angle is known, which can be obtained through measurement.

Meniscus Shape in Wide Wells

The radii of common MTP types are approximately 3.5 mm for MTP96, 8.25 mm for MTP24, and 17.5 mm for MTP6, which exceed the capillary length of water [Lew22]. Thus, the spherical approximation does not apply to menisci in these MTPs, as the cell media predominantly contain water.
Numerous approaches exist to analyze the meniscus shape in wide wells, as it is considerably more complex than in narrow wells due to an increased number of degrees of freedom. Nevertheless, the problem's rotational symmetry can often be exploited, enabling the description of the meniscus surface height z through a geometric equation $z(r)$ for a local radius r. By leveraging this symmetry alongside additional conditions, Equation 3.6 can be transformed into a more specific form, as shown in Equation 3.14 [Hen04]:

$$\Delta\rho g z(r) = 2\gamma H(r), \tag{3.14}$$

where $\Delta\rho$ represents the density difference with the surrounding air, and $H(r)$ is the mean curvature, defined by Equation 3.15 [Hen04]:

$$H = \frac{1}{2}\left(\frac{1}{R_1} + \frac{1}{R_2}\right). \tag{3.15}$$

Common approaches substitute $H(r)$ with known conditions, often resulting in a system of differential equations. These are typically solved via numerical integration with predefined boundary conditions [Das93; Esl19; Lew22; Orr77]. Numerical integration methods can start from the apex [Esl19], the three-phase contact line [Pad72], or other significant points [Che11]. These approaches require additional system information, such as known contact angles or the Helmholtz free energy [Esl19; Gao98]. While these values can be found in

literature for well-documented material combinations, they often necessitate extensive experimental determination [Das93]. In many cases, determining these values is impractical. Consequently, no universal solution exists for describing the meniscus shape in wide wells; a solution must be derived on a case-by-case basis. Direct measurement of the meniscus shape is often the only feasible alternative, which will be explored in Section 6.1.1.

3.3.2 Meniscus Effect on Phase Contrast Microscopy in Cell Culture Vessels

The meniscus acts as a concave lens for light passing through it (see Section 2.1.5). Its geometry modifies the path of passing light rays. When illuminated with parallel light, refraction occurs, directing rays away from the center [Hor06]. The refraction angle varies across different positions within the meniscus, as depicted in Figure 3.4. This effect is intensified for light rays traversing the steep-sloped sections near the MTP wall. In wells with larger radii, characterized by a nearly flat central region, the influence is less extensive due to the reduced share of the steep-sloped meniscus area. Conversely, wells with smaller radii exhibit a more pronounced effect.

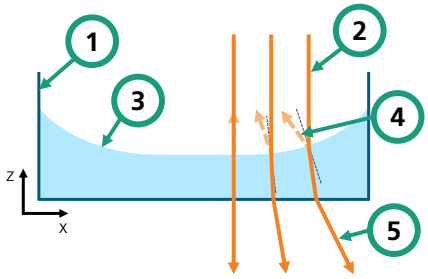

Figure 3.4: Refraction of three light rays passing through a liquid meniscus. Rays closer to the edge are refracted more strongly away from their original direction. (1) Well edge. (2) Incident light ray. (3) Meniscus surface. (4) Reflected light ray. (5) Refracted light ray.

When observing an object with spatial extension, rather than a point source, the light rays emanating from it pass through the meniscus at different positions, thereby undergoing varying angular changes. This variation results in Petzval field curvature (see Section 2.1.8) [Mat15].

The meniscus effect can significantly reduce the effectiveness of phase contrast microscopy in examining cell cultures within MTPs [Ben51]. Light refraction at the curved surface of the nutrient medium leads to a misalignment between the phase ring and the condenser annulus. This misalignment obstructs the establishment of phase contrast conditions, especially at the well's edge, where the liquid surface deviates from being flat. Figure 3.5 demonstrates this phenomenon.

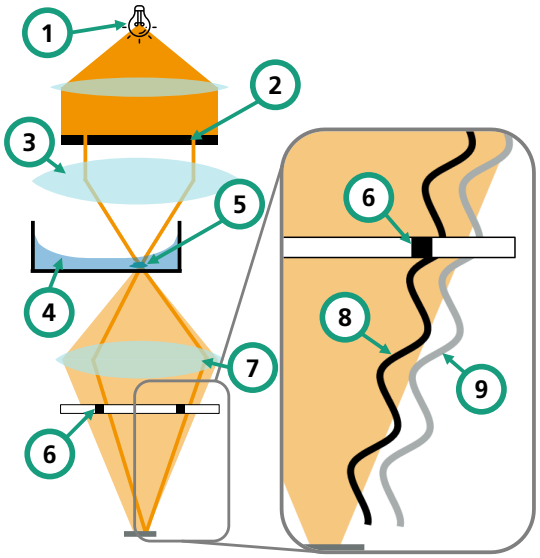

Figure 3.5: The meniscus effect in a phase contrast microscope. In contrast to Figure 2.9, the specimen is misaligned with the optical center. Refraction at the curved surface near the well edge causes the beam to deflect, disrupting the alignment between the condenser annulus and the phase ring. Consequently, the light passing through the specimen experiences no phase shift, as illustrated in the sectional view, resulting in the absence of phase contrast conditions. 1) Light source. 2) Condenser annulus. 3) Condenser lens. 4) Liquid meniscus. 5) Specimen. 6) Phase ring. 7) Objective lens. 8) Non-phase-shifted direct light wave. 9) Undisturbed scattered light wave.

Since the degree of refraction becomes more pronounced in smaller wells, the achievable relative phase contrast area reduces as the well size decreases [Hor06]. Figure 3.6 illustrates the restricted phase contrast area in MTPs.

Biological experts estimate this area to be approximately 25% in 6-well MTPs and about 2% in 96-well MTPs, though exact values depend on the optical setup [Nie23]. Given the subjective nature of expert opinions, quantifiable metrics are essential for comparing different MTPs and optical setups. The metric should characterize the percentage of the phase contrast area relative to the total well area and remain reliable under varying conditions, such as alterations in lighting and focus. These metrics must rely solely on images of the specimens within a well, ensuring comparability of images captured under diverse circumstances. A systematic literature review is therefore conducted in Section 3.4.

The reduced observation area resulting from the meniscus effect presents a notable challenge for laboratory automation systems aimed at comprehensive quality control. Variations in cell conditions between the central and peripheral regions of the well require examination of larger portions, rather than random sampling at the center. As a result, the utility of phase contrast microscopy is considerably restricted, often proving unsuitable for various applications.

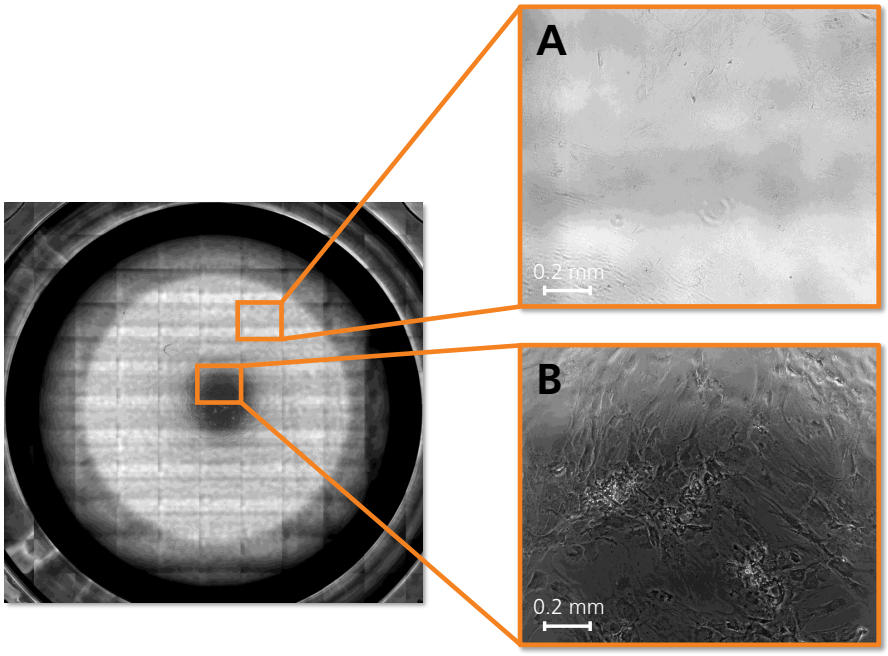

Figure 3.6: The meniscus effect in a 24-well MTP containing MSCs, with images captured at 4x magnification and assembled into a composite image of the entire well. Phase contrast conditions are confined to the central dark spot, where high-contrast observation of the specimen is feasible (B). Outside this dark central region, identifying the specimen becomes challenging (A).

Thus, identifying methods to mitigate the meniscus effect is essential to enhance the universal applicability of phase contrast microscopy. Such mitigation should be effective across large areas of the well. The curved shape of the meniscus introduces position-dependent refraction at different positions within the well, necessitating advanced approaches to address these refractive distortions. Such approaches may involve eliminating the meniscus entirely or employing adaptive optics to compensate for the distortions. Section 3.5 explores methods that incorporate these principles.

3.4 Quantification of Phase Contrast Conditions

The relative phase contrast area, which quantifies the share of a well in which phase contrast conditions are possible, is a meaningful metric to measure the limitation of phase contrast microscopy due to the meniscus effect. A systematic literature review was undertaken to identify scientific papers addressing methods to quantify phase contrast conditions. It was based on the preferred reporting items for systematic reviews and meta-analyses (PRISMA) methodology [Lib09; Pag21]. It involved a comprehensive search for publications and a subsequent selection procedure to pinpoint relevant works.
Suitable papers were identified and selected using predefined search strings and selection

criteria through a multi-step process. The online platform *Web of Science* served as the literature database, and the search string was applied to titles and abstracts of publications published between January 1, 1990, and December 31, 2024, as earlier works were deemed outdated.

The process comprised the following steps:

1. Database search,
2. removal of duplicates,
3. screening of titles and abstracts for eligibility,
4. assessment of full text for eligibility,
5. analysis of proposed methods in each eligible publication.

Database Search

The first step of the database search is the definition of the search string. To search for *phase contrast conditions*, potential synonyms must be considered. Additionally, the identified papers must be relevant to the field of microscopy. The following search string was ultimately selected:

("phase contrast condition*" OR "phase contrast characterist*" OR "phase contrast feature*" OR "phase contrast attribute*" OR "phase contrast trait*" OR "phase contrast area" OR "phase contrast imag* condition*" OR "phase contrast imag* feature*" OR "phase contrast imag* attribute*" OR "phase contrast imag* trait*") AND "microscop*"

Twelve papers were identified through the search, which were evaluated based on the selection criteria. They are listed in Table A.1 in the Appendices.

Literature Selection

The following inclusion criteria were established to identify relevant papers:

1. The study must use phase contrast microscopy for specimens in liquid solutions.
2. The study must focus on light microscopy. It must also not primarily utilize 3D, fluorescence, brightfield, or other microscopy methods.
3. The phase contrast area must be limited by the meniscus effect or otherwise curved liquid surfaces.
4. One of the following:
    a) The study must propose a quantifiable metric for determining the presence of phase contrast conditions within an image.

b) The study must present an algorithm for calculating the phase contrast area.

While the removal of duplicates did not eliminate any papers (step 2), applying these criteria to the titles and abstracts of all twelve papers resulted in only one publication remaining (step 3). Although this paper uses the phase contrast area as a metric, it lacks a quantifiable algorithm for calculating this area, relying instead on expert opinion, and was therefore excluded in step 4.

In conclusion, no single paper fulfills the criteria, indicating the absence of publications providing quantifiable metrics for phase contrast conditions. Thus, the systematic literature review identified a research gap. Addressing this gap by finding metrics and developing a new algorithm for validating novel meniscus effect compensation methods is essential as part of this thesis.

3.5 Existing Approaches for Meniscus Effect Compensation

Section 3.3 revealed that the meniscus effect imposes significant limitations on the efficacy of phase contrast microscopy, substantially decreasing the phase contrast area. Furthermore, Section 3.1 highlighted the substantial requirement for high-throughput solutions in cell cultivation. Thus, it is imperative to develop methods that mitigate the meniscus effect and are suitable for high-throughput applications. A comprehensive literature review was conducted to pinpoint approaches that fulfill these criteria. The identified publications were analyzed, and remaining research gaps were recognized.

3.5.1 Method

The systematic literature review followed the PRISMA methodology, utilizing the same five steps as the review in Section 3.4. In addition to scientific papers, patents were incorporated into the search process. Following the application of inclusion criteria in step 4, relevant publications were categorized into three distinct approach types in step 5.

The search for papers was conducted on the *Web of Science* platform, while patent families were explored using *Patbase*, employing identical search strings with minor syntax adjustments specific to each platform. Within patent families, one patent had to be selected for review. The original patent was preferred if available in English or German; otherwise, the corresponding European patent in English was selected. The search strings for the literature review are detailed in Table 3.1.

Table 3.1: Search strings used for the systematic literature review, along with the number of papers and patents identified through these searches.

Query	Search string	Papers	Patents	Sum
1	"phase contrast" AND microscop* AND (meniscus OR "meniscus effect$" OR "liquid lens")	14	13	27
2	meniscus AND ("phase contrast" OR mitigate OR compensate OR eliminate) AND ("microtiter plate*" OR "well plate" OR MTP)	5	7	12
3	"phase contrast" AND microscop* AND (brightfield OR "bright field" OR bright-field) AND meniscus AND (image analysis OR quantitative OR alternative OR software)	0	0	0
4	"phase contrast" AND microscop* AND method AND liquid AND ("optical unit" OR "optical element" OR "optical component")	0	11	11
	Total	19	31	50

Publications dated from January 1, 1990, to December 31, 2024, were included. During screening, papers or patents were selected based on the following inclusion criteria:

1. Utilization of phase contrast microscopy for analyzing specimens in liquid solutions.
2. Addressing issues caused by the meniscus effect that limit the phase contrast area or degrade image quality.
3. Presentation of methods enhancing image quality and increasing the area where phase contrast conditions apply in specimen images.

This search yielded 19 papers and 31 patents, totaling 50 publications. The results of this selection process are outlined in Table 3.2, with the number of records specified that passed each step. The twelve publications deemed eligible exhibited distinct characteristics, allowing for clear categorization into three groups, which are discussed in the following section.

Table 3.2: Multi-step selection process for identifying eligible solution approaches. All approaches deemed eligible based on their full-text articles were categorized into one of three distinct categories.

Step	Description	Number
Identification	Records identified through database searching	50
Duplicate removal	Records after duplicates removed	41
Screening	Titles and abstract screened for relevance	13
Eligibility	Full-text articles assessed for eligibility	12
Included into Category 1	Image analysis to simulate phase contrast conditions	1
Included into Category 2	Special MTPs	5
Included into Category 3	Alterations of the microscope's beam path	6

3.5.2 Results of the Literature Review

All identified solution approaches can be sorted into the three categories:

1. Image Analysis to Simulate Phase Contrast Conditions,
2. Special-MTPs,
3. Alterations to the Microscope's Beam Path.

They are presented in this section, followed by a discussion of their benefits and limitations in Section 3.5.3.

Image Analysis to Simulate Phase Contrast Conditions

The first category encompasses publications utilizing image analysis software to extract information from brightfield images to an extent that is supposed to match phase contrast conditions, or to simulate phase contrast images through image manipulation. Although the systematic literature review identified only one publication, this approach is significant due to its adoption in at least one commercial application. This application, Nikon's *Volume Contrast* [Eur25], was discovered through a Google search, supplementing the systematic literature review. It is discussed in this section, even though it does not appear in the literature review, as it is neither a paper nor a patent.

Kwee et al. 2018 [Kwe18] implement a scanning mechanism to observe iPSCs across an entire MTP well in phase contrast. They computationally compensate for the meniscus effect using reference interferogram images of a well filled with liquid but devoid of specimens. Image segmentation is employed to detect the foreground and background of the specimen image, and the background is corrected with information from the specimen image using a third-order polynomial fit, thereby enhancing contrast.

Nikon's Volume Contrast [Eur25] employs machine learning to adjust brightfield images, making them resemble phase contrast images. Due to its proprietary nature, details regarding the training methodology and benchmarking tests are not accessible to the public.

While these methods do not directly counteract the optical effects of the meniscus, they aim to extract comprehensive information from images lacking phase contrast conditions. Given that the source images do not exhibit phase contrast conditions throughout, their SNR is inferior to that of phase contrast images [Mur12]. Detailed information about the specimen and experimental setup, such as the meniscus shape of the vessel used and training images, is essential for studies like the one presented by Kwee et al., increasing the effort of these procedures [Kwe18]. Outputs generated by machine learning, such as Nikon's Volume Contrast [Eur25], require careful validation, as AI-modified images might display features not present in reality, a phenomenon known as *hallucination* [Mal24]. Additionally, a significant volume of training data is required, which is not accessible for all applications.

Special-MTPs

The review identified five patents detailing specialized cell culture vessels designed to mitigate the meniscus effect.

US2007274871 AA [Jia07] and **CA2675495 AA** [Dos08] describe variants of MTPs equipped with hydrophobic coatings to maintain a 90° angle at the cell medium–air–vessel wall interface, thus preventing meniscus formation.

US2010197004 AA [And10] and **US2022040689 AA** [Mil22] introduce MTPs with specialized lids that depress the liquid surface, creating a flat interface. The US2022040689 AA patent features a more complex lid geometry to avoid air bubble entrapment between the lid and cell medium. All approaches have in common that the lid actively prevents the meniscus from forming.

WO16120757 A1 [Bar16] proposes an approach where the liquid forms freely within an MTP, but a lens-shaped lid compensates for refraction induced by the sloped meniscus surface.

All designs offer the advantage of using standard phase contrast microscopes to produce images without meniscus effects. As a result, the phase contrast imaging area can potentially cover nearly 100% of the well, with limitations arising only from shading at the well's edges. However, each specialized MTP is optimized for specific applications, necessitating the use of standard operating conditions. Additionally, precise volume specifications are required for many configurations.
While special MTPs incur minimal initial costs due to their compatibility with standard phase contrast microscopes, they are consumables. Due to their more complex design and smaller production quantities, they are more expensive than regular cell culture vessels, leading to higher recurring expenses.

Alterations to the Microscope's Beam Path

This category explores modifications to microscopy techniques and equipment to compensate for the meniscus effect while maintaining specimens unchanged. Five patents and one paper outline potential solutions.

JP2017151132A [Shi17], **JP2017015856 A2** [Mat17], and **JP20170162052** [Tsu20] describe optical adjustment systems integrated into phase contrast microscopes, positioned between the condenser lens and meniscus. These systems can modify the beam path by adjusting the position, focal power, and optical axis of an adjustment element, such as a lens, to correct optical path deviations induced by the meniscus. The patents do not specify the details of the adjustment system; instead, they emphasize deriving system parameters through specimen observation. These parameters are subsequently used to configure the adjustment elements.

Hofmeister et al. 2020 [Hof20] propose replacing the static condenser unit with a DMD, enabling flexible illumination adjustments based on the imaging position within a well. By manipulating a virtual condenser annulus on the DMD, phase contrast conditions can be restored near the well edge. The original light house of the microscope is replaced by the DMD, and a new light source is introduced to provide the angled illumination necessary for the DMD.

US2012257040 AA [Bah12] suggests using an LCD in place of a fixed condenser annulus, allowing positional flexibility of the condenser annulus.

EP3323010 A2 [Die18] combines an LCD as a condenser annulus with a liquid-filled prism in the beam path between the condenser lens and meniscus. This configuration compensates for the meniscus surface slope and lateral displacement on the condenser plane caused by the oblique wavefront.

These sophisticated compensation mechanisms offer adaptability to diverse specimens, vessel types, and liquids. They hold the potential to produce high-quality images and establish genuine phase contrast conditions, unlike software solutions. However, these approaches are more complex than MTP-based methods, leading to higher initial costs. Despite this, as they utilize standard cell culture vessels, the recurring costs are similar to those of conventional phase contrast microscopes. A notable potential limitation of many of these methods is reduced acquisition speed due to the movement of mechanical components, even though this does not apply to US2012257040 AA.

3.5.3 Assessment of Existing Methods

The three categories of solution approaches identified in the previous section are analyzed: image analysis solutions are termed *software-based*, specialized well plates are labeled

special-MTPs, and alterations in the microscope's beam path are designated as *microscope-based*. A qualitative comparison of these categories is presented using a Harvey Balls diagram in Figure 3.7. The comparison primarily addresses the main functionalities, specifically enhancing the phase contrast area and accommodating high-throughput imaging. Additional criteria stem from applications in phase contrast microscopes for cell culture observation. Crucially, the image quality must remain intact, the approaches should be adaptable to the flexible production of various cell types, and costs associated with eventual commercialization should be minimal.

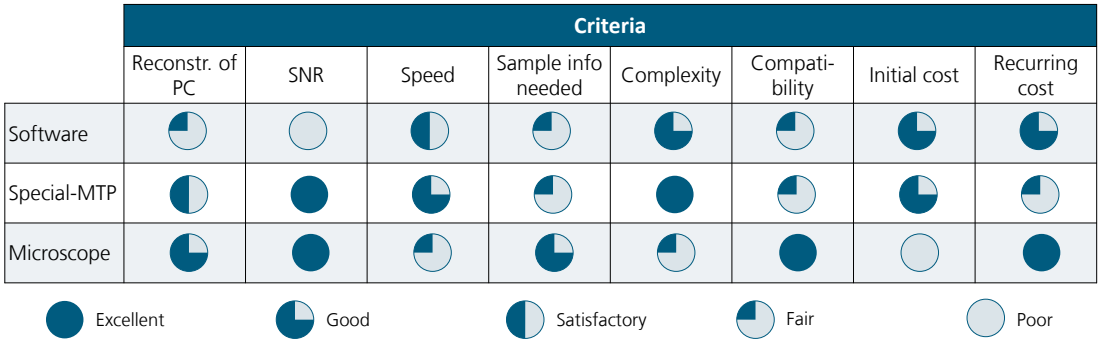

Figure 3.7: Harvey Balls representation of the three approach categories to mitigate the meniscus effect. Explanation of categories: *Reconst. of PC*: Reconstruction of phase contrast; the ability to create phase contrast conditions in areas where they were previously unattainable. *SNR*: Signal-to-noise ratio; the achievable contrast within the reconstructed phase contrast area. *Speed*: Potential acquisition time achievable with HSM. *Sample info needed*: The amount of information required to mitigate the meniscus effect, such as liquid properties or sample type. *Complexity*: The complexity of setup and process compared to regular phase contrast microscopy. *Compatibility*: Compatibility of the approach with various types of samples and liquids. *Initial cost*: Cost of procurement for the initial setup. *Recurring cost*: Cost per experiment, including consumables and license fees.

Software-based solutions benefit from utilizing straightforward hardware, such as brightfield microscopes. However, they often necessitate extensive training datasets. Introducing new specimen types, such as different cell types, typically requires additional training or reference measurements. A fundamental limitation of these methods is their dependence on lower contrast source images compared to phase contrast microscopy, which results in a reduced signal-to-noise ratio and provides less reliable information for image analysis algorithms. Consequently, this method is inherently limited and cannot achieve the same quality of data as authentic phase contrast microscopy.

Conversely, both special-MTPs and microscope-based methods modify illumination to establish genuine phase contrast conditions in areas where it was previously absent. Special-MTPs offer optimal imaging conditions for specific specimen types, such as a particular cell medium with a defined refractive index. However, they lack flexibility and are specialized for one application. In contrast, the microscope-based approaches are more versatile and can be designed to accommodate a wide range of liquid-filled vessels. Microscope-based

methods also offer the advantage of low recurring costs, comparable to conventional phase contrast microscopy, unlike specialized-MTP, which incur high recurring costs due to consumables. A notable drawback of the microscope-based approach, however, is the inherent complexity, leading to initially high hardware and development costs.

None of the presented methods has been explicitly optimized for rapid acquisition times. Since modifications to the microscope hardware are unnecessary, it is assumed that special-MTPs are most suited for high-speed imaging with current technology when placed in a high-speed microscope. However, mechanical adjustments to the microscope-based approaches could potentially yield similar performance, though a research gap exists as this has not been explored thus far.

Evaluating the requirements against the three categories of solution approaches to mitigate the meniscus effect, it was concluded that microscope-based solutions offer the greatest potential due to their meniscus compensation capability and versatility. Therefore, the method explored in this thesis falls within this category.

3.6 Summary and Interim Conclusion

Phase contrast microscopy is widely utilized in cell observation due to its ability to capture high-resolution images of transparent specimens. However, the meniscus effect confines observation under phase contrast conditions to small central areas of wells in MTPs. This effect results from refraction at the surface of the cell medium within the well.
Expanding the phase contrast area despite the meniscus is important for broadening the application scope of phase contrast microscopy. A systematic literature review was conducted to evaluate existing methods to counteract the meniscus effect. The most promising solutions involve integrating adaptive components into the microscope's beam path, which can steer illumination light beams to counteract refraction independently at each position within a well. Further analysis is necessary to determine which of these methods can significantly enhance the phase contrast area.
No precise data was found on the extent to which adaptive components can enlarge the phase contrast area, necessitating investigation within this thesis. To measure the phase contrast area, a quantifiable metric is essential. A systematic literature review identified the absence of such a metric, representing a research gap that will also be addressed in this thesis.

The restricted imaging region within well plates is not the only limitation for high-throughput cell observation. Another limitation is the slow acquisition speed of conventional microscopes, primarily due to their restricted field of view. HSM has been introduced as a solution to substantially reduce overall acquisition time for large specimens. To effectively address the meniscus effect, the continuous image acquisition process during sample movement introduced by HSM should be integrated into the approach to achieve competitive imaging durations. Thus, the meniscus compensation mechanism must also support high-speed

imaging. Additionally, the potential imaging time for a high-speed compensation method must be assessed.

In summary, based on the identified research gaps, the following sub-research questions are formulated:

SRQ1 How can the phase contrast area in microtiter plates be quantified?

SRQ2 Which adaptive components are suitable for high-speed implementation?

SRQ3 To what extent can the phase contrast area be increased using adaptive phase contrast microscopy compared to conventional phase contrast microscopy?

SRQ4 Which acquisition time is achievable for complete wells in microtiter plates? What are the influencing factors on acquisition time?

These supplement the main research question:

Can the optical compensation of the meniscus effect in phase contrast microscopy be performed during sample movement in combination with continuous image acquisition?

Answers to these questions are explored in the following chapters, with each chapter dedicated to one SRQ.

4 Quantitative Measurement of Phase Contrast Conditions

The literature review in Section 3.4 indicates the absence of a metric to quantify the phase contrast area in MTPs. Such metrics are crucial for assessing the experimental validation of adaptive phase contrast microscopy against conventional phase contrast microscopy. This chapter seeks to fill this research gap and consequently answers SRQ1 (see Section 3.6): *How can the phase contrast area in microtiter plates be quantified?*

The initial step involves identifying the conditions under which phase contrast occurs and determining methods to measure phase contrast within an MTP. Subsequently, a new approach is formulated to quantify the phase contrast area.

4.1 Characteristic Metric for Phase Contrast Conditions

The objective of this section is to identify characteristic patterns in images of specimens within MTPs that can effectively describe phase contrast conditions. These patterns are investigated to assess if they can be represented by a single numerical value, which can subsequently serve as an indicator of phase contrast conditions. Images captured by the microscope's main camera, intended to display the specimen within an MTP well, ideally under phase contrast conditions, are hereafter referred to as *specimen images*.

As outlined in Section 2.2.3, the presence of phase contrast conditions can be verified by observing the overlap of the condenser annulus and the phase ring through a Bertrand lens; images acquired through a Bertrand lens are subsequently referred to as *Bertrand images*. Concentric alignment of the condenser annulus and phase ring confirms the presence of phase contrast conditions.
However, this alignment is often challenging to observe directly. Although simultaneous observation of specimen images and Bertrand images is possible using a beam splitter, this approach is rarely practical. First, this method restricts comparisons to images acquired exclusively with setups that include the beam splitter. As a result, comparisons with phase contrast images obtained from other microscopes, which lack information about ring overlap, become unfeasible. Second, the beam splitter reduces the light intensity available for specimen images, thereby degrading image quality. Third, this technique cannot identify uneven phase contrast conditions within a single image. Such uneven conditions may arise when the camera's field of view is sufficiently large for the meniscus curvature to cause significant

variations in refraction across different regions of the image.
Consequently, the analysis must rely exclusively on visible features within specimen images. Image processing techniques can then be employed to extract the relevant metric.

The determination of these characteristics was conducted experimentally. During the experiments, specimen images were captured concurrently with Bertrand images, using the Bertrand images as a reference. The phase contrast amount was progressively reduced by modifying the illumination. Subsequently, the specimen images were compared to the alignment of the phase ring and condenser annulus observed in the Bertrand images. By examining the characteristics within specimen images and correlating them with the alignment, a metric was formulated that eliminates the requirement for direct observation of the alignment.

4.1.1 Experiments

Experiments were conducted utilizing a phase contrast microscope with MSCs in 24-well MTPs as specimens. The experiment comprised six runs, all executed in the same well, with images captured at three distinct locations: Position 0 at the center, Position 1 at a 2 mm offset, and Position 2 at a 4 mm offset from the center along the x-axis. Two magnifications, 4x and 10x, were employed during the experiments. Figure 4.1 illustrates the beam path within the experimental configuration, as well as an overview over the imaging positions within a well and the condenser annulus positions between images.

Two cameras were employed: the main camera focused on the specimen, while the secondary camera observed the phase ring and condenser annulus overlap through a Bertrand lens. A beam splitter divided the incoming light equally between both cameras. An LCD was utilized to display the condenser annulus, replacing the traditional condenser annulus (as detailed in Section 5.2.3). During each experimental run, various annulus positions were displayed on the LCD. The first image was captured with perfect alignment between the condenser annulus and the phase ring, where ideal phase contrast conditions were known to exist. For each subsequent image, the horizontal position of the condenser annulus was displaced by 0.25 mm in the x-direction. Thereby, the amount of phase contrast could be reduced from one image to the next. As the condenser annulus shifted further from alignment, phase contrast conditions weakened, causing the images to resemble those of brightfield microscopy. Figure 4.2 presents a subset of the image series.

Figure 4.2a shows a condenser annulus completely concentric with the phase ring, while Figure 4.2b is slightly displaced yet still within the ring, resulting in phase contrast images shown in Figure 4.2e and Figure 4.2f with minimal differences. In contrast, Figure 4.2c and Figure 4.2d depict annuli further removed from the center, leading to Figure 4.2g and Figure 4.2h with decreased phase contrast characteristics.

Comparing the images in Figure 4.2e and Figure 4.2f with Figure 4.2g and Figure 4.2h reveals two distinguishing features characteristic for phase contrast: increased sharpness

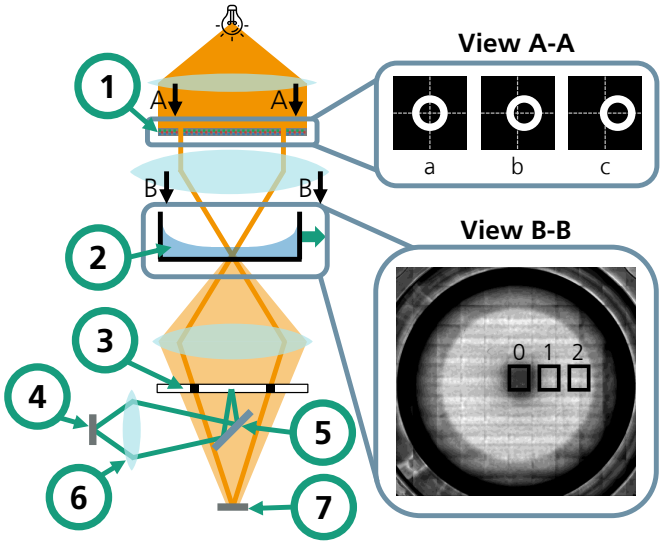

Figure 4.1: Simplified schematic representation of the experimental setup for identifying characteristic metrics of phase contrast conditions. The diagram depicts the beam path in a phase contrast microscope equipped with two cameras: the main camera targeting the sample and the Bertrand camera directed at the phase ring. Non-essential lenses are excluded from the illustration, and distances are not to scale. During each experimental run, the condenser annulus position was displaced horizontally, as detailed in section view A-A. Three experimental runs were conducted per MTP at three distinct positions within a well, indicated as 0, 1, and 2 in sectional view B-B. (1) LCD condenser annulus. (2) Meniscus in MTP well. (3) Phase ring. (4) Secondary camera. (5) Beam splitter. (6) Bertrand lens. (7) Main camera.

and a darker background. These features will be analyzed to develop a quantifiable metric for phase contrast.

4.1.2 Computational Analysis of Phase Contrast Images

To analyze sharpness and brightness in each image, scalar metrics representative of the entire image were selected for both.

The Tenengrad algorithm was chosen for contrast calculation due to its consistent performance under varying illumination conditions [Zhu13], a critical factor given the substantial differences in background brightness across the images (refer to Section 2.4.8) [Hua24]. The lower computational efficiency compared to other algorithms is not a concern, as rapid analysis is unnecessary for this process [Zhu23]. Although the algorithm is sensitive to noise, this issue is mitigated by the uniform environmental conditions under which all images were captured.

The assessment of background brightness relied on the observation that the background occupies a far larger area of the image compared to the specimens. Accordingly, the av-

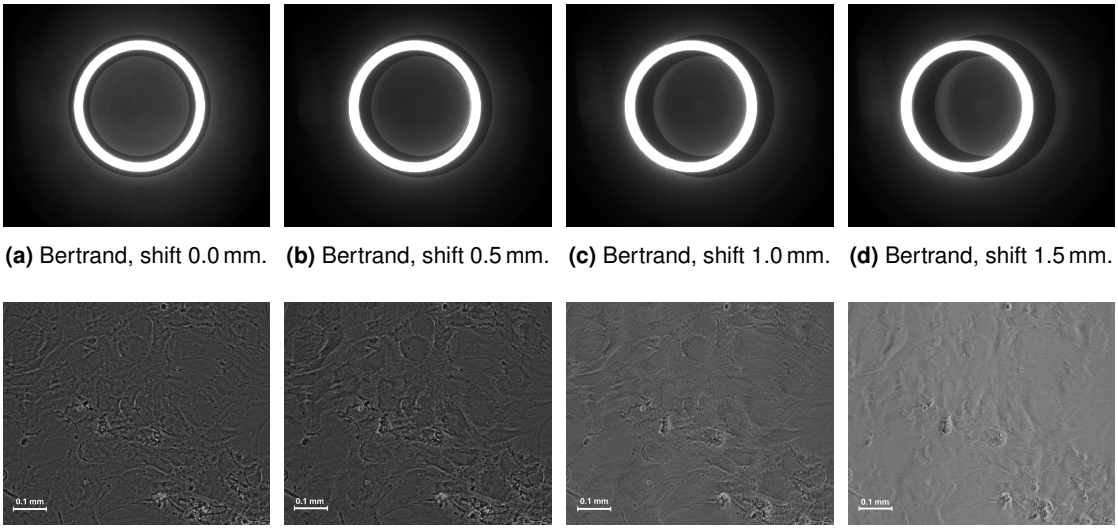

(a) Bertrand, shift 0.0 mm. **(b)** Bertrand, shift 0.5 mm. **(c)** Bertrand, shift 1.0 mm. **(d)** Bertrand, shift 1.5 mm.

(e) MSCs, shift 0.0 mm. **(f)** MSCs, shift 0.5 mm. **(g)** MSCs, shift 1.0 mm. **(h)** MSCs, shift 1.5 mm.

Figure 4.2: The overlay of the condenser annulus and phase ring, when seen through a Bertrand lens (a - d), and the corresponding phase contrast images of MSCs, as recorded by the primary camera (e - h) [Nie25]. All images were taken at the center of the well, magnification of 10x. In the experiments, the condenser annulus was shifted by 0.25 mm between consecutive images; every second image of the experiment is shown, shifts are noted in the captions of the subfigures.

erage gray value of the entire image effectively represents the background brightness, as features like cell boundaries constitute only a small portion of the image. The average gray value is determined by calculating the mean of the grayscale values of the image.

4.1.3 Results and Conclusion

Sharpness and brightness values were calculated for all images. For comparability across different experimental runs, all results were normalized to the respective values where the condenser annulus is exactly concentric with the phase ring. The results for 10x magnification are presented in Figure 4.3, with one curve plotted for each run of the experiment at different positions within the well.

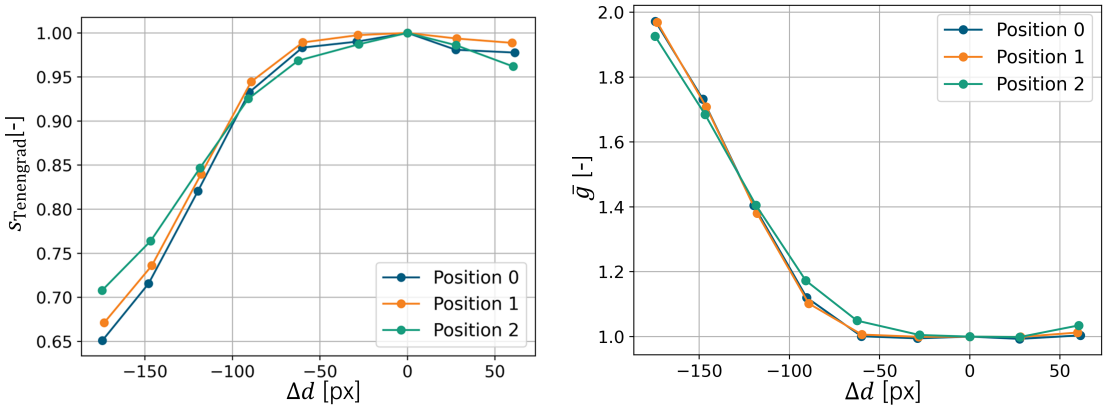

(a) Sharpness.

(b) Background brightness.

Figure 4.3: Sharpness $s_{\text{Tenengrad}}$ (a) and background brightness (represented by average gray values $\overline{g}$) (b) plotted over the condenser annulus displacement from the center Δd, as observed through the Bertrand lens with the secondary camera and calculated using image analysis [Nie25]. All values are normalized to the values at the central position. Position 0: exactly in the center. Position 1: 2 mm from the center. Position 2: 4 mm from the center. Magnification of 10x.

The sharpness values exhibit similar trends across all three experimental runs, as do the gray values [Nie25]. Images where the condenser annulus is slightly displaced but still within the phase ring (either side of the center) show values almost identical to the central position, confirming that phase contrast conditions are present in these images. Beyond this, sharpness decreases, and gray values increase as the condenser annulus position deviates further from the center.

There is a strong negative correlation between sharpness and average brightness. The Pearson correlation [Ben09] coefficient between the curves acquired at the same well position is -0.994 for experiments with 10x magnification and -0.974 for those with 4x magnification. This strong negative correlation implies that either metric alone can reliably predict phase contrast conditions. Nonetheless, this correlation is valid only if ambient conditions remain consistent throughout the experiment. In practical applications, ambient conditions are subject to variability. Sharpness is influenced by factors such as focus position and the number of objects within an image. For instance, a clear image with few cell colonies may have a lower sharpness value than a blurry image with high colony density. Background brightness, however, is less sensitive to such variations, assuming consistent illumination conditions and relatively similar samples across all images. Therefore, background brightness, as a more robust metric, is chosen as the sole indicator of phase contrast conditions within an MTP well in this thesis. However, as experiments were exclusively conducted with MSCs samples, further studies need to determine the universal applicability of this metric to different sample types.

It is important to note that brightness can predict phase contrast conditions only under specific circumstances. Brightness is meaningful as a relative metric, meaning that a base

gray value from a position with known phase contrast conditions must be established. A significant deviation from this base value indicates that phase contrast conditions no longer apply.

4.2 Algorithm for Calculating Phase Contrast Area in a Well-Plate

An algorithm has been developed to quantify the phase contrast area across an entire well of an MTP. This algorithm leverages the dependency between relative brightness and phase contrast conditions. The development process entails identifying a continuous region surrounding the well center that exhibits uniform background brightness. The algorithm comprises the following steps [Nie25]:

1. Image blurring,
2. identification of the base gray value,
3. defining thresholds,
4. binarization,
5. erosion and dilation.

The methodology is illustrated with an example in Figure 4.4.

Step 1: Image Blurring The algorithm processes composite images of an entire well, with an example image shown in Figure 4.4a. Due to the large size of these images (often exceeding 1 GB), compression is necessary as the first step to prevent overloading the computer and to keep computation times manageable. The bit depth is scaled to 8 bits, enabling representation of pixel values ranging from 0 to 255. Next, a Gaussian blur filter with a sigma of 10 pixels is applied to smooth individual features and assign each pixel the average background color of its surroundings. This step is illustrated in Figure 4.4b.

Step 2: Identification of the Base Gray Value With the image now consisting of smooth background colors, the base gray value representing phase contrast is determined as the pixel value exactly at the image center. Given the meniscus shape, it is assumed that phase contrast conditions are present at the exact center of the well. From this point onward, all other gray values in the image are compared to this base value.

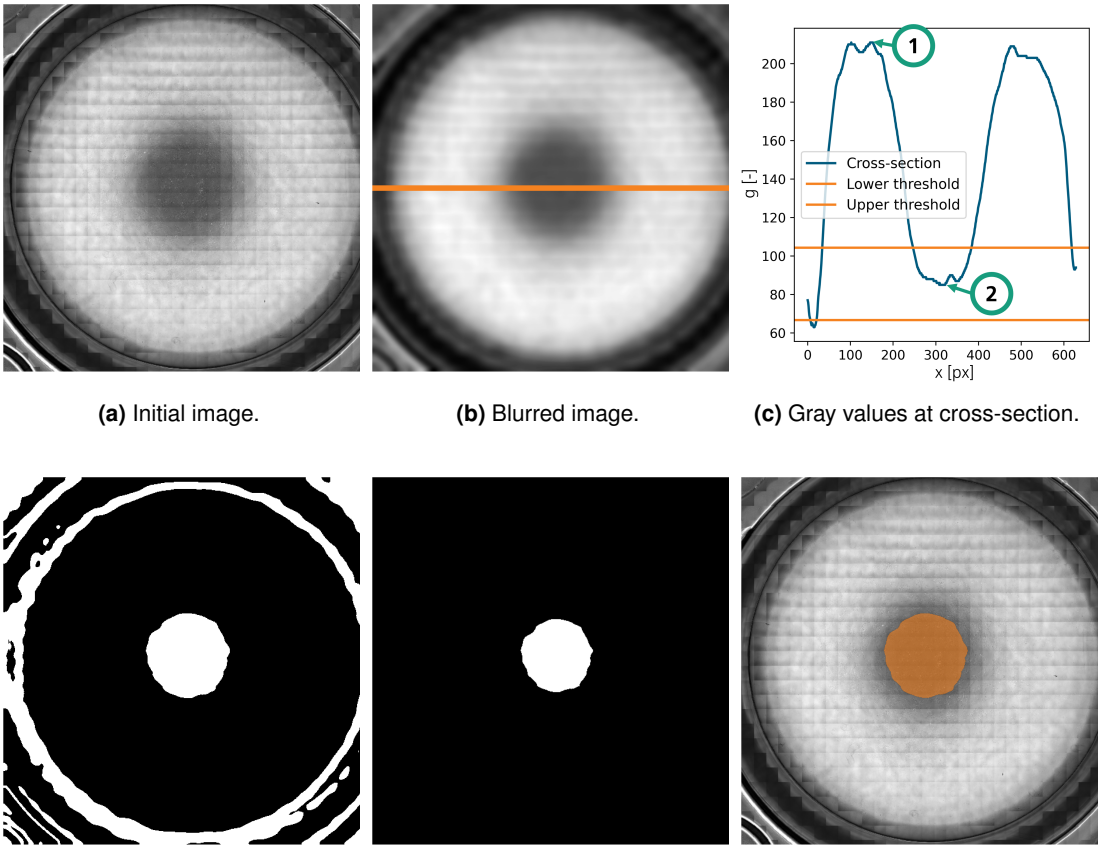

(a) Initial image. **(b)** Blurred image. **(c)** Gray values at cross-section.

(d) Binarized image. **(e)** Post-erosion image. **(f)** Final result.

Figure 4.4: Algorithm for analyzing phase contrast area [Nie25]. (a) The initial image of a well, obtained using adaptive phase contrast microscopy. (b) The processed image after blurring and compression, with the orange line indicating the central cross-section. (c) Gray value distribution g along the cross-section x, including the applied threshold, (1) maximum gray value, (2) base gray value. (d) Binarized version of image (b), where white regions fall within the threshold range. (e) Resultant image post-erosion, highlighting the central white region. (f) The phase contrast area superimposed on the original image.

Step 3: Defining Thresholds To identify a continuous area with values similar to the base gray value, lower and upper thresholds are defined. Gray values within these thresholds are considered to indicate phase contrast conditions. The upper threshold is quantified as a percentage T_{pc} of the difference between the base gray value and the brightfield value, which is the maximum observed value in a cross-sectional analysis centered on the image. Conversely, the lower threshold is determined by subtracting the aforementioned range from the base gray value. Figure 4.4c provides a cross-sectional depiction through the blurred image along the orange line drawn in Figure 4.4b, showing both thresholds, alongside the maximum value (denoted as (1)) and the base gray value (denoted as (2)).
A percentage of $T_{\text{pc}} = 15\%$ has been found effective, ensuring that areas classified by

experts as phase contrast fall within the thresholds while minimizing false positives. The thresholds t_{upper} and t_{lower} are calculated by Equation 4.1:

$$\begin{pmatrix} t_{\text{upper}} \\ t_{\text{lower}} \end{pmatrix} = \begin{pmatrix} g_{\text{ph}} + T_{\text{pc}} \left(g_{\text{br}} - g_{\text{ph}} \right) \\ g_{\text{ph}} - T_{\text{pc}} \left(g_{\text{br}} - g_{\text{ph}} \right) \end{pmatrix}, \tag{4.1}$$

where g_{ph} is the base gray value and g_{br} is the brightfield gray value.

Step 4: Binarization Binarization is performed on the blurred image, marking all values between the thresholds as *true* and all other values as *false*. The result is shown in Figure 4.4d.

Step 5: Erosion and Dilation Given that peripheral regions of the well might coincidentally exhibit the same gray value as the central patch, the central area must be isolated. A combination of erosion and dilation separates the central area, as described in Section 2.4.4. Erosion is performed using a circular kernel with a diameter of 5 pixels to thin out all shapes, thereby eliminating any narrow bridges of *true* values that might connect the central patch to outer regions. Following this step, all patches of *true* values are assigned to an individual instance each, and all patches except the central one are removed, as illustrated in Figure 4.4e. Finally, dilation is applied using the same kernel used for erosion to restore the original size of the central patch.

This central patch now represents the phase contrast area, which is 6.2% in the shown example. It is overlaid on the original image in Figure 4.4f. The proportion of the phase contrast area within a well is calculated as the ratio of the phase contrast patch size in pixels to the total area of the well bottom.

4.3 Summary and Interim Conclusion

This chapter explored the mathematical description of phase contrast conditions. The appearance of phase contrast images was analyzed experimentally to identify common parameters. Images of MSCs in MTPs were captured. Sharpness and background brightness emerged as key metrics defining phase contrast conditions. Further analysis demonstrated a strong negative correlation between these metrics, with background brightness proving more resilient against fluctuations in ambient conditions and sample density. An algorithm was subsequently implemented to identify regions in whole well images where phase contrast conditions are applicable, based on background brightness.

In conclusion, this chapter addresses the research gap concerning the quantification of phase contrast conditions in biological specimens within MTPs. Thus, SRQ1, described as *How can the phase contrast area in microtiter plates be quantified?*,
is conclusively answered.

5 Assessment of Adaptive Components

As previously concluded, it is necessary to modify the beam path within the phase contrast microscope based on its position in the well. Adaptive components are employed for this purpose, enabling the modulation of illumination on the meniscus. This chapter examines various adaptive components, which addresses SRQ2 (refer to Section 3.6):
Which adaptive components are suitable for high-speed implementation?

Section 5.1 drafts four approaches to implementing adaptive components alongside evaluation criteria. Section 5.2 delves into potential implementation strategies. Optical simulations are conducted using Zemax OpticStudio in Section 5.3. Section 5.4 presents experiments designed to evaluate the effectiveness of these approaches in mitigating the meniscus effect. Section 5.5 discusses the simulation and experimental outcomes, evaluating the adaptive components against the predefined criteria. Finally, Section 5.6 summarizes the evaluation results.

5.1 Consideration of Different Adaptive Components

Various adaptive components are assessed to enhance adaptive illumination, aiming to expand the phase contrast area. These components are incorporated into the illumination beam path of the microscope and are intended to either replace or supplement the existing fixed condenser annulus. The evaluation is based on criteria established from cell culture imaging requirements, as detailed below:

1. **Phase contrast area**: Maximizing the area where phase contrast conditions can be achieved is essential.
2. **High-speed capability**: The component must enable rapid switching to allow the acquisition of numerous images over a large well area in a short time.
3. **Flexibility**: The system must be adaptable to various samples and function effectively under diverse ambient conditions. It should also allow easy integration into and removal from a conventional phase contrast microscope.
4. **Complexity**: The number of interacting mechanisms and parts should be minimized to ensure simplicity.

5. **Robustness**: In biological research environments prone to wet or contaminated conditions, the module must exhibit durability and operate reliably over extended periods without maintenance.
6. **Cost**: For successful commercialization, the setup should be designed to incur low manufacturing and recurring costs.

To achieve optimal optical performance, the illumination's wavefront must be tilted and shifted when passing through the meniscus surface. This can be achieved using standalone components or a combination thereof. The following components were considered for these purposes:

- Digital Mirror Device,
- horizontally movable lens or condenser annulus,
- Liquid Crystal Display,
- liquid-filled prism.

The DMD, LCD, and the movable condenser annulus were evaluated for their capacity to move the beam horizontally, while the liquid prism and movable lens were assessed for their ability to manipulate the beam angle. This section provides an overview of these technologies and how they can compensate for the meniscus effect.

5.1.1 Digital Mirror Device

DMDs facilitate rapid light modulation, as elaborated in Section 2.3.3. The application of DMDs to compensate for the meniscus effect in phase contrast microscopy has been previously investigated by Hofmeister et al. [Hof20]. DMDs can transition between states within microseconds, a highly advantageous characteristic for high-speed meniscus compensation [Ren15]. The DMD can be employed to display a condenser annulus, which can be translationally repositioned to adjust refraction at various positions within the meniscus. This modification alters the path of light beams through the condenser lens, consequently changing the illumination angle at the meniscus surface, thereby compensating for the meniscus effect. Figure 5.1 illustrates an example of a light path through such a microscope.

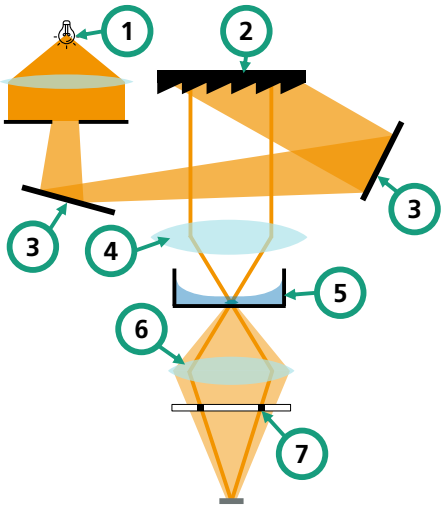

Figure 5.1: A possible, simplified beam path for a microscope equipped with a DMD (compare to a regular phase contrast microscope in Figure 2.9). (1) Light source. (2) DMD. (3) Mirrors. (4) Condenser lens. (5) Meniscus. (6) Objective lens. (7) Phase ring.

5.1.2 Horizontally Movable Lens or Movable Condenser Annulus

Mounting the condenser lens on horizontally movable axes enables precise control of the illumination angle, effectively counteracting refraction at the meniscus. Similarly, the condenser annulus can be mounted on horizontally movable axes to direct the illumination beam path. The angle of the incoming light is adjusted as it passes through the condenser lens at different positions, thus creating a counter-refraction effect at the meniscus surface. Given that both the movable lens and the movable condenser annulus utilize the same actuation system, their advantages and disadvantages are mostly similar and can be discussed collectively.

The movable lens, due to its curved shape, provides a continuous range of angles between 0° and the maximum angle at its edge. Thus, the angle of the transmitted light can be

precisely controlled based on the lens position. Movement can be facilitated using stepper motors or servo motors, combined with spindle axes, or alternatively, with linear motors. Figure 5.2 illustrates the operating principle.

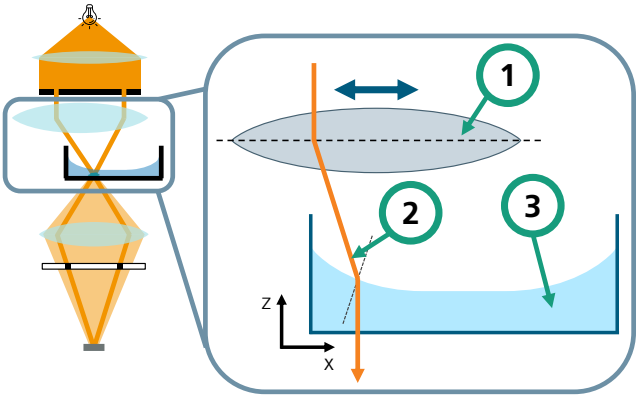

Figure 5.2: The operating principle of a movable lens. The lens position is adjusted horizontally to compensate for the meniscus effect at various well positions. (1) Movable lens. (2) Light ray. (3) Meniscus.

5.1.3 Liquid Crystal Display

Instead of using a physical condenser annulus cut into a plate, a virtual condenser annulus can be displayed on an LCD as a white ring on a black background. Due to their inherent translucency, LCDs can be integrated into the microscope's condenser unit, replacing the conventional condenser annulus. The meniscus effect can be compensated by adjusting the position of the virtual condenser annulus on the LCD. Similar to the DMD, translating the condenser annulus results in the light passing through the condenser lens at different positions, as depicted in Figure 5.3. This digital approach eliminates the necessity for mechanical components, thereby enhancing robustness.

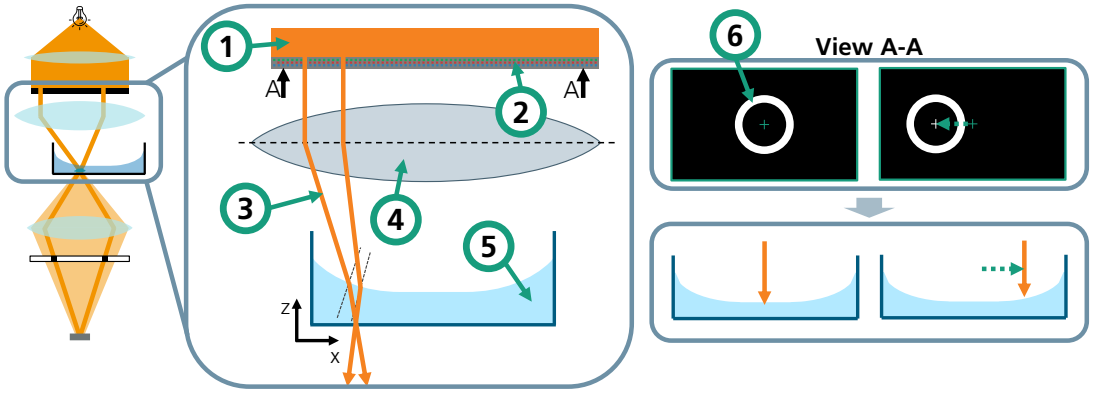

Figure 5.3: Working principle of an LCD for beam path steering. Components are not depicted to scale. Refraction at the meniscus surface is compensated through a combination of shifting the condenser annulus and the angular change induced by the condenser lens. Light is represented by orange arrows, with green arrows indicating the transition from one image to the next. (1) Incoming light. (2) LCD. (3) Light ray. (4) Condenser lens. (5) Meniscus. (6) Virtual condenser annulus.

5.1.4 Liquid-Filled Prism

As shown in Section 2.1.6, light passing through a prism undergoes refraction twice, resulting in a directional change. By adjusting the angles between the prism surfaces, the light's output angle can be controlled. This principle can be applied to counteract refraction at the meniscus surface. Since solid structures are not easily deformable, a flexible structure is required to achieve an adjustable prism angle. This can be implemented using two glass plates with a clear liquid in between and a flexible shell enclosing the liquid. Actuators can dynamically change the prism angle by tilting one or both glass plates. Figure 5.4 illustrates the optical working principle.

The liquid-filled prism can also be utilized in conjunction with approaches that shift the condenser annulus horizontally, such as the LCD, DMD, or a horizontally movable condenser annulus. This combination can enhance performance by providing two additional degrees of freedom, allowing independent control of the illumination angle at the meniscus surface and the horizontal position of the illumination. However, this combination also increases the setup's complexity.

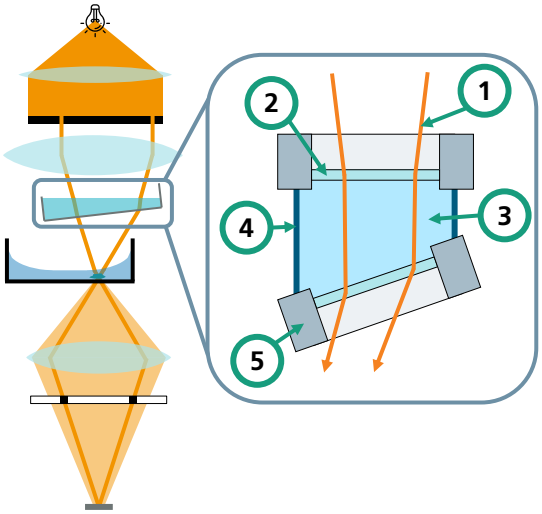

Figure 5.4: Schematic depiction of the light beam path in an phase contrast microscope that incorporates a liquid filled prism (compare to a regular phase contrast microscope in Figure 2.9). The wavefront of the illumination light is tilted by refraction at the interfaces to compensate for refraction at the meniscus surface. (1) Light ray. (2) Glass plate. (3) Liquid. (4) Flexible shell. (5) Housing.

5.2 Implementation of Adaptive Components

To evaluate the concepts, demonstrators were developed for the four described approaches. Comprehensive considerations regarding the implementation of these concepts were undertaken, followed by preliminary tests. Designs failing to satisfy the evaluation criteria outlined in Section 5.1 were omitted from subsequent optical simulations and experimental investigations.

5.2.1 Digital Mirror Device

DMDs are capable of precisely steering the illumination light path. However, implementing this method requires a complex configuration of the illumination unit. DMDs demand oblique illumination with a precise angle, making it impossible to directly replace the conventional condenser unit in the illumination path of a conventional phase contrast microscope. Consequently, the entire illumination system must be redesigned. Figure 5.5 illustrates a possible setup, comparing the illumination of a conventional phase contrast microscope with that of a DMD side-by-side.

The incorporation of a DMD necessitates a complex illumination unit, posing challenges for integration into a conventional phase contrast microscope. Calibrating the beam path with a DMD introduces additional complexity for the user, and the setup lacks the flexibility to switch to other illumination modes. Thus, this approach does not meet the objectives of low

complexity and low cost. For these reasons, this approach was not further pursued in this thesis.

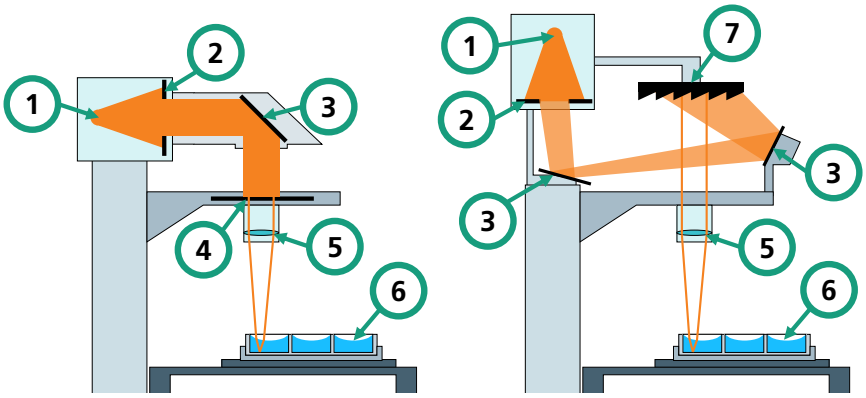

Figure 5.5: A possible configuration of a DMD included in the illumination beam path of a phase contrast microscope (right) compared to a conventional phase contrast microscope (left). (1) Light source. (2) Aperture. (3) Mirrors. (4) Conventional condenser annulus. (5) Condenser lens. (6) Specimen in MTP. (7) DMD.

5.2.2 Horizontally Movable Lens or Movable Condenser Annulus

A demonstrator of a movable lens was designed and constructed to identify the real-world challenges of implementation. In addition to the condenser lens, a secondary lens, specifically a 2 inch lens, was incorporated between the condenser lens and the specimen. Direct mounting of the condenser lens onto the actuation system was infeasible due to mechanical constraints. This setup was theoretically capable of achieving meniscus compensation equivalent to moving the condenser lens itself, but it altered the system's focal point.

Lens positioning in the x and y directions was managed by motorized axes. Rapid lens repositioning is required for high-speed imaging, and highly precise positioning within a few micrometers' tolerance is necessary for precise beam steering. While linear motors can provide precise high-speed actuation, they were not employed due to their high cost. Instead, stepper motors were utilized, with encoders monitoring their precise positions. An STM32 microcontroller served as the control unit. A computer aided design (CAD) of the setup is shown in the Appendices in Figure A.1.

Two experiments were conducted to evaluate the demonstrator's performance: one assessed absolute positioning precision, and the other measured speed. Results indicated low positioning precision and only acceptable accuracy for microscopy applications with resolutions under 10 µm. For a movement of 1.02 mm (equivalent to 50 motor encoder steps), the mean deviation was 43 µm with a standard deviation of 126 µm. Movement times significantly exceeded expectations, at 60 ms for a 1.02 mm distance, largely due to limitations in the closed-loop control system.

Given these challenges, the movable lens or movable condenser annulus approach does not meet the high-speed criterion with manageable complexity and cost. These approaches will therefore not be further investigated.

5.2.3 Liquid Crystal Display

To facilitate the shifting of the condenser annulus, an LCD unit replaces the fixed condenser annulus in a phase contrast microscope in this setup. The LCD unit comprises a metal housing that encloses the LCD, with protective glass plates on both sides of the LCD to avoid mechanical damage, such as scratches, while permitting light transmission. The entire LCD unit can be mounted onto the microscope similarly to a conventional condenser unit, with the condenser lens affixed to the lower side of the unit. A cross-sectional schematic drawing depicting the LCD unit design is illustrated in Figure 5.6, whereas a photograph is presented in Figure 5.7.

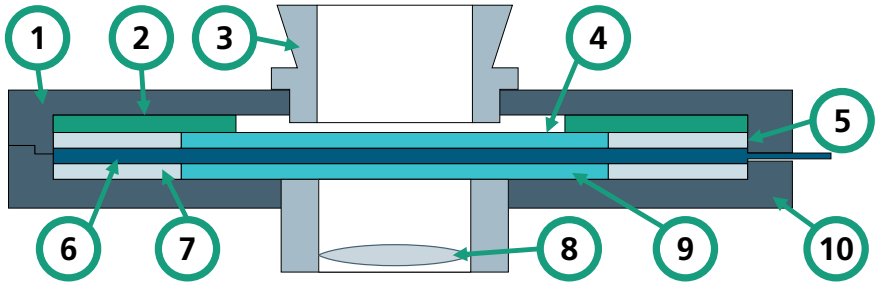

Figure 5.6: Schematic drawing of the LCD housing unit (cross-section), illustrating all components. (1) Upper part of the housing. (2) Distance holder. (3) Microscope connection adapter. (4) Upper protective glass plate. (5) Spacer for the upper glass plate. (6) LCD. (7) Spacer for the lower glass plate. (8) Condenser lens. (9) Lower protective glass plate. (10) Lower part of the housing.

Due to cost and time constraints, only commercially available LCDs were considered for the setup. Most standalone LCDs are designed for consumer electronics, particularly smartphones, given the large market demand [Che18]. This makes them affordable, often priced below $100 per piece, though their specifications are specifically tailored for these applications. For instance, because they are typically designed for human viewing, their refresh rates generally range from 24 Hz to 120 Hz. Higher frame rates are rarely implemented, as the improvement is imperceptible to the human eye. This is in contrast to the requirements of high-speed imaging, which demands the highest possible frame rates.
Smartphone LCDs typically have pixel densities ranging from 250 pixels per inch (ppi) to 600 ppi [Led21]. Moreover, most LCDs are available in sizes around 6 inch (152.4 mm) diagonal, which is suboptimal because they considerably exceed the necessary size, given that the condenser lens aperture is only approximately 25 mm.

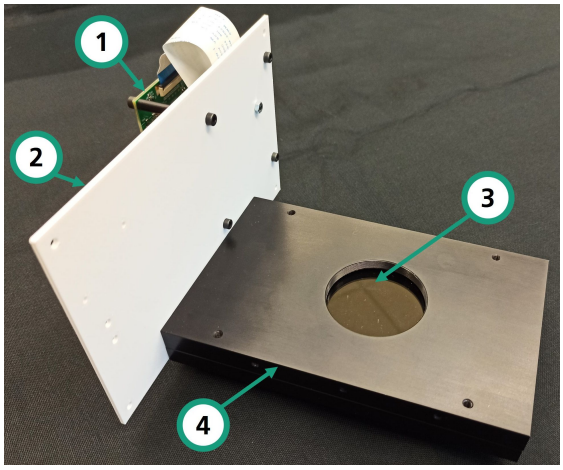

Figure 5.7: The adapter housing the LCD, with the LCD controller mounted on a plate at the backside. This housing replaces the condenser unit of the phase contrast microscope. The condenser lens is attached via the threaded center. (1) Controller. (2) Mounting plate for controller. (3) Aperture for LCD with cover glass. (4) Housing.

For the adaptive phase contrast microscope, the LCD must be translucent. While all LCDs are inherently translucent (see Section 2.3.4) [Yan14], most consumer devices include an integrated backlight. Removing the backlight is possible, but can render the LCD more fragile and may jeopardize the integrity of integrated circuits. Additionally, pixels can be permanently damaged during this process. Thus, it should be avoided. Given that the annulus will be displayed as a white ring on a black background, a color display is unnecessary for the LCD. Monochrome displays are preferred, as they lack color filters, theoretically offering at least three times the brightness of a color display.

Considering all requirements, a 6.08 inch monochrome LCD with a resolution of 1620×2560 pixels without backlight, designed for 3D printers, was selected (model: CHA608-X04, country of origin: China). The LCD was connected to a controller unit that translates HDMI signals to MIPI-DPI signals interpretable by the LCD. The controller was connected to a Raspberry Pi via HDMI. Running a program that renders condenser annuli, the Raspberry Pi was connected to the main PC, which sends instructions via Ethernet. The main PC sends the condenser annulus position in a custom encoding, which can be interpreted by the Raspberry Pi.

The LCD was consequently used in the following optical simulations and experiments.

5.2.4 Liquid-Filled Prism

The liquid-filled prism can be positioned in the beam path at two locations: between the condenser annulus and the condenser lens or between the condenser lens and the specimen. The latter configuration was chosen because the first option required a complete redesign of

the microscope's light house and illumination unit, which was not feasible with the available microscope. Approximately 75 mm of vertical assembly space is available to accommodate the prism unit. The prism unit can only be used in conjunction with the LCD because mounting points for the prism unit are only present on the LCD housing. Experiments were therefore consistently conducted using a combination of the prism and LCD. If the liquid-filled prism proved to be the optimal adaptive component, an additional condenser annulus unit with mounting points for the prism unit would have been designed. A photograph of the liquid prism with its actuation is shown in Figure 5.8.

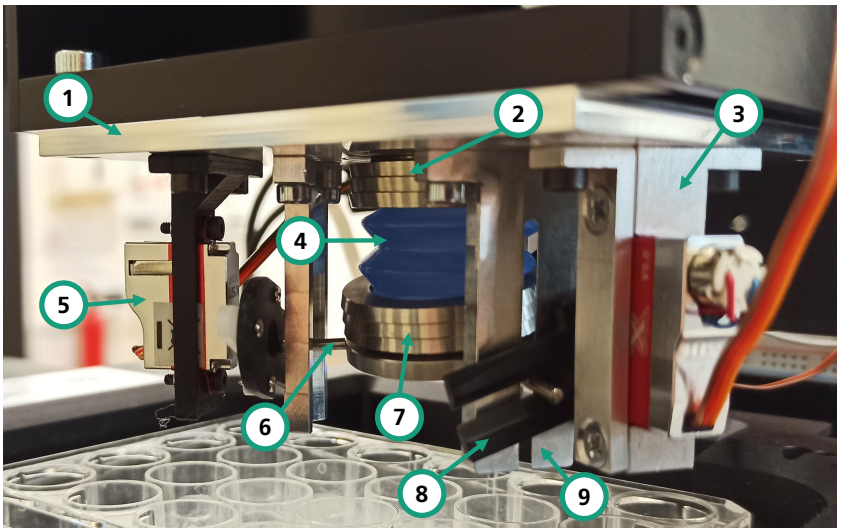

Figure 5.8: Photograph of the liquid-filled prism assembled in the demonstrator, with the lower glass plate tilted by the servo motors. (1) Base plate. (2) Upper glass plate within metal frame. (3) Servo mount. (4) Flexible silicone shell. (5) Servo motor. (6) Lever. (7) Lower glass plate within metal frame. (8) Servo handle. (9) Lever guidance.

To contain the liquid between the glass plates, a custom silicon shell was designed and cast (material: ADDV-25). A polyoxymethylene (POM) casting form was milled for this purpose, chosen for its low friction and, therefore, non-stick properties [Śar14]. It is depicted in the Appendices in Figure A.2.
Lathed stainless steel frames secured the glass plates and shell, utilizing a sealing ring to prevent liquid leakage. Distilled water, with a refractive index of approximately 1.33, served as the medium due to its ease of handling and non-toxicity [Tho85]. The movement of the lower glass plate was facilitated by three servo motors that actuate levers mounted to the stainless steel frame. The entire liquid-filled prism assembly was mounted on a plate connected to the LCD housing. A CAD drawing of the same assembly is depicted in the Appendices in Figure A.3. The geometric relations within the prism actuation unit are presented in Figure 5.9 [Nie23].

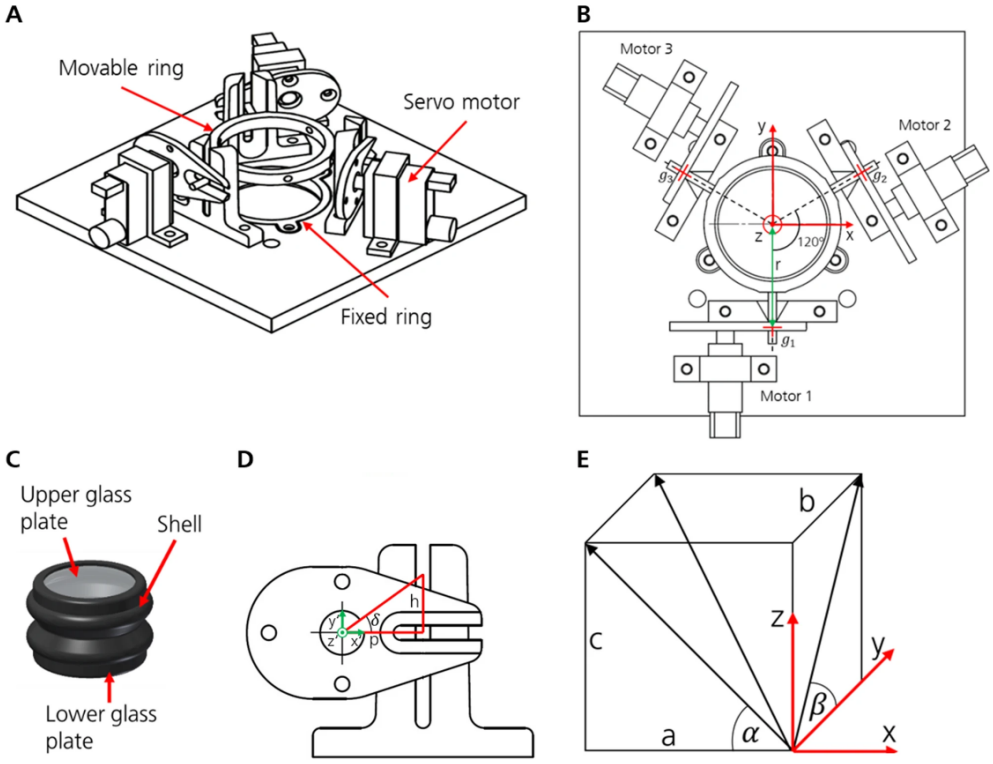

Figure 5.9: Geometric relations within the liquid filled prism [Nie23]. (A) Overview of the mechanical principle. (B) Bottom-up view with important geometric relations. (C) Silicon shell and glass plates. (D) Geometric relationships at the servo handle. (E) Orientation of angles within the coordinate system.

The servo motors are managed by a driver that receives commands from an Arduino Mega microcontroller. The Arduino interfaces with the main computer via USB to obtain position data as two angles, α and β, which determine the tilt of the lower glass plate. These commands are processed by the Arduino and translated into servo motor positions δ_i using Equation 5.1 [Nie23]:

$$\vec{\delta} = \arctan\left(\frac{\vec{h}}{p}\right), \tag{5.1}$$

where p is the servo handle length and $\vec{h}$ is calculated by Equation 5.2 [Nie23]:

$$\vec{h} = \begin{pmatrix} r\tan(\beta) \\ \cos(30°)r\tan(\alpha) - \sin(30°)r\tan(\beta) \\ -\cos(30°)r\tan(\alpha) + \sin(30°)r\tan(\beta) \end{pmatrix}, \tag{5.2}$$

where r is the lever length.

This design was used for the following optical simulations and experiments.

5.3 Optical Simulations

The experimental setups described in the previous section were replicated using optical simulations. Given that the DMD and movable lens had already failed several criteria, simulations were limited to the LCD and liquid-filled prism. The first simulation setup, referred to as *Configuration 1*, utilizes only the LCD. The second setup, termed *Configuration 2*, incorporates both the liquid-filled prism and the LCD, as the liquid-filled prism cannot be operated independently without the LCD (as detailed in Section 5.2.4).

5.3.1 Simulation Setup

Simulations were conducted using Zemax OpticStudio. The focus was on ray optics without modeling phase differences and interference. A simplified phase contrast microscope was modeled utilizing Zemax's Sequential Mode. An exact replica of the original system was unattainable due to the proprietary nature of several Nikon components, for which no black-box models were available. Consequently, these components were replaced with Thorlabs lenses having analogous properties, such as NA and working distance. These elements included the collimator lens, condenser lens, objective lens, and tube lens. Therefore, these simulations are unsuitable for quantitative analyses due to discrepancies with the real-world system; however, they provide qualitative insights. Figure 5.10 depicts the optical path through the microscope for both components.

The condenser annulus was modeled as a ring aperture with an inner diameter of 5.1 mm and an outer diameter of 5.8 mm. This corresponds to the Ph1 standard size for a condenser annulus used in 10x magnification. The meniscus shape for an MTP24 was approximated as parabolic. The base of the meniscus was aligned to be in focus. Prism dimensions from the CAD drawing were utilized; however, the hull was simplified, and the glass plates were omitted due to their minimal thickness. The phase ring was modeled as a ring obscuration, designed to be narrower than the condenser annulus, ensuring the visibility of its edges when overlapped by the phase ring.

Two distinct setups were employed in the simulations using Zemax's Multi-Configuration Editor: one for the liquid-filled prism and LCD and another solely for the LCD. Except for the inclusion of the liquid-filled prism in Configuration 2, the systems remained unchanged, with the sole exception being the adjustment of the focal distance between the condenser lens and the meniscus to achieve Köhler illumination (refer to Section 2.2.2). The initial simulations began with the meniscus centered, progressively shifting it by 1 mm to the side per iteration until the light beam reached the well's edge. Meniscus compensation was achieved by either displacing the condenser annulus perpendicular to the beam direction in Configuration 1 or tilting the lower surface of the prism in Configuration 2 until the images of the condenser annulus and phase ring converged. The focal distance between the condenser lens and the meniscus was slightly adjusted to account for variations in optical path length.

Zemax's Physical Optics Propagation was employed to render overlap images of the condenser annulus and the phase ring. The simulation rendering utilized an equidistant grid of 1024×1024 parallel rays, originating from a plane through the light source towards the collimator lens.

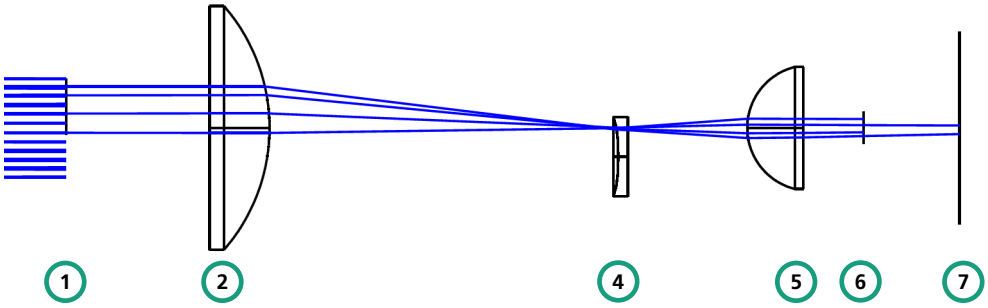

(a) Model for Configuration 1 (LCD).

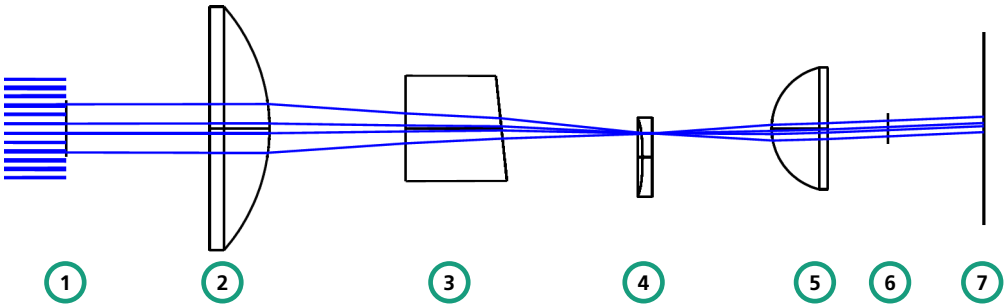

(b) Model for Configuration 2 (prism and LCD).

Figure 5.10: Cross-section of the Zemax OpticStudio simulation model, illustrating the beam path. Both configurations share the same setup and parameters, except for the inclusion of the liquid-filled prism in Configuration 2. Minor variations in focal distance are present to always focus on the specimen. (1) LCD condenser annulus. (2) Condenser lens. (3) liquid-filled prism. (4) Meniscus. (5) Objective lens. (6) Phase ring. (7) Image plane (tube lens omitted).

5.3.2 Simulation Results

The simulations demonstrated that alignment between the condenser annulus and the phase ring can be achieved in both configurations until close to the meniscus edge. Figure 5.11 illustrates that alignment between the condenser annulus and phase ring is attainable with both configurations.

Optimal alignment of the condenser annuli with the phase rings was achieved by selecting appropriate parameters for either the LCD shift or liquid-prism tilt. The variations in intensity are largely attributed to two factors. Firstly, the number and spacing of light beams used for rendering had a noticeable impact. Using different configurations of incoming light resulted in varying intensity distributions, though the overall shape remained unchanged. Secondly,

the focal position of the specimen significantly influenced the results. When the bottom of the meniscus was not in focus, the resulting light rays deviated markedly from an annular shape.
In Configuration 2, the LCD condenser annulus was not shifted. Consequently, the simulation results were independent of the inclusion of the LCD in this setup. Thus, the outcomes for Configuration 2 would remain unchanged if a regular fixed condenser annulus were used instead of an LCD.

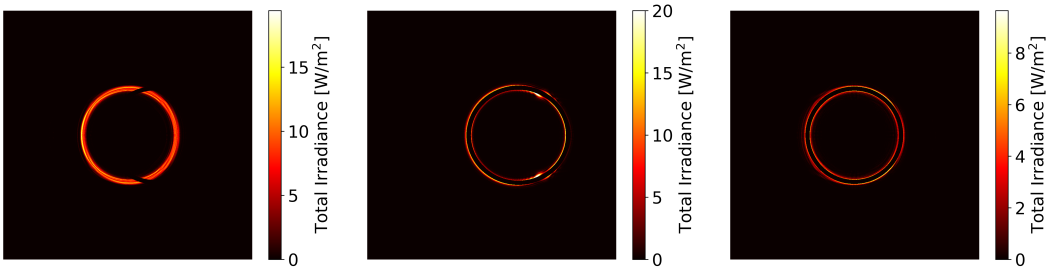

(a) Reference. **(b)** Configuration 1 (LCD). **(c)** Configuration 2 (prism).

Figure 5.11: Simulation results showing the relative positions between condenser annulus and phase ring with a meniscus shifted 5 mm horizontally from the center. The annulus in red and yellow shades represents the condenser annulus. The black ring obscuring part of the annulus is the phase ring. No meniscus effect compensation was applied for the reference image in (a). (b) shows the overlap due to the condenser annulus shifting on the LCD. (c) shows the overlap due to the tilt of the liquid-filled prism.

In summary, the simulations indicated that alignment of the phase ring and condenser annulus is feasible with both configurations.

5.4 Experimental Evaluation of Adaptive Components

Two sets of experiments were conducted to gain a deeper understanding of the adaptive components' capabilities in compensating for the meniscus effect near the well's walls. In both series, the components were incorporated into the beam path of a phase contrast microscope. The first set of experiments (Section 5.4.1) evaluated the adaptive component's overall ability to direct a light beam and examined the deformation of the condenser annulus within the microscope's optical path. The second series (Section 5.4.2) concentrated on identifying the proximity to the well's edge where phase contrast conditions can be effectively achieved.

5.4.1 Light Steering Experiments

The initial experiments were conducted to assess the performance of the adaptive components without accounting for the meniscus effect. For this purpose, no specimen was present. No MTP was placed in the microscope stage, ensuring the absence of a liquid meniscus that could potentially alter the light path.
The same two experimental Configuration 1s that were used in the optical simulations we assessed: Configuration 1 involving only the LCD integrated into the microscope, and Configuration 2 incorporating the prism unit mounted on the LCD housing (see Section 5.2.4).

Throughout the experiments, images were captured using the microscope's Bertrand lens at each step. In Configuration 1, the LCD condenser annulus was adjusted in increments of 0.2 mm. In Configuration 2, the prism was incrementally tilted by 1 ° with the LCD condenser annulus fixed at its default position. The images from both experimental configurations were subsequently compared. Figure 5.12 presents a pair of images from these experiments.

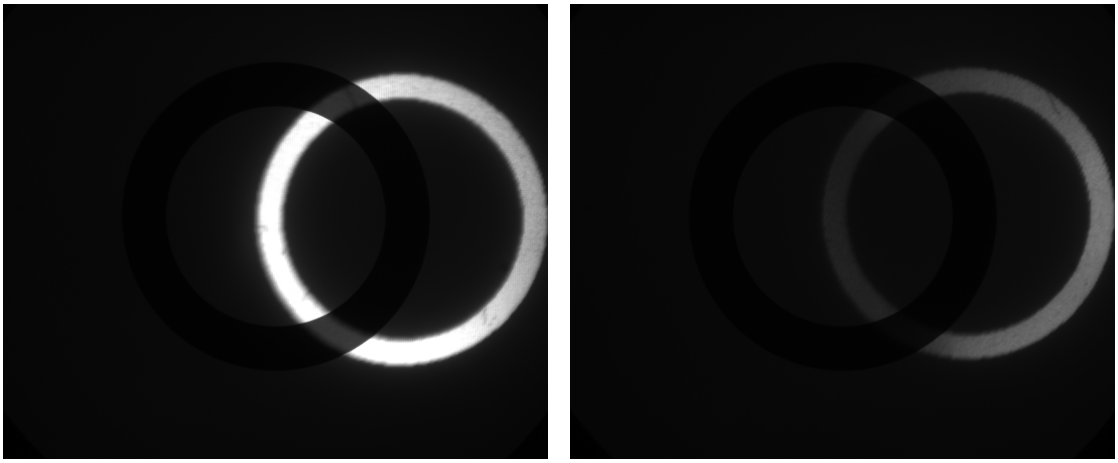

(a) Configuration 1 (LCD). **(b)** Configuration 2 (Liquid-filled prism).

Figure 5.12: Displacement of the condenser annulus from the phase ring, as observed through the Bertrand lens, without a specimen and refraction at a meniscus. Both displacements are similar but are achieved through different processes. (a) The LCD is solely active to shift the condenser annulus, with the prism in its default position. (b) The liquid-filled prism is tilted, while the LCD remains in the default position.

The analysis indicated that each displacement of the condenser annulus on the LCD corresponds to a similar position in the images with the tilted prism. The annuli exhibit fundamental similarity, being shifted from the center without significant distortion. The primary distinction lies in the brightness of the condenser annuli. When the LCD condenser annulus is displaced, the brightness remains relatively uniform across all images. Conversely, images with a tilted prism progressively darken as the annulus moves further from the center. Moreover, this darkening is not uniform but manifests as a gradient, as depicted in Figure 5.12b. Potential explanations for this phenomenon are examined in Section 5.5. To

enhance understanding, subsequent experiments will address compensating for the meniscus effect with MSCs present as specimens.

5.4.2 Meniscus Effect Compensation Experiments

The following experiments aimed to determine how close to the well's edge meniscus compensation is achievable using the given adaptive components. To closely simulate real-life imaging conditions, 24-well MTPs containing MSCs in a liquid medium were used as specimens. Configurations 1 and 2 were retained from the previous experiments.

Figure 5.13 illustrates the experimental procedure. Experiments were conducted at 4x and 10x magnifications. Two cameras were employed: a primary camera for specimen observation and a secondary camera for viewing the phase ring through the Bertrand lens. Each experiment comprised a series of images captured at various positions within a well, starting from the center and progressively moving towards the edge. Upon capturing the two images with each of the cameras, the specimen was moved in increments of 750 µm for 4x magnification and 300 µm for 10x magnification, approximately half of the cameras' FOV.

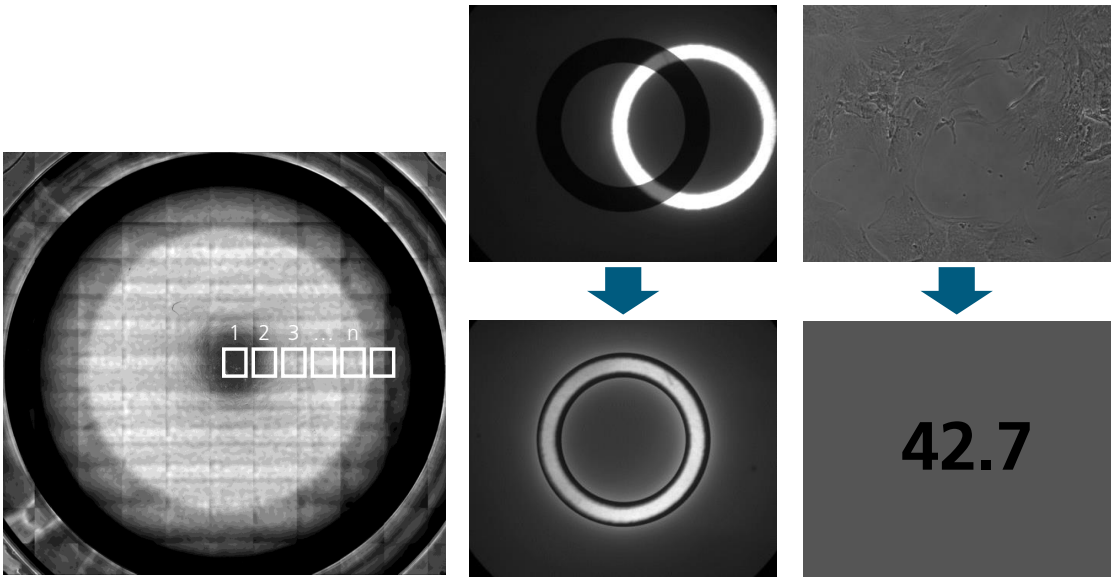

(a) Positioning within well

(b) Condenser annulus alignment.

(c) Gray value calculation.

Figure 5.13: Experimental setup to evaluate meniscus compensation of the LCD and liquid-filled prism. Imaging of different positions within a well is demonstrated in (a). In reality, imaging positions are overlapping, which is not shown for better readability. At each position, the condenser annulus is manipulated to align with the phase ring (b). The resulting specimen image is captured, and the average gray value is determined, which is written into the example image (c).

For both configurations, one reference series was conducted, wherein the LCD and prism remained in their default settings throughout all images. At each position, two images were

captured, one with each camera. This reference represents conventional phase contrast microscopy.
In subsequent measurements, the adaptive components were adjusted at each position to align the condenser annulus with the phase ring as observed by the secondary camera. Once alignment was achieved, both cameras captured one image each. Configuration 2 was utilized to test the capabilities of the liquid-filled prism. Since the LCD also needed to be included in Configuration 2, three experimental series were conducted: the main experiment series, where the prism was tilted and the LCD remained in its default position, and two additional reference series. In the first reference experiment series, the LCD condenser annulus was shifted while the prism was kept in the default position, and in the second reference experiment series, both the LCD and prism were adjusted alternately.

To analyze the results, the average image brightness was computed as described in Section 4.1. The brightness was compared to that at the center of the well, where optimal phase contrast conditions are known to exist. The results are presented in Figure 5.14 for Configuration 1 and in Figure 5.15 for Configuration 2, both using 10x magnification.

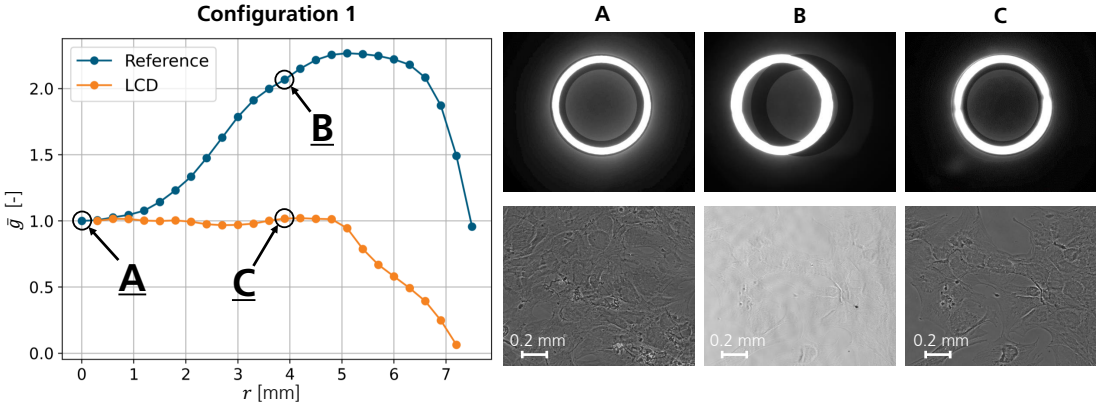

Figure 5.14: Plot of the average brightness of cell images $\overline{g}$ at a distance r from the well center, indicating phase contrast conditions. An MTP24 was observed with 10x magnification and Configuration 1. *Reference* denotes experiments where the LCD consistently displays the default annulus position. In *LCD*, the virtual condenser annulus on the LCD is shifted to maintain alignment with the phase ring. At the central position (A), phase contrast conditions are optimal. At 3.9 mm from the center without meniscus effect compensation, contrast decreases and background brightness increases (B). Meniscus compensation re-establishes phase contrast conditions at the same position by shifting the condenser annulus on the LCD (C).

The brightness of the reference measurements shows a consistent trend in both graphs, increasing steadily up to approximately 5 mm from the well center. Beyond this point, brightness decreases due to shading from the well walls. This suggests that phase contrast conditions are not achievable near the well walls, as shading reduces contrast.

In contrast, the brightness in Configuration 1 remains nearly constant until about 5 mm from the well center, indicating that the LCD effectively maintains phase contrast conditions further from the center, as exemplified by the difference between the images at positions B

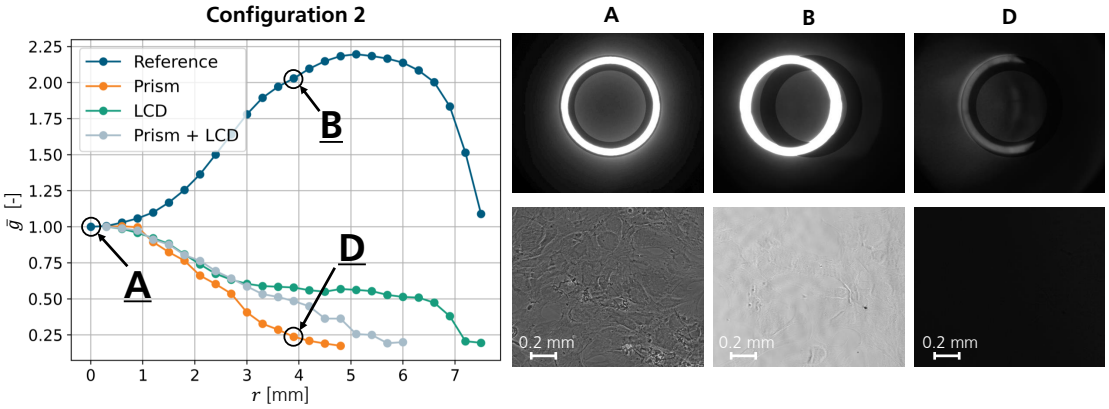

Figure 5.15: Plot of the average brightness of cell images $\overline{g}$ over the distance to the center r obtained by the same method as Figure 5.14, using Configuration 2. *Reference* denotes experiments where neither the LCD nor the prism is altered from the default position. *Prism* denotes the main experiment, where the prism is tilted at each position to keep the condenser annulus aligned with the phase ring, while the LCD remains in its default position. In *LCD*, the virtual condenser annulus on the LCD is shifted, with the prism in the default state. In *Prism + LCD*, both are adjusted. At the central position (A), phase contrast conditions are optimal. At 3.9 mm from the center without meniscus effect compensation, contrast decreases and background brightness increases (B). Low brightness is observed at position (D), 3.9 mm from the center, corresponding to position (C) in Figure 5.14.

and C in Figure 5.14. The brightness only decreases at approximately the same position as the reference measurements (around 5 mm from the center) due to shading at the well wall. This effect is illustrated in Figure A.4 in the Appendices.

Comparatively, the average brightness in Configuration 2 decreases almost immediately when moving away from the center. This suggests that the liquid-filled prism is not as effective at compensating for the meniscus effect as the LCD. However, all three curves in Figure 5.15 follow a similar trajectory, even though the series involving only the tilted prism (orange curve) results in the lowest brightness and, consequently, the poorest image quality. The poor image quality observed even when the prism was unchanged and the LCD was adjusted (green curve) suggests additional factors contributing to Configuration 2's inferior performance, which are examined in the following section.

5.5 Discussion

This section analyzes the technologies presented and concludes which are suitable for high-speed meniscus effect compensation in phase contrast microscopy. The comprehensive simulations and experiments identified certain limitations in both the LCD and liquid-filled prism technologies. These limitations are examined to enhance understanding of how they align with the criteria outlined in Section 5.1.

5.5.1 Limitations of the Liquid Crystal Display

The experiments identified three drawbacks in the LCD design: limited commercial availability, light attenuation, and variation in illumination path length.

Commercial Availability

As detailed in Section 5.2.3, LCDs must fulfill specific requirements for effective high-speed meniscus effect compensation:

- Transparency (absence of attached backlight),
- high frame rate, and
- monochrome pixels.

Due to the sophisticated and complex manufacturing process, LCDs cannot be produced in small quantities specifically tailored for this thesis setup. Thus, only a limited selection of commercial models from a few suppliers meets the requirements. Consequently, the LCD chosen for the experiments may lack ideal properties, although this could improve in future commercial applications.

Light Attenuation

According to Malus's law (see Equation 2.8), the intensity of unpolarized light passing through a polarization filter is decreased. Even under optimal conditions, at least half of the light intensity is reduced if the incoming light consists of beams with uniform polarization angles.
In the experiments, the light intensity was reduced by more than half. Consequently, exposure time must be increased to achieve the desired image brightness, potentially extending acquisition time in HSM applications (refer to Section 3.2).

Variation in Path Length

Simulations revealed a variation in the optical path length between the condenser lens and the specimen when the condenser annulus was horizontally shifted. This variation induced a shift in the focal position, which required compensation through additional adjustments to maintain focus. The compensation process is challenging due to two degrees of freedom: the distance between the condenser lens and the specimen, and the distance between the specimen and the objective lens. As a result, two actuators for z-position correction are necessary, which is impractical for high-throughput imaging across the entire well. However, not implementing this repositioning leads to a significant reduction in image sharpness.

5.5.2 Limitations of the Liquid-Filled Prism

Experiments identified several limitations in the setup and handling of the liquid-filled prism, which impede meeting some evaluation criteria. This section addresses the most critical issues:

- Sealing and bubble formation,
- shading at the prism's walls, and
- reduction of overall brightness.

Sealing and Bubble Formation

Preventing gas bubbles from forming is particularly challenging in the liquid-filled prism approach, as bubbles can unpredictably alter the light path. Once formed, bubbles can only be removed by disassembling and refilling the entire prism unit, a tedious process. Two sources of bubbles have been identified: gas dissolved in the liquid that outgases over time, and air penetrating through leakage in the elastic shell's sealing.

To minimize bubble formation from dissolved gas, the water was heated to near boiling before filling the prism, since warmer water dissolves less gas. For instance, water at 70 °C dissolves only 68% of the nitrogen that water at 20 °C can [Bat84]. However, completely eliminating dissolved gas is nearly impossible, making bubble formation inevitable over time.

Leakage can occur despite the elastic shell being sealed to the metal housing. This is particularly prevalent when the actuators apply force, inducing stress at the sealing. Preventing this requires precise coordination of the actuators to maintain a constant volume within the prism. Even in the absence of external force, achieving a tight seal proved challenging, frequently resulting in liquid leakage after several hours or days.

Shading at the Prism's Walls

One observation of the experiments was shading that occurred with Configuration 2, which transformed the condenser annulus projection into a sickle shape. This effect was evident even in reference measurements, where only the LCD condenser annulus was shifted without tilting the prism, suggesting an issue with the mechanical setup. A plausible explanation is that the sickle-shaped illumination results from inadequate aperture of the prism shell or housing, as illustrated in Figure 5.16.

Increasing the prism diameter might address this issue; however, spatial constraints prevent this solution. While there are no limitations in the x and y dimensions, the space in the z-direction between the condenser lens and MTP is constrained. When the prism is tilted, an increase in width translates to a decrease in height. A prism with radius r increases in

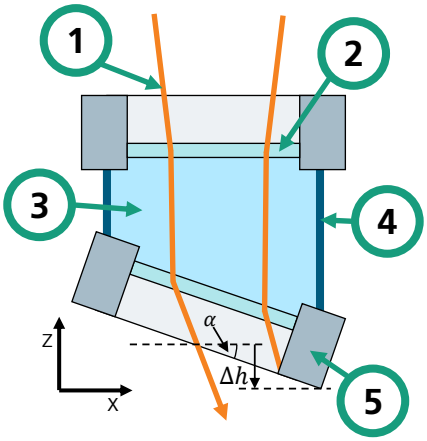

Figure 5.16: Schematic illustration explaining the reduced brightness observed in phase contrast images when utilizing the liquid-filled prism at a tilt angle α due to shading at the prism's walls. The cross-section depicts the trajectory of the outermost light rays through the liquid-filled prism. The right ray is obstructed by the housing, resulting in the condenser annulus appearing as a sickle rather than a ring. The tilt induces a height increase of the liquid-filled prism by Δh. (1) Light ray. (2) Glass plate. (3) Liquid. (4) Silicon shell. (5) Metal housing.

height by Δh at a tilt angle α according to the relation $\Delta h = r \tan \alpha$. Given the restricted vertical space, it is not feasible to increase the prism's radius without causing Δh to become excessively large. Additionally, increasing the prism diameter introduces further challenges, such as the need for more powerful servo motors.

Reduction in Overall Brightness

In the experiments, Configuration 2 experienced a notable reduction in image brightness compared to Configuration 1. Possible physical effects contributing to this observation include dispersion, absorption, and reflection. The presence of multiple tilted surfaces causes sequential reflections at interfaces within the prism, which decrease the intensity of transmitted light. Consequently, multiple reflections were identified as the most likely cause of the reduced brightness. Calculations were thus conducted to assess the magnitude of this effect.

The Fresnel equations describe the fraction of refracted and reflected light at each interface between different materials (refer to Section 2.1.4). Within the liquid-filled prism, a light ray sequentially traverses a glass plate, water, and another glass plate, resulting in four interfaces in total. These interfaces alter the angle of the light beam, changing it from the global incident angle ϵ (the angle after the condenser lens) to the refracted angle ζ. Figure 5.17 illustrates this process.

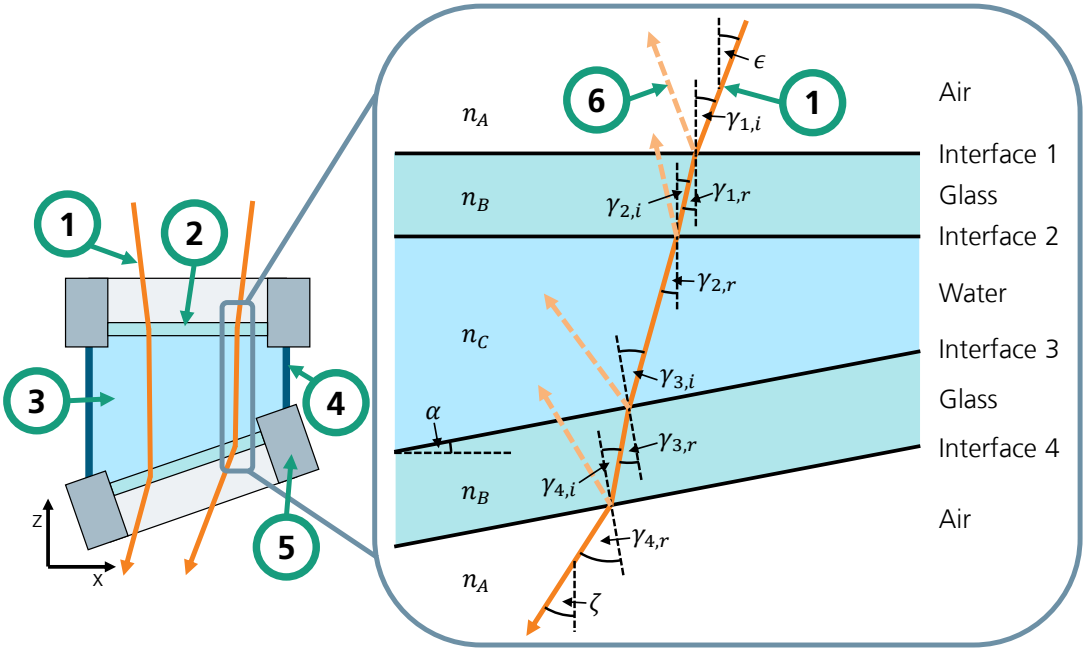

Figure 5.17: Reflection and refraction at the four interfaces within the liquid-filled prism, with a tilt of α. The incidence and refracted angles are labeled. Reflection occurs at each interface, progressively decreasing the light's intensity. (1) Incoming light ray. (2) Glass plate. (3) Liquid. (4) Silicon shell. (5) Metal housing. (6) Reflected light ray.

Calculations were carried out to determine the angles of incidence and refracted angles at each interface using Snell's law (see Equation 2.10). The relationships between the angles of incidence and refraction at successive interfaces are described by Equation 5.3:

$$\begin{aligned} \gamma_{1,i} &= \epsilon \\ \gamma_{2,i} &= \gamma_{1,r} \\ \gamma_{3_i} &= \gamma_{2,r} + \alpha \\ \gamma_{4,i} &= \gamma_{3,r}. \end{aligned} \tag{5.3}$$

Subsequently, the effective transmission coefficient T_{eff} and reflection coefficient R_{eff} were determined using the Fresnel equations (refer to Equation 2.15). The total transmission T_{total} is the product of the transmission coefficients from each interface. These calculations were performed for varying prism tilt angles α to evaluate the impact on transmission reduction at increased tilt angles. The parameters listed in Table 5.1 were consistently applied throughout the calculations.

Table 5.1: Parameters to calculate the effective transmission through the liquid-filled prism

Parameter	Value	Description
NA	0.29	NA condenser lens
n_A	1.00	Refractive index air
n_B	1.50	Refractive index glass
n_C	1.33	Refractive index water

Initially, the maximum possible value for ϵ was determined based on the maximum angle of light emerging from the condenser lens. This angle can be calculated from the lens's NA using Equation 2.20:

$$\epsilon = \arcsin\left(\frac{NA}{n_A}\right) = 16.9°. \tag{5.4}$$

The actual angle is likely smaller because the condenser annulus blocks light passing through the outer edges of the condenser lens. However, using the largest possible value is suitable for conducting a boundary value analysis, resulting in the smallest possible transmission. The total transmission results for various α values are presented in Table 5.2. The intermediate results of the calculations for $\alpha = 10°$ are provided in the Appendices in Table A.2.

Table 5.2: Total effective transmission T_{total} through the whole liquid-filled prism for different tilt angles α. ζ denotes the output angle with respect to a vertical line with a given incident angle of α = 16.9°.

Prism tilt α [°]	Output angle ζ [°]	T_{total} [%]
-10	13.5	91.5
0	16.9	91.5
10	20.7	91.3
20	25.8	90.4
30	34.2	84.3

The experiments detailed in Section 5.4.2 indicate that only tilt angles ranging from -10° to 10° are relevant to achieve alignment of the condenser annulus and phase ring up until the well's edge. Table 5.2 demonstrates that the transmission remains virtually unchanged between these angles, with only significantly larger angles, around 30°, resulting in a slight reduction in transmission rate. A transmission rate of 91.3% for $\alpha = 10°$ implies that no substantial darkening can be attributed to reflection at the multiple interfaces if the interfaces are smooth. For validation, calculations were also conducted with $\epsilon = 0°$ for perfectly central light, showing virtually no difference (e.g., T_{total} = 91.5% for $\alpha = 10°$).

Consequently, the observed decrease in brightness at positions further from the well center cannot be explained by this physical mechanism. It is more plausible that this effect results from other aspects of the mechanical setup or different physical phenomena.

5.6 Summary and Evaluation

This chapter presented four adaptive component approaches to manipulate the illumination beam path in a phase contrast microscope to counteract refraction at the meniscus surface. The approaches were evaluated based on criteria outlined in Section 5.1. The evaluation incorporated theoretical analysis, optical simulations, and experiments. The results are summarized using Harvey Balls in Figure 5.18.

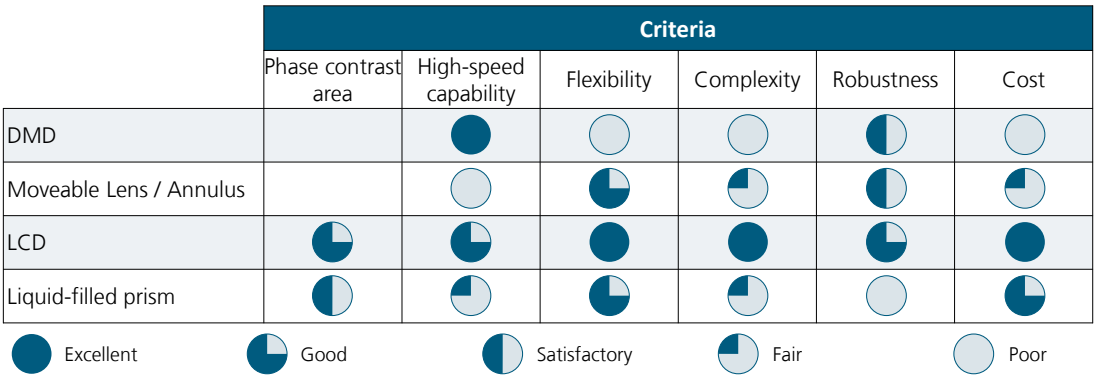

Figure 5.18: Harvey Balls representation of the four presented adaptive components. The achievable phase contrast area could not be evaluated for the DMD and the movable lens or movable condenser annulus because they were excluded from selection before experiments were conducted.

The DMD was deemed unsuitable due to its high complexity and low flexibility. No experiments were conducted to determine the phase contrast area as other criteria already disqualified this technology.

The horizontally movable lens or movable condenser annulus was implemented into a demonstrator. Experiments revealed low precision and speed, failing the high-speed capability criterion. A faster, more robust approach using linear actuators was considered but would not meet the cost criterion. Consequently, this approach was not further explored to determine its phase contrast area.

The LCD condenser annulus successfully compensated for the meniscus effect in experiments and simulations. This approach is the simplest, requiring no moving parts, and demonstrated high robustness. Drawbacks include limited availability of suitable models, light attenuation, and variations in optical path length.

The liquid-filled prism also performed well in the simulations for meniscus effect compensation. However, experimental results were inferior to simulation outcomes and did not match those achieved with the LCD. Image quality was compromised by a significant reduction in brightness, especially at large prism tilt angles. The primary cause of this effect remains

undetermined, though shading from limited aperture, dispersion and absorption in the liquid, and reflection at interfaces are likely contributors. Furthermore, handling the liquid-filled prism is challenging due to the risk of bubble formation.

In conclusion, SRQ2,
Which adaptive components are suitable for high-speed implementation?,
can be answered as follows:
Both the LCD and liquid-filled prism are suitable adaptive components for meniscus effect compensation. Due to higher robustness, flexibility, lower complexity, and capability for high-speed imaging, the LCD is selected for subsequent experiments.

6 Evaluation of Phase Contrast Area Through Stop-and-Go Meniscus Effect Compensation

This chapter addresses SRQ3 (refer to Section 3.6):
To what extent can the phase contrast area be increased using adaptive phase contrast microscopy compared to conventional phase contrast microscopy?

Initially, limiting factors for the phase contrast area are analyzed in Section 6.1 to consider them during the acquisition process. The demonstrator setup for the following experiments is presented in Section 6.2, which incorporates the LCD as an adaptive component. Subsequently, in Section 6.3, a process is developed to scan an entire MTP well. To minimize the adverse effects of motion during acquisition and ensure optimal image quality, the procedure halts at each imaging position. This process, known as the *stop-and-go* process or *non-continuous* process, will serve as a reference for the high-speed process to determine whether acquisition during sample movement negatively affects the phase contrast area. The process includes the calculation of the optimal condenser annulus position displayed on the LCD based on images acquired through the Bertrand lens. The resulting phase contrast area for multiple configurations of MTPs and magnifications is determined through experimental validation in Section 6.4.

6.1 Limiting Factors on the Phase Contrast Area

The achievable phase contrast area is determined by several factors inherent to the experimental setup. Three primary factors identified during the experiments in Section 5.4 are the shape of the meniscus, the focal position, and shading at the edges of the well.

6.1.1 Meniscus Shape

The meniscus present in an MTP causes incoming light rays to be refracted away from the center. Rays closer to the well's edge experience stronger refraction, as detailed in Section 3.3.2. The precise shape of the meniscus defines the regions within a well where phase contrast conditions are attainable and provides insights into the field curvature. Of interest is the maximum liquid surface angle up to which meniscus compensation is viable,

termed the *compensation angle* in subsequent sections. This angle serves to assess the effectiveness of a compensation method or to forecast the phase contrast area in a new vessel with a known meniscus shape.
The meniscus is characterized by its height $z(x)$ relative to its radial position x, with the surface angle expressed as

$$\alpha(x) = \arctan\left(\frac{dz}{dx}\right),$$

as illustrated in Figure 6.1. As discussed in Section 3.3.1, calculating the meniscus shape analytically is not feasible. Consequently, this section focuses on approximating the shape based on empirical measurements.

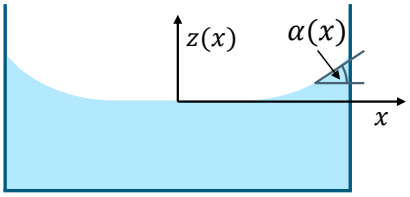

Figure 6.1: Meniscus shape in an MTP well.

The confocal chromatic 1D distance measuring principle was chosen to measure the meniscus shape. Being an optical metrology method, it does not alter the meniscus shape. Measurements are performed from above, necessitating a high NA to accurately measure steep slopes, though a high NA reduces the measurement range [Mur12].
The confocal chromatic sensor model MicroEpsilon IFS2407/90-0,3, with an NA of 0.5, was selected for its ability to measure slopes up to 27° as stated in the datasheet. The sensor was mounted above a microscope stage for moving the MTP, which was filled with water. Water was chosen over cell medium due to its availability and ease of handling. Since cell media primarily consist of water, their material properties are similar, although pure water exhibits slightly lower viscosity and density [Poo22]. The measurement involved moving the sample in parallel lines along the x-axis, akin to HSM image scanning, while the sensor measured the distance to the meniscus from above [Sch16b]. The setup is illustrated schematically in Figure 6.2.

The sensor's limited range of 300 µm prevented a measurement of the meniscus bottom and edges within one run. Therefore, the measurement was repeated three times, adjusting the sensor height by approximately 250 µm between measurements, and the results were later computationally combined to create a smooth curve. The measurements produced three text files containing lists of the distance from the liquid surface to the sensor over their respective x and y positions. The inter-point distance was 10 µm in the x-direction and 100 µm in the y-direction. Positions where the sensor was out of range were marked as *inf*. Due to the limited measurement range and sensor availability, only 24-well MTPs could be measured.

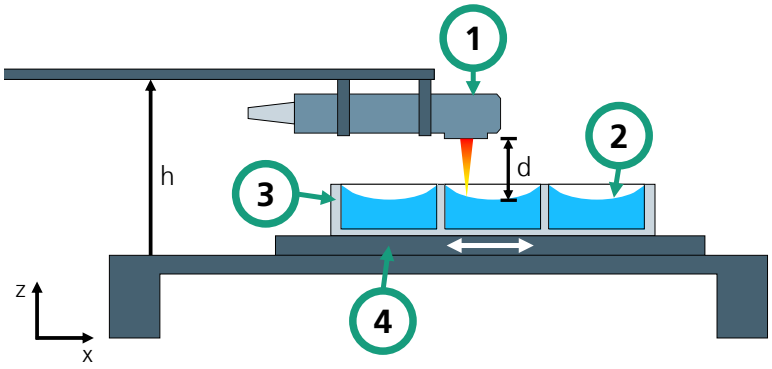

Figure 6.2: Setup to measure the meniscus shape. The confocal chromatic sensor (1) is mounted above the meniscus (2), which is contained inside an MTP (3). The microscope stage (4) is moved during measurement to cover the whole meniscus. The sensor measures the distance d between itself and the meniscus surface. Due to the limited sensor range, the height h is adjusted between measurements to scan the whole depth of the meniscus.

The meniscus shape was approximated from the three files using a Python script. Due to the rotational symmetry of the meniscus, a single cross-section through the center of the well can effectively represent the entire 3D geometry. The process of approximating the meniscus shape involved several steps:

1. Determining the center of the well,
2. Aligning the z-positions of the curves from the three data files,
3. Merging the aligned curves into a single continuous curve,
4. Applying polynomial approximation to smooth the resultant curve.

Determining the Well Center Since the well's center was not known a priori, it first had to be determined from the measurement data that included the well bottom. Cross-sections along the y-axis were analyzed for each x-coordinate to find the y-coordinate of the well's center. Parabolic interpolation was applied to all cross-sections on these data points to pinpoint the y-coordinate of the lowest point on each parabola, and the median of these lowest-point y-coordinates was selected to represent the well's center in the y-direction most accurately.

Alignment of Z-Positions With the center of the well established, a cross-section in the x-direction was extracted from each of the three files through the determined y-coordinate. The three curves were then imported into the script with *inf* values removed, as illustrated in Figure 6.3a. These curves were combined into a continuous curve by calculating the displacement between them and adjusting their positions accordingly. In addition to the vertical

displacement from varying sensor heights, the horizontal displacement was also considered due to slight sample movements between measurements. The optimal alignment of adjacent curves was determined by applying various shifts and minimizing the error in overlapping regions using the L1-norm. The configuration exhibiting the smallest L1-norm was selected.

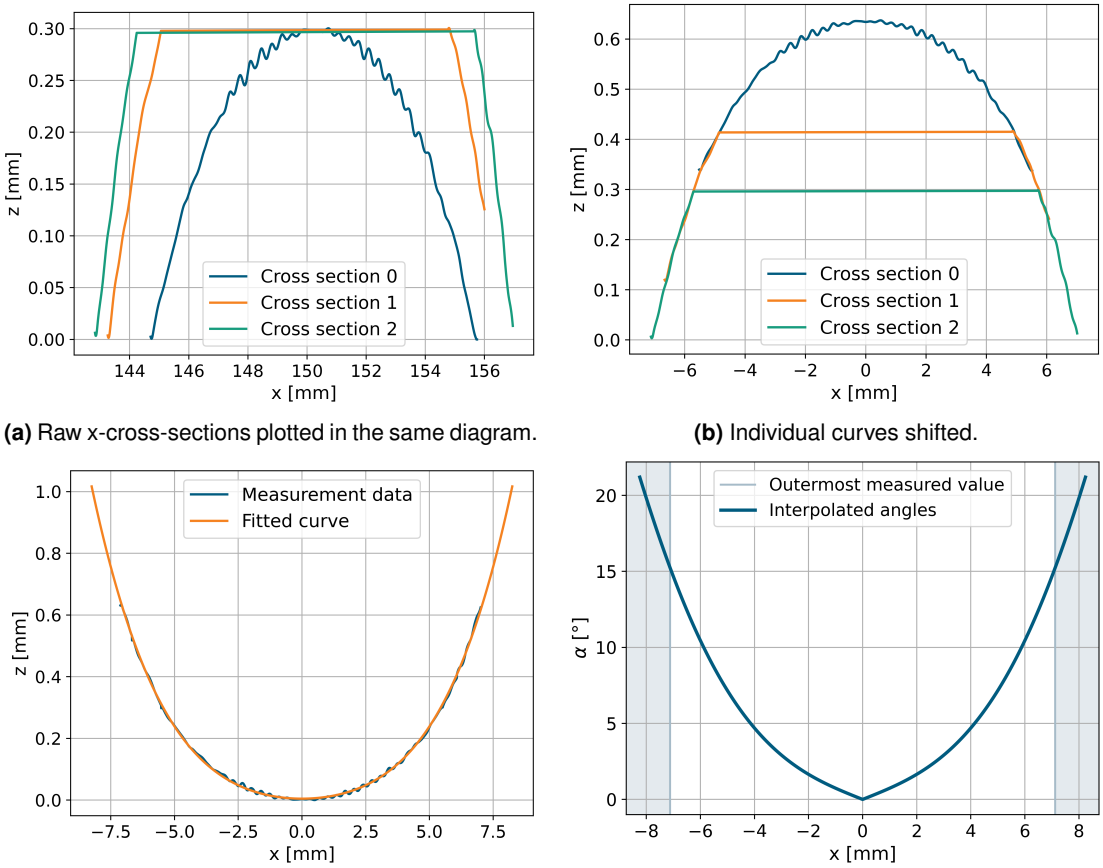

(a) Raw x-cross-sections plotted in the same diagram.

(b) Individual curves shifted.

(c) Interpolated meniscus shape.

(d) Angle α derived from the meniscus shape. Areas of interpolation and extrapolation are marked.

Figure 6.3: Deriving the meniscus shape $z(x)$ and angle α from distance measurements once the well's center is established. Shifting the raw curves (a) results in (b). Applying a polynomial fit and extrapolating values to the well's edge produces (c), where the interpolated curve is overlaid over the merged raw curve. The angle α throughout the meniscus is depicted in (d), where the values calculated through extrapolation instead of interpolation are marked. The x and z axes are not to scale.

Merging the Curves Upon applying the optimal shift, duplicate values at identical x-positions were eliminated, and the curves were merged. The curves were mirrored and adjusted to ensure that the lowest point corresponded to a height of 0 mm, as depicted in Figure 6.3b.

Polynomial Approximation The final step involved smoothing the curve by fitting it with a polynomial. Tests revealed that a fourth-order polynomial most accurately represented the data. Due to symmetry, all odd-order terms were eliminated. The 0^{th} order term was omitted because it depends on the liquid level, ensuring that a height of 0 mm represents the lowest point of the meniscus. The meniscus height $z(x)$ is thus approximated by Equation 6.1:

$$z(x) = 0.00618164 \frac{1}{\text{mm}} x^2 + 0.0001277 \frac{1}{\text{mm}^3} x^4. \tag{6.1}$$

The fitted curve is superimposed on the measurement data in Figure 6.3c.

For further analysis, the angles at the liquid surface were calculated at each position using the derivative $\alpha = \arctan\left(\frac{dz}{dx}\right)$ and trigonometric relationships. The results are plotted in Figure 6.3d. It is evident that measurements with the confocal chromatic sensor were feasible only up to $\alpha = 15°$, contrary to the manufacturer's claim of 27°. This discrepancy is likely due to shading at the well edge and the lower reflectivity of water compared to solid surfaces. Therefore, the meniscus height at angles α exceeding 15° was determined by extrapolation instead of interpolation.

6.1.2 Focal Position

Another limiting factor affecting the phase contrast area is the focal position. Maintaining the specimen in focus is crucial not only for obtaining sharp images but also to ensure that the incident light traverses the specimen, inducing a phase shift necessary for phase contrast conditions. The precise focusing of both the objective lens and the condenser lens is vital to establish Köhler illumination (see Section 2.2.2). Any misalignment in focus can distort the illumination of the condenser annulus, causing misalignment with the phase ring [Mur12]. Achieving this is particularly challenging during continuous image acquisition across the entire well because the z-position of the condenser lens can only be adjusted manually. While Köhler illumination might be successfully established at the center of the well, focal misalignments can occur toward the well's edges, thereby reducing phase contrast.

6.1.3 Shading at the Well Edges

A notable limitation of phase contrast microscopy is the shading observed near the edges of wells, which became evident in the experiments discussed in Section 5.4.2. The shading caused by the MTP wall significantly darkens the image, consequently reducing overall contrast, even in the absence of adaptive components. As a result of this effect, achieving a phase contrast area of 100% is not feasible.

To address this limitation, a method was developed to quantify the maximum achievable phase contrast area, which serves as an upper bound for meniscus effect compensation. This upper bound is determined by analyzing the brightness gradient in phase contrast images covering entire wells, from the center to the edge. A cut-off point is defined as the

location beyond which the average gray value falls below a threshold of 70% of the maximum brightness after applying a median filter, indicating a decrease in brightness past this point. A circle is subsequently fitted to closely correspond with this cut-off boundary. An illustration of this method using a 24-well MTP at 4x magnification is shown in Figure 6.4.

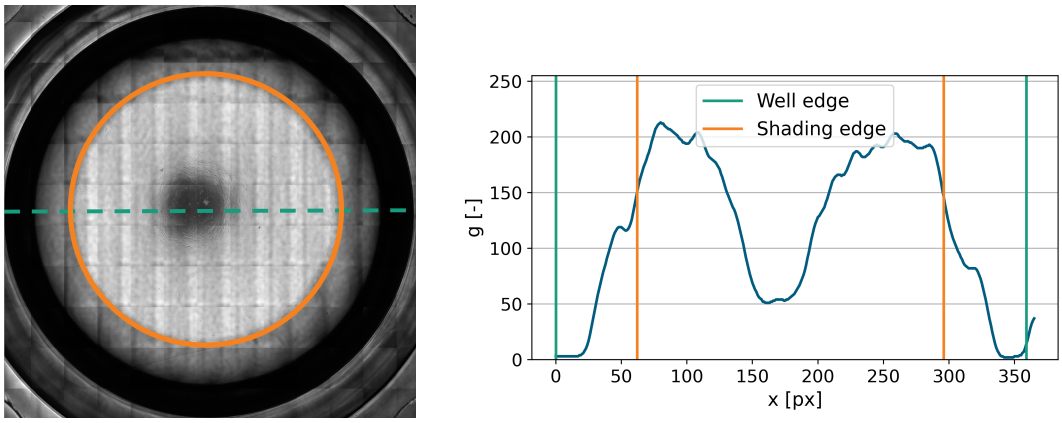

(a) MTP.

(b) Cross-section.

Figure 6.4: Determining the upper bound for the phase contrast area due to shading. The upper bound is indicated by an orange circle for a 24-well MTP in (a). The green dashed line represents the position of a cross-section along the x-axis through the image. The gray values g are analyzed along this cross-section in (b). The diameter of the well is marked in green, and the upper bound for the phase contrast area is marked in orange.

The phase contrast areas obtained for various configurations of MTPs and magnification levels are presented in Table 6.1. The findings demonstrate that both the magnification and the numerical aperture of the objective lens significantly influence the results. The upper bound of only 40% phase contrast area in the case of 24-well MTPs with 4x magnification indicates that the shaded area can constitute the majority of the image in small wells observed with a low-NA objective. Additional example images are provided in the Appendices in Figure A.5.

Table 6.1: Approximate maximum possible phase contrast area for different configurations of MTPs and magnifications when considering shading.

MTP	Magnification	NA	Upper Bound Phase Contrast Area [%]
6	4	0.13	73
24	4	0.13	40
24	10	0.30	82
96	10	0.30	83

6.2 Demonstrator Setup

The demonstrator incorporates the LCD condenser annulus unit and is used for all subsequent experiments. It is based on the Ti2-E (Nikon, Japan), a commercial phase contrast microscope. Numerous modifications were implemented to enable adaptive phase contrast microscopy. Figure 6.5 presents a schematic drawing, while Figure 6.6 shows a photograph of the setup.

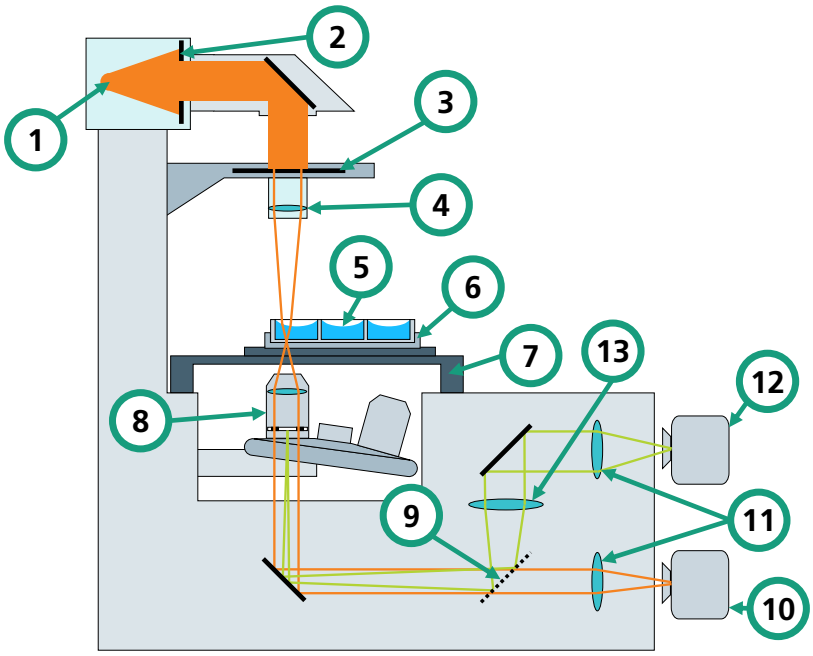

Figure 6.5: Schematic drawing of microscope setup used for all following experiments (adapted from [Nie25]). (1) Light source. (2) Aperture. (3) LCD condenser annulus. (4) Condenser lens. (5) MTP. (6) Piezo z-stage. (7) Microscope stage. (8) Objective lens with phase ring. (9) Motorized rotatable mirror. (10) Primary camera. (11) Tube lenses. (12) Secondary camera. (13) Bertrand lens.

Where feasible, the original components of the microscope were preserved. The internal mirrors, beam splitters, and objective lens revolver were retained. The ELWD condenser lens (Nikon, Japan) with an NA of 0.29 and a working distance of 75 mm was chosen. The objective lens revolver allows switching between two objective lenses. For 4x magnification, a CFI Plan Fluor DL 4x PhL (Nikon, Japan) with an NA of 0.13 was used, while for 10x magnification, a CFI Plan Fluor DLL 10x (Nikon, Japan) with an NA of 0.30 was employed. The microscope features a z-axis that adjusts the distance between the specimen and the objective lens by moving the objective revolver vertically. This axis has a range spanning several millimeters but operates relatively slowly. Because it lacks the precision of the piezo z-axis, it is referred to as the *coarse z-axis*.

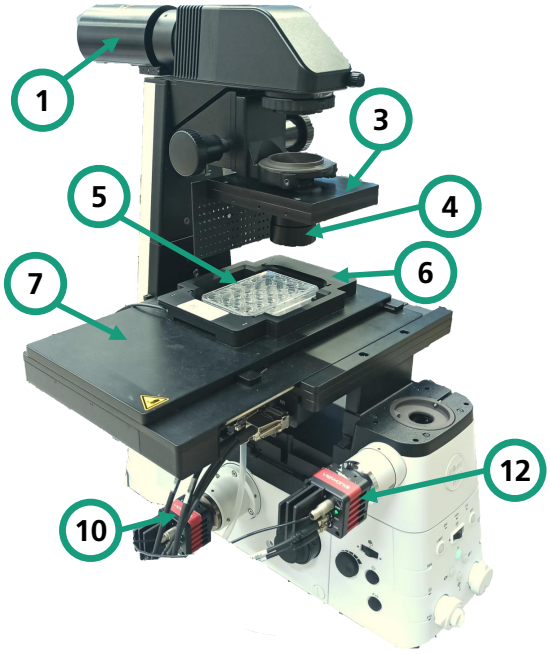

Figure 6.6: Photograph of the final demonstrator. The same numbers as in Figure 6.5 are used. (1) Light source. (3) LCD condenser annulus unit. (4) Condenser lens. (5) Specimen. (6) Piezo z-stage. (7) Microscope stage. (10) Primary camera. (12) Secondary camera. Non-visible important components: Objective lens, height-adjustable objective revolver, Bertrand lens.

To facilitate adaptive phase contrast microscopy, the following modifications were made:

Stage and Stage Controller The ScanPlus IM 130 x 85 (Märzhäuser Wetzlar, Germany; number 7 in Figure 6.5) is utilized for x and y directional movements, achieving velocities up to 120 mm/s and accelerations up to 500 mm/s^2. The Tango 4 controller (Märzhäuser Wetzlar, Germany) operates the stage. Its key feature for continuous scanning is the capability to emit path-synchronous trigger signals, which are vital for coordinating multiple components. Additionally, an extra axis can be connected as an external z-axis for rapid z-focusing.

Piezo Z-Stage Compared to the built-in coarse z-axis, the piezo z-stage (SPS-D90500-001, nanoFAKTUR, Germany; number 6 in Figure 6.5) offers greater precision and dynamic response, allowing focal distance adjustments within milliseconds. However, its limited range of 400 µm necessitates its use in combination with the microscope's coarse z-axis for focus adjustments. The analog input, scaling a signal from 0 V to 10 V to piezo height values between 0 µm and 400 µm, permits high-speed focal distance control.

Light Source Due to short exposure times during continuous scanning, a bright light source is essential [Sch16b]. The LED LE CG P3AQ (ams-Osram, Austria) delivers up to 18,000 lm luminous flux and is placed in the light house, in front of the collimator lens (number 1 in Figure 6.5). Its peak wavelength of 520 nm (green) aligns with the design wavelengths of the objectives' phase rings, enhancing contrast. The LED controller (PLCS-21, Picolas, Germany) and pulse generator (LDP-V 80-100 V3.3, Picolas, Germany) ensure rapid rise and fall times of less than 1 ms and include a trigger input. A custom aluminum housing accommodates the LED and its controllers and also serves as a cooling body.

LCD Condenser Unit The condenser unit was replaced with a configuration housing the LCD, as detailed in Section 5.2.3 (number 3 in Figure 6.5).

Cameras Adaptive phase contrast microscopy requires two cameras: a primary camera for specimen observation (number 10 in Figure 6.5) and a secondary camera (number 12 in Figure 6.5) to monitor the overlap between the condenser annulus and phase ring via the Bertrand lens. The Bertrand lens (number 13 in Figure 6.5) was already integrated into the microscope. The same camera model (VC-5MX2-M289, Vieworks, Korea Republic) was selected for both tasks to enhance software compatibility. This model was chosen for its small camera chip, measuring 6.5 mm $\times$ 5.4 mm (8.45 mm diagonal), which minimizes field curvature within an image, thereby creating more uniform phase contrast conditions (refer to Section 2.1.8). A small pixel pitch of 2.5 µm ensures a high sampling rate for capturing sharp images. The global shutter facilitates synchronization with the light source, avoiding artifacts associated with rolling shutters [Fan23]. With a maximum frame rate of 289 fps, the camera exceeds the LCD's refresh rate, preventing it from being a speed bottleneck. Since only monochrome images are needed, no color filter is used. The cameras communicate through the CoaXPress 2.0 standard with the frame grabber (Coaxlink Quad CXP-12-4GB, Euresys, Belgium), capable of handling concurrent data transfer from both cameras.

6.3 Scanning Procedure

This section outlines the adaptive phase contrast microscopy technique for capturing images of a complete MTP well using a stop-and-go approach. Initially, Section 6.3.1 introduces an algorithm that determines the position of the virtual condenser annulus displayed on the LCD, relying on observations of the displacement between the condenser annulus and the phase ring. Afterwards, Section 6.3.2 details the procedural steps for image acquisition of specimens located in MTPs.

6.3.1 LCD Condenser Annulus Parameter Calculation

A method has been devised to determine the optimal parameters for the LCD condenser annulus by analyzing the displacement between the condenser annulus and the phase ring, as observed through the Bertrand lens. This method is repeatedly employed throughout the procedure.
The approach is founded on empirical measurements. Utilizing camera images alone to calculate the necessary condenser annulus parameters, this method inherently accounts for all system variables affecting the condenser annulus position. This includes properties of the cell medium, environmental conditions, lens geometry, and optical component alignment, among others, thereby eliminating the need for separate consideration compared to an analytical method to calculate condenser annulus parameters. Furthermore, the procedure obviates the necessity for iterative adjustments, ensuring efficiency and facilitating integration into high-speed processes. The procedure consists of the four steps illustrated in Figure 6.7.

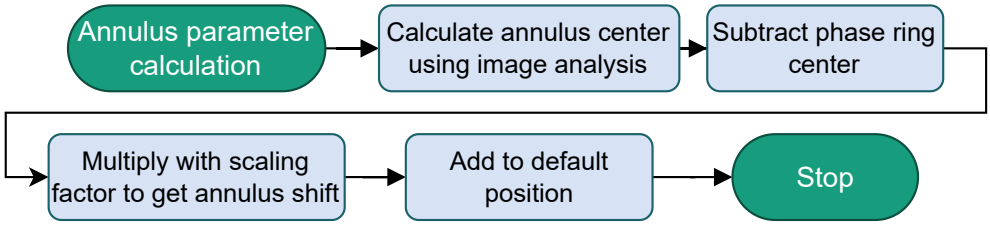

Figure 6.7: Flowchart showing the major steps of the LCD condenser annulus parameter calculation.

Before starting the process, images must be acquired with the Bertrand camera where the default condenser annulus is displayed on the LCD. During the first step of the process, image analysis is employed to ascertain the position of the condenser annulus (denoted as $\vec{d}$) as viewed through the Bertrand lens. The displacement between the condenser annulus and the phase ring, $\Delta\vec{d}$, is derived by subtracting the calibrated position of the phase ring center. To align the condenser annulus with the phase ring, the position of the condenser annulus displayed on the LCD must be adjusted according to the measured displacement. A linear relationship exists between $\Delta\vec{d}$ and the optimal shift of the condenser annulus on the LCD for meniscus effect compensation (denoted as $\Delta\vec{p}$), due to the linear characteristics of the optical components in the beam path. The shift is represented by Equation 6.2:

$$\Delta\vec{p} = K\Delta\vec{d}, \tag{6.2}$$

where K is a scaling factor. Due to symmetry, the same scaling factor K applies to both the x and y directions. The ideal LCD condenser annulus position $\vec{p}$ is then obtained by adding this shift to the default position $\vec{p}_0$, as expressed in Equation 6.3:

$$\vec{p} = \Delta\vec{p} + \vec{p}_0. \tag{6.3}$$

The image analysis process for obtaining $\Delta\vec{d}$ is elaborated in the subsequent section, followed by the calculation of the linear scaling factor K.

Condenser Annulus Calculation Using Image Analysis

The objective of this process is to compute the offset between the condenser annulus and the phase ring in images by identifying and subtracting their respective center points. Images are captured using the secondary camera through the Bertrand lens while the LCD condenser annulus is in its default position. The center of the phase ring is established through a calibration process, whereas the center of the condenser annulus is independently calculated for each position within the well. Both centers are determined using the same algorithm but require distinct parameter sets due to variations in lighting conditions. Figure 6.8 presents examples of images of the phase ring and condenser annulus, with their outlines and centers identified through image analysis.

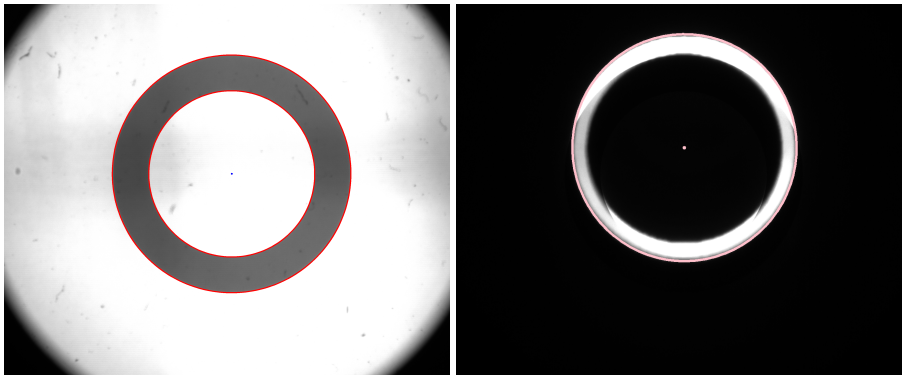

(a) Phase ring. **(b)** Condenser annulus.

Figure 6.8: Image analysis of images acquired through the Bertrand lens using the secondary camera. The detected phase ring outline is marked with red circles (a). The detected outline of the condenser annulus is indicated by a pink circle (b).

The image analysis begins by downscaling the images to 20% of their original size, significantly reducing computational time. Although this scaling might decrease precision, experiments demonstrate that it does not impede successful alignment between the phase ring and condenser annulus [Nie25].
Next, contrast-limited adaptive histogram equalization (CLAHE) is applied to enhance image brightness, particularly in dark regions affected by the phase ring [Piz87]. Subsequently, binary thresholding is used to highlight the ring's outline, enabling the segmentation of a continuous ring.
Contour detection is then employed to extract ring edges [Suz85]. To ensure accurate contour detection, only contours within expected size ranges are retained, discarding those significantly smaller or larger. Contours deviating considerably from a circular shape are

also excluded, determined by the roundness value o calculated by Equation 6.4 [Nie25]:

$$o = \frac{4\pi A}{P^2}, \tag{6.4}$$

where A is the area and P the perimeter.

If multiple contours remain (e.g., inner and outer edges of the ring), the largest contour is selected. To accommodate irregularities in the contour shape, an ellipse is fitted using an approximate mean square algorithm [Tau91]. An ellipse is preferred over a simple circle as the condenser annulus may appear distorted near the well's edge due to the changing slope of the meniscus. The center point of the ellipse is considered the ring's location.

Experiments demonstrated that the computation time is less than 10 ms, making it suitable for high-speed processing. A study was conducted to evaluate the accuracy of the image analysis in adjusting the condenser annulus. A total of 500 images were manually labeled, and the displacements of the condenser annuli were calculated using image analysis. The results of both methods were then compared.
It was determined that errors, defined as the difference between manually labeled and computationally calculated ring centers, of up to 15.0 pixels (after scaling down) were acceptable for maintaining alignment between the condenser annulus and the phase ring [Nie25]. In all 500 images, the error was below 15.0 pixels without exception, with a median error of 1.4 pixels and a mean error of 2.6 pixels.

Linear Regression to Determine the Scaling Factor

The linear relationship described in Equation 6.2 necessitates a constant scaling factor with K. This factor can be expressed by Equation 6.5:

$$K = \frac{\Delta|\vec{p}|}{\Delta|\vec{d}|}, \tag{6.5}$$

where $\Delta|\vec{d}|$ represents the magnitude of the observed displacement between the condenser annulus and the phase ring, and $\Delta|\vec{p}|$ corresponds to the magnitude of the condenser annulus shift on the LCD from its default to optimal position. Since the ratio between $\Delta\vec{d}$ and $\Delta\vec{p}$ is consistent in both the x and y directions, scalar values for K can be calculated using the absolute magnitudes. This relationship is expressed in Equation 6.6:

$$\frac{\Delta|\vec{p}|}{\Delta|\vec{d}|} = \frac{\Delta p_x}{\Delta d_x} = \frac{\Delta p_y}{\Delta d_y}, \tag{6.6}$$

where Δp_x and Δd_x denote the x-components of $\Delta|\vec{p}|$ and $\Delta|\vec{d}|$, respectively, while Δp_y and Δd_y denote their corresponding y-components.

To determine the scaling factor, experiments were performed by measuring pairs of $\Delta\vec{d}$ and $\Delta\vec{p}$ across multiple MTPs and under various magnifications. Although K varies with magnification, it remains independent of the well size [Nie25]. At multiple positions within each well with varying distances from the well center, the default LCD condenser annulus was displayed, and images were captured with the secondary camera. Image analysis was then performed to determine the annulus displacement $\Delta\vec{d}$. Subsequently, the condenser annulus was manually adjusted until alignment was visually confirmed by a human observer, and this position was recorded as $\vec{p}$. The different pairs of $\Delta|\vec{d}|$ and $\Delta|\vec{p}|$ were plotted in a graph. A linear regression was then performed to determine the scaling factor. The results for K were found to be 0.0037 mm/pixels for 4x magnification and 0.0098 mm/pixels for 10x magnification. The regression results are illustrated for 10x magnification in Figure 6.9.

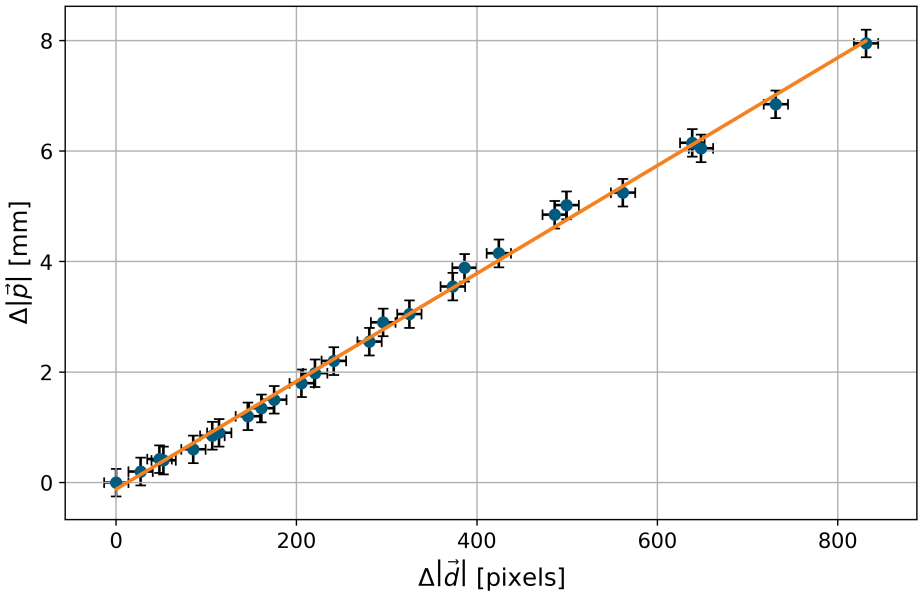

Figure 6.9: The necessary LCD condenser annulus shift, $\Delta|\vec{p}|$, to achieve concentricality with the phase ring plotted over the condenser annulus displacement, $\Delta|\vec{d}|$, from the phase ring at a given position with 10x magnification. A regression line is calculated based on these data points to determine the scaling factor K. Error bars in x-direction show the 75$^{\text{th}}$ percentile of the image analysis error, while the error bars in y-direction show the estimated deviation in the accuracy of the user to determine the condenser annulus position [Nie25].

6.3.2 Scanning Process Sequence

The measurement process is structured into a sequential workflow, comprising four main steps. The flowchart depicted in Figure 6.10 provides an overview of the entire procedure.

Prior to commencing the primary steps, the process begins with an initialization phase that involves establishing connections to all essential hardware, including cameras, the light

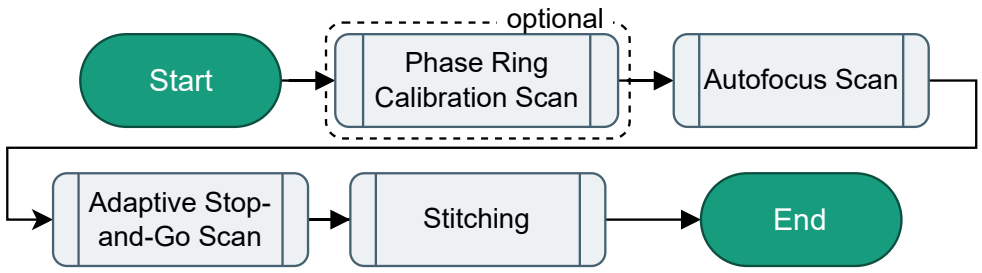

Figure 6.10: Flowchart of the non-continuous scanning process, showing the four main subroutines.

source, the microscope stage, and the LCD. Subsequently, the microscope is configured, such as by selecting the appropriate objective lens. The trajectory for the main scans is computed, specifying the coordinates for all imaging positions within the following primary steps. The primary steps – *Phase Ring Calibration Scan*, *Autofocus Scan*, *Adaptive Stop-and-Go Scan*, and *Stitching* – are detailed in the following sections.

Phase Ring Calibration Scan

The Phase Ring Calibration Scan is an optional procedure designed to identify the phase ring's position and adjust the default condenser annulus position. This step may be omitted to optimize time efficiency if previously completed. The process is depicted in Figure 6.11.

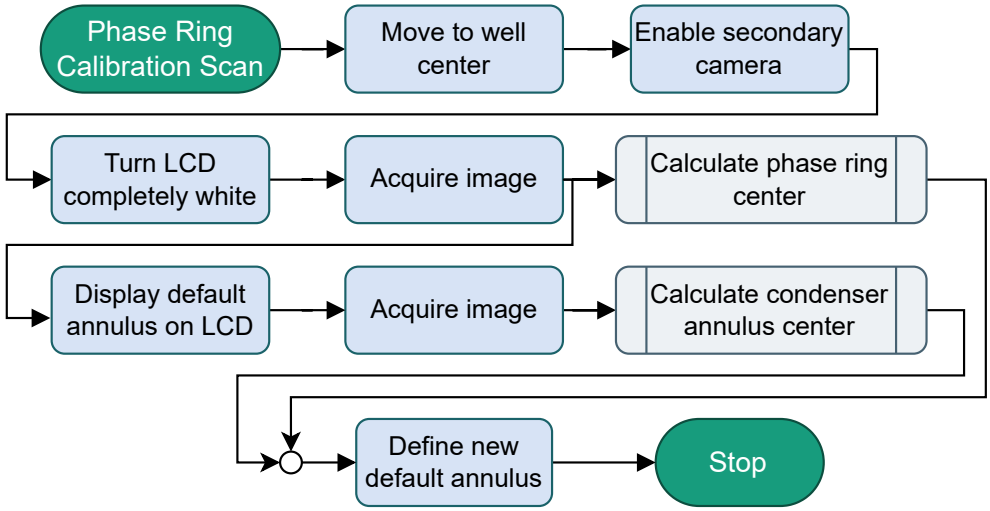

Figure 6.11: Flowchart of the Phase Ring Calibration Scan.

Initially, the specimen is positioned so that the well's center aligns with the microscope's optical path. This is accomplished by positioning the microscope stage at the known location of

the well's center. Following this, the rotatable mirror inside the microscope is automatically adjusted to enable the secondary camera to focus on the phase ring through the Bertrand lens. The LCD is commanded to display a completely white screen by rendering a ring with an inner radius of 0 and an outer radius exceeding the dimensions of the screen. This configuration allows the camera to visualize the phase ring as a black ring against a white background. The phase ring detection algorithm, detailed in Section 6.3.1, is applied to locate the phase ring's center. The position of the phase ring remains constant for all subsequent images as it is fixed within the objective lens.
Simultaneously to image analysis, the LCD is instructed to project the default condenser annulus corresponding to the specified magnification. The same image analysis algorithm, with modified parameters, is then utilized to identify the center displacement of the condenser annulus $\Delta\vec{d}$.
To establish a more accurate default condenser annulus position, the difference between the phase ring center and the latest condenser annulus center is calculated. The condenser annulus shift $\Delta\vec{p}$ is determined by Equation 6.2, which is used to calculate the new default condenser annulus position $\vec{p}_0$. The newly defined default condenser annulus position is now concentric with the phase ring. This position serves as the reference in all subsequent scans.

Autofocus Scan

The objective of the Autofocus Scan, illustrated in Figure 6.12, is to identify the focal positions (z-dimension) for all imaging points (x and y dimensions) during the subsequent Adaptive Stop-and-Go Scan. Although measuring the exact focus at each imaging position would ensure optimal accuracy, it is impractical due to the extensive time requirement, given the potentially hundreds or thousands of imaging positions involved. Consequently, the process involves scanning the z-height at a select few positions per well and interpolating the focus for the remaining points, as demonstrated by Schenk [Sch16a]. Schenk's research indicates that the bottom of a well can be approximated as a tilted plane, which is a principle applied in this scanning process. While a plane can technically be constructed from three base points, four points are employed in this implementation to enhance precision.

The stage is programmed to move the specimen to four distinct points per well, evenly distributed around the center of the well. The coarse z-axis remains at its default setting, which must be selected to ensure that the focused position is accessible within the piezo's range; this can be verified through a calibration process initiated after launching the microscope. At each designated point, image stacking is performed by incrementally adjusting the piezo from its lowest to highest position while capturing images. The optimal z-position for each point is determined using the Laplacian operator, which enables efficient evaluation due to its fast computational time (see Section 2.4.8). Subsequently, interpolation and extrapolation between these points are then utilized to ascertain the focus position for every scanning point.

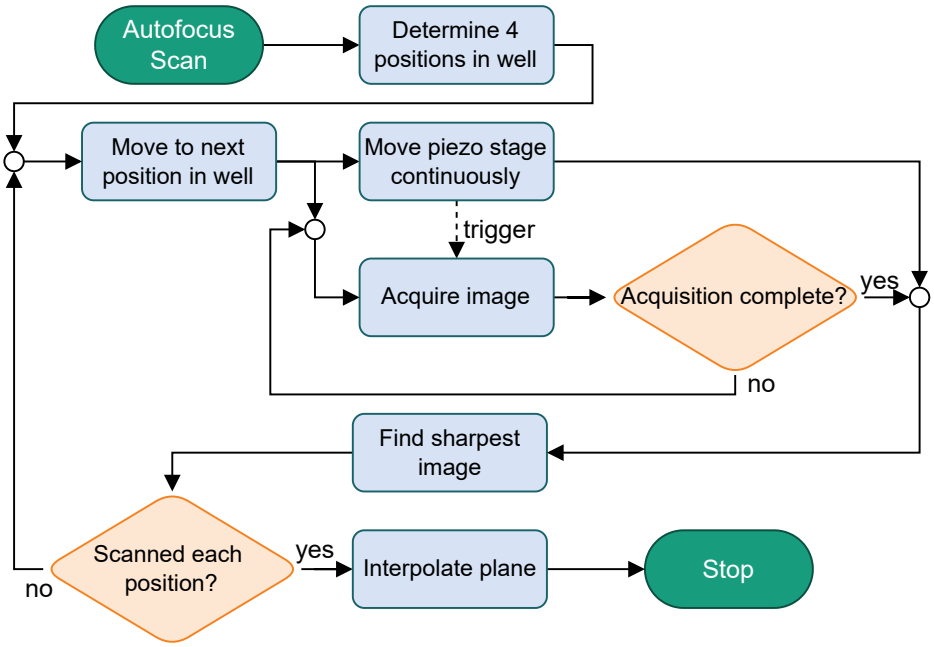

Figure 6.12: Flowchart of the Autofocus Scan.

Adaptive Stop-and-Go Scan

The Adaptive Stop-and-Go Process, depicted in the flowchart in Figure 6.13, is a method developed to obtain phase contrast images with meniscus compensation. At each image position, the microscope stage halts to ensure the specimen remains stationary during image capture. This technique eliminates motion artifacts from the images. Therefore, it can be presumed that this process achieves the optimum phase contrast area attainable using the LCD condenser annulus, making it suitable for benchmarking subsequent high-speed experiments.

The process involves sequentially moving to each imaging position, beginning with adjusting the focus via manipulation of the piezo z-axis. Images are captured with a slight overlap to each other of 5% the image size to correct positioning errors and facilitate stitching. Upon reaching an imaging position, a brief pause in the order of 500 ms is taken to allow the liquid in the MTP to stabilize. An acceleration of 30 mm/s^2 is used, as it was identified as the maximum without causing the liquid within the well to slosh. Subsequently, the LCD displays the condenser annulus in the default position $\vec{p}_0$. The secondary camera is engaged by rotating the mirror, and an image is captured. This image serves to determine the eventual LCD parameters. These parameters are calculated using the algorithm detailed in Section 6.3.1. Once computed, the correct position $\vec{p}$ is transmitted to the LCD controller and displayed. At this point, an optional image can be captured with the secondary camera, which, while

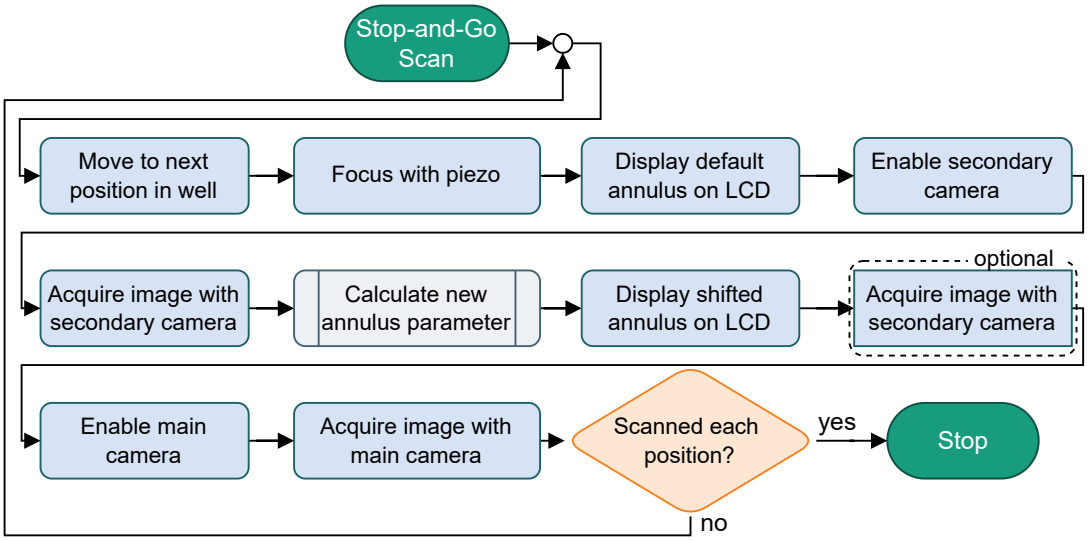

Figure 6.13: Flowchart of the image acquisition using the Adaptive Stop-and-Go Scan.

not critical to the process, can confirm the success of the annulus shift. Finally, the main camera is engaged by rotating the mirror, and an image of the specimen is captured and saved. Preprocessing, including histogram adjustment and shading correction, is applied to each image immediately after acquisition (see Section 2.4).

Stitching

Stitching is performed to combine individual images into a continuous compound image of the entire well. If images of multiple wells are acquired in a single scan, they are stitched separately into individual images for each well. A simplified flowchart of the process is presented in Figure 6.14.

Before stitching, preprocessing steps such as histogram adjustment and shading correction are performed to standardize conditions across different images (refer to Section 2.4). The stitching process itself is divided into three stages: feature recognition, matching, and placing images on a canvas. Although not depicted in the flowchart for simplicity, feature recognition is carried out immediately after each image acquisition in a parallel thread alongside image preprocessing to save time, allowing matching to commence as soon as the acquisition process concludes. Users have the option to select from SIFT, SURF, or ORB algorithms for feature recognition.
During the matching process, all pairs of neighboring images are iterated to compute their optimal relative placement. Once matching is complete, all images are placed on a canvas. The first image serves as an anchor, with subsequent images positioned relative to those

already placed. In overlapping regions, the image placed later is displayed on top of the previous one.

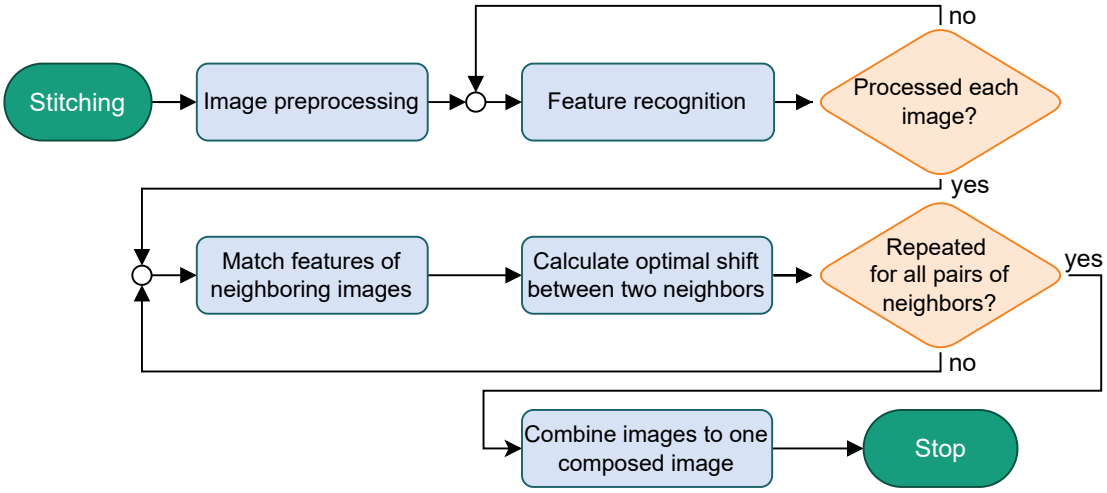

Figure 6.14: Flowchart of the stitching procedure.

6.4 Validation Through Experiments to Determine the Phase Contrast Area

The ability of adaptive phase contrast microscopy to mitigate the meniscus effect was validated experimentally. Employing the non-continuous scanning method described in Section 6.3.2, these experiments were designed to identify the maximum phase contrast area achievable using the LCD condenser annulus configuration. Acquisition time was also monitored, serving as a benchmark for assessing high-speed scanning capabilities, and is discussed further in the context of high-speed experiments in Section 7.4.3. This section begins with an introduction to the experimental design in Section 6.4.1, followed by the presentation of results in Section 6.4.2. Due to the challenges in evaluating the phase contrast area in 96-well MTPs, these results are examined separately in Section 6.4.3. Section 6.4.4 addresses the role of field curvature in producing varied outcomes for 96-well MTPs, and quantifies its effect on the phase contrast area. This section concludes with a discussion in Section 6.4.5.

6.4.1 Experimental Design

The experiments utilize the demonstrator described in Sections 6.2 and the methods described in Section 6.3. Various combinations of MTPs and magnifications were used, with MSCs as specimens. The configurations include: 6-well MTPs with 4x magnification, 24-well

MTPs with 4x magnification, 24-well MTPs with 10x magnification, and 96-well MTPs with 10x magnification. The 6-well and 96-well MTPs span the spectrum of well sizes, allowing an investigation into the method's effectiveness across different well sizes. The use of both 4x and 10x magnifications with 24-well MTPs demonstrates the impact of magnification and numerical aperture on the phase contrast area. For each configuration, a conventional phase contrast microscopy process acts as a benchmark for assessing the phase contrast area and the minimum achievable acquisition times. Three wells were imaged for each experimental run and configuration. The phase contrast area was calculated using the algorithm detailed in Section 4.2.

6.4.2 Resulting Phase Contrast Area

Figure 6.15 displays the phase contrast area achieved with a 24-well MTP under 10x magnification. This figure contrasts the adaptive phase contrast microscopy method with conventional phase contrast microscopy. Additional example results for different configurations are available in the Appendices, specifically in Figures A.6, A.7, and A.8.

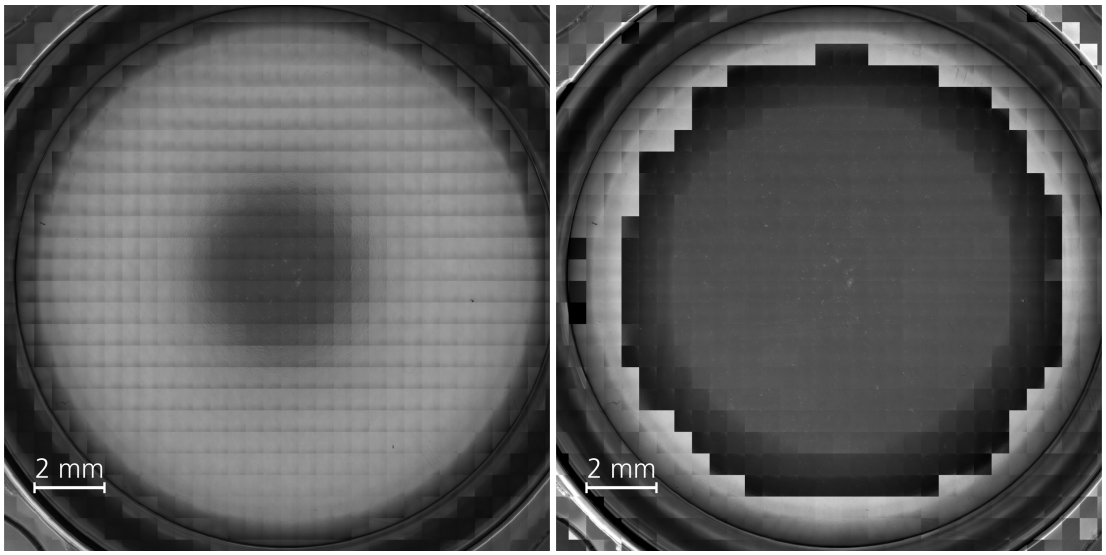

(a) Conventional phase contrast microscopy. **(b)** Adaptive phase contrast microscopy.

Figure 6.15: Images of a whole MTP24 well with 10x magnification as a result of the validation experiments.

Table 6.2 provides a summary of the phase contrast area results for 6-well MTPs with 4x magnification, 24-well MTPs with 4x magnification, and 24-well MTPs with 10x magnification. The findings for 96-well MTPs with 10x magnification are discussed separately in Section 6.4.3.

Table 6.2: Phase contrast areas for different MTPs and magnifications. *Std* represents the absolute standard deviation of the phase contrast area across different wells. The ratio is defined as the mean phase contrast area of the adaptive method and the regular method.

MTP	Magnification	Regular Phase Contrast		Adaptive Phase Contrast		Ratio
		Mean [%]	Std [%]	Mean [%]	Std [%]	
6	4	30.5	1.8	53.1	1.2	1.7
24	4	2.3	0.1	23.8	1.6	10.2
24	10	6.1	0.2	41.6	1.8	6.8

Table 6.2 reveals a substantial increase in the phase contrast area. The precise phase contrast area is significantly influenced by the MTP type and objective lens, which differ in magnification and numerical aperture. Higher-order MTPs tend to have a reduced phase contrast area for both conventional and adaptive phase contrast microscopy. Greater magnifications, associated with larger NAs of the utilized objective lenses, lead to an expanded phase contrast area. For 24-well MTPs with 4x magnification, an increase by a factor of 10.2 in the phase contrast area has been recorded. The smallest relative enhancement, a 1.7-fold increase, is observed for 6-well MTPs, where the initial value is already 30.5%. Figure 6.16 displays the phase contrast area superimposed on images for 6-well MTPs with 4x magnification.

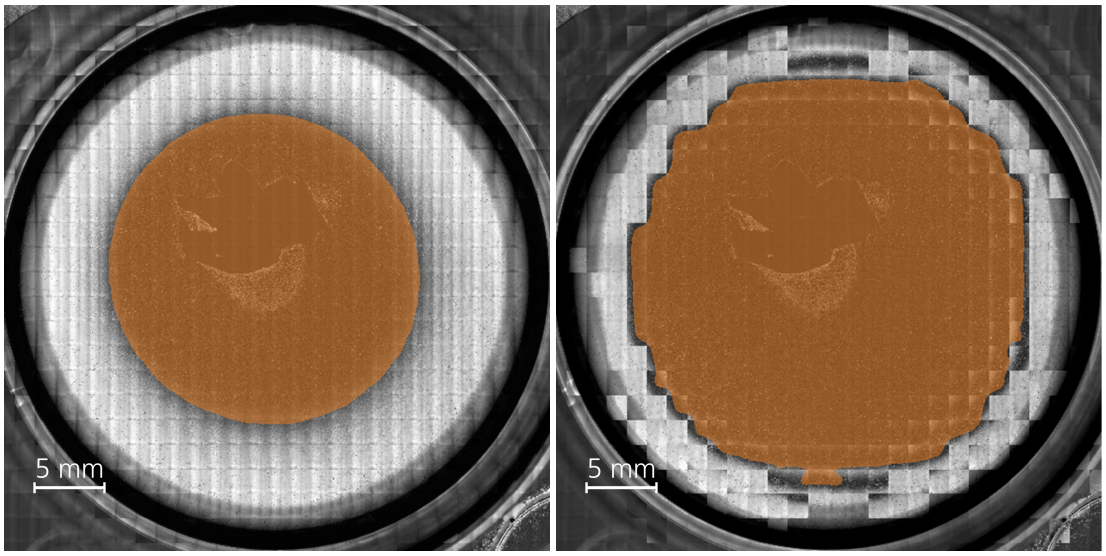

(a) Conventional phase contrast microscopy. **(b)** Adaptive phase contrast microscopy.

Figure 6.16: Images of a whole MTP6 well with 4x magnification as a result of the validation experiments. The phase contrast area is marked in orange.

Statistical Significance

To determine the statistical significance of the increase in the phase contrast area, a t-test for two independent samples was performed. The null hypothesis, H_0, posited that there is no significant difference in phase contrast areas. Conversely, the alternative hypothesis, H_1, suggested that the phase contrast area is greater when using adaptive phase contrast microscopy. A significance level of $\alpha = 1\%$ was selected as the threshold for rejecting the null hypothesis. Table 6.3 presents the results of the hypothesis tests. The p-values obtained are each below 0.0001, or 0.1%, which is significantly lower than α. This indicates, with statistical significance, that the phase contrast area can be increased across all three configurations.

Table 6.3: Results of the hypothesis test (t-test) for two independent samples to determine if the mean phase contrast area of adaptive phase contrast microscopy is larger than that of regular phase contrast microscopy. *Difference* indicates the disparity in mean phase contrast area. *99% Lower Limit* describes the 99% probability of not falling below this value. *t-values* are the t-values from the hypothesis test, and *p-value* represents the significance level of the calculation.

MTP	Magnification	Difference [%]	99% Lower Limit [%]	t-value	p-value
6	4	22.5	16.8	17.83	0.000192
24	4	21.5	15.0	22.88	0.000952
24	10	35.4	28.3	34.51	0.000419

Comparison with Upper Bound of Phase Contrast Area

Although the phase contrast area achieved through adaptive phase contrast microscopy may initially appear limited, especially with 23.8% for 24-well MTP at 4x magnification, it is important to recognize that full compensation is restricted by shading at the edge of the well, as detailed in Section 6.1.3. Therefore, assessing the phase contrast area as a proportion of the upper bound for the achievable area offers a more accurate insight into the technology's capabilities. The findings are presented in Table 6.4. It is evident that, despite the seemingly small phase contrast area, the 23.8% for 24-well MTP at 4x magnification represents 60% of the optimal potential. For all three configurations in adaptive phase contrast microscopy, more than 50% of the well area is visible under phase contrast conditions relative to the upper bound.

6.4.3 Challenges with 96-Well MTPs

Evaluating the measurement results of the 96-well MTPs presents various challenges. Quantifying the phase contrast area for an entire well is difficult due to significant inhomogeneities within individual images. Figure 6.17 provides example images that illustrate these inhomogeneities.

Table 6.4: Phase contrast area of adaptive phase contrast microscopy as a share of the upper bound when considering shading at the edge of the well. *Relative Phase Contrast Area* represents the share of the phase contrast area compared to the upper bound. Phase contrast is abbreviated as *PC*.

MTP	Magnification	PC Area [%]	Upper Bound [%]	Relative PC Area [%]
6	4	53.1	73	73
24	4	23.8	40	60
24	10	41.6	82	51

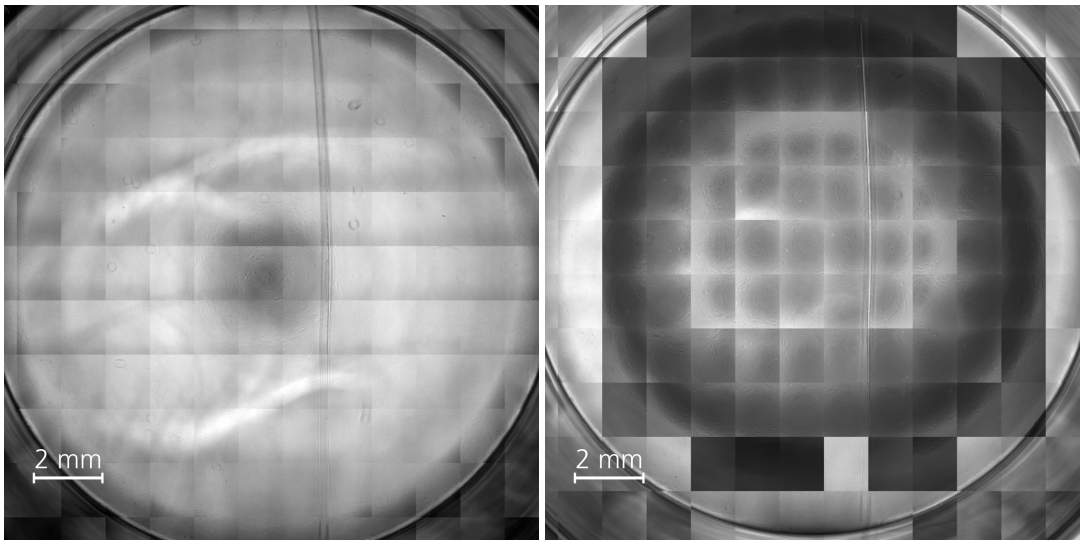

(a) Conventional phase contrast microscopy. **(b)** Adaptive stop-and-go phase contrast microscopy.

Figure 6.17: Comparison between regular phase contrast microscopy (a) and adaptive phase contrast microscopy (b) in 96-well MTPs. Inhomogeneities in phase contrast conditions within individual images can be observed.

The inhomogeneity in the images renders the phase contrast area algorithm, described in Section 4.2, sensitive to minor variations in exposure conditions. As a result, it is not possible to calculate a reliable phase contrast area. As a result, data from 96-well MTPs is excluded from the quantitative analysis of the phase contrast area. Nevertheless, qualitative analysis of the resulting images suggests a notable increase in the phase contrast area, despite the inability to quantify it.

The observed inhomogeneities in the images are primarily caused by field curvature induced by the meniscus (see Section 2.1.8). This curvature impedes the establishment of uniform phase contrast conditions within the images, which will be elaborated upon in the following section.

6.4.4 Impact of the Field Curvature on the Results

Images of wells in 96-well MTPs acquired with 10x magnification exhibited inhomogeneities within individual images, rendering the evaluation of the phase contrast area using the algorithm from Section 4.2 unreliable. This exhibits an inherent limitation of the meniscus effect compensation approach, which is analyzed within this section.

Inhomogeneous phase contrast conditions are evident in phase contrast images across different configurations of well sizes and magnifications, though the extent varies. Figure 6.18 offers a detailed view of an individual image within a 24-well MTP acquired with 4x magnification, emphasizing this effect.

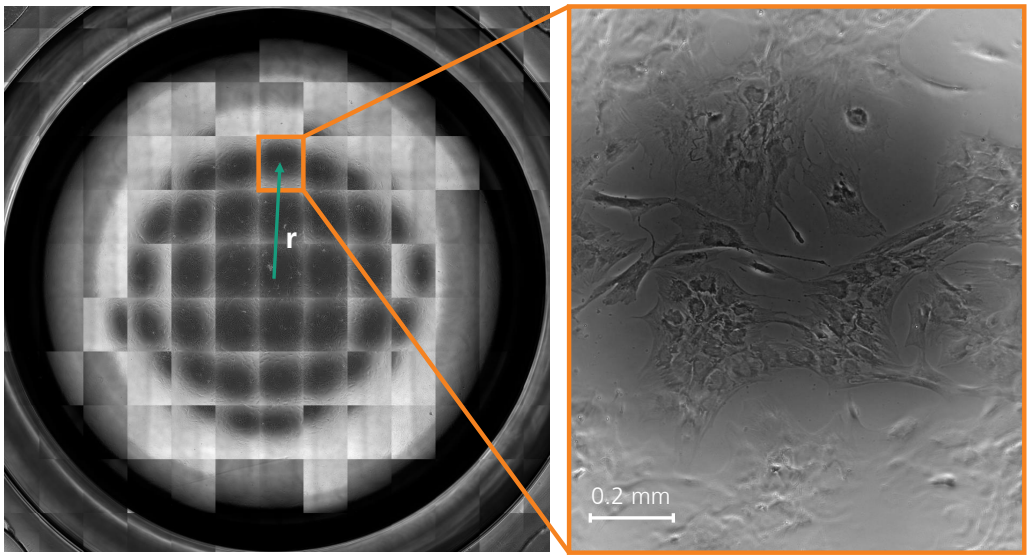

Figure 6.18: Composite image from adaptive phase contrast microscopy of an MTP24 at 4x magnification, featuring a highlighted single image that exhibits inhomogeneous phase contrast conditions. The inhomogeneities become stronger further from the center. The distance from the center of this single image to the well center, denoted as r, is approximately 3.6 mm.

The meniscus compensation strategy assumes a uniform meniscus surface angle across the area captured by a single image. This first-order approximation is necessary because only one condenser annulus adjustment can be executed for each imaging position. However, since each camera image captures a two-dimensional section of the well, it is distorted by the field curvature caused by the meniscus shape, as detailed in Section 2.1.8. Field curvature can lead to non-uniform phase contrast conditions within an image, resulting in brighter corners compared to the rest of the image. To quantify this phenomenon, the results from Section 6.4.2 are analyzed in conjunction with data on the meniscus shape. This analysis facilitates the determination of the maximum angle of the meniscus surface at which phase contrast conditions can be sustained, referred to as the *phase contrast angle*.

Phase Contrast Angle

This section outlines the procedure to calculate the phase contrast angle α based on measurements of the meniscus shape. The phase contrast angle is used to identify the radial distance from the well center where field curvature significantly affects imaging due to pronounced curvature within the camera sensor's coverage area. These calculations are conducted for 24-well MTPs, whose meniscus shape was measured in Section 6.1.1. A comparative analysis is performed for magnifications of 4x and 10x, as magnification influences the camera's field of view.

The phase contrast angle is directly derived from the phase contrast area. Because the wells of the MTP are circular, the phase contrast area is also assumed to be circular. The phase contrast angle is defined as the meniscus angle at the radial position corresponding to the edge of this area. The radii of the phase contrast area for different magnifications are determined using the phase contrast areas listed in Table 6.2. The maximum meniscus surface angles are derived by evaluating the meniscus angles at these radii. Table 6.5 lists the results. Figure 6.19 depicts the phase contrast area superimposed on the meniscus shape.

Table 6.5: Maximum tilt angle of the meniscus surface at the boundary of the phase contrast area for MTP24 (phase contrast angle). Explanation of columns: *Radius*: assumed circular radius of the phase contrast area in mm, α: phase contrast angle.

Magnification	Method	Phase Contrast Area [%]	Radius [mm]	α [°]
4	conventional	2.3	1.25	0.95
4	adaptive	23.8	4.02	4.76
10	conventional	6.1	2.04	1.68
10	adaptive	41.6	5.32	8.12

Field Curvature by Distance from the Well Center

The analysis of composite images in Section 6.4.2 demonstrates that, even after compensating for the meniscus effect, images positioned farther from the well center exhibit inhomogeneous phase contrast conditions. This phenomenon is attributed to field curvature. Beyond a certain well radius, this issue becomes significant, as phase contrast conditions cannot be maintained consistently within a single image or across a composite image. The goal of this section is to determine the minimum distance from the well center at which this problem arises.
An increase in field curvature leads to greater phase contrast angle differences within a single image. Inhomogeneous phase contrast conditions occur when the angle difference within an image exceeds a specific threshold. This angle difference can be quantified using the maximum phase contrast angle, which was determined in the previous section and is

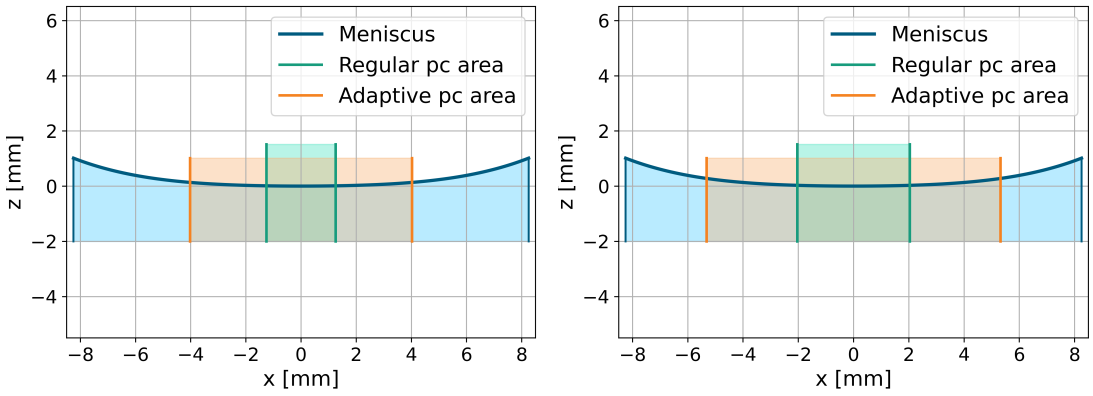

(a) 4x magnification.

(b) 10x magnification.

Figure 6.19: Overlay of phase contrast (*pc*) areas at various magnifications on the meniscus shape calculated in Section 6.1.1. The green patch marks the extent of phase contrast conditions with conventional phase contrast microscopy, while the orange patch marks adaptive phase contrast microscopy. The x and y axes are to scale.

summarized in Table 6.5. Due to the rotational symmetry of the meniscus, the angle difference within the phase contrast area is twice the phase contrast angle. If the meniscus angle difference within an image (denoted as $\Delta\alpha$) caused by the field curvature exceeds the phase contrast angle, uniform phase contrast conditions cannot be achieved across the image, even with optimal alignment of the condenser annulus and phase ring at the image center. The progressively increasing meniscus angle toward the well edge, depicted in Figure 6.3d in Section 6.1.1, suggests a minimum distance from the well center where this field curvature threshold is exceeded.

Calculations were performed to determine the minimum and maximum distance from the well center where inhomogeneous phase contrast conditions occur. Since images can be oriented differently, two scenarios were considered: a *best case* where the short side of the image aligns parallel to a direct line between the image center and well center, minimizing the effect of field curvature, and a *worst case* where the image diagonal aligns with this line, maximizing the effect of field curvature. The sizes of the individual images depend on the size of the camera chip, which is 5.4 mm $\times$ 6.5 mm, and the magnification.
Initially, curves representing angle differences within an image over well center distances for both scenarios are calculated. The intersection points of these curves with the phase contrast angle are determined, representing the nearest and furthest distances from the well center where field curvature exceeds the phase contrast angle for the first time, contingent on image orientation. These curves are presented in Figure 6.20. The resulting values are displayed in Table A.6 in the Appendices.

The minimum distance required to exceed the phase contrast angle is significantly lower for 4x magnification compared to 10x magnification. With 4x magnification, even images located near the well center (less than a full image diagonal distance) demonstrate inhomo-

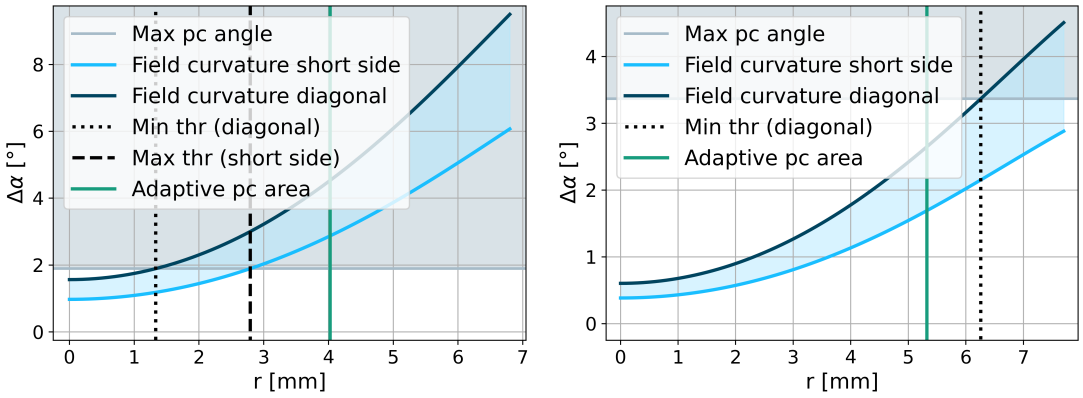

(a) 4x magnification.

(b) 10x magnification.

Figure 6.20: Difference between the largest and smallest meniscus angles, $\Delta\alpha$, within one image, plotted against the distance r from the well center to the image center for an MTP24. The smallest effect of field curvature occurs along the short side of the image (light blue curve), while the largest occurs along the diagonal (dark blue curve). Intermediate orientations are represented by the light blue area between the curves. The *Max pc angle* indicates the meniscus angle difference within the phase contrast area for standard phase contrast microscopy. *Min thr (diagonal)* marks the minimum distance from the well center beyond which homogeneous phase contrast conditions are unattainable across the image diagonal. Conversely, *Max thr (short side)* denotes the minimum distance along the short side. The edge of the adaptive phase contrast area is shown as a reference. Phase contrast is abbreviated as *pc*.

geneous behavior. In contrast, for 10x magnification, the minimum distance in the best-case scenario is so far outside that no such distance is present within the well. This is illustrated in Figure 6.21, where the highlighted image is 6.7 mm away from the center and still exhibits more homogeneous phase contrast conditions than the highlighted image in Figure 6.18, which is 3.6 mm from the well center.

In summary, the effect of field curvature on well images acquired at different magnifications and their corresponding NAs was quantified. The analysis demonstrated the extent to which images captured at lower magnifications are more susceptible to inhomogeneities caused by field curvature when compared to those acquired at higher magnifications.

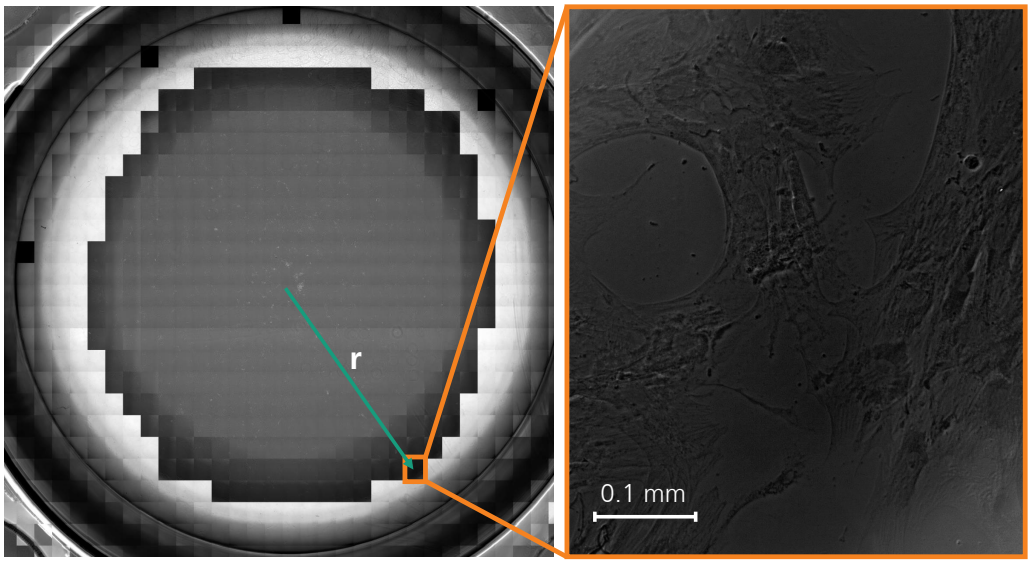

Figure 6.21: Composite image from adaptive phase contrast microscopy of an MTP24 at 10x magnification, highlighting a single image located just beyond the area where homogeneous phase contrast conditions are achievable. The distance from the center of this single image to the well center, indicated as r, is approximately 6.7,mm.

6.4.5 Discussion and Critical Reflection

The experiments consistently and reliably increased the phase contrast area across all observed configurations of MTPs and magnifications. The increase is statistically significant for all configurations where a phase contrast area evaluation was feasible. Higher-order MTPs generally exhibit a smaller phase contrast area due to the more pronounced curvature of the meniscus shape. The relative increase in phase contrast area is greater for these configurations. Nonetheless, even in lower-order MTPs, adaptive phase contrast microscopy facilitates the observation of a substantially larger area, enhancing the utility of phase contrast microscopy. For all evaluated 6-well and 24-well plates, the phase contrast area exceeded 50% of the upper limit for the phase contrast area. However, some results can be reflected critically.

Firstly, it is important to acknowledge that the precise phase contrast area values depend on the quantification method used and may vary if a different method is employed – therefore, values can only be compared if the same method with identical parameters is applied. The algorithm for determining phase contrast conditions relies on multiple inputs, with the relative threshold T_{pc} being particularly significant, potentially causing variations of a few percent in the exact phase contrast area values.

A key factor affecting results is the field curvature, which leads to non-uniform phase contrast conditions. Despite the camera's small sensor chip, individual images captured at 4x magnification reveal brighter corners than the center, resulting in inhomogeneity in the

composite image. Field curvature presents a substantial challenge for adaptive phase contrast microscopy, particularly hindering accurate phase contrast area computation for 96-well MTPs. Alleviating this issue could be achieved by decreasing the FOV through higher magnification, utilizing a smaller camera sensor chip, or cropping the existing camera sensor. However, such a solution would increase image capture time, as more images would be required to capture a whole well.

6.5 Summary and Interim Conclusion

This chapter aimed to address SRQ3 (refer to Section 3.6):
To what extent can the phase contrast area be increased using adaptive phase contrast microscopy compared to conventional phase contrast microscopy?

This chapter first assessed the factors influencing the phase contrast area, identifying the meniscus shape and shading at the MTP walls as the most significant. It was determined that substantial portions of the well area remain unobservable under phase contrast conditions due to shading, even with adaptive phase contrast microscopy. Subsequently, a demonstrator setup for experiments incorporating an LCD condenser annulus was developed. A scanning methodology for capturing comprehensive images of entire MTP wells utilizing adaptive phase contrast microscopy was introduced. The method comprises four main steps: Phase Ring Calibration Scan, Autofocus Scan, Adaptive Stop-and-Go Scan, and Stitching. A two-step procedure for calculating the LCD condenser annulus position was also presented. It consists of image analysis of Bertrand lens images to determine the displacement of the condenser annulus, followed by linear regression.

The entire process was validated through experiments, which measured the phase contrast area for 6-well MTPs with 4x magnification, 24-well MTPs with 4x and 10x magnification, and 96-well MTPs with 10x magnification. The results demonstrated a significant and consistent increase in the phase contrast area. Additionally, it was discovered that field curvature within images caused inhomogeneities in phase contrast conditions, rendering the analysis of 96-well MTPs with 10x magnification unfeasible. The effect was quantified to determine the radius at which inhomogeneous conditions become unavoidable.

In conclusion, SRQ3 can be answered as follows:
The phase contrast area can be increased significantly across all assessed configurations of MTPs and magnifications, ranging from a 1.7-fold increase for 6-well MTPs with 4x magnification to a 10.2-fold increase for 24-well MTPs with 10x magnification.

While it has now been demonstrated that the phase contrast area can be enhanced by adaptive phase contrast microscopy, another requirement for the approach is a short acquisition time. The acquisition time is assessed in the following section.

7 High-Speed Meniscus Effect Compensation Using a Continuous Scanning Method

This chapter is dedicated to address the fourth and final sub-research question (refer to Section 3.6):
Which acquisition time is achievable for complete wells in microtiter plates? What are the influencing factors on acquisition time?

Initially, the influencing factors on acquisition time are evaluated in Section 7.1, which are vital for developing an optimized scanning procedure. Subsequently, the scanning procedure is detailed in Section 7.2. It builds upon the procedure used in Chapter 6 but operates by acquiring specimen images continuously without pausing for image capture, akin to the HSM method described in Section 3.2. The software implementation of this procedure is described in Section 7.3, emphasizing the communication and synchronization between various components, particularly the LCD, to achieve high-speed. Experimental validation is performed in Section 7.4 to assess the imaging time under various conditions with different parameters. Moreover, the phase contrast area is compared between a high-speed scan and the stop-and-go scan from Chapter 6 to evaluate whether increased acquisition speed affects the phase contrast area. In Section 7.5, the factors influencing these results are analyzed, followed by a comparison with alternative approaches to mitigate the meniscus effect. Finally, Section 7.6 summarizes this chapter and draws conclusions, focusing on the experimental outcomes and their alignment with the thesis's objectives.

7.1 Influencing Factors on Acquisition Time

Various factors influence the acquisition time in adaptive phase contrast microscopy, employing an HSM process as described in Section 3.2. Based on preliminary tests, the most impactful factors are stage velocity and range, limited acceleration due to liquid sloshing, camera exposure time and flash duration, and the LCD refresh rate and reaction time. These factors are evaluated within this section.

7.1.1 Stage Velocity and Range

This section explores the relationship between the microscope stage's velocity and range and the total acquisition time of an adaptive high-speed phase contrast microscopy process that acquires images during specimen movement. Each scan has an optimal velocity determined by acceleration and the available motion range, which can be calculated using Newton's laws of motion. It is assumed that linear acceleration can be applied and that deceleration matches the acceleration, a condition that is approximately achievable by the microscope stage. The acquisition of a continuous scan is divided into multiple parallel scan lines, comprising the phases of acceleration, steady velocity, and deceleration, described by Equation 7.1:

$$t_L = t_{\text{acc}} + t_v + t_{\text{dec}} \tag{7.1}$$
$$= 2t_{\text{acc}} + t_v \tag{7.2}$$
$$= 2\frac{v}{a} + \frac{d_v}{v}, \tag{7.3}$$

where t_L is the scan time for one line, t_{acc} is the acceleration time, t_v is the time at maximum velocity, t_{dec} is the deceleration time, v is the maximum velocity, a is the acceleration, and d_v is the distance at maximum velocity. To determine the optimal velocity, Equation 7.1 must be minimized by finding the roots of its derivative with respect to the target velocity, which yields Equation 7.4:

$$\frac{dt_L}{dv} = \frac{2}{a} - \frac{d_v}{v^2}. \tag{7.4}$$

Setting this equation to zero and solving for v results in Equation 7.5:

$$v = \sqrt{d_v \frac{a}{2}}. \tag{7.5}$$

Consequently, the optimal velocity is influenced by both available space and acceleration. Furthermore, achieving the optimal velocity is contingent upon the capabilities of the hardware. The Märzhäuser Wetzler SCAN IM 130x85 stage can attain a maximum acceleration of 500 mm/s^2 and a maximum velocity of 120 mm/s.
In addition, the stage's range affects the maximum velocity, as reaching the maximum velocity requires a minimum acceleration distance d_{acc}. This distance can be calculated using Equation 7.6 derived from Newton's laws of motion:

$$d_{\text{acc}} = \frac{1}{2}\frac{v^2}{a}. \tag{7.6}$$

If the available space for acceleration is less than d_{acc}, the maximum velocity must be reduced, thus increasing the acquisition time.
The Märzhäuser Wetzler SCAN IM 130x85 stage has a maximum range of 130 mm $\times$ 85 mm. Given that the size of an MTP is approximately 128 mm $\times$ 86 mm, this results in a con-

strained acceleration distance if the whole MTP is to be imaged, requiring a reduction in velocity.

7.1.2 Limited Acceleration due to Liquid Sloshing

Excessive acceleration of the specimen generates forces that cause the liquid to slosh, unpredictably altering the meniscus shape and complicating compensation efforts or rendering them impossible. Therefore, it is essential to minimize the specimen's acceleration. However, a high acceleration is crucial for rapid imaging, presenting a conflict of interest.
A high acceleration is particularly significant for wells near the edge of the MTP, due to the limited range of the microscope stage. This limited range means that the acceleration distance to the first column of wells is short; without a high acceleration, the maximum speed must be restricted, thereby prolonging the acquisition time.

To determine the influence of sloshing, experiments were conducted using HSM with a conventional phase contrast microscope to capture images of an entire well. The phase contrast area was monitored. Any observed changes in the phase contrast area or inhomogeneous brightness distributions indicated that the acceleration was too high. Initially, a 24-well MTP with 10x magnification was utilized. Two specimens were tested: one with a liquid level just covering the meniscus center by 1 mm and another with liquid occupying approximately two-thirds of the well volume. The experiments commenced with an acceleration of 10 mm/s^2, doubling in each subsequent experiment until it was capped at 500 mm/s^2, the maximum acceleration of the stage. The maximum velocity for each scan was calculated using Equation 7.5. When the first excessive acceleration was identified, further experiments were conducted using accelerations refined through interval halving to establish a more precise limit.

Images with three different accelerations in wells with low liquid levels are shown in Figure 7.1. No significant difference is observed between 10 mm/s^2 and 160 mm/s^2. However, at 500 mm/s^2, alternating rows of phase contrast conditions appear, caused by the meandering scanning procedure.

Results for experiments with a high liquid level are presented in Figure 7.2. In contrast to the low liquid level, sloshing begins to negatively impact the phase contrast area at accelerations as low as 160 mm/s^2. At 500 mm/s^2, sloshing becomes so erratic that no discernible pattern is recognizable. Consequently, sloshing negatively affects the image quality, and higher liquid levels are more problematic, necessitating a lower stage acceleration.

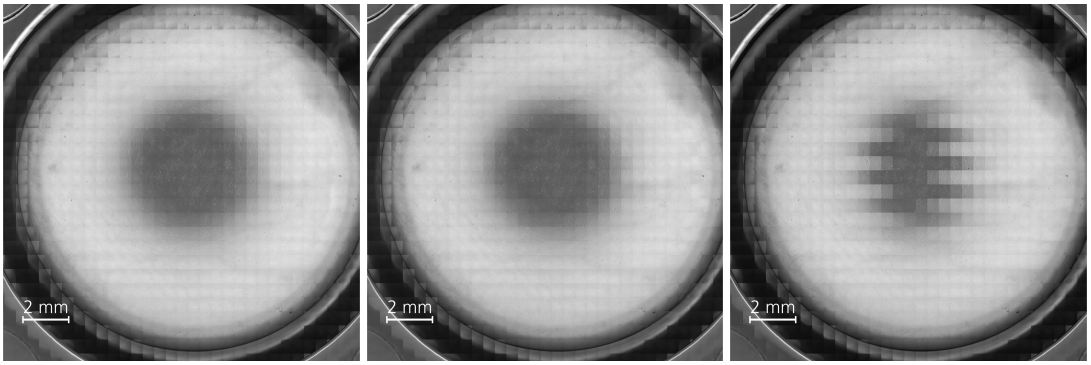

(a) a = 10 mm/s^2. **(b)** a = 160 mm/s^2. **(c)** a = 500 mm/s^2.

Figure 7.1: Images of a whole MTP24-well filled with a small amount of liquid, acquired with continuous scanning and different accelerations.

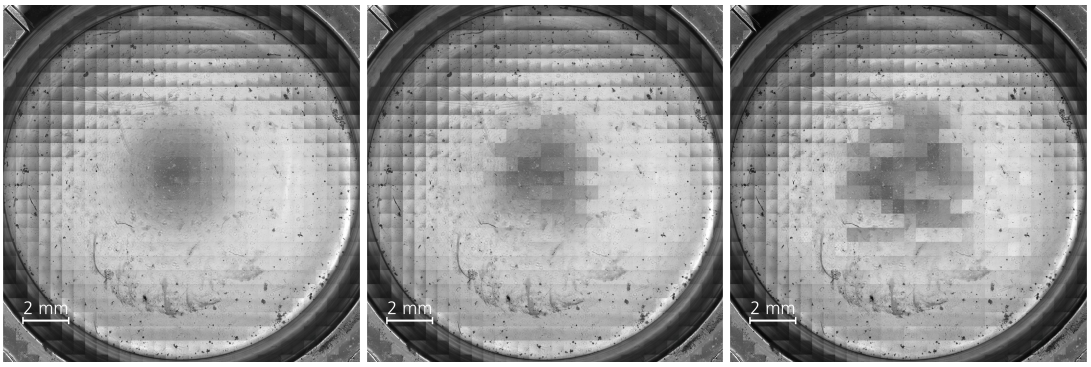

(a) a = 10 mm/s^2. **(b)** a = 160 mm/s^2. **(c)** a = 500 mm/s^2.

Figure 7.2: Images of a whole MTP24-well filled to about two-thirds of its volume, acquired with continuous scanning and different accelerations.

7.1.3 LCD Refresh Rate and Reaction Time

The LCD is the most time-critical component within the system. Since repositioning the condenser annulus is required for each new image position within a well, the refresh rate of the LCD inherently limits the system's overall frame rate. This section evaluates the maximum achievable frame rate and the delays associated with rendering a condenser annulus, which are critical for designing an efficient scanning procedure.

Experiments are conducted to confirm that the LCD refresh rate aligns with the manufacturer's specifications of 60 Hz and to assess any potential fluctuations or jitter. Furthermore, tests are carried out to determine if the rendering algorithm on the Raspberry Pi can update the LCD at the specified refresh rate. Even if the refresh rate conforms to the specified values and the Raspberry Pi can promptly control the LCD, uncertainties remain regarding the system's responsiveness. This includes the LCD, its controller, and the Raspberry Pi, in

terms of reacting swiftly enough to a signal that prompts a change in the condenser annulus, as well as the extent of any jitter present. These aspects are examined through separate experimental investigations.

Refresh Rate

An experiment was devised to measure the transition time between frames during repeated rendering at the maximum frame rate. A total of ten experimental runs were conducted. The LCD unit was mounted into the phase contrast microscope, employing the condenser annulus ring rendering code detailed in Section 7.3.3. The main computer transmitted 15 condenser annulus positions to the Raspberry Pi, which were displayed sequentially. These positions represented condenser annuli of the same dimensions, shifted incrementally from left to right along the x-direction in successive images.
The secondary camera observed the virtual condenser annulus through the Bertrand lens. To reduce data volume and enable a frame rate increase beyond the usual 289 fps, the camera's ROI was cropped to 496×200 pixels, as explained in Section 2.3.2. Consequently, the frame rate was set to 1000 Hz, equating to image intervals of one millisecond. This setup allowed the image counts to serve as timestamps for measuring frame transition times. To ensure an unobstructed view of the LCD, no specimen was inserted into the microscope. The Raspberry Pi, connected to an external trigger source set to 60 Hz, synchronized with the LCD's specified refresh rate. The rendering code updated the condenser annulus position upon detecting a trigger signal on the Raspberry Pi's digital input. The experiment commenced with the manual initiation of the camera stream and the trigger source. Once the LCD cycled through all annulus positions, the stream was stopped, and images were saved.

Table A.3 in the Appendices displays a segment of the resulting images from one experiment. Transitions between annulus positions are visibly distinct. However, these transitions are not instantaneous, as the LCD's pixels require several milliseconds to adjust to brightness changes, making the transition time between frames difficult to determine.
To analyze the x-positions of the annuli consistently, an image analysis algorithm was developed. The algorithm sums the columns in the y-direction to generate a 1D array. The center of gravity q of this array is then calculated and designated as the image center. This process is repeated for each image of an experimental run. Figure 7.3 illustrates the center of gravity over time for one experiment. Phases of constant center positions indicate settled LCD pixels, with steep gradients marking transitions. Each period comprises approximately equal durations of the constant and transition phases.

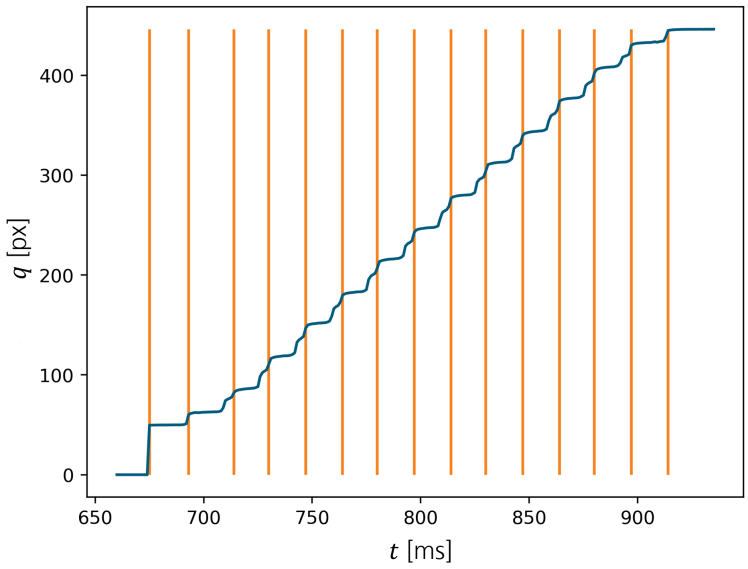

Figure 7.3: Refresh rate experiments: center of gravity q of the virtual condenser annulus plotted over the time t since the measurement started. Vertical lines indicate a full switch from one annulus to the next, as calculated by the algorithm.

To determine exact frame switch times, the algorithm segments the curve of centers of gravity into smaller sections at positions where the center remains constant, ensuring only one steep gradient per segment. The transition time for each segment is identified when the center of gravity first exceeds a threshold q_{thr}, defined by Equation 7.7:

$$q_{\text{thr}} \geq q_i + 0.7\,(q_{i+1} - q_i)\,, \tag{7.7}$$

where q_i is the center of gravity at the beginning of the section and q_{i+1} is the center of gravity at the end of the section.
Since initial images are black before the first annulus appears, the first gradient is nearly vertical, rendering transition times for the first and second frames less reliable. They are thus excluded. For each experiment, the mean, median, minimum, maximum times, and standard deviation were analyzed. Statistical analysis, as shown in Table A.4 in the Appendices, indicates no outliers. All frame switch times are within 1 ms of each other, either 16 ms or 17 ms, corresponding to the measurement's sampling rate. The average frame switch time is 16.7 ms $\pm$ 0.47 ms, consistent with the expected value for a 60 Hz display. This confirms that the LCD's performance aligns with the manufacturer's specifications and that the rendering code on the Raspberry Pi executes efficiently to maintain this refresh rate without failure. Moreover, all trigger signals are successfully received and processed. This confirms the effective operation of the process chain within the Raspberry Pi, covering the entire sequence from receiving the trigger signal to rendering an annulus on the LCD.

Reaction Time from Trigger Input Until Frame Rendering

Experimental results from the preceding section suggest that both the LCD and the rendering software function at 60 Hz, ensuring no trigger signals are overlooked. However, during the actual data acquisition, the trigger frequency may exhibit slight variations, as it is generated path-synchronously and can fluctuate due to changes in stage velocity. Additionally, it remains uncertain whether the LCD displays each frame immediately after rendering by the Raspberry Pi or if a constant latency exists. Further experiments are conducted to investigate this aspect.

An experimental protocol was devised to measure the rendering time for the initial frame upon receiving a trigger signal. The hardware setup replicated that of the previous experiment, with 15 experimental runs conducted. The approach involved sending a trigger signal simultaneously to both the camera and the LCD, then determining the initial detection of a change on the LCD by the camera. The Raspberry Pi was programmed with modified code to respond solely to the initial trigger signal and subsequently hold the image. Before trigger reception, the LCD displayed a black image. Upon trigger detection, it transitioned to a completely white image. This simplification allows the camera to detect a transition on the LCD more easily, compared to detecting moving rings. To aid this detection, the camera's ROI was restricted to 64×30 pixels centered on the camera chip, as only a few pixels are necessary to detect the switch from black to white. The camera was set to capture the first image upon receiving a trigger signal, ensuring synchronous acquisition with the Raspberry Pi, as they shared the same trigger source set for a rising edge trigger. The acquisition frame rate was 1000 Hz, with the image number used as a timestamp. Table A.5 in the Appendices section presents images from one segment of one experiment.

Each experiment began with the activation of the trigger source and ended once the camera detected only white images. As observed in prior experiments, the LCD undergoes a notable transition period before stabilization. Image analysis was employed to determine the completion of frame switching. Initially, the average brightness of each image in a series was calculated, reducing each image to a one-dimensional number. The reaction time was identified as the first instance when brightness exceeded a predefined threshold. This threshold b_{thr} was set to 80% of the difference between the minimum average brightness b_{min} and the maximum average brightness b_{max}, mathematically expressed by Equation 7.8:

$$b_{\text{thr}} = b_{\text{min}} + 0.8\,(b_{\text{max}} - b_{\text{min}})\,. \tag{7.8}$$

The resulting curve for one experiment, along with the reaction time and threshold, is depicted in Figure 7.4.

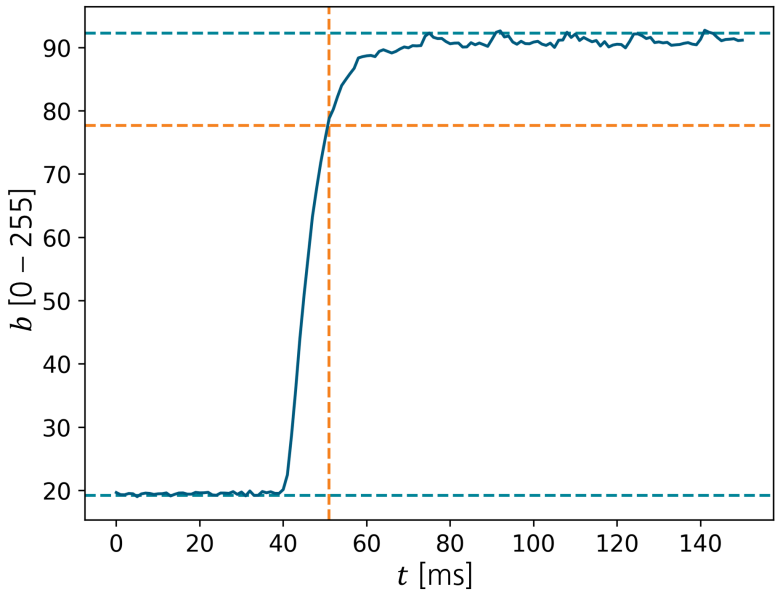

Figure 7.4: Change in the average image brightness b following a trigger signal sent at 0 ms, representing the reaction time of the LCD and Raspberry Pi to an input signal. The orange lines indicate the time when the image brightness reaches 80% of its peak brightness, marking the completion of the frame transition after 51 ms.

The key finding from all experiments is that the reaction time to render the first frame significantly exceeds the expected 16.7 ms for a 60 Hz display. The mean reaction time, $t_{\text{LCD,mean}}$, was 57.2 ms, which is more than three times the anticipated duration. Nevertheless, all reaction times fell within a narrow range of 15 ms, less than the duration of one frame (16.7 ms), indicating the absence of outliers. This observation is depicted in the boxplot shown in Figure 7.5.

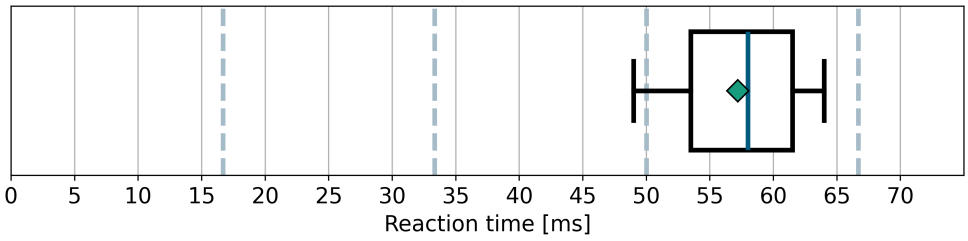

Figure 7.5: Boxplot illustrating the reaction times between the trigger input and the first frame across the 15 experiments. A green diamond represents the mean, calculated to be 57.2 ms, with a standard deviation of 4.9 ms. The median value is 58 ms. The whiskers include all recorded times, indicating the absence of outliers. Dashed lines are separated by the LCD's refresh rate.

The experiment in the previous section demonstrated that rendering a single ring reliably completes within one frame, indicating that the delay cannot be attributed to the Raspberry

Pi's processing time. While some delay, up to 10 ms, can be attributed to the LCD's response time, it does not account for the majority of the delay. Therefore, the most likely cause of the latency is the LCD controller's double or triple buffering, as discussed in Section 2.3.4. The controller presumably pre-stores multiple frames to remain independent of the connected device's rendering speed and to maintain a consistent refresh rate. This behavior is corroborated by the observation that the delay occurs solely before the first image. During the rendering of multiple images, as in previous experiments, all subsequent images adhere to the specified frame rate.

This behavior has been consistently observed across various LCD models, rendering a switch to an alternative model impractical, especially given the limited availability of monochrome displays without backlight. Since this behavior cannot be controlled in this project, the reaction time must be considered a fixed parameter, necessitating an adjustment of the adaptive high-speed phase contrast microscopy process.

The extended reaction times impose constraints on the synchronization of the LCD with the microscope stage, camera, piezo stage, and flash controller. One option for achieving a high-speed process was to implement a closed-loop acquisition system for the actual image scan, which is rendered impractical by the LCD's reaction time. This closed-loop approach would involve collecting data about the meniscus during continuous sample movement, with immediate processing of the information. The LCD parameters would then be communicated to the Raspberry Pi to display a new condenser annulus based on the collected data. However, this would introduce a delay between measurement and the display of a new condenser annulus, at least as long as the LCD's reaction time, significantly restricting the achievable process frame rate.
This is illustrated with an example calculation. To maintain the number of outliers below 0.15% under a normal distribution (3σ level), the frame time t_{frame} is calculated using Equation 7.9:

$$t_{\text{frame}} \geq \overline{t_{\text{LCD}}} + 3 \cdot \sigma_{t,\text{LCD}} = 57.2\,\text{ms} + 3 \cdot 4.9\,\text{ms} = 71.9\,\text{ms}, \tag{7.9}$$

where $\overline{t_{\text{LCD}}}$ is the mean reaction time and $\sigma_{t,\text{LCD}}$ denotes the standard deviation of the reaction time. Consequently, the maximum process frame rate for a closed-loop process f is determined by Equation 7.10:

$$f \leq \frac{1}{t_{\text{frame}}} = \frac{1}{71.9\,\text{ms}} = 13.9\,\text{Hz}. \tag{7.10}$$

This duration, excluding the image rendering time, constrains the entire process's capabilities. As a result, the latency renders the implementation of a closed-loop control system during continuous acquisition impractical.

7.1.4 Camera Exposure Time and Flash Duration

The camera operates at a frame rate of 289 fps, which sets an upper limit on the speed of the entire process. Nevertheless, the acquisition frame rate is effectively restricted to 60 fps by the refresh rate of the LCD, implying that the camera itself is not the limiting factor.

The exposure by flash light primarily determines the brightness of the captured images. To prevent motion blur, the maximum permissible flash illumination time is constrained, as outlined in Equation 3.2 in Section 3.2. Conversely, the minimum illumination time is dictated by the pulse controller and the electrical circuit. Experimental evidence indicates that the illumination time cannot be shortened beyond 1 µs due to the circuit's inherent rise and fall times.

7.2 Scanning Procedure

The image scanning procedure for the continuous scan is analogous to the stop-and-go scan (refer to Section 6.3). It comprises multiple consecutive steps, as depicted in Figure 7.6.

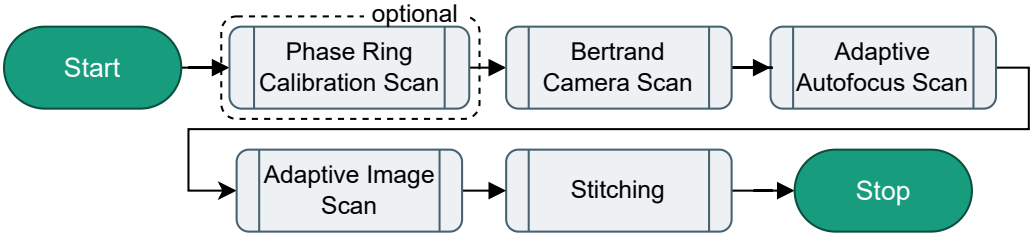

Figure 7.6: Flowchart of the entire continuous acquisition process.

The Phase Ring Calibration Scan and Stitching remain unchanged compared to the stop-and-go process. The autofocus mechanism is also largely similar but has been slightly enhanced to compensate for the meniscus effect. However, the Adaptive Stop-and-Go Scan has been supplanted by the *Bertrand Camera Scan* and *Adaptive Image Scan*.

In contrast to the stop-and-go process, the condenser annulus on the LCD must be adjusted within a fraction of a second. Due to the latency introduced by the slow reaction time of the LCD, implementing a closed-loop control is not feasible (see Section 7.1.3). Instead, an open-loop control strategy is adopted, comprising two steps: the Bertrand Camera Scan, which determines the LCD parameters at each imaging position, and the Adaptive Image Scan, which utilizes these pre-computed condenser annulus positions to acquire specimen images.

7.2.1 Bertrand Camera Scan

To determine the parameters of the condenser annulus for each image position during the Adaptive Image Scan, it is essential to capture images during the Bertrand Camera Scan (also referred to as the *Bertrand Scan*) at exactly the same locations. The objective of this scan is to evaluate the displacement of the condenser annulus due to the meniscus at each imaging position. During the scan, the LCD displays the condenser annulus with default parameters, for which it is known that the annulus is concentric with the phase ring in the absence of a meniscus. The deformation of the condenser annulus, as observed by the camera, is subsequently converted into LCD parameters for the Adaptive Image Scan through image analysis and regression outlined in Section 6.3.1.
This scan is implemented as a simplified version of the Adaptive Image Scan, maintaining the same ROI, velocity, acceleration, and other parameters. Most of the software can be shared. Figure 7.7 illustrates the procedure.

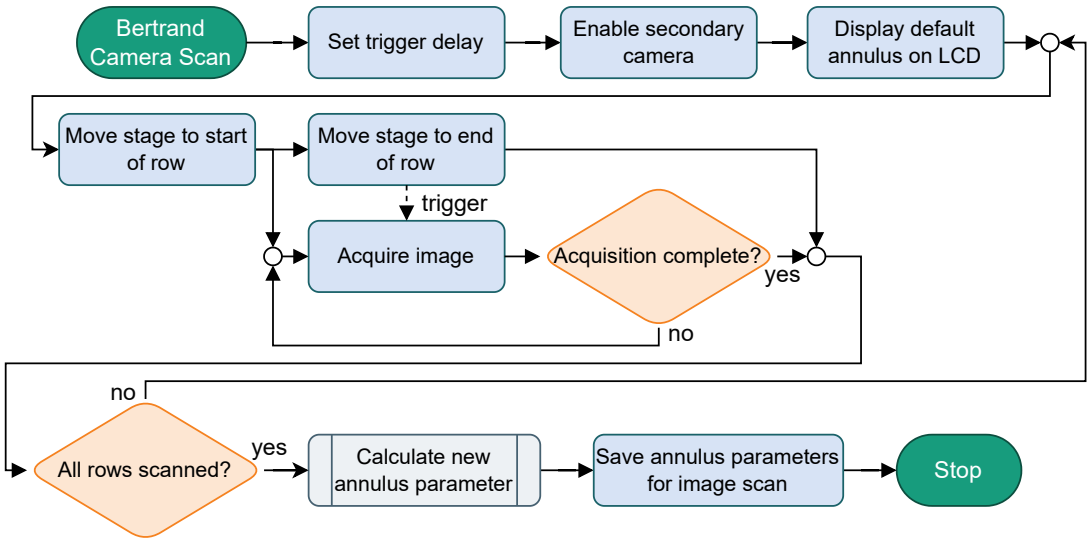

Figure 7.7: Flowchart of the Bertrand camera scan used to determine the LCD condenser annulus parameters.

Initially, the trigger delay between the LCD, camera, and light source is configured in all controllers. Subsequently, the condenser annulus on the LCD is set to its default state, and the light path is adjusted to activate the secondary camera. The ROI is segmented into parallel lines for scanning during continuous motion.
The stage first moves to the starting point of the first line and proceeds to its endpoint. This movement comprises three phases: acceleration, constant velocity, and deceleration. Images are captured only during the constant velocity phase. During this phase, trigger signals are sent at equidistant stage positions to both the camera and the light source. No trigger signals are dispatched during acceleration and deceleration phases, as synchronization necessitates a consistent delay between components. Furthermore, acceleration during image

acquisition is undesirable as it influences the liquid, distorting the meniscus shape and affecting meniscus compensation (refer to Section 7.1.2). Images are captured by the camera for each trigger signal. Once all scan lines are completed, image analysis computes the necessary adjustments to the condenser annulus for the Adaptive Image Scan and stores them in a buffer. The image analysis process utilizes multithreading to accelerate calculations.

7.2.2 Adaptive Autofocus Scan

The Adaptive Autofocus Scan operates on the same principle as the conventional Autofocus Scan discussed in Section 6.3.2, with the additional feature of meniscus compensation. The entire process is depicted in Figure 7.8.

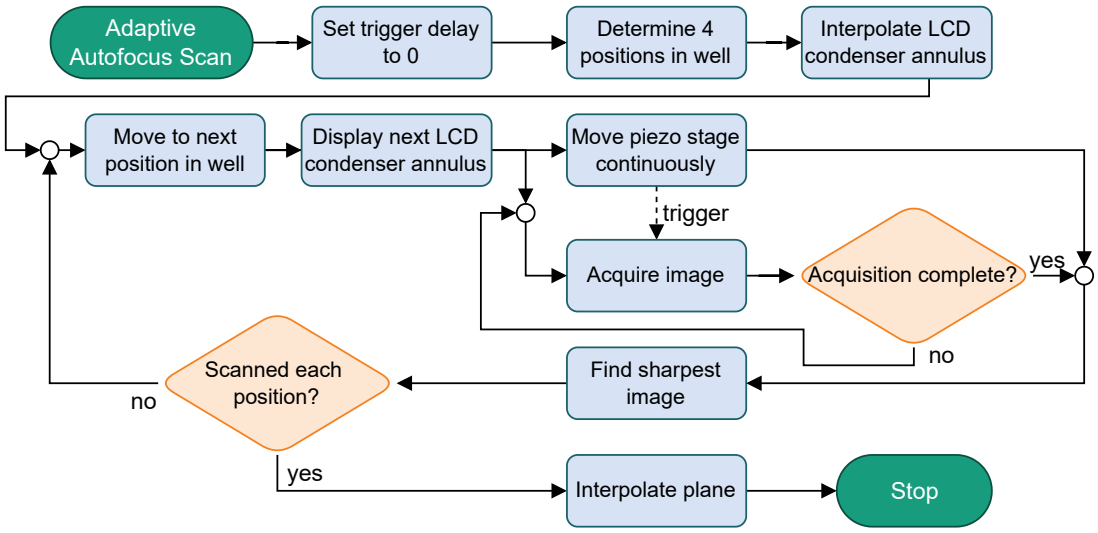

Figure 7.8: Flowchart of the Adaptive Autofocus scan, which shifts the LCD condenser annulus to obtain sharp images over a larger area of the well.

Utilizing the results from the Bertrand Scan allows for the estimation of the optimal condenser annulus position at each imaging point of the Adaptive Autofocus Scan, as opposed to relying on default parameters. This enhances the accuracy of focal height calculations, as phase contrast conditions can be achieved around the focal plane of the objective lens. Similar to the conventional Autofocus Scan, the bottom of the well is approximated as a tilted plane, determined using four support points equally distributed around the well center. However, the optimal condenser annulus positions at these four points are not directly obtained from the Bertrand Scan, as its imaging positions do not match these points. Instead, they are interpolated from the four nearest neighbors using bilinear interpolation, illustrated in Figure 7.9. After interpolation, the process proceeds similarly to the conventional Autofocus Scan. The only alteration is the adjustment of the condenser annulus position on the LCD upon moving to a new scan position.

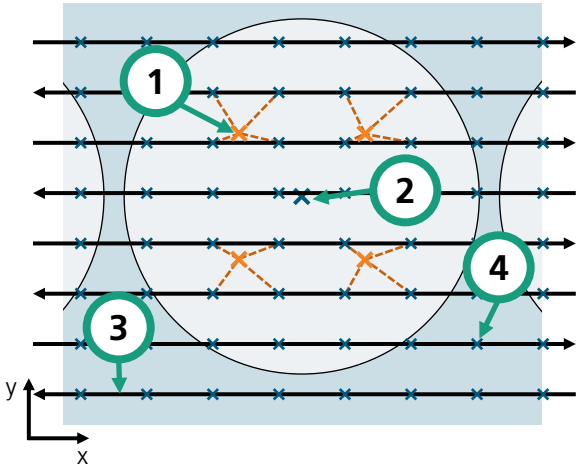

Figure 7.9: Interpolation of condenser annulus parameters for the Adaptive Autofocus Scan within a single well, with the Bertrand Scan path superimposed. The orange crosses (1) indicate the measurement points from the Adaptive Autofocus Scan, evenly spaced around the well center (2). Black arrows (3) represent the scan trajectory of the Bertrand Scan, with its corresponding imaging locations indicated by blue crosses (4). The properties of the condenser annulus are interpolated based on the values from the four nearest Bertrand imaging positions.

7.2.3 Adaptive Image Scan

The Adaptive Image Scan generates the final phase contrast images of the specimen. The scanning procedure closely resembles the Bertrand Scan, with images acquired at the same positions. This process is depicted in Figure 7.10.

The ROI is divided into the same parallel lines as in the Bertrand Scan, and images are captured continuously without pausing stage movement. Before scanning each line, the coarse z-axis of the Nikon microscope is set to an optimal value that maximizes the number of focal points within the range of the piezo actuator. The stage's motion controller synchronizes with the piezo actuator, adjusting its height in tandem with the stage's movement along the x-axis. A pre-computed batch of condenser annulus parameters is sent to the Raspberry Pi, with one condenser annulus position assigned to each scanning point. A path-synchronous trigger signal from the stage controller synchronizes the main camera, light source, and Raspberry Pi. A new condenser annulus is rendered each time a trigger signal is detected. Precise synchronization ensures that the condenser annulus is displayed milliseconds before the camera begins exposure, and the light source flashes slightly later, with a delay of less than a millisecond. The camera's exposure time is minimized to reduce noise from stray light, yet it must be long enough to encompass the light source flash.
Once images are transferred from the camera to the main computer's RAM, histogram adjustment and shading correction are applied, similar to the Adaptive Stop-and-Go Scan (see Section 6.3.2). Upon receiving the expected number of images after one scan line, the next line is processed. The procedure concludes when all lines are completed.

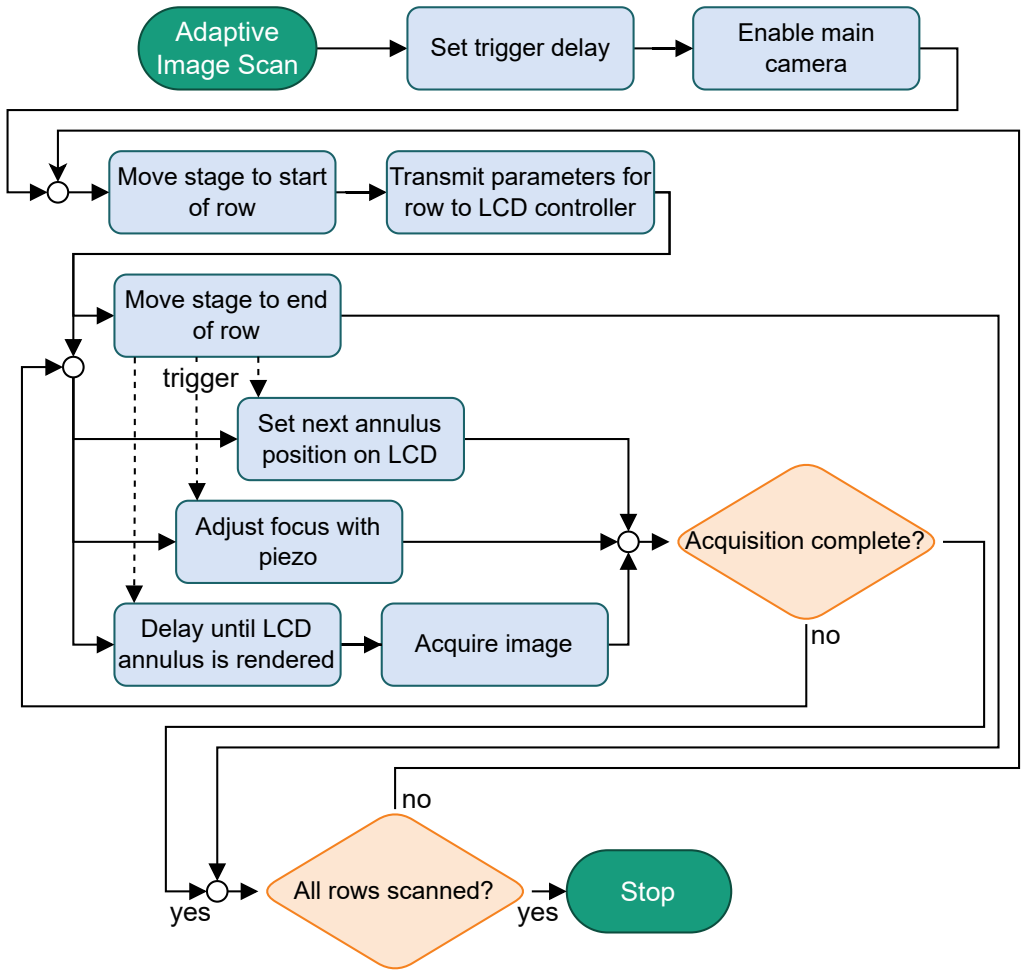

Figure 7.10: Flowchart of the Adaptive Image Scan, illustrating continuous image acquisition with meniscus compensation.

7.3 Software Implementation

Multiple software programs are necessary to orchestrate the entire process due to the variety of controllers and diverse scanning procedures involved. A primary software program acts as the master to coordinate these programs. It is described in Section 7.3.1. The interrelationship between different hardware components and software is detailed in Section 7.3.2. Given the importance of the LCD controller, its software implementation is discussed in greater detail in Section 7.3.3.

7.3.1 Master Software

The master software, named *HSM-Library*, operates on a Windows PC. Developed in C++, the HSM-Library manages the scanning process and communicates with all connected devices. It is used for the high-speed scan as well as the stop-and-go scan. A configuration file specifies essential parameters, such as scanning speed, ROI dimensions, and IP addresses of peripheral devices. Multiple scans can be executed sequentially.

After initializing all devices and calculating all imaging positions within an ROI, the HSM-Library commands the microscope to adjust the coarse z-axis, selects the appropriate objective lens, and configures the light path for the designated camera. The Bertrand Scan and Adaptive Image Scan partition the ROI into several segments composed of parallel rows, with each row considered as a cohesive unit. Images captured by a camera during a single row are treated as one batch.
Before scanning a row, a batch of condenser annulus positions for the upcoming line is sent to the Raspberry Pi, which stores them until a trigger signal is received. At the start of a row, the HSM-Library instructs the stage controller to move to its final position. The stage controller dispatches trigger signals to other components at predetermined intervals, indicating when images should be captured. The HSM-Library processes incoming images in a parallel thread while the main thread waits for the stage controller to complete its movement. Once all images are received, the row is marked as complete, and the process advances to the next row.

7.3.2 Communication Between Components

The Windows PC hosts the primary application and interfaces with all peripheral devices via Ethernet or USB connections. Among these devices, the Raspberry Pi and Arduino are each programmed to execute specific applications, facilitating inter-device communication. These programs configure the remaining non-programmable controllers. Figure 7.11 illustrates the communication between the relevant devices.

In addition to the programmable computers, the stage controller plays a critical role by sending path-synchronous trigger signals and managing the height of the piezo z-stage. The piezo is connected to the stage controller via an analog signal. This configuration allows the stage controller to treat the piezo as one of its own axes, synchronizing the z-position of the specimen with the x and y positions, thereby enhancing the dynamics of the actuation system.
As identified in Section 7.1.3, the LCD exhibits significant latency, approximately 57 ms. This latency implies that if the trigger signals for the camera, light source, and LCD were sent simultaneously, the image would be captured long before the condenser annulus is rendered. To mitigate this latency, an Arduino Uno controller delays the trigger signals for the camera and light source, as detailed in Section 7.3.4.

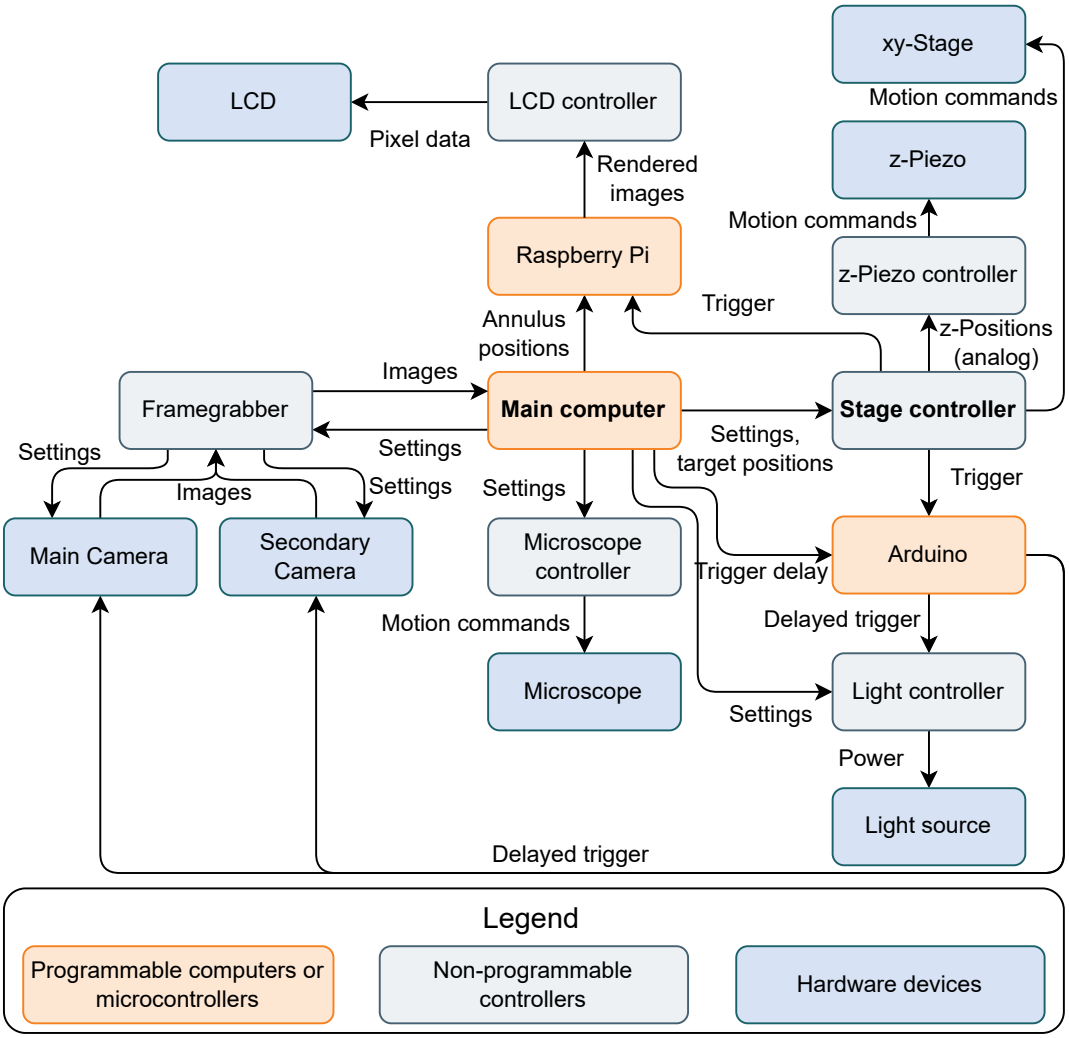

Figure 7.11: Connections between relevant hardware components.

7.3.3 Software Implementation of the LCD

The Raspberry Pi, running the Linux Raspbian operating system and controlling the LCD, operates a state machine programmed in Python. Time-critical functions are implemented using external libraries such as *OpenGL* and *Numpy* to ensure efficient program execution. Upon startup of the main program, the Raspberry Pi immediately connects to the Windows PC via Ethernet. A state machine is then operated, transitioning between states based on incoming signals from the Windows PC.

State machine

In the default (idle) state, the state machine executes an infinite loop, awaiting instructions from the Windows PC via Ethernet. The first byte of an incoming instruction determines the next state transition. In addition to the idle state, the following states are defined:

- Modify annulus dimensions,
- Adjust magnification,
- Receive and store array,
- Static mode,
- Trigger mode.

Modify annulus dimensions: The Raspberry Pi receives custom inner and outer condenser annulus diameters in millimeters from the Windows PC. These values are stored until new instructions are received, but the condenser annulus dimensions are only updated upon receiving the next display command (*Static mode* or *Trigger mode*). This mode can be used to set custom condenser annulus dimensions, for example, for the LCD reaction time experiments described in Section 7.1.3.

Adjust magnification: In this mode, the inner and outer diameters of the condenser annulus are modified to match predefined magnification values. Aside from magnifications of 4 and 10, a setting of 0 emulates brightfield conditions, featuring an inner radius of 0 and an outer radius surpassing the microscope's aperture.

Receive and store array: The HSM-Library transmits an array comprising pairs of x and y values, representing the condenser annulus's distance from the LCD's center in millimeters. Up to 500 values can be stored internally and displayed in sequence. They are completely overwritten upon receipt of a new array.

Static mode: This mode instantly displays the initial position of the condenser annulus array. It is employed to display the default condenser annulus during the Bertrand Camera Scan, as well as to display static positions during the Adaptive Stop-and-Go Scan.

Trigger mode: This mode is designed for time-critical synchronization during the Adaptive Image Scan. It is used to display one batch of condenser annulus positions during one row of the scan. This is done by iterating over trigger signals until the number of triggers equals the length of the position array, indicating one scan row is complete.
The principle of double buffering is used for efficient rendering (see Section 2.3.4). At the outset of each iteration, the next condenser annulus is fully rendered and saved to the frame buffer, but not displayed. Upon detecting a trigger, an interrupt is generated, which causes the Raspberry Pi to swap the buffer, sending the pre-rendered image of the condenser annulus to the LCD. The LCD displays this image upon refresh, which occurs at a constant rate every 16.7 ms (refer to Section 7.1.3). The subsequent condenser annulus is rendered (but not displayed) immediately afterward to prevent delays before the buffer swap.

Condenser Annulus Rendering

Efficient rendering of the condenser annulus is essential to prevent delays when a trigger is received. The *OpenGL* library is employed to approximate the annulus within a window on the LCD. This is achieved by constructing the annulus as a composition of white triangles on a black canvas. It was determined that using 100 triangles provides ring images free from significant discretization artifacts while ensuring a reasonable computation time.

The LCD has a native resolution of 1620×2560 monochrome pixels. However, due to a misinterpretation in the communication protocol, the Raspberry Pi incorrectly assumes that the LCD has a resolution of 540×2560 colored pixels. This misunderstanding treats each actual pixel as one of three sub-pixels, causing the display to be distorted by a factor of three in the x-direction.
Since this distortion cannot be corrected through adjustments in the screen configuration, the rendering software is designed to compensate for it. To address this issue, the condenser annulus is rendered as an ellipse, which appears as a proper ring after accounting for the display distortion. However, this compensation reduces the x-direction resolution by one-third, leading to pixelated annulus outlines, as shown in Figure 7.12a.
To mitigate this limitation, the three ellipses drawn on each color channel vary slightly, each shifted by 1/3 of a pixel in the x-direction. The outcome, as viewed on a true RGB screen, exhibits different colors on the ring's edges, as depicted in Figure 7.12b. On a monochrome black-and-white screen, however, the result is a smooth and continuous ring, as illustrated in Figure 7.12c. The entire rendering process is completed within 2 ms, which is significantly faster than the LCD's refresh time of 16.7 ms.

(a) No sub-pixel shift. **(b)** Sub-pixel shift on RGB display. **(c)** Sub-pixel shift on monochrome display.

Figure 7.12: Rendering of a condenser annulus is presented both without and with sub-pixel level consideration. The images differ in scale and resolution. (a) Schematic representation of distortion occurring in the x-direction when an ellipse is rendered on a monochrome LCD. (b) A condenser annulus with sub-pixel correction as viewed on an RGB monitor, where different colors manifest along the edges. The red component of the ring is displaced leftward, whereas the blue component is displaced rightward. Mixed colors emerge when multiple colored sub-pixels are active simultaneously. (c) A condenser annulus with sub-pixel correction displayed on a monochrome LCD and observed through a Bertrand lens.

7.3.4 Trigger Delay to Compensate the LCD Latency

As previously detailed in Sections 7.1.3 and 7.3.2, it is essential to compensate for the LCD latency to ensure that the condenser annulus rendering is finalized before the camera captures the image. The used strategy involves advancing trigger signals by an interval equivalent to the LCD latency. To synchronize the condenser annulus rendering with image acquisition, the camera and light source receive their trigger signals at later times. The light source is activated slightly after the camera, ensuring that illumination overlaps with the camera sensor's exposure period. With this method, the system's frame rate is solely constrained by the LCD refresh rate of 60 Hz. The operational principle is depicted in Figure 7.13.

Although the stage controller features two trigger outputs capable of introducing delays between them, these delays cannot be programmed as required for this application. The necessary delay of 57 ms requires multiple trigger signals to be sent to the Raspberry Pi before the first trigger reaches the camera and light source, which the current stage controller model cannot accommodate. Instead, an Arduino Uno microcontroller is incorporated into the trigger signal's electrical path, acting as a buffer. Operating at a clock speed of 16 MHz, the microcontroller is programmed to ensure that additional delays and jitter from program execution remain well below 1 ms, as confirmed by experimental validation [Ard25].

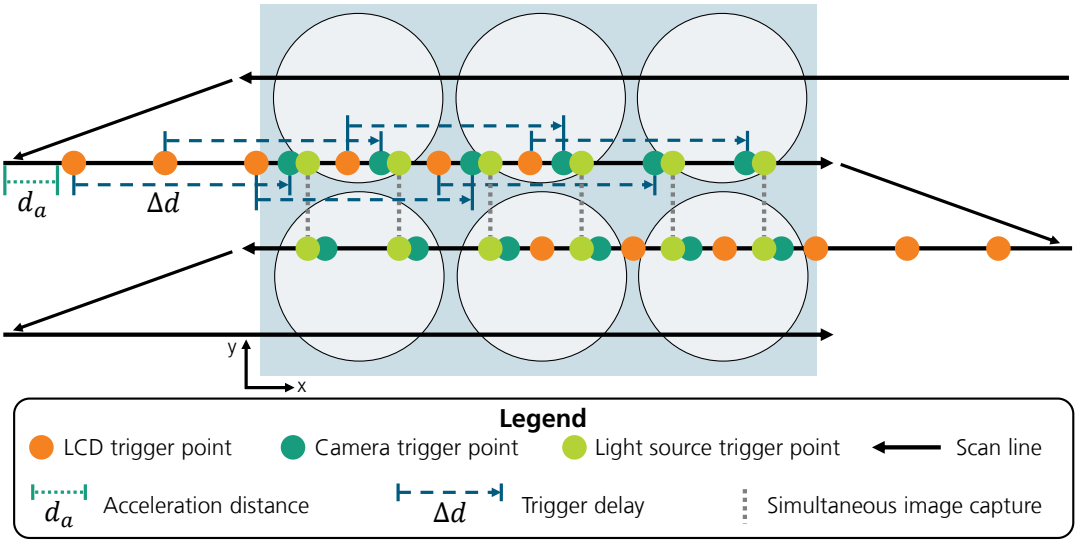

Figure 7.13: Schematic drawing of the acquisition process utilizing the trigger delay. The trigger delay guarantees synchronization between image acquisition and LCD rendering. Regardless of the microscope stage's directional movements, the x-position of images must remain consistently aligned.

The significant trigger delay results in considerable movement of the microscope stage between the emission of the trigger signal and image acquisition. Thus, the path-synchronous trigger signal is sent at an earlier position, advancing the start of the scan line by a distance Δd, as noted in Equation 7.11:

$$\Delta d = v\Delta t, \tag{7.11}$$

where Δt represents the trigger delay and v the stage velocity. Due to the meandering motion, acquiring adjacent images in the y-direction (perpendicular to the scan direction) at consistent x-positions involved precise synchronization. However, the trigger position varies with the motion direction, necessitating a constant stage velocity during the trigger delay phase to achieve images at a consistent x-position.

The Arduino Uno setup includes an input connection from the stage controller to an interrupt pin, and two digital pins for output connections – one for the light source and one shared between both cameras. In the Arduino code, the precise timing for upcoming outgoing trigger signals is recorded in microseconds. Upon detecting an incoming trigger via an interrupt, the outgoing trigger signal's timing is computed. The code continuously compares the current time with the next outgoing trigger time. Once the time aligns, a trigger signal is generated by setting the first output pin to 5 V and reverting it to 0 V 500 µs later, managed by a timer. The same procedure applies to the second output pin after a specified delay.

The trigger delay can be adjusted via the HSM-Library through a USB connection and a custom communication protocol. A trigger delay of 0 ms is necessary for the Adaptive Autofocus Scan, whereas both the Bertrand Scan and Adaptive Image Scan require a delay of

57 ms to ensure identical image indexing positions, allowing images with the same indices to be captured at the same position. An incorrect trigger delay may cause premature or delayed LCD rendering, leading to phase contrast shifts and non-uniform phase contrast within individual images. The meandering scanning motion results in a comb-like pattern if the delay is not configured correctly, as shown in Figure 7.14.

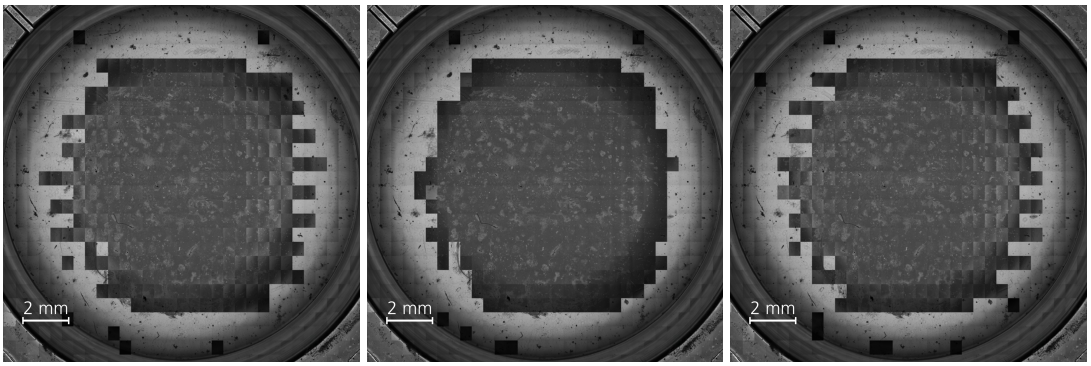

(a) 0 ms **(b)** 57 ms **(c)** 120 ms

Figure 7.14: Composite image of a whole MTP24 well with three different trigger delays of 0 ms, 57 ms, and 120 ms. A too-short or too-high trigger delay causes a comb-like pattern due to the condenser annulus shift appearing too early or too late. A trigger delay of 57 ms proves to be ideal.

7.4 Validation Through Experiments to Determine Phase Contrast Area and Acquisition Time

This section presents an experimental validation of the adaptive high-speed process. Acquisition times under various conditions are documented and compared with reference measurements. Additionally, the impact on the phase contrast area during continuous image acquisition is analyzed. These results are compared with those from the validation of stop-and-go scans (see Chapter 6.4.2) and HSM using standard phase contrast microscopy.

Initially, the experimental design is detailed in Section 7.4.1. Subsequently, Section 7.4.2 identifies the optimal velocities and accelerations for the experiments. The influence of the high-speed approach on the phase contrast area is discussed in Section 7.4.3. Finally, Section 7.4.4 outlines the achievable acquisition times.

7.4.1 Experimental Design

The same demonstrator described in Section 6.2 for stop-and-go scans was employed for high-speed scans. Scans followed the procedure outlined in Section 7.2, with software detailed in Section 7.3. The same MTPs with MSCs from the stop-and-go scans served as

specimens, generating data for a 6-well MTP at 4x magnification, a 24-well MTP at 4x and 10x magnification, and a 96-well MTP at 10x magnification. The MTPs were filled with cell medium so that the specimens were covered by only 1 mm of liquid to reduce sloshing.

Since the scanning time scales linearly with the number of rows, only one row of wells was captured per MTP to reduce experiment duration. The total time for the MTP was computed by multiplying the time for one row by the number of rows (e.g., for MTP24, one row of 6 wells was scanned, and the total time was determined by multiplying by 4). When scanning an entire MTP, multiple wells aligned with the scan direction were captured within the same scan lines, resulting in shorter acquisition times per well compared to scanning individual wells. A pre-study demonstrated that the phase contrast area remains unaffected by the number of wells acquired simultaneously, as shown in Table A.7 and Figure A.9 in the Appendices.

To evaluate the impact of the frame rate on the phase contrast area, experiments were conducted using two different frame rates per configuration of MTP and magnification. 30 fps and 60 fps were chosen whenever possible. However, these frame rates were not achievable for all experimental conditions, as the required acceleration distance could exceed the microscope stage's available range (see Sections 7.1.1 and 7.1.2). Consequently, individual wells of MTP6 were captured at 15 fps and 30 fps (only the two central wells were available at 30 fps), while entire rows were captured at 15 fps. Entire rows of MTP24 with 4x magnification could only be acquired at 30 fps.

Measurement times were determined using a log file automatically generated by the HSM-Library, which recorded the start and end times of individual processes. The experimental results are subsequently divided between the phase contrast area in Section 7.4.3 and the acquisition time in Section 7.4.4. The results of the phase contrast area and scanning times are based on experiments with 12 wells for 6-well MTPs at 4x magnification, 18 wells for 24-well MTPs at 4x magnification, 18 wells for 24-well MTPs at 10x magnification, and 30 wells for 96-well MTPs at 10 magnification.

The parameters used in the experiments are presented in Table 7.1. Certain parameters, such as pixel pitch and NA, were hardware-defined. The camera's exposure time was minimized to decrease stray light and improve the signal-to-noise ratio, while the flash duration t_{flash} was calculated using Equation 3.2 from Section 3.2. Accelerations and velocities depended on the MTP type and the number of wells scanned, and will be explored in the following section.

Table 7.1: Parameters for image scans conducted at 60 fps with 4x magnification and at 15 fps with 10x magnification are presented, representing the scans with the fastest and slowest stage movements, as well as the shortest and longest flash durations, respectively.

Property	Symbol	60fps @ 4x	15fps @ 10x	Unit
Illumination wavelength	λ	520		nm
Pixel pitch	Π	2.5		µm
Pixel number in motion direction	n_{Pixel}	2160		-
Safety factor for flash duration	k	2		-
Overlap	o	5		%
Camera exposure time	t_{exp}	1		ms
LED voltage	U_{LED}	35.0		V
Magnification	M	4	10	-
Numerical aperture	NA	0.13	0.3	-
Frame rate	f	60	15	1/s
Resolution limit	d	2.00	0.88	µm
Stage velocity	v	76.95	7.70	mm/s
Flash duration	t_{flash}	13.00	57.14	µs

7.4.2 Optimal Velocity and Acceleration

This section aims to identify the optimal velocities and accelerations for various experimental configurations. As established in Section 7.1.1, the ideal velocity is contingent upon both acceleration and scanning distance, as expressed in Equation 7.5. Acceleration is limited by the liquid sloshing effect detailed in Section 7.1.2. Thus, this section presents experiments designed to ascertain the maximum viable acceleration across all setups without inducing sloshing. Based on these acceleration values, the optimal velocity is calculated.
The experiments build upon those in Section 7.1.2, but with different MTP types. Figure 7.15 illustrates the results for a 6-well MTP with 4x magnification at varying accelerations.

The experiment with an acceleration of 40 mm/s^2 reveals minor asymmetry, rendering it unsuitable for adaptive high-speed phase contrast microscopy. An acceleration of 30 mm/s^2 was deemed appropriate for this configuration, notably lower than the microscope stage's maximum acceleration of 500 mm/s^2.
Higher-order MTPs were only affected by higher accelerations, yet the limit due to sloshing was still lower than the maximum acceleration of the stage.

Different scan lengths yield varying results. In scenarios where a single well is scanned, the scan length decreases, yet the potential acceleration distance increases, impacting the optimal velocity. Optimal frame rates are computed from velocities using Equation 3.3. Table 7.2 displays all velocities and accelerations. Owing to the stage's limited range, frame rates and velocities often require capping due to restricted acceleration distances. These capped values are included in the table, providing upper limits for accelerations, velocities, and frame rates for the following experiments.

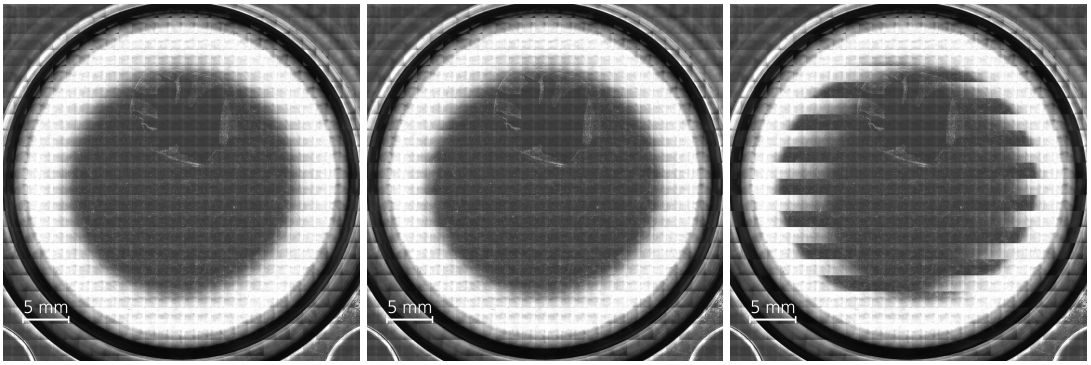

(a) a = 10 mm/s^2. **(b)** a = 40 mm/s^2. **(c)** a = 320 mm/s^2.

Figure 7.15: Images of a whole MTP6-well, acquired with continuous scanning and different accelerations.

Table 7.2: Maximum accelerations, velocities, and frame rates for continuous scanning in various MTPs. The optimum velocity and corresponding frame rate differ for scans that only acquire individual wells compared to whole rows, according to Equation 7.5. Due to the limited range of the microscope stage, the maximum velocity must often be capped for the acceleration distance not to exceed the available space.

MTP and magnification	MTP6 4x		MTP24 4x		MTP24 10x		MTP96 10x	
Scan length	**Well**	**Row**	**Well**	**Row**	**Well**	**Row**	**Well**	**Row**
Acceleration [mm/s^2]	30	30	200	200	200	200	200	200
Ideal Velocity [mm/s]	23	41	39	106	40	106	26	103
Ideal Frame Rate [fps]	18	32	30	83	78	207	51	201
Capped Velocity [mm/s]	23	21	39	54	40	55	26	67
Capped Frame Rate [fps]	18	16	30	42	78	108	51	131

7.4.3 Phase Contrast Area Results

This section explores the impact of the high-speed scanning mode on the phase contrast area by analyzing experimental results. Phase contrast areas were compared under various conditions. Initially, a comparison was made between different acquisition speeds. This analysis was followed by a comparison between the high-speed adaptive phase contrast microscopy process, the adaptive non-continuous acquisition process, and high-speed regular phase contrast microscopy. Due to inhomogeneity in phase contrast conditions within MTP96 at 10x magnification, as described in Section 6.4.3, a quantitative analysis was not conducted for this configuration.

Acquisition Speed

Experiments were conducted to evaluate the influence of varying frame rates on the phase contrast area. Example images of MTP24 at 4x and 10x magnifications are shown in Figure 7.16, while results are summarized in Table 7.3.

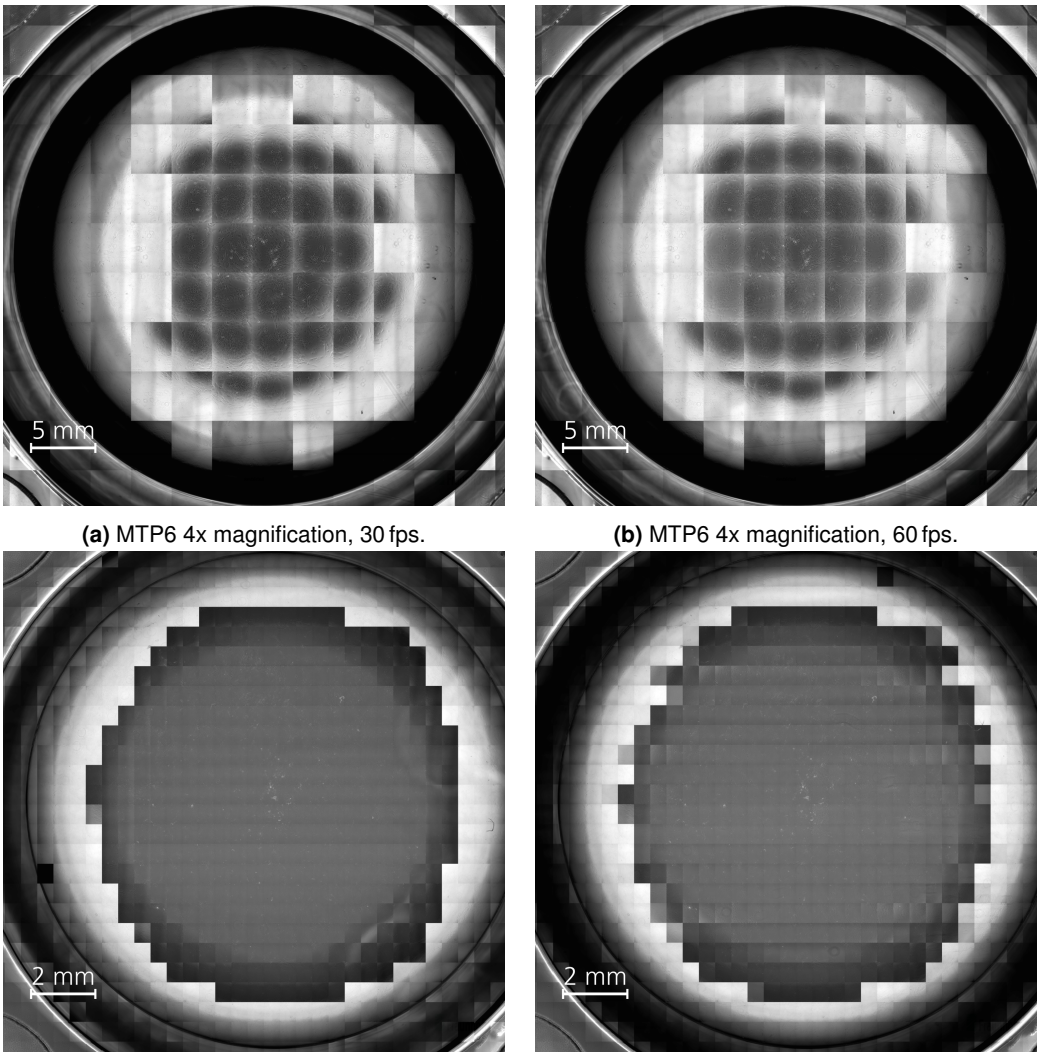

(a) MTP6 4x magnification, 30 fps.

(b) MTP6 4x magnification, 60 fps.

(c) MTP24 10x magnification, 30 fps.

(d) MTP24 10x magnification, 60 fps.

Figure 7.16: Comparison between composite images captured at varying acquisition rates, corresponding to different stage velocities.

Table 7.3: Comparison of phase contrast areas between high and low frame rates. Frame rates differ between the well sizes and magnifications because of the available acceleration distance. Abbreviations: *Fr*: Frame rate, *Image Par*: Imaging parameters, *M*: magnification, *Std*: standard deviation in percentage points.

Image Parameters		Low frame rate			High frame rate		
MTP	M	Fr [fps]	Mean [%]	Std [%]	Fr [fps]	Mean [%]	Std [%]
6	4	15	53.9	1.8	30	54.3	1.4
24	4	30	21.3	2.0	60	19.1	2.8
24	10	30	43.7	0.9	60	44.9	1.5

Overall, the findings indicate no significant difference in mean phase contrast areas across different frame rates. For MTP24 with 4x magnification, the images display no discernible difference between 15 fps and 30 fps, corroborating the numerical data. Images of MTP24 at 10x magnification show consistent central well areas but minor variations between 30 fps and 60 fps. While the edge is distinctly defined at 30 fps, small outliers are observed at 60 fps. Some images near the well edge show a gray value gradient. Yet, these gradients are small enough to allow these images to be classified as phase contrast regions. The images remain sharp, and the phase contrast area evaluation algorithm is unaffected by these variations. Therefore, differences between 30 fps and 60 fps are considered negligible. It can be inferred that employing the maximum frame rate for each setup does not compromise the phase contrast area. The phase contrast area remains consistent even at the maximum achievable frame rates.

Comparison with Stop-and-Go Approach and Conventional Phase Contrast Microscopy

This section compares the phase contrast area achieved with adaptive high-speed phase contrast microscopy with the adaptive stop-and-go approach. Conventional phase contrast microscopy serves as a reference. Theoretically, the stop-and-go method should maximize the phase contrast area, assuming high acquisition speeds negatively affect it. If no significant difference is detected, it implies that acquisition speed does not impact the phase contrast area. These findings are detailed in Table 7.4.

Across all configurations of MTPs and magnifications, the phase contrast area is comparable between the high-speed and stop-and-go methods. The phase contrast area ratios between the high-speed and stop-and-go approaches range from 0.9 for MTP6 at 4x magnification to 1.1 for MTP24 at 10x magnification. All methods exhibit minor standard deviations, indicating high reproducibility across measurements. However, some minor discrepancies are observed. It remains uncertain whether these variations arise from the acquisition method or the image analysis algorithm, or are merely random fluctuations.

Table 7.4: Comparison of the average phase contrast area among adaptive high-speed phase contrast microscopy (1), adaptive stop-and-go phase contrast microscopy (2), and conventional high-speed phase contrast microscopy (3). Abbreviations: *Image Par*: Imaging parameters, *Adap HS*: adaptive high-speed phase contrast microscopy, *Adap SG*: adaptive stop-and-go phase contrast microscopy, *Reg*: regular high-speed phase contrast microscopy, *M*: magnification, *Mn*: mean value in percent, *Std*: standard deviation in percentage points.

Image Par		(1) Adap HS		(2) Adap SG		(3) Reg		Ratio	
MTP	M	Mn [%]	Std [%]	Mn [%]	Std [%]	Mn [%]	Std [%]	(1)/(2)	(1)/(3)
6	4	53.9	1.7	53.1	1.2	30.5	1.8	1.0	1.8
24	4	20.9	2.2	23.8	1.6	2.3	0.1	0.9	9.0
24	10	44.3	1.3	41.6	1.8	6.1	0.2	1.1	7.2

Hypothesis Tests Hypothesis tests were performed to assess the statistical significance of these differences. The tests included t-tests for two independent samples, with the null hypothesis H_0 asserting no difference in mean phase contrast area, and the alternative hypothesis H_1 proposing a difference. A significance level α of 5% was chosen. Table 7.5 shows the hypothesis test results.

Table 7.5: Results of the hypothesis test (t-test) for two independent samples to determine if the mean phase contrast area differs between the high-speed approach and the stop-and-go approach in adaptive phase contrast microscopy. Δ: difference in mean phase contrast area, *M*: magnification, *95% Lower*: lower limit for the difference with 95% probability, *95% Upper*: upper limit greater than the difference in 95% of all cases, *t-values*: t-values of the hypothesis test, *p-value*: significance level.

MTP	M	Δ [%]	95% Lower [%]	95% Upper [%]	t-value	p-value
6	4	0.9	-1.5	3.2	1.01	0.370
24	4	-2.9	-6.3	0.5	-2.71	0.073
24	10	2.7	-1.9	7.3	2.54	0.126

The p-value exceeds α for all configurations, often by a considerable margin, necessitating the retention of the H_0 hypothesis. Thus, a reduced phase contrast area with the high-speed scanning approach compared to the stop-and-go method cannot be concluded with statistical significance. Conversely, these results of both methods significantly surpass those obtained with conventional phase contrast microscopy. The results are visually compared using example images of MTP6 at 4x magnification in Figure 7.17. Both adaptive phase contrast microscopy images show minimal differences from each other but exhibit a substantial increase in phase contrast area compared to the conventional approach.

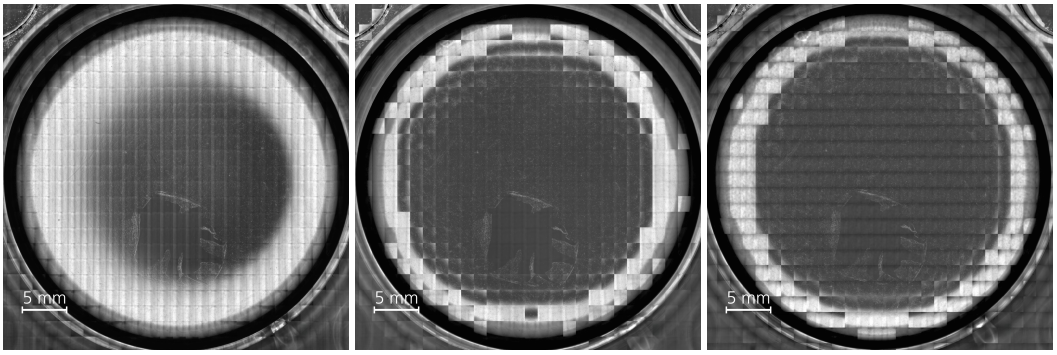

(a) Conventional high-speed scan. **(b)** Adaptive stop-and-go scan. **(c)** Adaptive high-speed scan.

Figure 7.17: Comparison between composite images of the same specimens in a 6-well MTP acquired at 4x magnification. (a) illustrates the outcome using conventional HSM at 15 fps. (b) depicts the result obtained through the adaptive stop-and-go approach. (c) presents the result using the adaptive high-speed approach, also at 15 fps.

Detailed Views To validate that image quality does not degrade with the adaptive high-speed phase contrast microscopy compared to conventional phase contrast microscopy and the adaptive stop-and-go method, detailed analyses of composite images were conducted. Figure 7.18 presents the results from a 24-well MTP acquired with 10x magnification, including a detailed view of the specimen.

These detailed views extend beyond the phase contrast area of the conventional method but fall well within the phase contrast area of the adaptive phase contrast microscopy. The detailed views reveal that images captured using conventional phase contrast microscopy, particularly away from the center, exhibit low contrast and a bright background, whereas those acquired through adaptive phase contrast methods show sharp phase contrast on a dark background. Both adaptive images are suitable for experts or image analysis algorithms to detect cell structures and derive biological insights, indicating that the acquisition processes have successfully met their objectives of providing large-area phase contrast images that reveal small details throughout the well. This is further emphasized by the depiction of the phase contrast areas for these images, shown in Figure A.11 in the Appendices. All phase contrast areas are nearly circular, indicating a functioning compensation mechanism; a circular shape is expected for an ideal acquisition process due to the rotational symmetry of the wells.

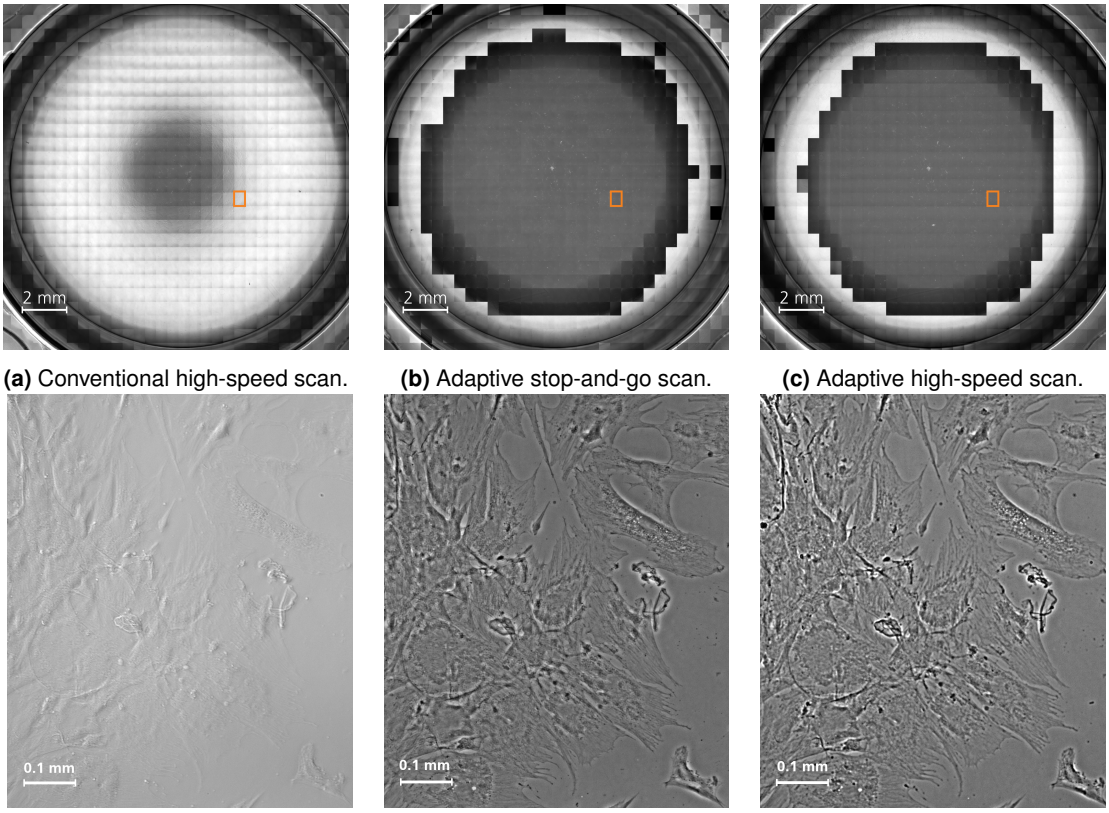

(a) Conventional high-speed scan.

(b) Adaptive stop-and-go scan.

(c) Adaptive high-speed scan.

(d) Detail view: conventional high-speed scan.

(e) Detail view: adaptive stop-and-go scan.

(f) Detail view: adaptive high-speed scan.

Figure 7.18: Comparison between composite images (a, b, and c) of the same specimen in a 24-well MTP acquired at 10x magnification using various imaging techniques. The zoomed-in views (d, e, and f) display high-resolution details of the specimen. (a) employs conventional phase contrast microscopy in high-speed mode at 108 fps. (b) utilizes the adaptive non-continuous phase contrast microscopy scan. (c) applies the adaptive high-speed acquisition process at 30 fps. Orange boxes indicate the locations of the detailed views.

Overlap Between Condenser Annulus and Phase Ring Another perspective on the compensation success is provided in Figure 7.19, which illustrates the overlap of the condenser annulus with the phase ring throughout a well. This figure shows that, further from the center, the condenser annuli are more displaced from the phase ring with the conventional approach. However, with the adaptive approach, the annuli remain concentric until a sharp cutoff occurs.

In conclusion, the phase contrast area is not adversely affected by high-speed imaging. Although the exact values may vary based on well size, magnification, and potentially the analysis algorithm, the phase contrast area does not significantly differ between the high-speed scanning approach and the stop-and-go scanning method. The small deviations between measurements suggest a high reproducibility of the meniscus compensation mechanism.

Both methods yield sharp phase contrast images that extend much closer to the well edge than the conventional procedure.

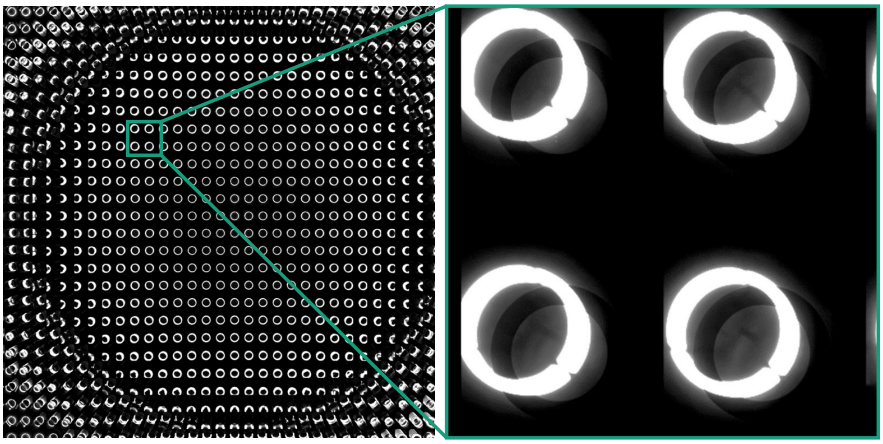

(a) Regular phase contrast microscopy.

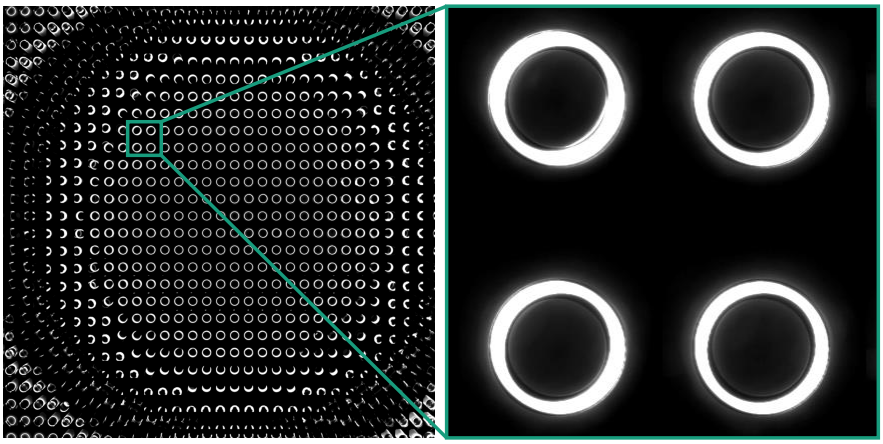

(b) Adaptive phase contrast microscopy.

Figure 7.19: Composite image of condenser annulus and phase ring overlap within an entire 24-well at 10x magnification. A portion of the well is highlighted to demonstrate that phase contrast conditions cannot be achieved in (a) but are established in (b).

7.4.4 Acquisition Time Results

This section investigates the acquisition times achieved during the experiments. The analysis of acquisition times is divided into two parts. Initially, the proportion of various process steps in relation to the total imaging time is evaluated (refer to Section 7.2 for details on the process steps). The exclusive steps of the adaptive high-speed process, namely the Bertrand Camera Scan and Adaptive Image Scan, are quantified. Subsequently, the adaptive high-speed phase contrast microscopy process is evaluated against the adaptive

stop-and-go scan and the conventional high-speed scan to derive conclusions on the technology.

Proportion of Actual Image Acquisition Compared to Total Time

Within the multiple stages of the adaptive high-speed process, only the Bertrand Camera Scan and Adaptive Image Scan are unique to this process. Thus, the combined duration of the Bertrand Camera Scan and Adaptive Image Scan was the optimization goal of this thesis, whereas other scans are influenced by factors beyond the thesis's scope, such as computer hardware. Consequently, the proportion of these scans to the total acquisition time needed to be determined. Table 7.6 details the share of different scan steps across various configurations, defined by well size and magnification.

Table 7.6: Distribution of the total acquisition time for an entire MTP with the adaptive high-speed process among various scan steps for different configurations of MTPs and magnifications. All times are in minutes. Abbreviations: *M*: magnification, *f*: frame rate, *Num im*: number of images, *Pha Cali*: phase ring calibration, *Bertrand*: Bertrand Scan, *Autofoc*: Autofocus Scan, *Image*: Adaptive Image Scan, *Stitch*: Stitching.

MTP	M	f	Num im	Pha Cali	Bertrand	Autofoc	Image	Stitch	Total
6	4	15	4224	0:05	7:12	2:49	7:07	1:21	18:34
24	4	30	4128	0:04	3:44	10:44	3:36	0:44	18:52
24	10	60	22176	0:04	10:28	10:48	11:48	4:40	37:48
96	10	60	18720	0:06	9:04	43:04	8:48	2:00	63:02

Total scan time is predominantly influenced by magnification, with 10x magnification being markedly slower than 4x due to the increased number of lines requiring scanning. Throughout the acquisition process, the time demanded by the Phase Ring Calibration Scan is negligible. The durations of the Bertrand Scan and Adaptive Image Scan are nearly identical, as both algorithms capture the same number of images at identical positions and speeds, with variations arising solely from image processing. The share of the combined Bertrand Camera Scan and Adaptive Image Scan to total scanning time is summarized in Table 7.7.

Table 7.7: Proportion of the acquisition time attributed to the Bertrand Scan and Adaptive Image Scan relative to the total imaging time. All times are in minutes. Abbreviations: *M*: magnification, *f*: frame rate, *B+I*: sum of Bertrand Scan and Adaptive Image Scan.

MTP	M	f	B+I	Total	Share [%]
6	4	15	14:19	18:34	77.1
24	4	30	07:20	18:52	38.9
24	10	60	22:16	37:48	58.9
96	10	60	17:52	63:02	28.3

The autofocus time is considerable, especially for 96-well MTPs. This is caused by the Autofocus Scan requiring the same duration for each well, leading to total time scaling linearly with the number of wells, whereas Adaptive Image Scan time is primarily influenced by the number of scan lines, maximum velocity, and acceleration. Thus, the Autofocus Scan becomes predominant when scanning 96-well MTPs but has a minor impact on 6-well MTPs. The Stitching time scales non-linearly with the number of images per well, taking longer for fewer large wells than for numerous small wells. This time also incorporates saving images to the solid-state drive of the computer, which can account for a significant share of the stitching time, considering the largest composite images exceed 1 GB in file size, such as for MTP6 with 4x magnification and MTP24 with 10x magnification. Although stitching contributes between 3.1% of the total acquisition time for MTP96 with 10x magnification and 12.3% for MTP24 with 10x magnification, it is not the primary determinant of overall time. However, if necessary, time could be reduced with more efficient algorithms or enhanced computer hardware.

In summary, the total scanning time is significantly influenced by the supporting scans, particularly the Autofocus Scan. Optimizing these scans was not the focus of this thesis. Thus, for a more accurate comparison with the adaptive stop-and-go process and the conventional high-speed scan, only the times for the Bertrand Camera Scan and Adaptive Image Scan are evaluated against other scanning methods.

Comparison with Stop-and-Go Approach and Conventional High-Speed Phase Contrast Microscopy

The acquisition time of the adaptive high-speed process is compared with both the adaptive stop-and-go process and the conventional high-speed process. As certain steps, such as stitching, remain largely consistent across methods, the analysis focuses on the defining process steps for a more insightful technological evaluation:

- Adaptive high-speed process: Bertrand Camera Scan and Adaptive Image Scan,
- Adaptive stop-and-go process: Adaptive Stop-and-Go Scan,
- Regular high-speed process: Image Scan.

For each configuration involving well sizes and magnification, the frame rate that minimized the total acquisition time was chosen for comparison (15 fps for MTP6 with 4x magnification, 30 fps for MTP24 with 4x magnification, and 60 fps for MTP24 with 10x magnification and MTP96 with 10x magnification). The acquisition time for a whole MTP using the adaptive stop-and-go process was linearly extrapolated by multiplying the number of wells in an MTP by the time required to capture a single well, as only one well was captured at a time due to the lengthy duration. Reference measurements with regular high-speed phase contrast microscopy were conducted similarly to the adaptive approach. Figure 7.20 illustrates acquisition time differences between scan modes, as well as the contribution of the Bertrand

Camera Scan and Adaptive Image Scan to the overall imaging time of the adaptive high-speed process. The exact values are summarized in Table 7.8.

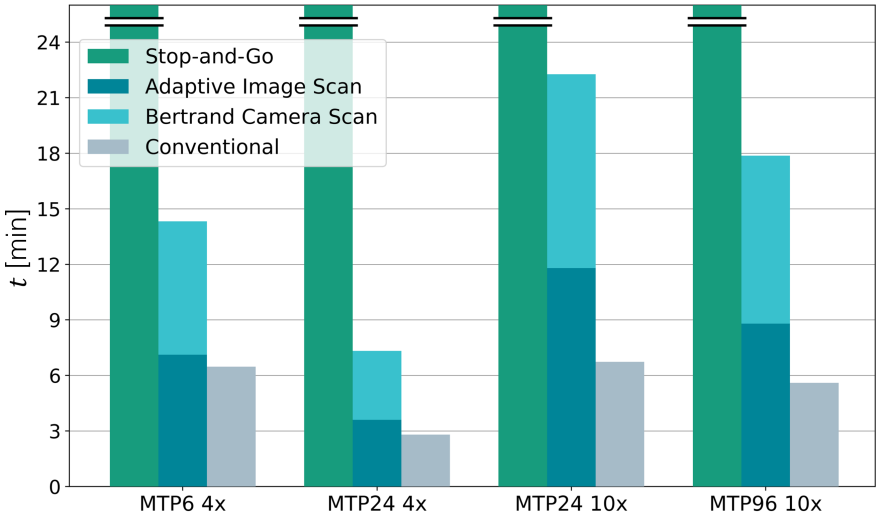

Figure 7.20: Comparison of imaging times t across the three tested processes with different configurations of MTPs and magnifications. The times for the Bertrand Camera Scan and Adaptive Image Scan are stacked to indicate their consecutive execution. Adaptive Stop-and-Go Scan times frequently exceed the scale and are thus truncated.

Table 7.8: Comparison of scanning times between adaptive high-speed and stop-and-go phase contrast microscopy, alongside conventional HSM. The adaptive high-speed scan employs the same frame rates as in Table 7.7, whereas the conventional scan utilizes the optimized frame rates indicated in Table 7.2. Abbreviations: *M*: magnification, *Num Images*: number of images, *Conv*: conventional high-speed scan, *Adap HS*: adaptive high-speed scan, *Adap SG*: adaptive stop-and-go scan, *SG/HS*: ratio of times of stop-and-go and adaptive high-speed scan, *HS/Conv*: ratio of times of adaptive high-speed scan with conventional scan.

MTP	M	Num Images	Conv	Adap HS	Adap SG	SG/HS	HS/Conv
6	4	4224	6:28	14:19	110:24	7.7	2.2
24	4	4128	2:48	7:20	111:48	15.2	2.6
24	10	22176	6:44	22:16	499:00	22.4	3.3
96	10	18720	5:36	17:52	439:12	24.6	3.2

The findings reveal a significant disparity in acquisition times between both high-speed scans and the Adaptive Stop-and-Go Scan. It is evident that the imaging time for the Adaptive Stop-and-Go Scan primarily depends on the number of images. This dependency arises from the near-constant acquisition time for each image while the stage is stationary, coupled with nearly identical switching times between images due to similar distances between them. In contrast, imaging times using the high-speed mode exhibit more variability across different MTP configurations and magnifications. This variation is attributed to differing maximum accelerations and velocities, as well as varying travel distances. Given that high-speed ap-

proaches allocate most of the time to stage movement, these parameters are particularly relevant.

Both high-speed scans outperform the stop-and-go approach by more than an order of magnitude, indicating that the adaptive high-speed process effectively achieved its primary objective of reducing image acquisition time. When comparing only the Adaptive Image Scan (excluding the Bertrand Camera Scan) with the regular high-speed scan, only minor differences are discernible. This is especially true for scans involving 6-well MTPs at 4x magnification, where the time ratio of the regular process to the adaptive process is merely 1.1. In contrast, the ratio is more pronounced for 24-well MTPs at 10x magnification, though it remains below 1.8, with the other configurations falling in between. The difference between 4x and 10x magnification is primarily due to the LCD refresh rate, which restricts the acquisition frame rate at 10x magnification. For 4x magnification, the optimal velocity is below 60 fps, avoiding the need for capping the stage velocity due to LCD limitations. Furthermore, the trigger delay (see Section 7.3.4) extends the scan line length, further contributing to the time difference.

Overall, this demonstrates that the meniscus compensation process using the LCD does not significantly constrain the achievable acquisition speed. Moreover, while the regular high-speed scan was conducted at the optimal frame rate for prevailing conditions, the adaptive scans utilized 15 fps, 30 fps, or 60 fps, slightly deviating from the optimal frame rate for each configuration.

The main difference in acquisition times between the high-speed processes is not observed during the Adaptive Image Scan itself but rather in the Bertrand Camera Scan. The necessity of employing the Bertrand Camera Scan effectively doubles the acquisition time, rendering the overall process slower than the conventional Image Scan. Nevertheless, the ratio of total acquisition times does not exceed 3.3 times the acquisition time of the regular Image Scan, even when combining the Bertrand Camera Scan and Adaptive Image Scan.

In summary, the adaptive high-speed phase contrast microscopy process significantly enhances speed relative to the adaptive stop-and-go process while remaining within the same order of magnitude as the conventional scan. It is noteworthy that the LCD exerts only a minor influence on reducing the maximum frame rate, primarily affecting 10x magnification. The most substantial challenge is the Bertrand Camera Scan, which doubles the acquisition time.

7.5 Discussion

The validation of the adaptive high-speed phase contrast microscopy process demonstrates its capability to effectively address the meniscus effect while preserving rapid acquisition

rates. This section first analyzes the experimental results presented in Section 7.5.1. Subsequently, it critically examines the strengths and limitations of adaptive phase contrast microscopy in Section 7.5.2. The findings are compared with alternative methods found in the scientific literature that also tackle the meniscus effect, as discussed in Section 7.5.3.

7.5.1 Interpretation of Results

Adaptive high-speed phase contrast microscopy significantly enhances the phase contrast area across all evaluated MTPs compared to conventional methods, achieving the goal of compensating for the meniscus effect over large well areas. For 6-well MTPs with 4x magnification, the phase contrast area increases by approximately 1.8 times; for 24-well MTPs with 10x magnification, it increases by 7.2 times; and for 24-well MTPs with 4x magnification, it increases by 9.0 times. The low standard deviations indicate substantial robustness. The comparable performance of both high-speed and stop-and-go approaches indicates that continuous sample movement does not compromise phase contrast quality.
It is important to recognize that the specific values for the phase contrast area are influenced by the demonstrator design, hardware, software implementation, and analysis algorithm. Therefore, the primary conclusion is that the proposed method is effective, leading to a substantial increase in the phase contrast area without solely emphasizing the precise numerical values.

The notable increase in the phase contrast area underscores the effectiveness of the proposed method compared to the conventional process. Even if the acquisition time is higher than with the conventional method, the expanded phase contrast area allows for the extraction of more information within the same time frame. For instance, while the acquisition time for 24-well MTPs at 4x magnification is 2.6 times longer with the adaptive approach, the phase contrast area is expanded 9.0 times, resulting in 3.5 times more information being obtained per unit of time. This comparison does not even account for the time required to remove the MTP from the microscope and load a new one.

The acquisition time for the adaptive high-speed process, considering only the Adaptive Image Scan, is not significantly longer than the conventional high-speed process. This suggests that the added complexity of the LCD and its control mechanism does not greatly impede acquisition speed. However, the Bertrand Scan, which is necessary for determining the parameters for the condenser annulus shift, doubles the acquisition time. Yet, even with the Bertrand Scan, the acquisition time of the high-speed process is still orders of magnitude faster than the stop-and-go process. Without the high-speed approach, compensating for the meniscus effect would be impractical, with acquisition times for a single MTP reaching up to 500 minutes (over 8 hours), making biological experiments unfeasible [Kor20].

7.5.2 Critical Reflection on the High-Speed Meniscus Effect Compensation

During the experiments, various limiting factors were identified that influenced both the phase contrast area and acquisition times. These factors hindered the attainment of a complete phase contrast area and contributed to longer acquisition times. This section examines these factors and proposes potential improvements for certain issues. The identified factors are detailed in Table 7.9.

Table 7.9: Limiting factors affecting the phase contrast area and acquisition time in the adaptive high-speed phase contrast microscopy process, which are critically discussed in this section.

Factor	Influence on
Shading at the edge of a well	Phase contrast area
Condenser annulus detection	Phase contrast area
Field curvature	Phase contrast area
Meniscus slope	Phase contrast area
LCD refresh rate	Acquisition time
Bertrand Scan	Acquisition time
Microscope stage range	Acquisition time
Acquisition at constant velocity	Acquisition time
Autofocus Scan	Acquisition time
Liquid sloshing	Acquisition time

Shading at the Edge of a Well

As detailed in Section 6.1.3, achieving phase contrast conditions across the entire well is limited by shading from the MTP walls. Considering this effect, the proportion of the phase contrast area relative to the upper limit for the phase contrast area using adaptive phase contrast microscopy is considerably higher than raw numbers suggest. For 6-well MTPs with 4x magnification, the proportion is about 74%; for 24-well MTPs with 4x magnification, it is 53%; and for 24-well MTPs with 10x magnification, it is 54%. These values show slight variations between the high-speed and stop-and-go process experiments, yet remain within a similar range. Due to its physical nature, surpassing this limitation is nearly impossible. The sole influencing factor examined in this thesis is the NA of the objective lens, where a higher NA corresponds to a larger maximum phase contrast area. For future applications, this effect could potentially be alleviated through alternative well designs featuring less steep walls.

Condenser Annulus Detection

The image analysis for determining the position of the condenser annulus via Bertrand lens images is effective when the entire annulus is visible as a ring or ellipse (refer to Sec-

tion 6.3.1). However, if the annulus is only partially visible or outside the FOV, the analysis defaults to standard condenser annulus parameters for the LCD, failing to yield a result. This limitation arises from the implementation chosen for this thesis rather than an inherent procedural limitation.
Enhancing image analysis techniques or increasing the FOV (e.g., by using a secondary camera with a larger chip size) could improve condenser annulus detection near the well edge. However, further experimentation is necessary to ascertain whether such changes would lead to significant improvements. For instance, in 24-well MTPs with 10x magnification, the detection area of the condenser annulus already exceeds the phase contrast area. Even if alignment of the condenser annulus with the phase ring closer to the well edge were possible, limited brightness due to shading at the well edge would prevent these regions from being interpreted as phase contrast. Additionally, the angle difference resulting from field curvature outside the phase contrast area is substantial, preventing the achievement of homogeneous image conditions at small magnifications, regardless of the alignment between the condenser annulus and phase ring.

Field Curvature

Field curvature impacts the phase contrast area across all observed well-size and magnification combinations, except for 24-well MTPs with 10x magnification. The inhomogeneity in phase contrast conditions due to field curvature is undesirable for microscope users and complicates the determination of the phase contrast area. While these differences are not significant for 6-well MTPs with 4x magnification and 24-well MTPs with 4x magnification, they make the application of the phase contrast analysis algorithm impractical for 96-well MTPs with 10x magnification. This is a physical limitation that cannot be eliminated, but can be managed by selecting an appropriate camera.

There are three options to mitigate this limitation: using a camera with a smaller chip size, cropping the FOV of the existing camera chip (which has the same effect as using a smaller chip), or employing higher magnification. All three options inadvertently increase acquisition time as an undesirable consequence. This occurs because a smaller camera chip necessitates more scan lines, and a higher frame rate would be required to maintain the same stage velocity. This issue is particularly problematic for magnifications of 10x or higher, where the refresh rate already acts as a bottleneck for faster acquisition.
The enhancements associated with higher magnifications, typically paired with a higher NA, are illustrated in Figure 7.21, which depicts a 6-well MTP captured at 10x magnification. In comparison to images acquired at 4x magnification, such as those in Figure 7.17, the phase contrast area is substantially expanded, nearly covering the entire image. However, a drawback of increased magnification is the resultant growth in data volume. For an MTP6, the size of a single composite image of one well is increased from 1.0 GB to 6.9 GB.

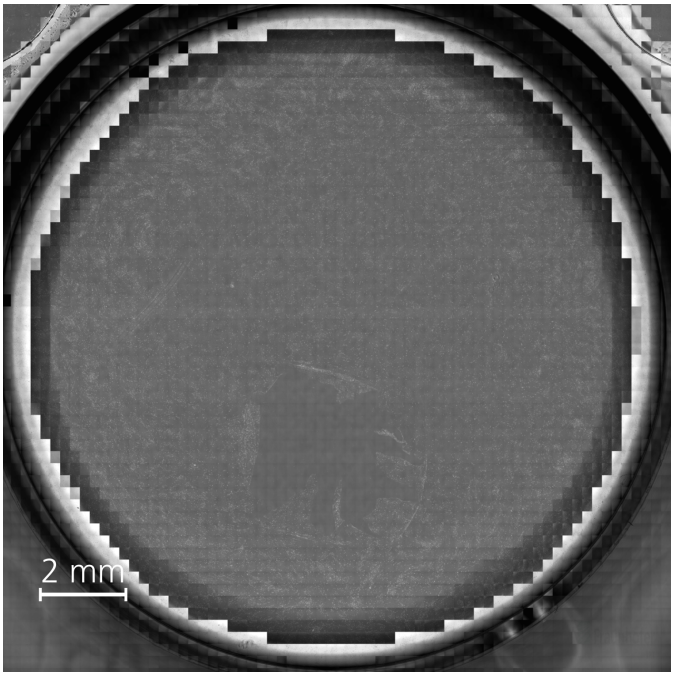

Figure 7.21: 6-well MTP acquired with 10x magnification. The phase contrast area is further enhanced compared to 4x magnification. The presented compound image is significantly compressed from the original, which comprises 3990 individual images and occupies 6.9 GB of disk space, illustrating a disadvantage of using large magnifications.

Meniscus Slope

As the slope of the liquid surface increases near the well's edge, a larger portion of incoming light is reflected rather than refracted, potentially leading to total internal reflection (refer to Section 2.1.4). Even before total internal reflection occurs, the contrast of structures diminishes due to decreased overall brightness, as observed in 24-well MTPs at 10x magnification. This physical limitation is difficult to overcome and represents a significant obstacle to further expanding the phase contrast area. The current approach, which involves using an LCD to shift the condenser annulus, is limited to operating at meniscus angles smaller than those required for total internal reflection. During validation, meniscus compensation was achieved up to maximum meniscus angles of approximately 4.8° with 4x magnification and 8.1° with 10x magnification for 24-well MTPs (see Section 6.4.4). The higher NA of the 10x objective lens may explain this difference, suggesting that objectives with higher NA could expand the phase contrast area.

Compensating for large meniscus slopes can only be accomplished by tilting the wavefront of the illumination light, thereby altering the angle between the incoming light and the meniscus surface. This method has been attempted using a liquid-filled prism (see Section 5.2.4). Empirically, the prism did not enhance image quality and primarily resulted in reduced im-

age brightness, largely due to the challenging hardware setup. It is conceivable that a more advanced design might increase the phase contrast area.

LCD Refresh Rate

The refresh rate of the LCD limits the demonstrator to a maximum frame rate of 60 fps, making it a bottleneck for enhancing acquisition speeds, particularly at 10x magnification. This limitation is strictly hardware-related and could potentially be resolved by employing an LCD with a higher refresh rate. However, refresh rates above 60 fps are rare in combination with other essential features such as monochromaticism and the absence of a backlight. Since most LCDs are designed for consumer electronics, higher refresh rates are not considered useful due to the limited temporal resolution of the human eye. Therefore, the development of LCDs with refresh rates beyond the current maximum of around 120 fps is improbable. Such advancements would require custom-developed LCDs for adaptive high-speed phase contrast microscopes, which would only be feasible with sufficient market demand.

Bertrand Scan

The Bertrand Scan requires approximately the same duration as the Adaptive Image Scan, effectively doubling the total acquisition time. Eliminating the Bertrand Scan altogether would thus save considerable time. However, it is crucial for the LCD controller to ascertain the condenser annulus shift for each imaging position. Two alternatives are conceivable: first, recording the condenser annulus positions once using a Bertrand Scan and employing a lookup table for subsequent scans; second, implementing a closed-loop Adaptive Image Scan that determines the condenser annulus shift between image acquisitions and dynamically adjusts the LCD. The first option is straightforward to implement and can be employed when identical conditions are expected across various specimens. However, it lacks the universality of the process involving a Bertrand Scan. The second option would be ideal, but it is currently impractical due to the high latency of the LCD controller, as discussed in Section 7.1.3. Future solutions may involve purpose-built LCDs with lower latency, but this is not feasible with existing hardware. Therefore, given the current commercial hardware, the proposed solution utilizing the Bertrand Scan remains the preferred approach.

Microscope Stage Range

Due to limited acceleration, the required acceleration distance to achieve optimal velocity often exceeds the available space, given the restricted range of the microscope stage. This challenge can be easily overcome by using a stage with a larger range, thereby increasing the maximum velocity and reducing acquisition time.

Acquisition at Constant Velocity

Image acquisition is performed only when a constant velocity is reached, not during the acceleration phase of the scan line, due to synchronization challenges between key components when the stage velocity varies. Utilizing the acceleration and deceleration phases for image acquisition could reduce overall scan time and simultaneously address the issue of limited microscope stage range. However, this complicates synchronization between the LCD, camera, and light source, as the trigger points would not be equidistant. Since actual stage acceleration is not perfectly linear, calculating these trigger points involves greater uncertainty, leading to imprecise positioning of individual images and potential mismatches in illumination and camera exposure. The necessary delay caused by the LCD latency further complicates the problem. Nonetheless, this challenge could be overcome with a well-controlled stage and if the individual components are perfectly synchronized with each other.

Autofocus Scan

Although not part of the primary acquisition process, the Autofocus Scan is vital for ensuring sharp images. Its duration significantly impacts the total acquisition time, especially when scanning numerous small wells, such as in 96-well MTPs. While some form of automatic focusing is necessary, more efficient methods exist compared to the image-stacking approach currently employed [Sch16a]. The image-stacking-based Autofocus Scan could be replaced with a continuously moving scan using an external distance sensor, such as confocal chromatic sensors or optical coherence tomography. This sensor could even gather measurement data during the image scan for a closed-loop inline-focus control, thereby minimizing acquisition time while simultaneously improving measurement accuracy. Yet, one challenge posed by inverse microscopes like the one used in this thesis is the limited assembly space, meaning that the sensor must be considered during the microscope design.

Liquid Sloshing

Liquid sloshing, as discussed in Section 7.1.2, significantly constrains the maximum acceleration of the microscope stage, thereby substantially increasing the acquisition time. This issue is particularly problematic for 4x magnification, where the LCD does not limit the maximum achievable frame rate, so that higher velocities could lead to higher frame rates. Since sloshing is an intrinsic property of the liquid, it cannot be entirely eliminated while the specimen requires movement. However, it has been suggested that minimizing jerk, which is the first-order derivative of acceleration, can mitigate liquid sloshing [Sim24].

7.5.3 Comparison with Existing Approaches

A quantitative comparison of the validation results with other approaches described in the literature is desired. However, most proposed solutions are presented in patents, where no experimental data is available. Among the approaches discussed in Section 3.5.2, only two are detailed in scientific papers.

Kwee et al. (2018) [Kwe18] describe a specialized algorithm for counting iPSCs, utilizing a combination of phase contrast images and reference interferogram images. Since this method is fundamentally different from the approach in this thesis and requires reference images without a specimen, it cannot be quantitatively compared to the approach of this thesis.

Hofmeister et al. (2020) [Hof20] perform experiments to compensate for the meniscus effect at various positions within a 24-well plate using a 10x objective lens with an NA of 0.22. However, images are not systematically taken of an entire well, preventing the exact calculation of the phase contrast area. They claim that compensating for the meniscus effect is theoretically possible up to 90% of the distance from the well center to the edge, equating to a phase contrast area of 81%. This represents the maximum possible area when considering shading by the MTP wall, as detailed in Section 6.1.3. However, their results indicate that at a radius of 50% of the well radius, the background of the images begins to darken, a phenomenon also observed in the results of this thesis. An image acquired at 63% of the radius is notably darker than images from the center, barely qualifying as phase contrast when applying the criteria detailed in Section 4.1.
Without imaging entire wells, an exact number for the phase contrast area cannot be measured. However, when using 50% of the radius as a threshold where image contrast begins to deteriorate, the phase contrast area can be calculated to be around 25%. This would be lower than the results of this thesis under similar circumstances (MTP24, 10x magnification), but only experiments under identical conditions can provide a quantitative comparison.

Based on this analysis, there is no publication presenting an approach that measurably increases the phase contrast area more than the method proposed in this thesis. Furthermore, no publication analyzed in the systematic literature review, whether a scientific paper or patent, considers a high-speed meniscus effect compensation approach, suggesting that this thesis presents the first of its kind.

7.6 Summary and Conclusion

This chapter addressed SRQ4:
Which acquisition time is achievable for complete wells in microtiter plates? What are the influencing factors on acquisition time?
Therefore, the chapter outlined the implementation of a high-speed imaging method, which was validated through a demonstrator.

Initially, factors negatively affecting the acquisition time during continuous scanning were analyzed. Based on these insights, the scanning procedure was developed, incorporating the Adaptive Autofocus Scan, Bertrand Camera Scan, and Adaptive Image Scan, alongside techniques from the stop-and-go process, such as stitching and image analysis. A high-speed scanning process was implemented, featuring dynamic LCD condenser annulus adjustment. As a result, a frame rate of 60 fps was achieved, which matches the maximum refresh rate of the LCD. Thus, with 4x magnification, the LCD refresh rate does not limit acquisition speed; instead, the maximum velocity is constrained by slow acceleration, necessary to avoid liquid sloshing and the short acceleration distance.

Experimental results indicated that the acquisition speed has no significant impact on the phase contrast area, as no statistically significant differences were observed compared to the stop-and-go process. Across all configurations evaluated, the phase contrast area was substantially increased, ranging from a factor of 1.8 for 6-well MTPs with 4x magnification to 9.0 for 24-well MTPs with 4x magnification. Thus, the adaptive phase contrast microscopy can be considered a great success.

Acquisition times varied across different configurations. For a complete MTP, the acquisition time was reduced by approximately 8-fold for MTP6 with 4x magnification and up to 25-fold for MTP96 with 10x magnification compared to a stop-and-go process. Consequently, acquisition times are comparable to those of a high-speed image scan using a conventional phase contrast microscope, albeit still extended, primarily due to the Bertrand Camera Scan, which effectively doubles the acquisition time. As previously noted, the Bertrand Camera Scan remains essential as long as LCD latency persists. Further improvements have been discussed, such as increasing the stage's range to allow for greater acceleration distance, potentially reducing acquisition time further.

In conclusion, the fourth SRQ has been thoroughly addressed. The acquisition time is influenced by several factors, most importantly LCD refresh rate and latency, microscope stage range, limited acceleration to prevent liquid sloshing, the necessity for the Bertrand Camera Scan, and the Autofocus Scan. This demonstrator setup achieves acquisition times for a complete well, considering only the necessary Bertrand Scan and Image Scan, ranging from 7 to 22 minutes, and for the entire process, between 18 and 63 minutes. This outcome marks a significant achievement and demonstrates that the selected approach is an effective scanning method.

8 Summary and Outlook

The aim of this thesis was to develop and evaluate a method for adaptive high-speed phase contrast microscopy that compensates for the meniscus effect in cell culture vessels. This chapter summarizes the thesis in Section 8.1 and concludes how the requirements have been met. Subsequently, an outlook is provided in Section 8.2.

8.1 Summary of Results

Initially, fundamental principles and key methods were introduced in Chapter 2. Subsequently, Chapter 3 highlighted the prevalent use of phase contrast microscopy for screening biological specimens in cell culture vessels, such as MTPs. However, its applicability is limited by the meniscus effect, which restricts observations to specimens at the center of MTP wells. Additionally, biological specimens must remain in controlled environments, necessitating the minimization of imaging duration. It was therefore concluded that a phase contrast microscopy method capable of compensating for the meniscus effect and enabling rapid imaging was required. A systematic review of scientific literature and patents revealed twelve existing solution approaches addressing aspects of the problem. These were categorized into three distinct groups: image analysis-based methods, specialized MTPs, and modifications to the microscope's beam path. Notably, no solutions offered rapid imaging capabilities. Consequently, multiple research gaps were identified, leading to the formulation of four sub-research questions in Section 3.6. Each chapter was dedicated to answering one of these sub-research questions.

Chapter 4 answered the first sub-research question:
How can the phase contrast area in microtiter plates be quantified?
A study was conducted to identify quantifiable criteria for evaluating phase contrast conditions in MTPs. The study demonstrated that image background brightness is a reliable indicator of phase contrast conditions when observing entire well images, surpassing the reliability of overall image sharpness as criterion. Building on this insight, an algorithm was developed to calculate the phase contrast area in whole well images, effectively addressing SRQ1.

Chapter 5 addressed the second sub-research question:
Which adaptive components are suitable for high-speed implementation?
It was determined that compensating for the meniscus effect at different positions across a well in an MTP required adaptive components within the microscope's beam path. Chapter 5

evaluated various adaptive components based on criteria derived from the application. This evaluation involved three steps: general considerations regarding the components, optical simulations, and experiments. Optical simulations suggested that meniscus effect compensation is feasible using an LCD as condenser annulus, as well as a liquid-filled prism. Experimental results indicated that the LCD achieved phase contrast conditions closest to the well edge. A comparative evaluation using a Harvey Balls diagram assessed the proposed adaptive components. It was determined that the LCD is most proficient in compensating for the meniscus effect. Consequently, the LCD was selected for the validation experiments of the remaining SRQs, as it received the highest scores across most categories. Notably, its advantages include ease of handling and potential for high-speed processes, owing to the absence of moving parts and its simplicity. Therefore, SRQ2 is conclusively answered.

Chapter 6 dealt with answering the third sub-research question:
To what extent can the phase contrast area be increased using adaptive phase contrast microscopy compared to conventional phase contrast microscopy?
A demonstrator setup was constructed incorporating the LCD condenser annulus as an adaptive component. A process was developed where each position within a well was approached using a stop-and-go mode. At each position, the condenser annulus displayed on the LCD was adjusted, and an image of the specimen was captured. This adjustment was facilitated by a method that recorded images of the condenser annulus displacement in relation to the phase ring using a Bertrand lens. Subsequent image analysis, followed by linear regression, was employed to determine the necessary LCD parameters.
Experiments utilizing various configurations of MTPs and magnifications validated the proposed approach, demonstrating that the adaptive phase contrast microscope significantly enhanced the phase contrast area. Specifically, it increased from 30.5% to 53.1% for 6-well MTPs at 4x magnification, from 2.3% to 23.8% for 24-well MTPs at 4x magnification, and from 6.1% to 41.6% for 24-well MTPs at 10x magnification. Additionally, shading at the MTP walls was found to obscure large parts of a well, reducing the attainable phase contrast area by up to 60%. Considering this, more than 50% of the achievable phase contrast area was attained in all cases.
Another finding was that the field curvature induced by the meniscus shape caused inhomogeneities in phase contrast conditions. This phenomenon was more pronounced in wells with smaller diameters and at lower magnifications, rendering the evaluation of the phase contrast area of 96-well MTPs at 10x magnification unfeasible.
In conclusion, this chapter successfully answered SRQ3.

Chapter 7 assessed the fourth sub-research question:
Which acquisition time is achievable for complete wells in microtiter plates? What are the influencing factors on the time?
Initially, factors affecting the high-speed process were analyzed. It was determined that medium sloshing poses a significant challenge, requiring a restriction of acceleration to $30\,\mathrm{mm/s^2}$ for 6-well MTPs and to $200\,\mathrm{mm/s^2}$ for 24-well and 96-well MTPs. Another factor extending the acquisition time was the limited range of the microscope stage, which constrained the acceleration distance, thereby reducing the maximum velocity.
An additional critical constraint is the latency introduced by the LCD controller, which adds

approximately 57 ms between image transmission and display. This latency necessitates incorporating a delay between the LCD and other time-sensitive components within the acquisition process. As a result, implementing a closed-loop process to determine LCD parameters during the same scan as image acquisition is impractical. An open-loop process proves to be more efficient, even though determining LCD parameters represents an additional step prior to the actual scan.
Based on these findings, a scanning process was developed, comprising multiple steps, two of which are crucial for adaptive phase contrast microscopy. The first key step is the Bertrand Camera Scan, which determines the LCD parameters before the actual image scan. During this phase, the sample is moved in the same manner as during the image acquisition, but images are captured through the microscope's Bertrand lens. These images are analyzed, and linear regression is applied to determine the shift of the condenser annulus at each imaging position. The main scan, termed the Adaptive Image Scan, utilizes this information to capture the specimen images, which are subsequently stitched into a continuous image.
Experiments demonstrated that the phase contrast area remains consistent with the stop-and-go process, achieving acquisition frame rates of up to 60 fps. Compared to a conventional high-speed phase contrast microscope configured for optimal acquisition time, the Adaptive Image Scan alone was found to be only 1.1 to 1.8 times slower. The entire process, including the Bertrand Camera Scan, was only 2.2 to 3.3 times slower. Compared to the stop-and-go process, the adaptive high-speed phase contrast microscopy process achieved acquisition times approximately one order of magnitude faster for all configurations, thereby successfully addressing SRQ4.

These findings affirmatively answer the main research question:

Can the optical compensation of the meniscus effect in phase contrast microscopy be performed during sample movement in combination with continuous image acquisition?

The results demonstrate that the proposed method is suitable for high-speed meniscus effect compensation. The phase contrast area is substantially increased, while the acquisition time is only marginally longer than that of a HSM scan without meniscus effect compensation, yet significantly shorter than with a stop-and-go approach. These results are based on the current demonstrator, which could be further refined with upgraded components. Consequently, even faster acquisition could be achieved through hardware optimization.

8.2 Outlook

Adaptive phase contrast microscopy has been successfully demonstrated in this thesis, providing a substantial improvement over conventional phase contrast microscopy. Future research could expand upon these findings, particularly by extending the phase contrast area beyond current limitations and reducing the acquisition time. The critical reflection of the results obtained with the demonstrator, as discussed in Section 7.5.2, has already proposed enhancements to overcome the deficiencies of the current demonstrator design. This

section further suggests additional viable options for advancing adaptive phase contrast microscopy through more significant alterations to the hardware configuration.

8.2.1 Mechanical Liquid-Filled Prism

The liquid-filled prism was thoroughly analyzed in Chapter 5 and demonstrated promising results. Yet, significant limitations included the complexity of the mechanical setup, constrained available space, and low robustness, leading to leakages and bubble formation. Constructing a setup that addresses these critical shortcomings could potentially lead to further improvements in the phase contrast area.
An enhanced prism design would require a more compact housing that can accommodate motor levers and a cover glass, and ensure a tight seal between the elastic hull, glass, and the housing itself. Improvements in the process of filling the prism with liquid are essential to prevent air entrapment and bubble formation. A more reliable sealing mechanism is crucial to prevent leakage throughout the prism's lifespan. Substituting water with immersion oil could elevate the refractive index, thereby necessitating smaller tilt angles. A wider aperture would ensure that light is not obstructed by the shell or housing. Actuators must be capable of tilting the prism quickly and precisely despite high inertia; alternatives such as piezo actuators or linear motors should be considered alongside servo motors.

8.2.2 Non-Mechanical Liquid Prism or Lens

A 3D beam steering mechanism, proposed by Lee et al. [Lee19], utilizes an electrowetting-based liquid lens and prism, offering an alternative to the mechanical liquid-filled prism. Applying an electric voltage to the walls of a liquid-filled container changes the shape of the liquid-liquid interface. This configuration theoretically enhances the adaptability of the illumination beam path, as tilt angles can be combined with the focusing and defocusing properties of a lens. Since this method does not rely on mechanical components, many issues associated with the mechanical liquid-filled prism could be mitigated. However, the study did not concentrate on optimizing the speed of switching between states, leaving uncertainty regarding its suitability for high-speed applications. Further research could investigate potential challenges arising from liquid inertia or oscillations at the liquid-liquid interface.

8.2.3 Digital Mirror Device (DMD)

Section 5.6 ruled out the use of a DMD due to the necessity of remodeling the entire illumination unit of the phase contrast microscopy, resulting in high complexity, low flexibility, and high cost. However, in setups where these criteria are secondary, this approach could be implemented. Hofmeister et al. [Hof20] effectively utilized a DMD for compensating for the meniscus effect. Further studies could explore this technique, comparing the phase contrast area with the method outlined in this thesis under identical conditions. Additionally,

this setup could be adapted for high-speed applications. Alternatively, other spatial light modulators could be investigated to modify the microscope's illumination.

8.2.4 Closed-Loop Control Without Bertrand Camera Scan

A drawback of the current method is the requirement for the Bertrand Camera Scan, which doubles the acquisition time. If an optimized LCD with minimal latency and a high refresh rate were developed, a new condenser annulus could be displayed almost immediately after its parameters are sent to the LCD controller. This advancement would eliminate the need for the Bertrand Camera Scan, as the displacement between the condenser annulus and the phase ring could be monitored during the Image Scan itself, with information transmitted to the LCD controller instantaneously.

A challenge in this approach is the rapid measurement of condenser annulus displacement. This could still be achieved using a camera to capture images through the Bertrand lens, followed by image analysis and regression. However, the image analysis process might be too time-consuming, as it introduces additional latency. Alternatively, non-imaging sensors, such as a photodiode that detects brightness shifts, could be employed. Once measured, condenser annulus data would need to be transmitted quickly to ensure minimal changes occur between measurement and display due to the moving sample.

This strategy hinges on the development of an LCD with suitable characteristics, such as immediate screen refreshment after rendering a new image. While LCDs with dynamic refresh rates have been researched for some time, the focus has mostly been on reducing power consumption rather than achieving faster reaction times to changing inputs [Hua14]. Therefore, it is uncertain if such a device will be produced in the near future, as LCDs are predominantly manufactured for consumer electronics. In this realm, faster response times and higher frame rates are unnecessary since the human eye's temporal resolution does not exceed the refresh rate of most LCDs, and human reaction times are significantly longer than the LCD controller's latency [Ng12].

8.2.5 Movable Optics

HSM requires relative movement between the specimen and the microscope's optics. This thesis employed a method where the specimen is moved while the optics remain static, offering a simpler implementation. However, maintaining a stationary specimen and moving the optical components could potentially enhance acquisition speed further. This approach could overcome the issue of low acceleration needed to prevent liquid sloshing, allowing acceleration to be constrained only by hardware capabilities, inertia, and the need to avoid mechanical oscillations. Nevertheless, aligning the optical path in such a setup is more complex due to the necessity for precise synchronization of movements. The entire illumination unit of the microscope would need to move in coordination with the observation unit around the specimen.

Once this challenge is addressed, the acquisition time becomes constrained by the refresh rate of the LCD or the frame rate of the camera, necessitating a more advanced LCD. An advantage of this method is that all moving parts can be enclosed and sealed within a housing, ensuring compliance with hygiene standards such as *GMP* [Man13].

Bibliography

[And10] G. A. Andrews Jr, B. W. Gutting, R. S. Mackie (2010) “Microtiter Plate to Mitigate Cell Distribution Bias from Meniscus Edge” US2010197004 AA.

[Ard25] Arduino (2025) *Arduino Uno R3: Product Reference Manual: SKU: A000066* URL: https://docs.arduino.cc/resources/datasheets/A000066-datasheet.pdf. Accessed: 04 March 2025.

[Axe01] D. Axelrod (2001) “Total internal reflection fluorescence microscopy in cell biology” *Traffic (Copenhagen, Denmark)*, 2, 11. Accessed: 764–774. DOI: 10.1034/j.1600-0854.2001.21104.x.

[Bah12] A. B. Bahnson, D. J. Koebler (2012) “Adaptive Phase Contrast Microscope” US2012257040 AA.

[Bal12] J. M. Baltz (2012) “Media composition: salts and osmolality” *Embryo Culture*, 912. Accessed: 61–80. DOI: 10.1007/978-1-61779-971-6_5.

[Bar16] Y. Barrandon, S. Beguin, D. V. Bonzon et al. (2016) “Observation Device with Optical Compensation” WO16120757 A1.

[Bat84] R. Battino, T. R. Rettich, T. Tominaga (1984) “The Solubility of Nitrogen and Air in Liquids” *Journal of Physical and Chemical Reference Data*, 13, 2. Accessed: 563–600. DOI: 10.1063/1.555713.

[Ben09] J. Benesty, J. Chen, Y. Huang et al. “Pearson Correlation Coefficient”. In: *Noise reduction in speech processing*. Ed. by Jacob Benesty. Springer topics in signal processing. Berlin and Heidelberg: Springer, 2009, Accessed: 1–4. ISBN: 9783642002953. DOI: 10.1007/978-3-642-00296-0_5.

[Ben51] A. H. Bennet (1951) *Phase Microscopy: Principles and Applications*. Wiley.

[Bie21] F. Biermann, J. Mathews, B. Nießing et al. (2021) “Automating Laboratory Processes by Connecting Biotech and Robotic Devices—An Overview of the Current Challenges, Existing Solutions and Ongoing Developments” *Processes*, 9, 6. Accessed: 966. DOI: 10.3390/pr9060966. URL: https://www.mdpi.com/2227-9717/9/6/966.

[Bla20] V. Blay, B. Tolani, S. P. Ho et al. (2020) “High-Throughput Screening: today’s biochemical and cell-based approaches” *Drug Discovery Today*, 25, 10. Accessed: 1807–1821. DOI: 10.1016/j.drudis.2020.07.024.

[Bor86] M. Born, E. Wolf (1986) *Principles of optics: Electromagnetic theory of propagation, interference and diffraction of light*. Pergamon Press. ISBN: 0080264824.

[Bou15] M. Boutros, F. Heigwer, C. Laufer (2015) “Microscopy-Based High-Content Screening” *Cell*, 163, 6. Accessed: 1314–1325. DOI: 10.1016/j.cell.2015.11.007. URL: https://www.cell.com/cell/fulltext/S0092-8674(15)01487-7.

[Boy13] F. Boyer, P. Fabrie (2013) *Mathematical tools for the study of the incompressible Navier-Stokes equations and related models*. Springer. DOI: 10.1007/978-1-4614-5975-0. ISBN: 978-1-4614-5974-3.

[Cer24] J. Cerneckis, H. Cai, Y. Shi (2024) “Induced pluripotent stem cells (iPSCs): molecular mechanisms of induction and applications” *Signal Transduction and Targeted Therapy*, 9, 1. Accessed: 112. DOI: 10.1038/s41392-024-01809-0. URL: https://www.nature.com/articles/s41392-024-01809-0.

[Che18] H. Chen, J. Lee, B. Lin et al. (2018) “Liquid crystal display and organic light-emitting diode display: present status and future perspectives” *Light: Science & Applications*, 7, 3. Accessed: 17168. DOI: 10.1038/lsa.2017.168. URL: https://www.nature.com/articles/lsa2017168.

[Che16] H. Cheng, Y. Chang, C. Cheng et al. (2016) “High–power–factor dimmable LED driver with low–frequency pulse–width modulation” *IET Power Electronics*, 9, 10. Accessed: 2139–2146. DOI: 10.1049/iet-pel.2015.0664. URL: https://ietresearch.onlinelibrary.wiley.com/doi/full/10.1049/iet-pel.2015.0664.

[Che11] B. H. Cheong, T. W. Ng, Y. Yu et al. (2011) “Using the meniscus in a capillary for small volume contact angle measurement in biochemical applications” *Langmuir: the ACS journal of surfaces and colloids*, 27, 19. Accessed: 11925–11929. DOI: 10.1021/la202800s.

[Com23] Wikimedia Commons (2023) *File:Electromagnetic wave2.svg - Wikimedia Commons* URL: https://commons.wikimedia.org/wiki/File:Electromagnetic_wave2.svg. Accessed: 21 March 2025.

[Con25] Confovis (2025) *SIM & Fokusvariation | confovis* URL: https://www.confovis.com/applikationen/sim-und-fokusvariation. Accessed: 21 February 2025.

[Das93] S. DasGupta, J. A. Schonberg, I. Y. Kim et al. (1993) “Use of the Augmented Young-Laplace Equation to Model Equilibrium and Evaporating Extended Menisci” *Journal of Colloid and Interface Science*, 157, 2. Accessed: 332–342. DOI: 10.1006/jcis.1993.1194.

[Dav07] P. J. Davis, E. A. Kosmacek, Y. Sun et al. (2007) “The large-scale digital cell analysis system: an open system for nonperturbing live cell imaging” *Journal of microscopy*, 228, Pt 3. Accessed: 296–308. DOI: 10.1111/j.1365-2818.2007.01847.x.

[Die18] B. Diederich, F. Schenk (2018) “Phase-Contrast Microscopy Method, Optical Unit, and Phase-Contrast Microscope” EP3323010 A2.

[Dos08] G. Dossantos, J. Dowd, O. Egeler et al. (2008) “Method of Reducing Curvature in a Meniscus of Liquid Medium” CA2675495 AA.

[Due07] W. A. Duetz (2007) “Microtiter plates as mini-bioreactors: miniaturization of fermentation methods” *Trends in Microbiology*, 15, 10. Accessed: 469–475. DOI: 10.1016/j.tim.2007.09.004. URL: https://www.cell.com/molecular-cell/fulltext/S0966-842X(07)00172-2.

[Ela20] A. Elanzew, B. Nießing, D. Langendoerfer et al. (2020) “The StemCellFactory: A Modular System Integration for Automated Generation and Expansion of Human Induced Pluripotent Stem Cells” *Frontiers in Bioengineering and Biotechnology*, 8. Accessed: 580352. DOI: 10.3389/fbioe.2020.580352. URL: https://www.frontiersin.org/articles/10.3389/fbioe.2020.580352/full.

[Elz12] T. Elze, T. G. Tanner (2012) “Temporal properties of liquid crystal displays: implications for vision science experiments” *PloS one*, 7, 9. Accessed: e44048. DOI: 10.1371/journal.pone.0044048.

[Ern16] R. Erni (2016) “Coherent Chromatic Effect in the Transmission Electron Microscope” *Physical review letters*, 116, 11. Accessed: 116101. DOI: 10.1103/PhysRevLett.116.116101.

[Esl19] F. Eslami, J. A. W. Elliott (2019) “Gibbsian Thermodynamic Study of Capillary Meniscus Depth” *Scientific reports*, 9, 1. Accessed: 657. DOI: 10.1038/s41598-018-36514-w.

[Eur25] Nikon Europe (2025) *Eclipse Ti2 Serie* URL: https://www.microscope.healthcare.nikon.com/de_EU/products/inverted-microscopes/eclipse-ti2-series. Accessed: 01 January 2025.

[Fan23] B. Fan, Y. Dai, H. Li (2023) “Rolling Shutter Inversion: Bring Rolling Shutter Images to High Framerate Global Shutter Video” *IEEE transactions on pattern analysis and machine intelligence*, 45, 5. Accessed: 6214–6230. DOI: 10.1109/TPAMI.2022.3212912.

[Fer03] A. F. Fercher, W. Drexler, C. K. Hitzenberger et al. (2003) “Optical coherence tomography - principles and applications” *Reports on Progress in Physics*, 66, 2. Accessed: 239–303. DOI: 10.1088/0034-4885/66/2/204.

[Fin86] R. Finn (1986) *Equilibrium Capillary Surfaces*. Springer New York. DOI: 10.1007/978-1-4613-8584-4. ISBN: 9781461385844.

[Flu96] J. Flusser, T. Suk, S. Saic. “Recognition of Images Degraded by Linear Motion Blur without Restoration”. In: *Theoretical Foundations of Computer Vision*. Ed. by W. Kropatsch, R. Klette, F. Solina, et al. Computing Supplement. Vienna: Springer, 1996, Accessed: 37–51. ISBN: 978-3-7091-6586-7. DOI: 10.1007/978-3-7091-6586-7_3. URL: https://link.springer.com/chapter/10.1007/978-3-7091-6586-7_3.

[Fox04] R. W. Fox, A. T. McDonald, P. J. Pritchard (2004) *Introduction to fluid mechanics*. Wiley. ISBN: 0471376531.

[Fuc23] H. Fuchs, K. Jahn, X. Hu et al. (2023) “Breaking a Dogma: High-Throughput Live-Cell Imaging in Real-Time with Hoechst 33342” *Advanced healthcare materials*, 12, 20. Accessed: e2300230. DOI: 10.1002/adhm.202300230.

[Gao98] C. Gao, P. Dai, A. Homola et al. (1998) “Meniscus Forces and Profiles: Theory and Its Applications to Liquid-Mediated Interfaces” *Journal of Tribology*, 120, 2. Accessed: 358–368. DOI: 10.1115/1.2834435.

[Gha20] M. S. Ghamsari, I. Carlescu (2020) *Liquid Crystals and Display Technology*. IntechOpen. DOI: 67707. ISBN: 9781789853681.

[Gio01] M. Giorgi, A. Taurino, A. Passaseo et al. (2001) “Interpretation of phase and strain contrast of TEM images of InxGa1−xAs/GaAs quantum dots” *Physical Review B*, 63, 24. DOI: 10.1103/PhysRevB.63.245302.

[Gon18] R. C. Gonzalez, R. E. Woods (2018) *Digital image processing*. Pearson Education. ISBN: 9781292223070.

[Goo75] C. H. Gooch, H. A. Tarry (1975) “The optical properties of twisted nematic liquid crystal structures with twist angles $\leqslant$ 90 degrees” *Journal of Physics D: Applied Physics*, 8, 13. Accessed: 1575–1584. DOI: 10.1088/0022-3727/8/13/020. URL: https://www.researchgate.net/publication/230945657_The_optical_properties_of_twisted_nematic_liquid_crystal_structures_with_twist_angles_90_degrees.

[Gre04] J. E. Greivenkamp (2004) *Field guide to geometrical optics*. SPIE Press. ISBN: 9780819478160.

[Gro85] F. C. Groen, I. T. Young, G. Ligthart (1985) “A comparison of different focus functions for use in autofocus algorithms” *Cytometry*, 6, 2. Accessed: 81–91. DOI: 10.1002/cyto.990060202.

[Gui22] J. Guiot, A. Vaidyanathan, L. Deprez et al. (2022) “A review in radiomics: Making personalized medicine a reality via routine imaging” *Medicinal Research Reviews*, 42, 1. Accessed: 426–440. DOI: 10.1002/med.21846.

[Haz22] L. Hazra (2022) *Foundations of Optical System Analysis and Design*. CRC Press Taylor & Francis Group. DOI: 10.1201/9780429154812. ISBN: 9780429154812.

[Hen04] U. Henriksson, C. Eriksson (2004) “Thermodynamics of Capillary Rise: Why Is the Meniscus Curved?” *Journal of Chemical Education*, 81, 1. Accessed: 150. DOI: 10.1021/ed081p150.

[Her19] L. Her, X. Yang. “Research of Image Sharpness Assessment Algorithm for Autofocus”. In: *2019 IEEE 4th International Conference on Image, Vision and Computing*. Piscataway, NJ: IEEE, 2019, Accessed: 93–98. ISBN: 978-1-7281-2325-7. DOI: 10.1109/ICIVC47709.2019.8980980.

[Her23] L. Herbst, F. Groten, M. Murphy et al. (2023) “Automated Production at Scale of Induced Pluripotent Stem Cell-Derived Mesenchymal Stromal Cells, Chondrocytes and Extracellular Vehicles: Towards Real-Time Release” DOI: 10.24406/PUBLICA-1977.

[Hic21] S. M. Hickey, B. Ung, C. Bader et al. (2021) “Fluorescence Microscopy-An Outline of Hardware, Biological Handling, and Fluorophore Considerations” *Cells*, 11, 1. DOI: 10.3390/cells11010035.

[Hof20] A. Hofmeister, G. Thalhammer, M. Ritsch-Marte et al. (2020) “Adaptive Illumination for Optimal Image Quality in Phase Contrast Microscopy” *Optics Communications*, 459. Accessed: 124972. DOI: 10.1016/j.optcom.2019.124972.

[Hol11] G. C. Holst (2011) *CMOS/CCD sensors and camera systems*. DOI: 10.1117/3.2524677. ISBN: 9780819486530.

[Hop20] J. Hopkins, P. A. Keane, K. Balaskas (2020) “Delivering personalized medicine in retinal care: from artificial intelligence algorithms to clinical application” *Current Opinion in Ophthalmology*, 31, 5. Accessed: 329–336. DOI: 10.1097/ICU.0000000000000677.

[Hor06] E. Horn, R. Zantl (2006) “Phase-Contrast Light Microscopy of Living Cells Cultured in Small Volume”

[Hua24] C. Huang, Z. Wu, H. Yin et al. (2024) “Sharpness Evaluation Algorithm for Nailfold Microvascular Images” *Signal, Image and Video Processing*, 18, 2. Accessed: 1515–1523. DOI: 10.1007/s11760-023-02873-9. URL: https://link.springer.com/article/10.1007/s11760-023-02873-9.

[Hua14] Y. Huang, M. Chen, L. Zhang et al. “Intelligent frame refresh for energy-aware display subsystems in mobile devices”. In: *Proceedings of the 2014 international symposium on Low power electronics and design*. Ed. by Yuan Xie. ACM Digital Library. New York, NY: ACM, 2014, Accessed: 369–374. ISBN: 9781450329750. DOI: 10.1145/2627369.2627612.

[Hyn16] K. Hynes, D. Menicanin, S. Gronthos et al. (2016) “Differentiation of iPSC to Mesenchymal Stem-Like Cells and Their Characterization” *Methods in Molecular Biology (Clifton, N.J.)*, 1357. Accessed: 353–374. DOI: 10.1007/7651_2014_142.

[Iri09] K. Irie, I. M. Woodhead, A. E. McKinnon et al. “Measured effects of temperature on illumination-independent camera noise”. In: *2009 24th International Conference Image and Vision Computing New Zealand (IVCNZ 2009)*. Ed. by D. Bailey. Piscataway, NJ: IEEE, 2009, Accessed: 249–253. ISBN: 978-1-4244-4697-1. DOI: 10.1109/IVCNZ.2009.5378403.

[Jai11] S. Jain, D. Sondervan, P. Rizzu et al. (2011) “The complete automation of cell culture: improvements for high-throughput and high-content screening” *Journal of biomolecular screening*, 16, 8. Accessed: 932–939. DOI: 10.1177/1087057111413920.

[Jia07] Y. Jiang (2007) “Well Plate” US2007274871 AA.

[Jia12] Y. Jiang, Y. Li, D. Ban et al. “Frame Buffer Compression without Color Information Loss”. In: *2012 IEEE 12th International Conference on Computer and Information Technology (CIT 2012)*. Ed. by Xingang Liu. Piscataway, NJ: IEEE, 2012, Accessed: 12–17. ISBN: 978-1-4673-4873-7. DOI: 10.1109/CIT.2012.29.

[Jin24] Y. Jin, C. Zhou, W. Dai (2024) “Sharpness-Based Distance Detection” *Applied Sciences*, 14, 19. Accessed: 8913. DOI: 10.3390/app14198913.

[Kas17] L. Kastl, M. Isbach, D. Dirksen et al. (2017) “Quantitative phase imaging for cell culture quality control” *Cytometry Part A*, 91, 5. Accessed: 470–481. DOI: 10.1002/cyto.a.23082.

[Kau23] K. Kaur, B. Gurnani (2023) *StatPearls: Prisms*. StatPearls Publishing.

[Ker19] I. Kernier, A. Ali-Cherif, N. Rongeat et al. (2019) “Large field-of-view phase and fluorescence mesoscope with microscopic resolution” *Journal of biomedical optics*, 24, 3. Accessed: 1–9. DOI: 10.1117/1.JBO.24.3.036501.

[Kor20] D. Korakaki, S. Mouroutsos, G. Tripsianis et al. (2020) “Temperature Decline in Embryological Culture Dishes outside Incubator” *International Journal of Fertility & Sterility*, 14, 1. Accessed: 63–67. DOI: 10.22074/ijfs.2020.5917. URL: https://pmc.ncbi.nlm.nih.gov/articles/PMC7139228/.

[Kri21] J. Krieger, B. Nießing, S. Snowball et al. (2021) ““Jointpromise”: concept of a multi-step, automated platform for precision manufacturing of joint implants” *Cytotherapy*, 23, 5. Accessed: S31. DOI: 10.1016/S1465324921002929.

[Kui15] R. Kuis (2015) “An Introduction to Practical Laboratory Optics” *Physics Today*, 68, 6. Accessed: 56. DOI: 10.1063/PT.3.2821.

[Kwe18] E. Kwee, A. W. Peterson, M. Halter et al. (2018) “Large field of view quantitative phase imaging of induced pluripotent stem cells and optical pathlength reference materials” *Quantitative Phase Imaging IV*, 10503. Accessed: 86. DOI: 10.1117/12.2290691.

[Lai18] S. Laiwejpithaya, P. Wongkrajang, K. Reesukumal et al. (2018) “UriSed 3 and UX-2000 automated urine sediment analyzers vs manual microscopic method: A comparative performance analysis” *Journal of clinical laboratory analysis*, 32, 2. DOI: 10.1002/jcla.22249.

[Led21] F. Ledermann (2021) “The Effect of Display Pixel Density on the Minimum Legible Size of Fundamental Cartographic Symbols” *The Cartographic Journal*, 58, 4. Accessed: 314–328. DOI: 10.1080/00087041.2022.2055938.

[Lee19] J. Lee, J. Lee, Y. H. Won (2019) “Nonmechanical three-dimensional beam steering using electrowetting-based liquid lens and liquid prism” *Optics Express*, 27, 25. Accessed: 36757–36766. DOI: 10.1364/OE.27.036757. URL: https://opg.optica.org/oe/fulltext.cfm?uri=oe-27-25-36757&id=423846.

[Lew22] K. Lewis, T. Matsuura (2022) “Calculation of the Meniscus Shape Formed under Gravitational Force by Solving the Young-Laplace Differential Equation Using the Bézier Curve Method” *ACS omega*, 7, 41. Accessed: 36510–36518. DOI: 10.1021/acsomega.2c04359.

[Li22] X. Li, I. Lazić, X. Huang et al. (2022) “Imaging biological samples by integrated differential phase contrast (iDPC) STEM technique” *Journal of structural biology*, 214, 1. Accessed: 107837. DOI: 10.1016/j.jsb.2022.107837.

[Lib09] A. Liberati, Douglas G. Altman, J. Tetzlaff et al. (2009) “The PRISMA statement for reporting systematic reviews and meta-analyses of studies that evaluate health care interventions: explanation and elaboration” *PLoS Medicine*, 6, 7. Accessed: e1000100. DOI: 10.1371/journal.pmed.1000100. URL: https://www.ncbi.nlm.nih.gov/pmc/articles/PMC2707010/.

[Lin20] S. Lin, K. Schorpp, I. Rothenaigner et al. (2020) “Image-based high-content screening in drug discovery” *Drug Discovery Today*, 25, 8. Accessed: 1348–1361. DOI: 10.1016/j.drudis.2020.06.001.

[Lin16] M. Linck, P. Hartel, S. Uhlemann et al. (2016) “Chromatic Aberration Correction for Atomic Resolution TEM Imaging from 20 to 80 kV” *Physical review letters*, 117, 7. Accessed: 076101. DOI: 10.1103/PhysRevLett.117.076101.

[Lip19] G. Lippi, G. Da Rin (2019) “Advantages and limitations of total laboratory automation: a personal overview” *Clinical Chemistry and Laboratory Medicine (CCLM)*, 57, 6. Accessed: 802–811. DOI: 10.1515/cclm-2018-1323. URL: https://www.degruyter.com/document/doi/10.1515/cclm-2018-1323/html.

[Loo96] J. Loos, J. Petermann (1996) “A comparison of the lamellar morphology of melt-crystallized isotactic and syndiotactic polypropylene” *Polymer*, 37, 19. Accessed: 4417–4420. DOI: 10.1016/0032-3861(96)00268-6.

[Ma15] J. Ma (2015) “Advanced MEMS-based technologies and displays” *Displays*, 37. Accessed: 2–10. DOI: 10.1016/j.displa.2014.10.003. URL: https://www.sciencedirect.com/science/article/pii/S0141938214000717.

[Mal24] N. Maleki, B. Padmanabhan, K. Dutta. “AI Hallucinations: A Misnomer Worth Clarifying”. In: *2024 IEEE Conference on Artificial Intelligence*. Ed. by Ferrante Neri, Guansong Pang, and Mengmi Zhang. Piscataway, NJ: IEEE, 2024, Accessed: 133–138. ISBN: 979-8-3503-5409-6. DOI: 10.1109/CAI59869.2024.00033.

[Man13] L. Manning (2013) *Food & drink: Good manufacturing practice : a guide to its responsible management*. Wiley-Blackwell. DOI: 10.1002/9781118318225. ISBN: 1118318242.

[Man21] M. Mansoury, M. Hamed, R. Karmustaji et al. (2021) “The edge effect: A global problem. The trouble with culturing cells in 96-well plates” *Biochemistry and biophysics reports*, 26. Accessed: 100987. DOI: 10.1016/j.bbrep.2021.100987.

[Mar21] D. K. Martin, O. Vicente, T. Beccari et al. (2021) “A brief overview of global biotechnology” *Biotechnology & Biotechnological Equipment*, 35, sup1. Accessed: S5–S14. DOI: 10.1080/13102818.2021.1878933.

[Mat17] K. Matsubara (2017) “Phase-Contrast Microscope and Imaging Method” JP2017 015856 A2.

[Mat15] S. Matsunaga, S. K. Nayar (2015) “Field Curvature Correction Using Focal Sweep” *IEEE Transactions on Computational Imaging*, 1, 4. Accessed: 259–269. DOI: 10.1109/TCI.2015.2491181. URL: https://www.infona.pl/resource/bwmeta1.element.ieee-art-000007298421?locale=pl.

[Mau08] C. Maurer, A. Jesacher, S. Bernet et al. (2008) “Phase contrast microscopy with full numerical aperture illumination” *Optics Express*, 16, 24. Accessed: 19821–19829. DOI: 10.1364/OE.16.019821. URL: https://opg.optica.org/oe/fulltext.cfm?uri=oe-16-24-19821&id=174811.

[Mey09] G. Meynants, G. Lepage, J. Bogaerts et al. (2009) “Limitations to the frame rate of high speed image sensors: IISS (Int. Image Sensors Society)” *High-Speed, High-Sensitivity Digital CMOS Image Sensor With a Global Shutter and 12-bit Column*. DOI: 10.60928/NJDW-SIL4.

[Mil22] G. F. Milne, T. Y. Wang (2022) “Apparatus for Resolving Imaging Problems Caused by the Meniscus” US2022040689 AA.

[Moh10] I. A. Mohamed Ahmed, J. Arima, T. Ichiyanagi et al. (2010) “Isolation and characterization of homocholine-degrading Pseudomonas sp. strains A9 and B9b” *World Journal of Microbiology and Biotechnology*, 26, 8. Accessed: 1455–1464. DOI: 10.1007/s11274-010-0320-z.

[Mua18] F. Mualla, M. Aubreville, A. Maier (2018) “Medical Imaging Systems: An Introductory Guide: Microscopy” *Medical Imaging Systems*. Accessed: 69–90. DOI: 10.1007/978-3-319-96520-8_5. URL: https://link.springer.com/chapter/10.1007/978-3-319-96520-8_5.

[Mur12] D. B. Murphy, M. W. Davidson (2012) *Fundamentals of Light Microscopy and Electronic Imaging*. John Wiley & Sons, Inc. DOI: 10.1002/9781118382905.

[Nar23] F. Narrog, R. Lensing, T. Piotrowski et al. (2023) “LIFTOSCOPE: development of an automated AI-based module for time-effective and contactless analysis and isolation of cells in microtiter plates” *Journal of Biological Engineering*, 17, 1. Accessed: 10. DOI: 10.1186/s13036-023-00329-9. URL: https://jbioleng.biomedcentral.com/articles/10.1186/s13036-023-00329-9.

[Nav11] F. Navarro, F. J. Serón, D. Gutierrez (2011) “Motion Blur Rendering: State of the Art” *Computer Graphics Forum*, 30, 1. Accessed: 3–26. DOI: 10.1111/j.1467-8659.2010.01840.x.

[Nec22] V. Nechyporuk-Zloy (2022) *Principles of Light Microscopy: From Basic to Advanced*. Springer International Publishing. DOI: 10.1007/978-3-031-04477-9. ISBN: 9783031044779.

[Ng12] A. W. Y. Ng, A. H. S. Chan (2012) “Finger Response Times to Visual, Auditory and Tactile Modality Stimuli” *Proceedings of the International MultiConference of Engineers, Hong Kong*.

[Nie25] F. Nienhaus, F. Burkhardt, N. König et al. (2025) “Compensating the Meniscus Effect in Phase Contrast Microscopy Using an LCD for Adaptive Condenser Annulus Shifting” *Microscopy research and technique*. DOI: 10.1002/jemt.24808.

[Nie23] F. Nienhaus, T. Piotrowski, B. Nießing et al. (2023) “Adaptive Phase Contrast Microscopy to Compensate for the Meniscus Effect” *Scientific Reports*, 13, 1. Accessed: 5785. DOI: 10.1038/s41598-023-32917-6. URL: https://www.nature.com/articles/s41598-023-32917-6.

[Nie21] B. Nießing, R. Kiesel, L. Herbst et al. (2021) “Techno-Economic Analysis of Automated iPSC Production” *Processes*, 9, 2. Accessed: 240. DOI: 10.3390/pr9020240.

[Niu21] R. Niu, C. Zhang, X. Li et al. (2021) “Wide viewing angle polarization interference filter using double liquid crystal layers with opposite twisted direction” *Optics Express*, 29, 24. Accessed: 40310–40322. DOI: 10.1364/OE.444591. URL: https://opg.optica.org/oe/fulltext.cfm?uri=oe-29-24-40310&id=464947.

[Och21] J. Ochs, F. Biermann, T. Piotrowski et al. (2021) “Fully Automated Cultivation of Adipose-Derived Stem Cells in the StemCellDiscovery—A Robotic Laboratory for Small-Scale, High-Throughput Cell Production Including Deep Learning-Based Confluence Estimation” *Processes*, 9, 4. Accessed: 575. DOI: 10.3390/pr9040575.

[Och22] J. Ochs, M. P. Hanga, G. Shaw et al. (2022) “Needle to needle robot-assisted manufacture of cell therapy products” *Bioengineering and Translational Medicine*, 7, 3. Accessed: e10387. DOI: 10.1002/btm2.10387.

[Orr77] F. M. Orr, R. A. Brown, L. E. Scriven (1977) “Three-dimensional menisci: Numerical simulation by finite elements” *Journal of Colloid and Interface Science*, 60, 1. Accessed: 137–147. DOI: 10.1016/0021-9797(77)90264-8. URL: https://www.sciencedirect.com/science/article/pii/0021979777902648.

[Pad72] J.F Padday, A. Pitt (1972) “Axisymmetric meniscus profiles” *Journal of Colloid and Interface Science*, 38, 2. Accessed: 323–334. DOI: 10.1016/0021-9797(72)90249-4.

[Pag21] M. J. Page, J. E. McKenzie, P. M. Bossuyt et al. (2021) “The PRISMA 2020 statement: an updated guideline for reporting systematic reviews” *Systematic Reviews*, 10, 1. Accessed: 89. DOI: 10.1186/s13643-021-01626-4. URL: https://systematicreviewsjournal.biomedcentral.com/articles/10.1186/s13643-021-01626-4.

[Pat05] K. Patel, E. Macii, M. Poncino (2005) “Frame buffer energy optimization by pixel prediction” *ICCD*. URL: https://www.semanticscholar.org/paper/Frame-buffer-energy-optimization-by-pixel-Patel-Macii/c162a3abbf5d6b02fa01cdc13905c276278cd024.

[Pel20] R. Pelc, Z. Hostounský, T. Otaki et al. (2020) *Conventional, Apodized, and Relief Phase-Contrast Microscopy*. Springer US and Imprint Humana. DOI: 10.1007/978-1-0716-0428-1_10. ISBN: 978-1-0716-0426-7.

[Pet79] J. H. Peters (1979) “Zeitraffer-Anlage zur Lebendbeobachtung von Zellen in der Kultur” *Microscopica acta*, 81, 3. Accessed: 217–225.

[Pip12] T. Piper, J. Piper (2012) “Axial Phase-Darkfield-Contrast (APDC), a new technique for variable optical contrasting in light microscopy” *Journal of microscopy*, 247, 3. Accessed: 259–268. DOI: 10.1111/j.1365-2818.2012.03641.x. URL: https://pubmed.ncbi.nlm.nih.gov/22906013/.

[Piz87] S. M. Pizer, E. P. Amburn, J. D. Austin et al. (1987) “Adaptive histogram equalization and its variations” *Computer Vision, Graphics, and Image Processing*, 39, 3. Accessed: 355–368. DOI: 10.1016/S0734-189X(87)80186-X. URL: https://www.sciencedirect.com/science/article/pii/S0734189X8780186X.

[Poo22] C. Poon (2022) “Measuring the density and viscosity of culture media for optimized computational fluid dynamics analysis of in vitro devices” *Journal of the Mechanical Behavior of Biomedical Materials*, 126. Accessed: 105024. DOI: 10.1016/j.jmbbm.2021.105024. URL: https://www.sciencedirect.com/science/article/pii/S1751616121006500.

[Pre25] Premteco (2025) *Was ist ein LCD-Bildschirm?* URL: https://www.ptcled.com/de/academy/what-is-a-lcd-screen.html. Accessed: 20 February 2025.

[Ren15] Y.-X. Ren, R.-D. Lu, L. Gong (2015) “Tailoring light with a digital micromirror device” *Annalen der Physik*, 527, 7-8. Accessed: 447–470. DOI: 10.1002/andp.201500111.

[Sal20] B. E. A. Saleh, M. C. Teich (2020) *Optik und Photonik*. Wiley-VCH. DOI: 10.1002/9783527825936. ISBN: 9783527347230.

[Śar14] Śaratcandran, S. Lüftl, T. Sabu et al. (2014) *Polyoxymethylene handbook: Structure, properties, applications and its nanocomposites*. Wiley. DOI: 10.1002/9781118914458. ISBN: 1118914422.

[Sch16a] F. W. Schenk (2016) *Hochdurchsatz-Mikroskopie von Mikrotiterplatten auf Basis einer kontinuierlichen Objektbewegung: High-throughput microscopy of microtiter plates based on a continuous object movement*. Apprimus Wissenschaftsverlag. ISBN: 9783863594640.

[Sch16b] F. W. Schenk, N. Brill, U. Marx et al. (2016) “High-speed microscopy of continuously moving cell culture vessels” *Scientific Reports*, 6, 1. Accessed: 34038. DOI: 10.1038/srep34038. URL: https://www.nature.com/articles/srep34038.

[Sch15] F. W. Schenk, M. Kulik, R. H. Schmitt (2015) “Metrology-based quality and process control in automated stem cell production” *tm - Technisches Messen*, 82, 6. Accessed: 309–316. DOI: 10.1515/teme-2015-0036.

[Shi17] H. Shiraishi, Y. Shiraishi (2017) “Phase Contrast Microscope and Imaging Method” JP2017151132A.

[Sho05] M. R. Shortis, J. W. Seager, E. S. Harvey et al. “Influence of Bayer filters on the quality of photogrammetric measurement”. In: *Videometrics VIII*. Ed. by J.-Angelo Beraldin, Sabry F. El-Hakim, Armin Gruen, et al. SPIE Proceedings. SPIE, 2005, Accessed: 164. DOI: 10.1117/12.588217.

[Sim24] M. C. Simone, S. Veneziano, R. Pace et al. (2024) “Multibody Analysis of Sloshing Effect in a Glass Cylinder Container for Visual Inspection Activities” *Applied Sciences*, 14, 11. Accessed: 4522. DOI: 10.3390/app14114522. URL: https://www.mdpi.com/2076-3417/14/11/4522.

[Ste03] D. J. Stephens, V. J. Allan (2003) “Light Microscopy Techniques for Live Cell Imaging” *American Association for the Advancement of Science*. URL: https://www.science.org/doi/full/10.1126/science.1082160.

[Sun06] C. Sun, R. Beare, V. Hilsenstein et al. (2006) “Mosaicing of Microscope Images with Global Geometric and Radiometric Corrections” *Journal of Microscopy*, 224, Pt 2. Accessed: 158–165. DOI: 10.1111/j.1365-2818.2006.01687.x. URL: https://onlinelibrary.wiley.com/doi/full/10.1111/j.1365-2818.2006.01687.x.

[Suz85] S. Suzuki, A. Keiichi (1985) “Topological structural analysis of digitized binary images by border following” *Computer Vision, Graphics, and Image Processing*, 30, 1. Accessed: 32–46. DOI: 10.1016/0734-189X(85)90016-7.

[Sze06] R. Szeliski (2006) *Image Alignment and Stitching: A Tutorial*. Now Publ. ISBN: 1933019042.

[Tal24] A. Talebipour, M. Saviz, M. Vafaiee et al. (2024) “Facilitating long-term cell examinations and time-lapse recordings in cell biology research with CO2 mini-incubators” *Scientific Reports*, 14, 1. Accessed: 3418. DOI: 10.1038/s41598-024-52866-y. URL: https://www.nature.com/articles/s41598-024-52866-y.

[Tau91] G. Taubin (1991) “Estimation of planar curves, surfaces, and nonplanar space curves defined by implicit equations with applications to edge and range image segmentation” *IEEE Transactions on Pattern Analysis and Machine Intelligence*, 13, 11. Accessed: 1115–1138. DOI: 10.1109/34.103273.

[The19] The Standardization Committee — CoaXPress Working Group (2019) *CoaXPress Version 2.0: JIIA CXP-001-2019* URL: https://www.coaxpress.com/. Accessed: 22 March 2025.

[Tho85] I. Thormählen, J. Straub, U. Grigull (1985) “Refractive Index of Water and Its Dependence on Wavelength, Temperature, and Density” *Journal of Physical and Chemical Reference Data*, 14, 4. Accessed: 933–945. DOI: 10.1063/1.555743.

[Tri03] F. Triaud, C. Darmon, Y. Cariou et al. (2003) “Evaluation of an Automated Cell Culture Incubator: The Autocell 200” *JALA: Journal of the Association for Laboratory Automation*, 8, 6. Accessed: 87–95. DOI: 10.1016/s1535-5535(03)00024-8.

[Tsu20] T. Tsujimoto (2020) “Learning Device, Method, and Program for Discriminator, and Discriminator” JP20170162052.

[Ulr81] H. Ulrich (1981) *Die Betriebswirtschaftslehre als anwendungsorientierte Sozialwissenschaft*. Pöschel. ISBN: 3791003089.

[Vol80] D. Vollath (1980) “Verfahren und Einrichtung zur automatischen Scharfeinstellung eines jeden Bildpunktes eines Bildes: Europäisches Patent” EP0017726A1.

[Wad78] R. H. Wade (1978) “The phase contrast characteristics in bright field electron microscopy” *Ultramicroscopy*, 3, 3. Accessed: 329–334. DOI: 10.1016/s0304-3991(78)80043-6.

[Wan14] Y. Wang (2014) “Advanced Theory of Field Curvature” URL: https://www.semanticscholar.org/paper/Advanced-Theory-of-Field-Curvature-Wang/db04023f26ba09ffaee904e9a1e3f9aa3000040f.

[Wan20] Z. Wang, Z. Yang (2020) “Review on image-stitching techniques” *Multimedia Systems*, 26, 4. Accessed: 413–430. DOI: 10.1007/s00530-020-00651-y.

[Wik25] Wikimedia Commons (2025) *File:Oeffnungswinkel.png* URL: https://commons.wikimedia.org/wiki/File:Oeffnungswinkel.png. Accessed: 22 March 2025.

[Wil10] C. Willert, B. Stasicki, J. Klinner et al. (2010) “Pulsed operation of high-power light emitting diodes for imaging flow velocimetry” *Measurement Science and Technology*, 21, 7. Accessed: 075402. DOI: 10.1088/0957-0233/21/7/075402.

[Yan20] C. Yang, M. Chen, F. Zhou et al. (2020) “Accurate and Rapid Auto-Focus Methods Based on Image Quality Assessment for Telescope Observation” *Applied Sciences*, 10, 2. Accessed: 658. DOI: 10.3390/app10020658. URL: https://www.mdpi.com/2076-3417/10/2/658.

[Yan14] D. Yang (2014) *Fundamentals of liquid crystal devices*. John Wiley & Sons Inc. DOI: 10.1002/9781118751992. ISBN: 1118751981.

[Yas09] M. Yasumoto, R. Kuroda, H. Ikeura-Sekiguchi et al. (2009) “X-ray imaging with laser-Compton scattering X-ray at AIST” *Journal of Physics: Conference Series*, 186. Accessed: 012039. DOI: 10.1088/1742-6596/186/1/012039.

[Yin12] Z. Yin, T. Kanade, M. Chen (2012) “Understanding the phase contrast optics to restore artifact-free microscopy images for segmentation” *Medical image analysis*, 16, 5. Accessed: 1047–1062. DOI: 10.1016/j.media.2011.12.006.

[Yoo15] Y. Yoo, J. Im, J. Paik (2015) “Low-Light Image Enhancement Using Adaptive Digital Pixel Binning” *Sensors (Basel, Switzerland)*, 15, 7. Accessed: 14917–14931. DOI: 10.3390/s150714917.

[Yu21] L. Yu, W. Wan, K. M. Yu et al. (2021) “High order phase contrast and source divergence in low energy electron microscopy” *Ultramicroscopy*, 225. Accessed: 113284. DOI: 10.1016/j.ultramic.2021.113284.

[Zer42] F. Zernike (1942) “Phase contrast, a new method for the microscopic observation of transparent objects” *Physica*, 9, 7. Accessed: 686–698. DOI: 10.1016/S0031-8914(42)80035-X.

[Zer55] F. Zernike (1955) “How I discovered phase contrast” *Science*, 121, 3141. Accessed: 345–349. DOI: 10.1126/science.121.3141.345.

[Zha22] X. Zhao, R. Kerpes, T. Becker (2022) “Evaluation of microtiter plate as a high-throughput screening platform for beer fermentation” *European Food Research and Technology*, 248, 7. Accessed: 1831–1846. DOI: 10.1007/s00217-022-04009-8. URL: https://link.springer.com/article/10.1007/s00217-022-04009-8.

[Zhu13] B. Zhu, L. Xie, G. Song et al. (2013) “An Efficient Projection Defocus Algorithm Based on Multi-Scale Convolution Kernel Templates” *Journal of Zhejiang University SCIENCE C*, 14, 12. Accessed: 930–940. DOI: 10.1631/jzus.C1300080. URL: https://link.springer.com/article/10.1631/jzus.C1300080.

[Zhu23] M. Zhu, L. Yu, Z. Wang et al. (2023) “Review: A Survey on Objective Evaluation of Image Sharpness” *Applied Sciences*, 13, 4. Accessed: 2652. DOI: 10.3390/app13042652. URL: https://www.mdpi.com/2076-3417/13/4/2652.

List of Related Publications

In the course of this dissertation, two scientific papers were published, each presenting partial findings of the research. These publications are as follows:

1. F. Nienhaus, T. Piotrowski, B. Nießing et al. (2023) “Adaptive Phase Contrast Microscopy to Compensate for the Meniscus Effect”, *Scientific Reports* [Nie23].
2. F. Nienhaus, F. Burkhardt, N. König et al. (2025) “Compensating the Meniscus Effect in Phase Contrast Microscopy Using an LCD for Adaptive Condenser Annulus Shifting”, *Microscopy research and technique* [Nie25].

List of Contributing Theses

Various bachelor's and master's theses by students contributed to this dissertation. The author of this dissertation thesis supervised all students involved. Their findings were integrated into multiple sections of this work, aiding in addressing the research questions. The following theses were partially incorporated into this dissertation:

1. Optimierung und Erweiterung der Steuer-Software eines Mikroskopie-Demonstrators des Fraunhofer IPT (July 2023), Bachelor Thesis, Jonas Krämer.
2. Development of an Adaptive Prism Unit to Compensate for the Meniscus Effect in Phase Contrast Microscopes (January 2024), Master Thesis, Vedhashruthi Harinath.
3. Implementation of a Machine-Learning-Model capable of controlling a phase-contrast microscope from image-data (February 2024), Master Thesis, Luca Frenken.
4. Implementation of a Model to Simulate the Optical Path of a Phase Contrast Microscope (February 2024), Master Thesis, René Joel Banczyk.
5. Implementation of a procedure for a demonstrator to compensate for the meniscus effect in phase contrast microscopes (March 2024), Master Thesis, Shiva Kumar Kodihalli Puttaswamy.

List of Figures

List of Tables

Acronyms

AI artificial intelligence
CAD computer aided design
DMD digital mirror device
FOV field of view
fps frames per second
HSM high-speed microscopy
iPSC induced pluripotent stem cell
LCD liquid crystal display
LED light-emitting diode
MP Megapixel
MSC mesenchymal stem cell
MTP microtiter plate
NA numerical aperture
PRISMA preferred reporting items for systematic reviews and meta-analyses
RGB red, green, blue
ROI region of interest
SNR signal-to-noise ratio
SRQ sub-research question

List of Symbols

Symbol	Description	Unit
$*$	Convolution operator	-
∇	Laplace operator	1/m
α	Aperture angle	°
$\alpha(x)$	Meniscus angle	°
α	Tilt angle of the prism around the y-axis	°
α	Significance level of hypothesis test	%
$\Delta\alpha$	Meniscus angle difference within one image	°
β	Tilt angle of the prism around the x-axis	°
γ	Surface tension	N/m
γ_{LV}	Liquid-vapor surface energy	N/m
$\gamma_{n,i}$	Angle within the prism at the interface n	°
γ_{SL}	Solid-liquid surface energy	N/m
γ_{SV}	Solid-vapor surface energy	N/m
δ_i	Servo motor positions	°
ϵ	Global incidence angle before prism	°
ζ	Global refracted angle after prism	°
θ	Contact angle between liquid and solid	°
θ_i	Angle of incidence	°
θ_n	Angle of the n^{th} minimum light intensity	°
θ_r	Angle of refraction	°
$\theta_{\text{reflection}}$	Angle of reflection	°
λ	Wavelength	m
ξ	Angle of polarization	°
Π	Camera's pixel pitch	m
ρ	Density	kg/m^3
σ	Standard deviation	-
$\sigma_{t,\text{LCD}}$	Standard deviation of the LCD's reaction time	s
τ	Twist angle in liquid crystals	°
ϕ	Phase of light	-
ψ	Wave function	-
A	Area	m^2
a	Acceleration	m/s^2
B	Magnetic field	-
B	Bond number	-

Symbol	Description	Unit
b	Bit depth	-
b	average image brightness	-
b_{max}	Maximum brightness during LCD experiments	-
b_{min}	Minimum brightness during LCD experiments	-
b_{thr}	Brightness threshold for LCD experiments	-
c	Speed of light	m/s
c_0	Speed of light in vacuum	m/s
d	Resolution limit	m
d_{crystals}	Thickness of liquid crystal layers	m
d_i	Image distance from a mirror	m
d_o	Object distance from a mirror	m
Δd	Trigger distance	m
$\Delta\vec{d}$	Condenser annulus shift observed through Bertrand lens	-
F	Focal point	-
f	Focal length	m
f	Frequency	Hz
f	Camera frame rate	1/s
$\vec{f}$	External force	N
$f_{\text{black}}(x, y)$	Black reference image	-
$F(u, v)$	Fourier-transformed image of f(x,y)	-
$f_{\text{white}}(x, y)$	White reference image	-
$f(x, y)$	Digital image	-
g	Gravitational acceleration	m/s^2
$\overline{g}$	Average gray value	-
g_{br}	Brightfield gray value	-
g_{ph}	Base gray value for phase contrast	-
$g(x, y)$	Gaussian kernel	-
H	Electric field	-
H	Mean curvature of meniscus	m
h	Height of fluid column	m
h_i	Servo handle height	m
$H(u, v)$	Fourier-transformed image of h(x,y)	-
$h(x, y)$	Transformed digital image	-
I	Intensity	-
K	Constant scaling factor	-
k	Safety factor	-
L	Laplacian filter kernel	-
l_c	Capillary length	m
l_{lever}	Prism lever length	m
l_{max}	Upper gray value limit	-
l_{min}	Lower gray value limit	-
l_{servo}	Servo handle length	m

Symbol	Description	Unit
m	Width of a digital image	-
M	Magnification	-
n	Refractive index	-
n	General positive integer	-
n	Height of a digital image	-
NA	Numerical aperture	-
n_{pixel}	Pixel count in direction of motion	-
Δn	Birefringence	-
o	Relative overlap	-
o	Roundness	-
P	Petzval sum	1/m
P	Perimeter	m
p	Pressure	N/m^2
$\vec{p}$	Optimal condenser annulus position	m
$\vec{p}_0$	Default condenser annulus position	m
p_0	Atmospheric pressure at a fluid's surface	N/m^2
$\Delta\vec{p}$	Shift of condenser annulus position	m
q_i	Center of gravity at section i for LCD experiments	-
q_{thr}	Center of gravity threshold for LCD experiments	-
R	Reflective coefficient	-
R	Local radius of curvature of a meniscus	m
r	Radius	m
r	Prism lever length	m
$\vec{r}$	Spatial position	m
R_{eff}	Effective reflective coefficient	-
R_i	Principal radius of curvature of a surface at position i	m
R_p	Reflective coefficient for p-polarized light	-
r_P	Petzval radius	m
R_s	Reflective coefficient for s-polarized light	-
r_{well}	Radius of a well	m
$s_{\text{Tenengrad}}$	Tenengrad sharpness	-
s_x	Sobel gradient in x-direction	-
$S(x, y)$	Sobel operator	-
s_y	Sobel gradient in y-direction	-
T	Transmission coefficient	-
T	Threshold	-
t	Time	s
t_{acc}	Acceleration time during a scan	s
t_{dec}	Deceleration time during a scan	s
t_{flash}	Flash duration	s
t_{frame}	Time between two frames of the LCD	s
t_L	Scan time of one line	s
$\overline{t_{\text{LCD}}}$	Mean reaction time of the LCD	s

Symbol	Description	Unit
t_{lower}	Lower threshold for phase contrast algorithm	-
T_{pc}	Relative threshold for phase contrast	-
T_{total}	Total effective transmission through prism	-
t_{upper}	Upper threshold for phase contrast algorithm	-
t_v	Time at constant velocity during a scan	s
Δt	Trigger delay	s
U	Wave amplitude	-
U_{LED}	LCD voltage	V
v	Velocity	m/s
w	Aperture width	m
$W(u, v)$	Fourier-transformed image of w(x,y)	-
$w(x, y)$	Filter kernel	-
x	x-coordinate in an image	-
y	y-coordinate in an image	-
Z	Depth of field	m
$z(x)$	Measured meniscus height at position x	m

Appendices

Table A.1: Publications identified via database search for *phase contrast conditions*. The fourth column indicates the step at which a publication was excluded, the fifth column lists the exclusion criterion, and the sixth column provides the reason for exclusion.

Primary author	Year	Title	Step	Exclusion criterion	Exclusion argument
Nienhaus, F [Nie23]	2023	Adaptive phase contrast microscopy to compensate for the meniscus effect	4	4	Phase contrast area determined by experts, no quantifiable criteria
Peters, JH [Pet79]	1979	Device for time-lapse studies on living cells in vitro	3	3	No meniscus effect
Loos, J [Loo96]	1996	A comparison of the lamellar morphology of melt-crystallized isotactic and syndiotactic polypropylene	3	2	No light microscopy
Yasumoto, M [Yas09]	2009	X-ray imaging with laser-Compton scattering X-ray at AIST	3	1	Not focussed on phase contrast microscopy
Ahmed, IAM [Moh10]	2010	Isolation and characterization of homocholine-degrading Pseudomonas sp strains A9 and B9b	3	3	No meniscus effect
De Giorgi, M [Gio01]	2001	Interpretation of phase and strain contrast of TEM images of InxGa1-xAs/GaAs quantum dots	3	2	No light microscopy
Laiwejpithaya, S [Lai18]	2018	UriSed 3 and UX-2000 automated urine sediment analyzers vs manual microscopic method: a comparative performance analysis	3	1	Not focussed on phase contrast microscopy
Yu, L [Yu21]	2021	High order phase contrast and source divergence in low energy electron microscopy	3	2	No light microscopy
Wade, RH [Wad78]	1978	Phase-contrast characteristics in bright field electron microscopy	3	2	No light microscopy
Erni, R [Ern16]	2016	Coherent Chromatic Effect in the Transmission Electron Microscope	3	2	No light microscopy

Primary author	Year	Title	Step	Exclusion criterion	Exclusion argument
Linck, M [Lin16]	2016	Chromatic Aberration Correction for Atomic Resolution TEM Imaging from 20 to 80 kV	3	2	No light microscopy
Li, XJ [Li22]	2022	Imaging biological samples by integrated differential phase contrast (iDPC) STEM technique	3	2	No light microscopy

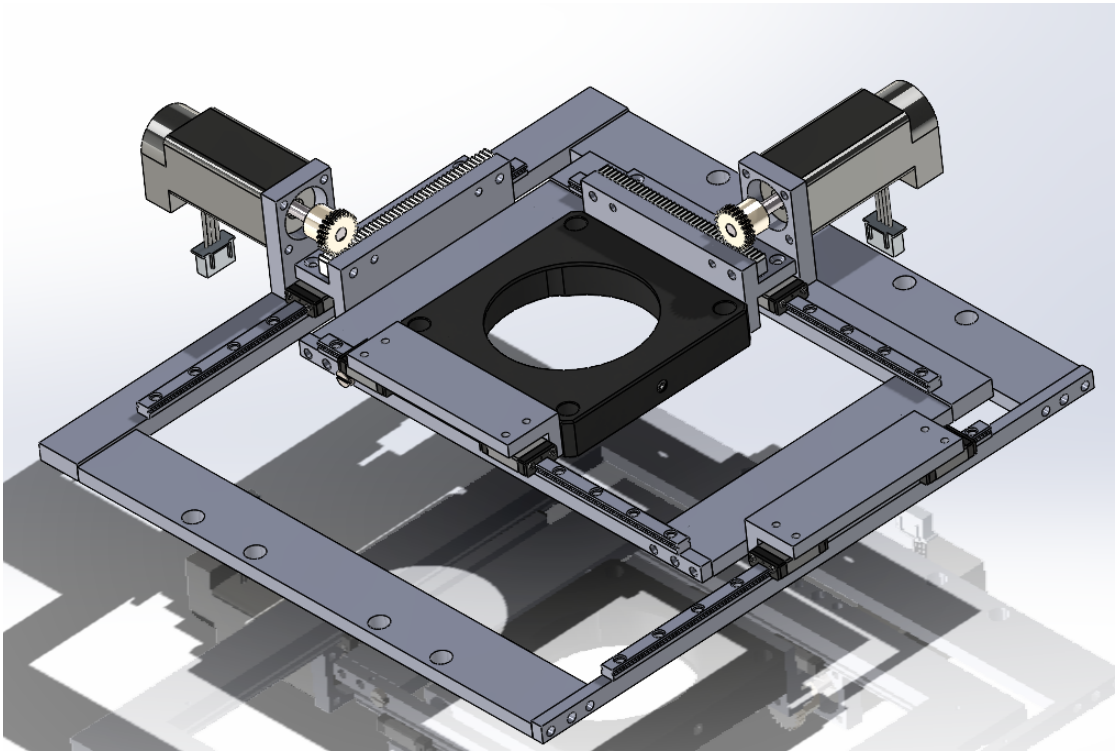

Figure A.1: CAD drawing of a movable lens demonstrator.

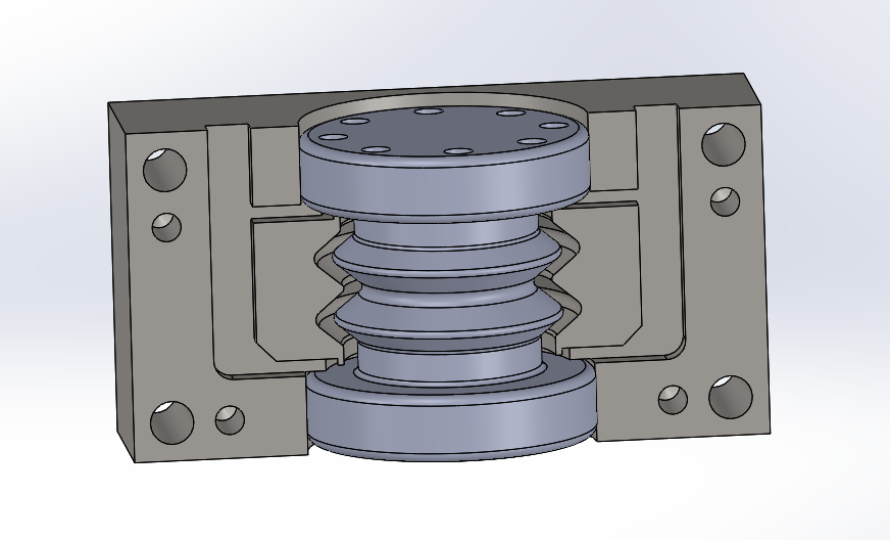

Figure A.2: Casting mold for the prism's flexible silicon shell, comprising two mirror-symmetrical parts and a rotationally symmetric (excluding the ventilation holes) core. One mold part is omitted to reveal the interior.

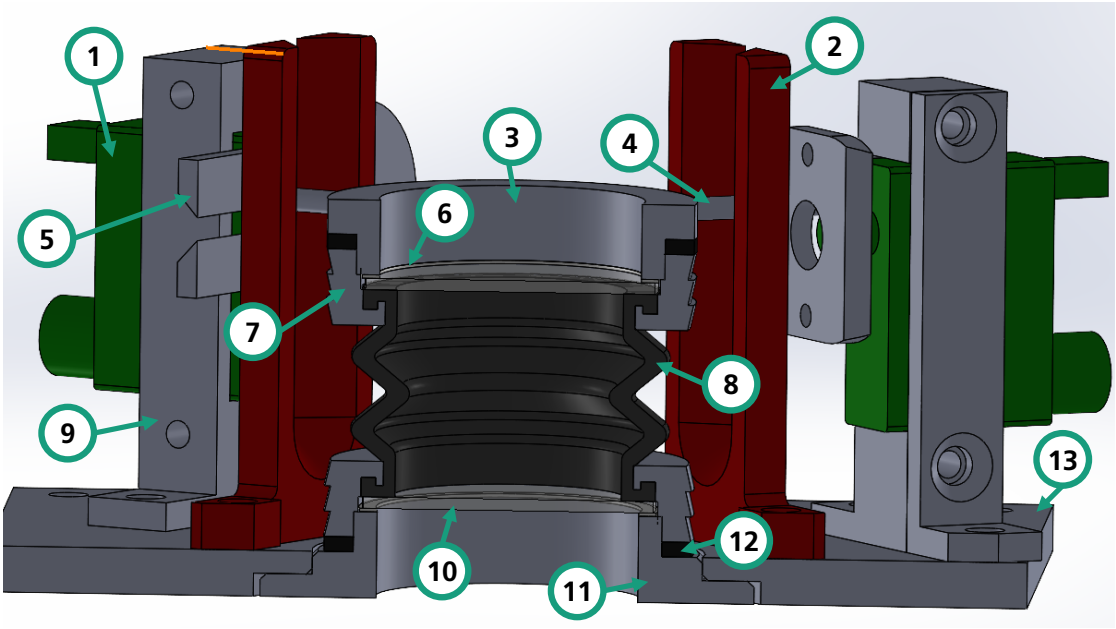

Figure A.3: Cross-section through a CAD drawing of the liquid-filled prism and its actuation. (1) Servo motor. (2) Lever guidance. (3) Metal housing outer part with lever connection. (4) Lever. (5) Servo handle. (6) Spacer. (7) Metal housing inner part. (8) Flexible silicon shell. (9) Servo mount. (10) Glass plate. (11) Metal housing outer part with base plate connection. (12) Spacer. (13) Base plate.

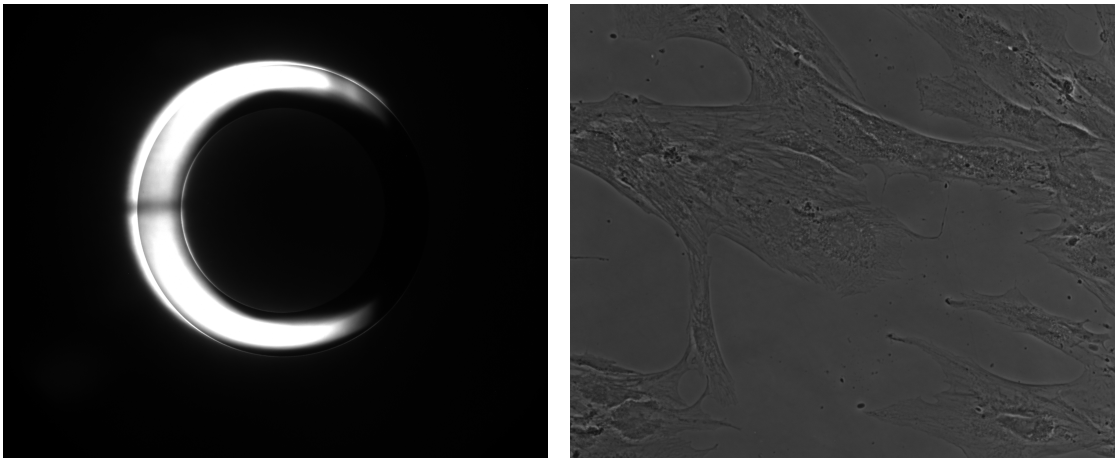

(a) Phase ring. **(b)** Sample.

Figure A.4: Bertrand lens image (a) and sample image (b) obtained during the experimental sequence illustrated in Figure 5.14. These images correspond to the 19th position of the LCD measurements situated 5.7 mm from the center. The sample image exhibits reduced brightness due to partial shadowing, likely caused by the well wall.

Table A.2: Transmission T_{eff} and reflection R_{eff} coefficients at each interface of a liquid-filled prism, with a prism tilt of $\alpha = 10°$. The overall transmission is calculated as the product of individual transmissions, yielding 91.3°. Here, n_1 and n_2 are the refractive indices of Surfaces 1 and 2, respectively. The angle of incidence is denoted by γ_i, and γ_r refers to the refracted angle.

Surface 1	Surface 2	n_1	n_2	γ_i	γ_r	R_{eff}	T_{eff}
Air	Glass	1.00	1.50	16.9°	11.1°	4.0%	96.0%
Glass	Water	1.50	1.33	11.1°	12.6°	0.4%	99.6%
Water	Glass	1.33	1.50	22.6°	19.9°	0.4%	99.6%
Glass	Air	1.50	1.00	19.9°	30.7°	4.2%	95.8%

Table A.3: Experiments to determine the frame switch time. Ring positions are depicted at the given time since the start of the measurement. The orange line indicates the center of mass in x-direction.

Time [ms]	Image	Center of mass in x [pixels]
1109	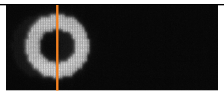	119
1110	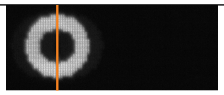	119
1111	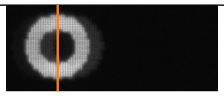	121
1112	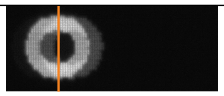	123
1113	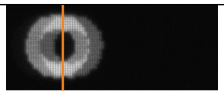	133
1114	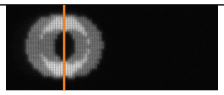	135
1115	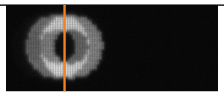	137
1116	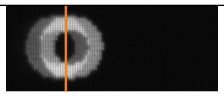	139
1117	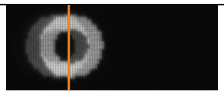	146
1118	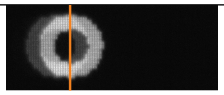	150
1119	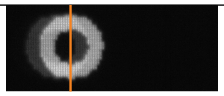	151
1120	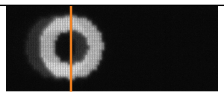	151
1121	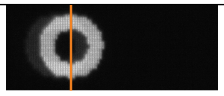	151
1122	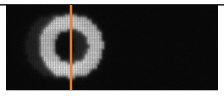	152
1123	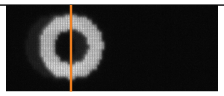	152

Table A.4: Times to switch between two frames during LCD switching time experiments, extracted from ten experiments.

Series	1	2	3	4	5	6	7	8	9	10	All
Mean [ms]	16.7	16.7	16.7	16.7	16.7	16.6	16.6	16.8	16.7	16.7	**16.7**
Median [ms]	17	17	17	17	17	17	17	17	17	17	**17**
Std [ms]	0.47	0.47	0.47	0.47	0.46	0.48	0.48	0.43	0.47	0.47	**0.47**
Min [ms]	16	16	16	16	16	16	16	16	16	16	**16**
Max [ms]	17	17	17	17	17	17	17	17	17	17	**17**
Max - Min [ms]	1	1	1	1	1	1	1	1	1	1	**1**

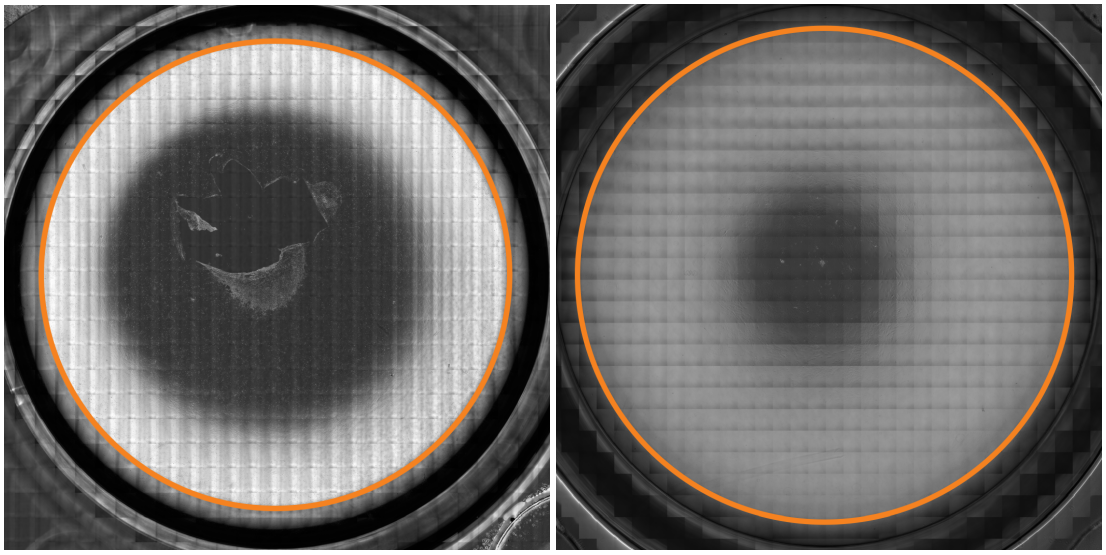

(a) MTP6, 4x magnification.

(b) MTP24, 10x magnification.

Figure A.5: The maximum achievable phase contrast area in two different well plates and magnifications is outlined by orange circles. Shading by the MTP walls reduces brightness outside of this circle.

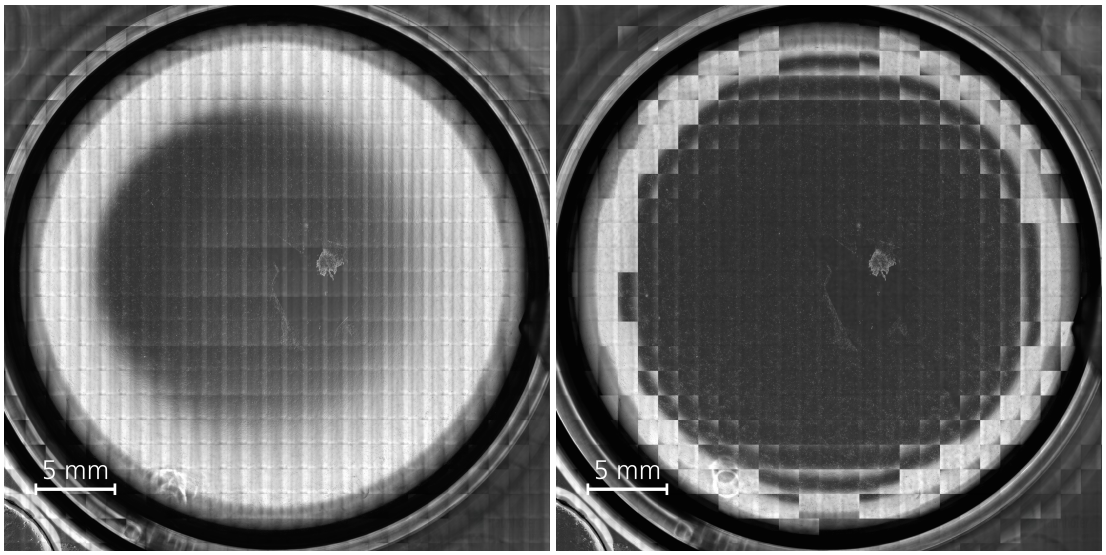

(a) Regular phase contrast microscopy.

(b) Adaptive phase contrast microscopy.

Figure A.6: Images of a whole well in an MTP6 with 4x magnification as result of the validation experiments to determine the phase contrast area using a stop-and-go scanning process.

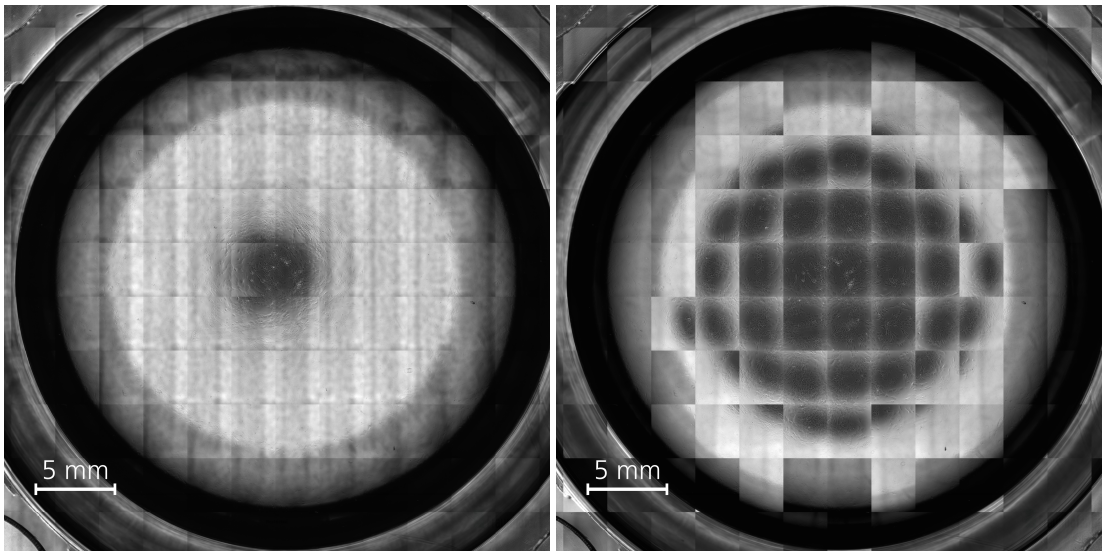

(a) Regular phase contrast microscopy. **(b)** Adaptive phase contrast microscopy.

Figure A.7: Images of a whole well in an MTP24 with 4x magnification as result of the validation experiments to determine the phase contrast area using a stop-and-go scanning process.

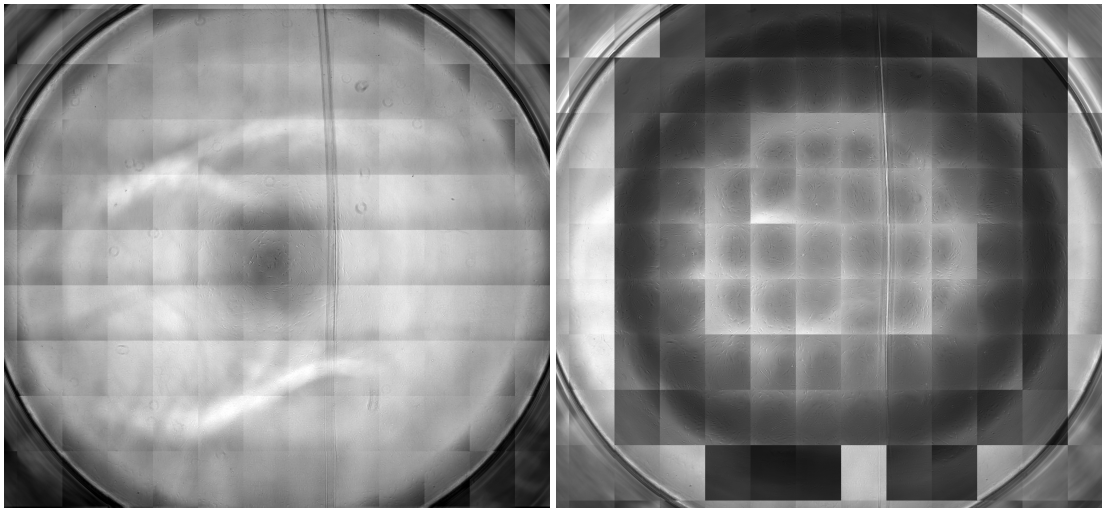

(a) Regular phase contrast microscopy. **(b)** Adaptive phase contrast microscopy.

Figure A.8: Images of a whole well in an MTP96 with 10x magnification as result of the validation experiments to determine the phase contrast area using a non-continuous scanning process.

Table A.5: Images captured during experiments to assess the reaction time of the LCD. These images illustrate the gradual transition from black to white. The *Gray value* denotes the average brightness of the entire image, utilized to identify the moment when the image is completely rendered.

Index	Image	Gray Value
48	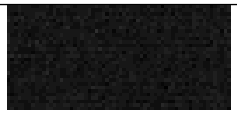	22.6
49		29.2
50		36.2
51		43.7
52		50.9
53	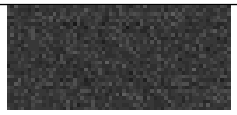	57.4
54	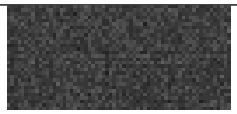	63.1
55	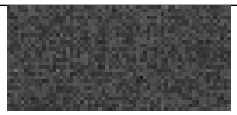	68.6
56	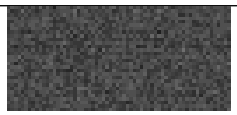	72.2
57	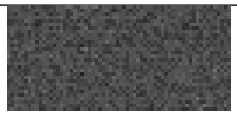	75.4
58	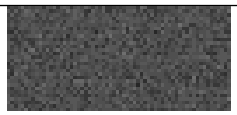	78.2
59	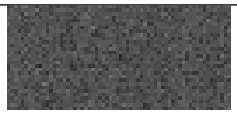	80.9

Table A.6: Minimum distance from the well center, denoted as *Min thr*, where phase contrast conditions cannot be maintained across the entire image. Distinctions exist based on whether the image diagonal or the shortest side is considered. *Num images* indicates the number of images this position is from the well center, assuming images are captured adjacently without overlap. *M*: magnification. Applicable only to MTP24.

	Sensor dimensions [mm]		Min thr [mm]		Num images	
M	diagonal	short side	diagional	short side	diagonal	short side
4	2.11	1.35	1.33	2.79	0.6	2.1
10	0.85	0.54	6.26	outside of well	7.4	-

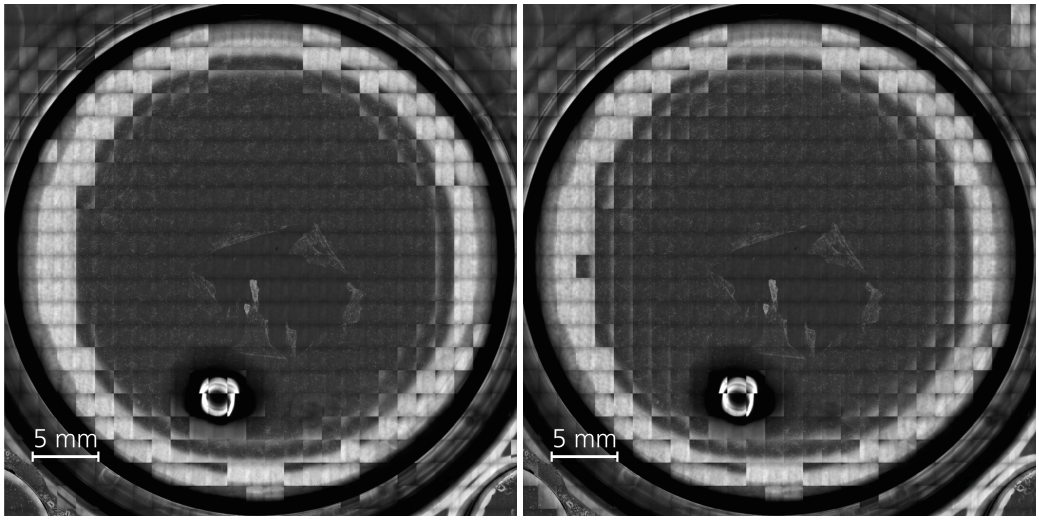

(a) Single well. **(b)** Row of wells.

Figure A.9: Comparison of composite images for MTP6 at 4x magnification to determine whether it makes a difference if wells are captured individually or as part of a whole MTP. (a) Image acquired from a single well. (b) Image acquired from an entire row of wells. The white ring-like shape with a black halo in the lower left is due to a droplet on the lid of the well.

Table A.7: Comparison of relative phase contrast areas between single wells and wells acquired as part of a whole row across various MTP sizes, magnifications, and frame rates. Abbreviations: *Image Par*: Imaging parameters, *M*: Magnification, *f*: Frame rate, *Std*: Standard deviation in percentage points.

Image Par			Single well		Well within row	
MTP	M	f	Mean [%]	Std [%]	Mean [%]	Std [%]
6	4	15	54.0	2.1	53.7	1.8
24	4	30	19.6	0.8	21.7	2.0
24	10	30	42.7	0.1	44.2	0.6
24	10	60	45.3	0.4	44.7	1.8

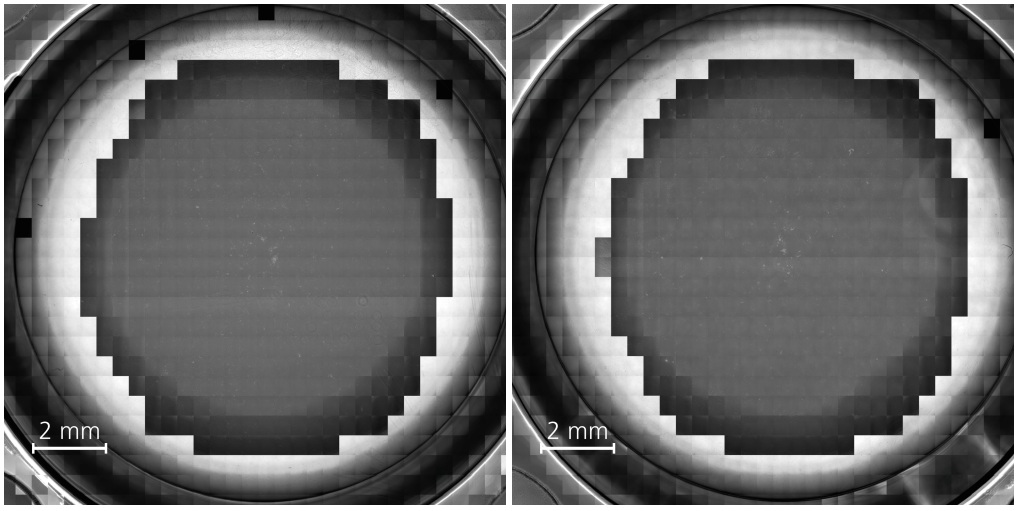

(a) Single well. **(b)** Row of wells.

Figure A.10: Comparison between composite images of MTP24 at 10x magnification, captured using the high-speed process. In (a), an image of only one well was acquired at a time, whereas in (b), multiple images within a row were captured simultaneously.

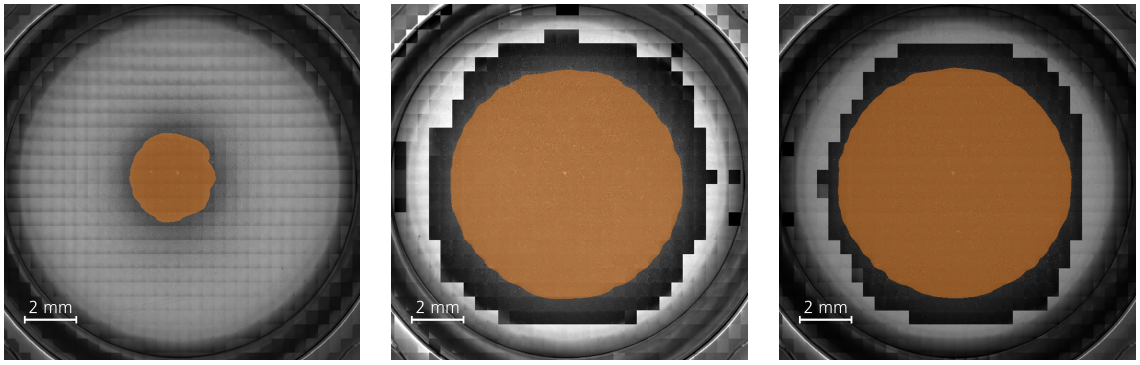

(a) Conventional phase contrast microscopy. **(b)** Adaptive stop-and-go scan. **(c)** Adaptive high-speed scan.

Figure A.11: Evaluation of the images in Figure 7.18. (a), (b), and (c) correspond to Figures 7.18d, 7.18e, and 7.18f, respectively. Phase contrast area evaluation utilizes the algorithm described in Section 4.2. The phase contrast areas are quantified as 6.0%, 42.3%, and 42.6%. Variations in brightness levels across images result from preprocessing and do not indicate image quality.